Comportement vieillissant du béton en fluage : application au béton VeRCoRs

Shun Huang

UNIVERSITÉ PARIS-EST

PhD Thesis

Université Paris-Est, France
École Doctorale Sciences, ingénierie et environnement - (SIE) ED 531

Doctorat Sciences des Matériaux

Shun HUANG

Comportement vieillissant du béton en fluage
Application au béton VeRCoRs

Ageing behaviour of concrete creep
Application to the VeRCoRs concrete

Soutenue à Champs-sur-Marne le 4 Décembre 2018

J.M.	TORRENTI	Président
A.	SELLIER	Rapporteur
J.F.	SHAO	Rapporteur
F.	BENBOUDJEMA	Examinateur
J.	SANAHUJA	Examinateur
B.	BARY	Examinateur
E.	LEMARCHAND	Examinateur
G.	CARATINI	Invité
L.	DORMIEUX	Directeur

Remerciements

Je souhaite tout d'abord remercier Julien Sanahuja d'$EDF - R\&D$. Il m'a fait confiance dans ce travail de longue haleine. Je lui dois tout l'environnement particulièrement propice à un travail de thèse qu'il a bien voulu créer pour moi, ainsi que toute l'ouverture d'esprit qu'il m'a proposée en m'intégrant dans ses différentes activités. Qu'il sache qu'il a été un encadrant très apprécié par ses qualités professionnelles et humaines.

Qu'il me soit aussi permis de remercier l'ensemble des membres du groupe T25 du département MMC d'$EDF - R\&D$. Parmi les personnalités que j'ai eu le loisir de rencontrer et qui m'ont le plus marqué ou influencé, je me dois de citer plus particulièrement : Laurent Charpin, Didier Leroy, Romain Thion, Jean-Philippe Mathieu, Jean-Luc Adia, Chaveli Bitsindou, Laurent Petit, Justin Kinda et Khai Quynh Dinh. Ils ont bien voulu répondre à mes nombreuses questions, me conseiller et m'accueillir chaleureusement à la réalisation de mon programme expérimental, à la fabrication des éprouvettes, aux calculs sur différents modèles, aux rencontres amicales au Laboratoire C22 à 9 heures autour d'un café; je sais qu'ils se reconnaîtront. Je remercie particulièrement Régis Nhili, Eric Molinie, Hing-Ip Wong, Cécile Miller et Youcef Sirsalane du département MMC, pour leur remarquable professionnalisme, leurs qualités humaines et leurs conseils pertinents lors de nos discussions. Je remercie aussi l'ensemble des membres du groupe T24 pour leur gentillesse et leur aide tout au long de ma carrière au département MMC.

Je remercie de même Luc Dormieux (Professeur du Laboratoire NAVIER - UMR 8205), Benoît Bary (Chercheur du Laboratoire LECBA de CEA) et Eric Lemarchand (Chargé de recherche du Laboratoire NAVIER - UMR 8205) qui ont été respectivement mon directeur de thèse, mon encadrant au CEA et mon encadrant au Laboratoire NAVIER. Ils sont pour beaucoup dans ce travail de thèse qui s'inspire largement de leurs nombreux travaux. Je remercie à Benoît Bary aussi pour le temps qu'il m'a consacré, la simplicité de son contact et l'enthousiasme qu'il m'a fait partager pour la recherche scientifique.

Je remercie tout autant les membres du Laboratoire LECBA de CEA, qu'ils soient chefs de laboratoire, chercheurs, assistants, personnels administratifs, techniciens ou secrétaires, thésards et stagiaires pour les nombreux services que je leur ai demandés. Stéphane Poyer, Christophe Imbert et Etienne Amblard ont largement participé à ma culture scientifique, aux discussions très intéressantes et acharnées. Si je garde un aussi bon souvenir de ces trois années, c'est bien grâce à eux aussi.

Au cours de ma thèse j'ai eu l'occasion d'échanger avec les chercheurs et les ingénieurs dans deux autres départements d'$EDF - R\&D$ et d'EDF DI. Je les en remercie, ils m'ont beaucoup apporté dans des domaines scientifiques très complémentaires.

Qu'il me soit aussi permis de remercier globalement toutes les autres personnes que j'ai rencontrées pendant ces trois ans à $EDF - R\&D$, au CEA et au Laboratoire Navier de l'ENPC dont le nom n'apparaît pas dans ces quelques lignes mais que je remercie individuellement.

Qu'il me soit surtout permis de remercier mes deux rapporteurs, Prof. Shao et Prof. Sellier ainsi que les autres membres de mon jury, Prof. Torrenti, Prof. Benboudjema et Dr. Caratini pour l'honneur qu'ils me font et le temps qu'ils ont bien voulu m'accorder.

Enfin, je remercie l'ensemble des personnes de ma famille qui m'ont soutenu au cours de mes

études et dans mon projet de thèse. Je remercie surtot mon grandpère, Min Huang, qui m'a aidé et encouragé tout au long de cette expérience. Je remercie aussi Georges, Qiwei, Eric, Ziling, Fengjuan, Hao, Barbara, Zhuangzhuang et d'autres amis pour leur soutien quotidien.

Merci et bonne lecture !

Shun HUANG

Résumé

Le béton est un matériau présentant du fluage propre (déformation différée évoluant dans le temps, sous charge mécanique constante et température constante, en l'absence d'échanges hydriques avec l'extérieur). Ce comportement en fluage est de plus vieillissant (l'évolution de la déformation dépend de l'instant d'application de la charge constante ; il ne s'agit pas d'une simple translation en temps). Ce comportement vieillissant traduit le caractère « vivant » du matériau, dont la microstructure évolue considérablement au fil du temps.

L'étude du fluage du béton est particulièrement critique pour les enceintes de confinement précontraintes, puisque le fluage a pour conséquence une relaxation de cette précontrainte dans le temps. Or les bétons d'enceinte sont mis en charge (application de la précontrainte) au bout de 2-3 ans environ, alors que les essais de fluage sur éprouvettes sont réalisés après 3 mois de maturation. Évidemment, la réponse en fluage mesurée sur un essai en moins d'un an ne peut être directement transposée sur un calcul de structure pour un chargement à 3 ans. Il est de même exclu d'attendre plusieurs années pour réaliser un essai de fluage sur éprouvette. Afin de relier ces deux réponses en déformation, obtenues par chargement à deux instants différents, un modèle de comportement matériau intégrant le fluage vieillissant s'avère nécessaire.

Pour développer un tel modèle, compte tenu de la nature multi-échelle et multi-physique du béton, l'approche micromécanique représente une piste particulièrement attractive. En effet, plusieurs ordres de grandeur de dimensions séparent l'échelle des mécanismes physiques responsables du fluage de celle d'usage. La validation se fera vis à vis d'essais sur béton Vercors. Ces approches micromécaniques sont l'objet d'une action de recherche en collaboration avec l'EDF, l'ENPC et le CEA Saclay.

La thèse vise à construire une loi de comportement de fluage propre vieillissant d'un béton, sur la base d'arguments physiques, par une démarche micromécanique, et à la valider expérimentalement.

Le volet modélisation de la thèse présente deux objectifs principaux : déterminer le comportement vieillissant du béton à partir de celui de la pâte, et estimer le comportement vieillissant de la pâte elle-même à partir d'informations sur les micro-mécanismes sous-jacents. Le premier point constitue une application d'outils développés à EDF [160]. Pour le second point, on commence par aborder le phénomène de solidification (précipitation progressive d'hydrates). Il s'agit alors d'étendre une approche mise au point à EDF [159] à des modèles morphologiques évolutifs de pâte de ciment.

Ces modèles micromécaniques sont développés de façon semi analytique (homogénéisation en champs moyens) et de façon numérique (homogénéisation en champs complets), afin de compléter le domaine couvert par la modélisation, ou de réaliser des intercomparaisons de résultats. L'homogénéisation numérique fait appel à la méthode des éléments finis appliquée sur des échantillons numériques 3D générés par des outils développés au CEA..

Cette double approche permettra en outre de vérifier le bon fonctionnement des outils développés.
Le volet expérimental présente deux objectifs visant à compléter les données expérimentales concernant le comportement de fluage au jeune âge disponibles sur béton Vercors, dans deux directions :

- sur béton, compléter le programme de quelques échéances de chargement,
- caractériser le comportement aux échelles inférieures (du mortier et de la pâte de ciment).

Ces essais sont réalisés dans le laboratoire génie-civil des Renardières (EDF) et servent notamment de données de validation des modèles micromécaniques.

Mots-clés :
Fluage au jeune âge, Comportement vieillissant, Caractérisation expérimentale

Abstract

Concrete is a material presenting basic creep (delayed strain evolving over time, under constant mechanical load, constant temperature and sealed conditions with respect to the humidity). This creep behaviour is also ageing (dependence of the evolution of the strain on the instant of application of the constant load, which does not correspond to a simple translation in time). This behaviour can be attributed to the "living" character of the material, whose microstructure evolves significantly over time at different scales.
The concrete creep is critical for the prestressed containment building of nuclear power plants, since creep yields prestress relaxation. Obviously, the creep response measured on a test at 3 months cannot be directly transposed to a structural calculation for a load at 3 years. It is also excluded to wait several years to perform a creep test on a specimen. In order to connect these two strain responses, obtained by loading at two different instants, a material behaviour model integrating the ageing creep is necessary.
To develop a model of material behaviour incorporating the ageing creep, given the multi-scale and multi-physics nature of concrete, creep experiments combined with the micro-mechanical modelling approach are attractive and are applied to the study of the VeRCoRs concrete, which is a typical mix design for the construction of the containment building. In fact, several orders of magnitude of dimensions separate the scale of physical mechanisms from the macroscopic scale. The validation will be done with regard to experiments on the VeRCoRs concrete.
These micromechanical approaches are the subject of a research action in collaboration with EDF, ENPC and CEA Saclay.
Homogenization of random media is a widely used practical and efficient tool to estimate the effective mechanical behavior of composite materials. However, when the microstructure evolves with respect to time, due to phase transformations, care should be taken when upscaling behaviors that themselves involve time, such as viscoelasticity. The improved approach in this thesis is able to overcome this limitation, building an equivalent composite replacing transforming phases by fictitious ageing viscoelastic phases to carry out the upscaling process [160]. Applications to cement paste, to mortar and to the VeRCoRs concrete are proposed, referring to a simplified morphological model. Then it extends the approach developed at EDF [159] to evolving morphological models of cement paste.
Besides, we have generated a 3D numerical polycrystalline microstructure and compared the finite element simulation results with the analytical ones in the case of ageing viscoelasticity.
Finally, the experimental campaign is carried out to characterize the ageing basic creep at different scales and at different ages of loading with the formulation of the VeRCoRs concrete in two ways:

- on concrete, complete the experimental program at different ages of loading,

- apply behaviour at lower scales (mortar and cement paste).

These tests are carried out in the civil engineering laboratory in EDF les Renardières. A direct confrontation between the experimental results and the modelling results is performed. The ageing basic creep behaviour is compared with the application of mean-field homogenisation schemes.

Keywords:
Young age creep, Ageing behaviour, Experimental characterization

Table des matières

Introduction

Context of the thesis

0.1 Industrial context

As the owner of the fleet of nuclear, thermal and hydraulic power plants, the Electricité de France (EDF) is required to ensure the safety and availability of its production sites. Civil engineering structures are subject to ageing phenomena associated with environmental conditions, in-service conditions and potential internal pathologies. As the future owner of new installations, EDF plays the role of prescriber for the definition of concretes used (types of concrete and properties required depending on the destination of the material in the civil engineering structures). In these situations (existing and future installations), the control of ageing behaviour and the anticipation of the properties of the concrete is a crucial point in the development of the safe control of the installations. The process of manufacturing the material from local constituents makes it very difficult to unify a systematic experimental approach to study all the types of concretes in the nuclear park. Under these conditions, an alternative and more realistic approach is that of virtual experimentation, whose objective is, from the available elements on the mix design parameters of materials, to estimate the properties of materials and their evolution of the ageing behaviour. The multi-scale and multi-physics characteristics of concrete naturally lead to micro-mechanical approaches to carry out the modeling work.
For the Pressurized Water Reactors (PWRs) of nuclear power plant in EDF, the reactor containment building is part of the third barrier ensuring the containment of radioactive materials after the fuel cladding and the primary circuit. It is for this reason that it constitutes an important element for safety ; Code of the Environment, Article L591-1 [1] stipulates that it must limit the effects of a possible accident.
24 of EDF French containment buildings are double-walled containments (DWCs) whose leak-tightness is primarily dependent on the inner Prestressed Reinforced Concrete Containment Building (PRCCB). The post-tensioning of tendons is calibrated in order to ensure that in case of an accident the concrete remains in compression [126].

0.1.1 Research at EDF

EDF collaborations in several research projects and works has been decisive to improve its recent understanding of physical phenomena [45][184] and to achieve their modelling at different scales [110][128][65]. Measurements and instrumentation are also important topics [49], and coupled to

modelling approaches it can provide new insights in large concrete structure monitoring.
Experimental programs have also been conducted in order to substantiate these knowledge [99][88] and to demonstrate their ability to fulfil a leakage prediction on mock-ups structurally representative of containment buildings. These projects are presented in [68] along with a review of EDF's recent efforts in computational methods dedicated to civil engineering research topics.

0.1.2 Research on VeRCoRs mock-up

As part of EDF's continuous effort for the management of Long Term Operation (LTO) of its fleet of Nuclear Power Plants, an experimental mock-up of a reactor containment-building at 1/3 scale has been built at Moret sur Loing, near Paris. Named VeRCoRs (French acronym : Vérification Réaliste du Confinement des Réacteurs), this mock-up has been completed in 2015.

0.2 Scientific and technical context

Concrete is a material presenting basic creep (delayed strain evolving over time, under constant mechanical load, constant temperature and sealed conditions with respect to the humidity). This creep behaviour is also ageing (dependence of the evolution of the strain with respect to the instant of application of the constant load, which does not equal to a simple translation in time).
This behaviour can be attributed to the "living" character of the material, whose microstructure evolves significantly over time at different scales.
However, the concretes of the containment building of nuclear power plants and of the VeRCoRs mock-up [67] are loaded at very different times :

- 3 months for the test samples of the different mix designs of the VeRCoRs concrete (the formula are chosen during the tests),
- 1 year (after the start of construction) for the prestressing of the VeRCoRs mock-up,
- 2 to 3 years (after the start of construction) for the prestressing of real containment buildings.

Obviously, the creep response measured on a test at less than 1 year cannot be directly transposed to a structural calculation for a load at 3 years. It is also excluded to wait several years to perform a creep test on a specimen. In order to connect these two strain responses, obtained by loading at two different instants, a material behaviour model integrating the ageing creep is necessary. Moreover, it is advisable to consider the age of the concrete for each lever of the casting of the concrete of the containment building.
It should be noted that the study of the behaviour of the structure in concrete for storage also requires taking into account the effect of ageing. In this case, the concrete is naturally loaded at a very young age.

These two applications call for the need for a material behaviour model that integrates ageing creep. To develop a model of material behaviour incorporating ageing creep, given the multi-scale and multi-physics nature of concrete, the micro-mechanical approach is attractive. In fact, several orders of magnitude of dimensions separate the scale of physical mechanisms from the macroscopic scale. The validation will be done with regard to experiments on the VeRCoRs concrete. This study will also enrich the data of experimental results on this concrete which tends to become a material of reference to EDF and to other laboratories (many laboratories realize physico-chemical, mechanical and transport characterizations on this concrete at the same time, but actually the Civil engineering Lab in EDF is the unique lab that has worked on the scale of cement paste and mortar).

0.3 Context on the plan of modeling work

0.3.1 Time-dependent behaviour of cementitious materials

Regulatory or academic models exist to estimate the long-term mechanical behaviour of concretes. The total time-dependent strain is often divided into several contributions [51].
In the absence of external loading and in the absence of exchange of water with the surrounding environment, the concrete exhibits a time-dependent strain related to its hydration : the autogenous shrinkage. Before its setting, the concrete has already a significant volume reduction related to chemical reactions, called the Le Chatelier contraction. These reactions persist after the setting of the concrete but subsequently result in a smaller strain, then related to the capillary forces modified by the change in the internal hygrometry of the material. It induces only a slight loss of prestress, as it changes significantly only in the first months after the setting. That is well before the prestress of the containment building. However, it is important to consider the results of creep experiments [80][81].
In the absence of exchange of water with the surrounding environment, under the effect of a constant stress, the strain of a concrete specimen changes : the concrete actually exhibits a viscoelastic behaviour. This basic creep strain ϵ_{bc} represents a non-negligible part of the prestress loss and the time-dependent strain of the concrete.This behaviour will be the subject of a special attention in this study.

0.3.2 Theory of linear viscoelasticity

Concrete, like other materials studied in this thesis, is therefore modeled as a linear viscoelastic material. In these materials, the stress tensor $\underline{\underline{\sigma}}(t)$ depends on the history of the strain tensor $\underline{\underline{\epsilon}}(t)$. The linearity of the strain story according to the stress story makes it possible to apply the Boltzmann superposition principle [29][157][109]. The linear viscoelastic constitutive law is thus

fully characterized by the relaxation function (the fourth order tensor) $\mathbb{C}(t,t')$ such as :

$$\underline{\underline{\sigma}}(t) = \int_0^t \mathbb{C}(t,t') : \frac{d\underline{\underline{\epsilon}}}{dt}(t')dt' \tag{1}$$

If we start at time $t = 0$ as a state of natural reference free of stress. Similarly, The creep compliance $\mathbb{J}(t,t')$ is strictly defined as the change in strain as a function of time under instantaneous application at t' of a constant stress. The compliance (fourth order tensor) $\mathbb{J}(t,t')$ is such as :

$$\underline{\underline{\epsilon}}(t) = \int_0^t \mathbb{J}(t,t') : \frac{d\underline{\underline{\sigma}}}{dt}(t')dt' \tag{2}$$

If the period calculated from the loading time $t - t'$ is the unique influencing parameter, the material is non-ageing.
If the behaviour of the material is isotropic, the spherical part $k(t,t')$ and the deviatoric part $\mu(t,t')$ of the relaxation tensor can be defined such as :

$$p(t) = \int_0^t 3k(t,t')\frac{de}{dt}(t')dt' \tag{3a}$$

$$\underline{\underline{\sigma}}^{dev}(t) = \int_0^t 2\mu(t,t')\frac{d\underline{\underline{\epsilon}}^{dev}}{dt}(t')dt' \tag{3b}$$

where $e(t) = tr(\underline{\underline{\epsilon}}(t))/3$, $p(t) = tr(\underline{\underline{\sigma}}(t))/3$, $\underline{\underline{\sigma}}^{dev}(t)$ and $\underline{\underline{\epsilon}}^{dev}(t)$ are respectively the deviatorical part of $\underline{\underline{\sigma}}(t)$ and $\underline{\underline{\epsilon}}(t)$:

$$\sigma_{ij}^{dev}(t) = \sigma_{ij}(t) - p(t)\delta_{ij} \tag{4a}$$

$$\epsilon_{ij}^{dev}(t) = \epsilon_{ij}(t) - e(t)\delta_{ij} \tag{4b}$$

where δ_{ij} is the Kronecker delta.

The non-ageing compliance may be approached by the generalized Kelvin model or Maxwell

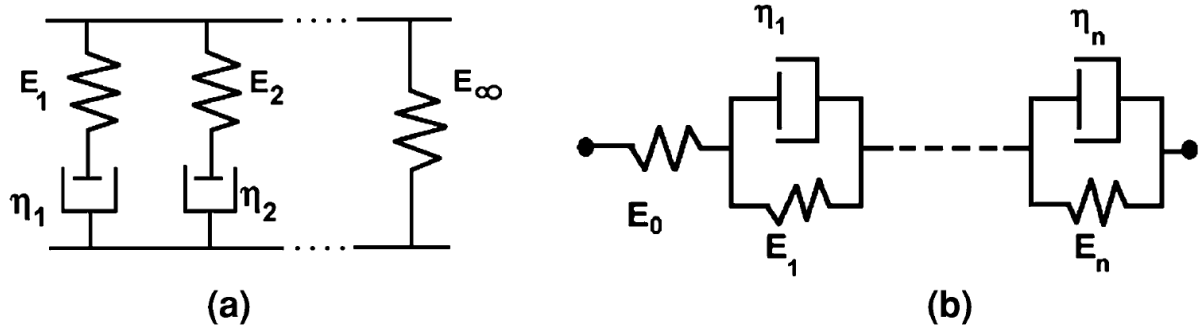

FIGURE 1 : Maxwell and Kelvin chains with instantaneous elasticity (generalized Maxwell model and Kelvin model).

model (Fig. 1). For example, for the generalized Kelvin model, the compliance is :

$$\mathbb{J}_K(t-t') = \sum_{i=1}^{n}(1-e^{-\frac{t-t'}{\tau_k}})\mathbb{C}_k^{-1} + \mathbb{C}_0^{-1} \tag{5}$$

where $\mathbb{C}_0$ is the instantaneous elastic stiffness (fourth order tensor) and $\mathbb{C}_k(1 \leqslant k \leqslant n)$ is the stiffness corresponding to the characteristic time τ_k. The long time flexibility of series of Kelvin chain corresponds to the setting of the springs (Fig. 1), so that it equals to $\sum_{i=1}^{n} \mathbb{C}_k^{-1} + \mathbb{C}_0^{-1}$.

0.3.3 Concrete models

Several physical mechanisms may explain the basic creep of concrete. All the existing models are established at small scale of the cement paste [56][202][191]. A detailed presentation of these models can be found in [24][91]. It should be reminded, however, that other models exist such as those proposed by Rossi [153][154] and Sellier et. al [175][90]. These models introduce phenomena to explain experimental results and to broaden the range of validity of the material behaviour (range of loading, of temperature).

In addition, the concretes appear as heterogeneous structural materials : the aggregates (sands and coarse aggregates) are distinguished from the cement paste. The cement paste plays the role of the glue between the aggregates. The microstructure of the cement paste at the scales less than $100\mu m$ depends on the cement, the water, the admixture and the finest particles. The hydration reactions and the water movements during the early-age of hydration are at the origin of the capillary structure that composes the most important part of the porosity.

This makes the upscaling or downscaling approach useful, to bridge the microscopic cement paste scale and the concrete meso scale by upscaling the mechanical properties of cement paste to obtain the concrete parameters, in taking into account the composition of the concrete. An separation of scale is introduced by the definition of a cement matrix : which is defined as corresponding to the cement paste and the sands when the mortar Representative Elementary Volume (REV) size passes $100\mu m$. Then concrete is usually defined as a matrix of mortar and aggregates. This separation of scale makes it possible to remain in dimensions larger than those of the bigger grain of cement paste : mortars and concretes are thus considered as mixtures of aggregates immersed in a cement paste matrix. But this separation of scale does not satisfy the conditions of scale separation introduced in the homogenization theory : the properties of the matrix probably fluctuate over lengths comparable to the size of the smallest inclusions. In most of the studies, however, the matrix of the cementitious materials is considered as a homogeneous material. So in these studies, homogenization techniques are therefore used to estimate the elastic stiffness or the viscoelastic behaviour of the concrete, considered as a composite material.

The first studies of homogenization of concrete were based on the parallel models to predict the elastic or viscoelastic strains based on the elastic properties of the aggregates and the elastic and the viscoelastic properties of the cementitious matrix [48][84][93][78][131][43]. Tests on concretes made of aggregates with different stiffness and have shown that these stiffnesses influence the strains of the concrete [93][43]. The Hashin-Shtrikman bounds [86] was then used with mixed

results [131][43][108]. The fact that the measured macroscopic elastic stiffness is sometimes inferior to the estimated stiffness justified the introduction of a third phase, which is more flexible, called a transitional zone [192]. More advanced models of homogenization, such as the generalized self-consistent model [89], have been used to account for the heterogeneity of the cement matrix [135].

Moreover, for High Performance Concrete, the de Larrard's tri-sphere model [108][156] tries to correct the gap between the macroscopic Young's modulus measurements and the theoretical estimates by taking into account an additional parameter : the compactness of the aggregate mixture reflecting the maximum volume fraction that can be achieved by compacting the aggregates. The experimental results, not in agreement with the Hashin Shtrikman's lower limit, are explained by a lesser adherence between cement paste and aggregate, the shrinkage of which is prevented by the aggregates. The cement paste matrix in the concrete would therefore have lower mechanical properties than the reconstituted cement matrix for the homogenization models.

Granger [80] compared the results of two homogenization models to the experimental Young's modulus on six nuclear plant concretes. The results of homogenization models are not as good as in the results presented by F. de Larrard [108]. The experimental part of Granger's study is summarized in the experimental subsection in the Introduction of this thesis.

More recently, the Mori-Tanaka model [132] applied to spherical inclusions has been used to link the nanoindentation results on the cement paste to the basic creep of mortars and concretes [208]. Once again, the use of homogenization schemes allows to link the logarithmic trend of time-dependent strains at the low-scale with the logarithmic trend of the results measured at the higher scale [193]. The logarithmic trend of the results is also applied in this thesis for the identification of the parameters from experimental results.

Homogenization methods using numerical simulations have already been carried out at the scale of concrete. But computation times are much greater than those of mean-field homogenization schemes [69].

Numerical method was used by Gal in 2011 [66] to study the behaviour of fiber reinforced concrete with finite elements. The result is compared with experimental measurements [180].

The operation of the finite elements calculation [66] remains complicated. This difficulty is resolved by the methods of finite differences or finite elements on regular grids [58] and the Fast Fourier Transform method (FFT) [134]. The performance of these methods has been compared in [57]. Escoda [61] used the FFT method to examine microstructures derived from tomography images. A mortar image was used to find the Young's moduli of the material.

The Young's Moduli chosen for the aggregates are in the range of Granger's measurements [80]. On the other hand, the characteristics of cement paste are slightly overestimated compared to the experimental results of Granger (20GPa chosen against 18GPa measured). Granger further specifies that this module for the B11 concrete is surprising, since it is superior to that of the HPC of Civaux. In the studies of this thesis, the mechanical parameters of the aggregates and the sands are obtained from the software Vi(CA)2T of $EDF\ R\&D$.[170], in which the properties of aggregate and sand have also been obtained.

Besides the strains of the concrete, several composite viscoelastic materials have been studied to

predict their time-dependent strains. It is now necessary to briefly describe the different homogenization models applied for this purpose.

0.3.4 General analytical homogenization methods

Recent progress in the Department MMC of *EDF R&D* makes it possible to carry out the mean-field homogenization of ageing linear viscoelastic behaviours, and to estimate the macroscopic results of precipitation at the scale of the microstructure. A brief review of these two advances, the first of which opens a large field of applications, is applied in this thesis.
The mean-field homogenization of random media is well established in the context of elastic behaviour, and has been successfully applied to cementitious materials by many authors [25][46], the reference lists are not exhaustive. Non-ageing viscoelastic behaviours are also accessible, thanks to the correspondence principle [123], which, by exploiting the Laplace-Carson transform, changes non-ageing viscoelastic behaviours into fictitious elastic behaviours. The elastic approaches are therefore directly reusable, and the contributions are also quite numerous [59][85].
This technique is still used, with more and more complex homogenization schemes such as that of the equivalent inclusions [2][60]. It has yielded analytical results for incompressible isotropic viscoelastic behaviour including the Maxwell model[155]. There is a common limitation to all these studies : the concrete is modeled as a non-ageing viscoelastic material, which is only correct for late loading ages. The Laplace-Carson transform can then be used to transform the viscoelastic problem into equivalent elastic problems. But this method is no longer valid in ageing viscoelasticity and the homogenization methods should be extended to such behaviours.
In addition, the non-ageing modeling suffers from problems related to the bad condition of the inverse of the Laplace-Carson transform. The most commonly used inversion methods are the collocation method [171] and the Gaver-Stehfest formula [178]. The collocation method has evolved to reduce the errors in the identification of the compliance. Similarly, the number of terms in the Gaver-Stehfest formula can be reduced to ensure a greater stability which depends on the precision. Nevertheless, the inversion of the Laplace-Carson transform remains a delicate operation and the most modern homogenization methods no longer rely solely on the correspondence principle.
New homogenization methods are based on an iteration at successive time steps. The variational method of Ponte Castaneda [42] is applied to define a homogenous prediction in each phase and to solve the problem of homogenization at the time step. Recent developments make it possible to take into account the fluctuations of the fields in each of the phases and to estimate their variance [106][9].
To treat the case of non-ageing viscoelastic materials, a new homogenization method has been derived, based on the equivalence between the collocation method intended for the inversion of the Laplace-Carson transform and an internal variables formulation [127][198]. At each time step, the compliance is approximated by a non-ageing compliance at internal variables and the problem of homogenization is solved by using the collocation method. The continuity of the internal variables is imposed from one time step to another.

0.3.5 Homogenization to ageing viscoelastic behaviours

Very few applications of homogenization to ageing viscoelastic behaviours have been performed. Indeed, since the correspondence principle is no longer valid in ageing viscoelasticity, specific approaches must be developed : [120] for stratified media, [149] for random media with an incremental approach. These approaches remain either specific or relatively difficult to access.
In 2012-2013, the Department MMC of *EDF R&D* developed an original method of mean-field homogenization of ageing creep [160] which is as easy to use as the correspondence principle, even simpler because it is no longer necessary to reverse the Laplace-Carson transform. This method can take absolutely any linear isotropic ageing viscoelastic behaviours as the input parameters. In particular, it is not necessary to reveal internal variables or to introduce a constant "Poisson's ratio". The most common homogenization schemes are accessible : diluted, Mori-Tanaka, self-consistent. On the other hand, the approach is limited to the morphologies described by spherical particles. The fine description of cement pastes is therefore not conceivable. But the REVs of cement paste are usually regarded as being constituted of elongated or flattened particles (portlandite crystals, elementary C-S-H bricks, etc.). However, it is the delayed behaviour of the cement paste that dictates that of the concrete, the aggregates remaining a priori elastic at the applied time scales. The extension of the method to ellipsoidal particles has been realized and validated by M. DI CIACCIO during his internship at the Department MMC of *EDF R&D* in 2014 and by the researcher J-F. Barthelemy from CEREMA [10]. The application of this extension is being developed by I. Oubrahim during her internship at EDF.
On the other hand, the application of full-field homogenization techniques through the numerical simulation effectively treats the case of viscoelastic behaviours with internal variables. To simplify the modeling, the history of the strains of the material is summarized by some scalars. For each time step, the integration of the constitutive law defines an elastic problem that is solved by the homogenization method [134][130][133]. A careful integration of the constitutive law makes it possible to reduce the number of cycles without compromising the precision of the estimated mechanical response [53]. Another strategy is based on the observation that local stresses are similar between the time discretization of the same calculation, or even between different loadings. The NTFA (non-uniform transformation field analysis) [98][129] thus represents the strain as a linear combination of the chosen strain. It has been used to treat the case of ageing viscoelastic composite materials [107]. The periodic homogenization is mainly used to verify the capability of the faster semi-analytical homogenization methods [28][148][9] or to deal with complex microstructures [210].
As indicated in the cited report, there are still some efforts to be made to produce a fully exploitable code. We now have a set of homogenization schemes (diluted, Mori-Tanaka, self-coherent) and particle shapes (sphere, ellipsoid, multilayer heterogeneous sphere) that can be used in ageing viscoelasticity.
This new method of homogenization of ageing behaviours, by its great flexibility with regard to exploitable elementary behaviours, makes it possible now to extend the Bažant solidification theory to more realistic precipitation mechanisms. As a reminder, this theory [14] accounts for an ageing behaviour by the gradual precipitation of parallel layers of a material whose behaviour

is non-ageing once precipitated. The hypothesis of progressive precipitation of parallel layers has enabled Bažant to build a rigorous framework and to qualitatively produce ageing viscoelastic behaviours from simple ingredients (non-ageing behaviour of the precipitating material and evolution of the solidified volume fraction). On the other hand, the real precipitation mechanisms in cementitious materials are much more complex than this assembly of parallel layers. The application of [160] to solidification opens the way to other mechanisms : simplified cases are presented in [159]. Even if the precipitation mechanisms approached remain simplistic with respect to cement paste, this study has shown the great influence of both the mechanism and the kinetics of precipitation on the actual ageing behaviour.
For this study, we used some of the available methods. On one hand, the methods based on the ageing homogenization method proposed by [160] are chosen for their speed. On the other hand, the numerical homogenization method for the basic creep results are also calculated to validate the analytical modeling results. The application of the analytical solution of Sanahuja [160] will be the subject of the work. The other methods could complete the results obtained.

0.4 Context on the plan of experimental work

The experimental results reported in the NU-ITI database [23] can be used to quickly recall some established facts.
The creep strain increases with the temperature. For this reason, the temperature of the sample must be set during a creep test [52]. The influence of temperature can be modeled as an acceleration according to the Arrhenius equation [80][152]. This equation allows the definition of an equivalent time t_{eq}, a corrected age of the specimen, which depends on the history of the temperature T(t) :

$$t_{eq} = \int_{\tau=0}^{t} e^{-\frac{U}{R}(\frac{1}{T(\tau)}-\frac{1}{T_0})} d\tau \tag{6}$$

where $R = 8.3144621 J \cdot mol^{-1} \cdot K^{-1}$ is the ideal gas constant, $T = 20°C = 293\ K$ is the reference temperature and U is the activation energy. The U/R ratio is 5000 K [80] or 4000 K [152] depending on the model. The influence of the temperature on the hydration of cement can also be reduced to the definition of an activation energy measured by calorimetry, of the order from 35 to 40 $kJ \cdot mol^{-1}$ (4200-4800 K) for an ordinary Portland cement [199][209][103][100].
The strain of basic creep depends on the degree of humidity in the concrete. The experiments of [77] show that the time-dependent strains are generally proportional to the degree of humidity [77][4]. The finding is identical during experiments on hollow and thin cylinders (0.7mm) of cement paste placed in climatic chambers [22]. In addition, a completely dry mortar no longer exhibits basic creep strain [77][144][4]. Several existing models have therefore taken into account a fixed value of humidity via a change of amplitude of the strain rate proportional to the humidity [24] or increasing [19].
The strain of creep depends on the age of loading t_0 : the concrete is an ageing viscoelastic mate-

rial. It is known that the Young's modulus of the concrete, like its compressive strength, increases with the age because of the hydration of the cement. The same is true for the time-dependent strains, which decrease if the concrete is loaded at a later age of loading [114][74][35].
These experimental results identify the parameters of the modeling of the basic creep of cementitious materials for the viscoelastic models.

0.4.1 Test with a sealing coating

When carrying out a basic creep test, two main approaches are applied during the studies in order to prevent the concrete from drying : the test samples are either covered with a sealing layer or kept in water.[113] In the RILEM database, for instance, these two conditions are corresponding to basic creep tests. It should be noted that these two test conditions are not equivalent. For low water-to-cement ratios in particular – therefore for high strength and very high strength concretes – self-desiccation due to hydration reactions leads to internal moisture levels that are as low as 75% [205], which can limit hydration [64]. However, obviously, in the case of storage in water, the porosity of concrete is filled with water (saturation equal to 1), the relative humidity remains at 100% and hydration could continue. Shrinkage is also affected by these two different conditions (swelling is observed under water for instance in the creep and shrinkage tests [33] and the final results for basic creep are certainly different and not exactly comparable. And because of the couplings between autogenous shrinkage and basic creep [5][191], there is certainly an influence of the evaluation of basic creep. The phenomena that may affect long-term behaviour in both cases are also different.
In some tests with a sealing coating, the specimens are protected from desiccation by a surface coating. Several techniques are possible such as the application of a resin or self-adhesive aluminium sheets, or even a combination of both. However, maintaining tightness over a long period of time still poses serious difficulties. In the case of two layers of self-adhesive aluminium, found that water loss accelerates over time and measured a loss of mass of approximately 0.4% after about 2 years. The Part II of this thesis also indicates the relevant results on the loss of mass. The studied experimental results confirm that avoiding completely drying in a shrinkage or creep test with a long duration is still very difficult but the loss of mass could be reduced in a tolerable degree.
Creep is the result of the difference between total deformation strain and shrinkage strain. So, if shrinkage is measured at the same time as creep and the test samples have the same protection for both tests, the subtraction eliminates any autogenous deformation strain (drying shrinkage if drying occurs). But very often, the autogenous shrinkage test is stopped before the end of the creep test. This was the case for Le Roy's tests [113], where the autogenous shrinkage test was stopped after 1300 days while the creep tests were continued for more than 5000 days. Also, due to drying, the results of the basic creep test are affected by a proportion of the drying creep. The difference can be seen in Figure 2[113] between the measurements and a logarithmic relationship of the form : Eq.7 is of the order of $10^{-6}MPa^{-1}$ (for a period between 1000 and 5000 days approximately) and this value is compatible with deformation strain due to drying shrinkage

and desiccation creep.[113]

$$J(t, t-t_0) = \frac{1}{E(t_0)} + \frac{1}{\beta_1 C} ln(1 + \frac{t-t_0}{\beta_2 \tau(t_0)}) \tag{7}$$

For drying shrinkage only, at a relative humidity of 50% and for a concrete mean strength of 40 MPa, the amplitude is around $300\mu m/m$. If we assume that the mass loss is only 10% of the final value, the drying shrinkage is around $30\mu m/m$. If the applied stress in the creep test is 10 MPa, the effect of drying shrinkage will be $3\mu m/m/MPa$ which is close to the observed deviation.
Concerning the creep tests performed during this thesis, the technique of sealing coating has been improved to achieve a better sealing condition.

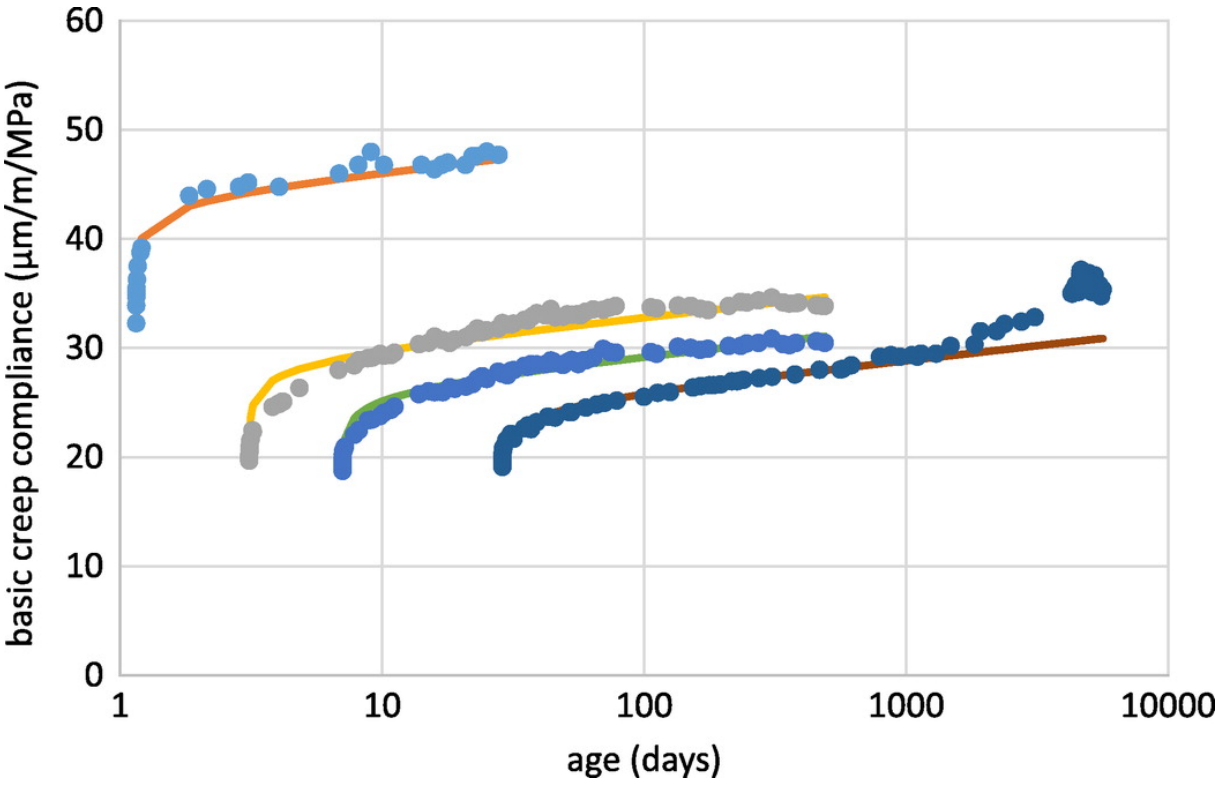

FIGURE 2 : Basic creep : concrete B2 (Water/Cement = 0.33) loaded after 1, 3, 7 and 28 days. Comparison between experimental results and modelling with Equation 7 (solid lines).[113]

0.4.2 Similar experimental study

The existing experimental results ([73][80][23]) show that the creep behaviour strongly depends on the composition of the concrete. The factors that may influence the time-dependent strains include the water-cement ratio, the volume fraction and the quality of the aggregates [73][83][33], in particular the Young's modulus of the concrete ([137][32][136]).
We mainly want to mention the scientific contributions by Bazant et al. from 1975 [13] and by

Granger [80] which constitute the basis of the work presented in the study in long-term behaviour of cementitious materials. The method presented, on the leading edge on many points at their time, still remains very interesting today.
In the article by Bazant et al. from 1975 [13] :

1. The study is carried out with a stable relative humidity.

2. A shrinkage test was carried out to identify the theoretical developments on a special kind of concrete of the studied reactor building. Each time, the authors use the experimental results (which were rare at that time) from the literature for the modeling applications, which the authors reuse for their study of, in particular, shrinkage and creep tests.

In the thesis by Granger [80], a practical model of concrete is proposed in an overall equivalent continuous material approach. The few parameters of the model are determined on the experimental results.
Granger [80] illustrates the difficulties of modeling the basic creep of concrete :

- p.248 : the creep is ageing. The final value is very high, when concrete is loaded at an early age and declines sharply with age of loading. With regard to the behaviour at later ages (in which we are interested more in this study), there is a very strong ageing effect at the age more than one year while at the same time, the elastic properties of concrete are stabilized. At an early age, it is reasonable to put the parameter study of concrete ageing effect compared to the progress of the hydration reaction. In the long term, it seems that it is necessary to find a second explanation for the phenomenon of ageing.

- p.258 : Coussy [50] shows that if we want to model the phenomenon of ageing, for example, we can set the parameters of one or several chemical reactions (the cause of aging, such as hydration, or polym érisation). however, it is difficult and even impossible to carry out the calculation. With regard to the Laplace-Carson transform, it is only suitable for the linear non-ageing case. we will return to this point in the Section 4.1.

- p.277 : extrapolation of the experimental data of long-term creep is a particularly difficult problem and can only be solved with the himiques physic phenomena, which are at the origin of the creep. The phenomenon of aging on the creep is also very difficult to model.

- p.348 (conclusion) : finally, in the long term, we believe it is essential to initiate a deep discussion of the origins of the chemical physical concrete creep and the creep of desiccation which is intrinsic to the material. Without this basic knowledge, it will be difficult to make progress in the modelling.

0.4.3 Experimental work in this thesis

The validation of the models passes obviously by tests. On the experimental level, the originality of this thesis lies in the study of the basic creep in uniaxial compression tests at different scales of materials of the VeRCoRs concrete and at different ages of loading.
Basic creep tests on the VeRCoRs concrete are already planned :

- As part of Abdusalam Aili's thesis [5] : basic creep tests in uniaxial compression, with loading maintained for at least 5 years and applied at the ages of loading $t_0 = 28$ days, 6 months and 1 year.
- The Direction $CEIDRE\,TEGG$ of EDF performs basic creep tests in uniaxial compression, with loading at the ages of loading $t_0 = 1$ day, 28 days and 3 months.
- LMDC Toulouse, in the course of a collaboration between EDF, IFSTTAR and LMDC, measured the creep compliance at 175, 390 days and performed the creep recovery experiment.

The experimental results in this thesis are supplemented by other tests, especially at lower scales of material.

Approach adopted for this work

0.5 Definition of the problem

We therefore note that the homogenization of the cementitious materials is based on a more and more detailed description of the morphology of the microstructure and the basic creep evolution based on real experiments. Homogenisation models, which may be based on the existing knowledge of small scale phenomena, may also take into account mix design parameters, such as the water–cement ratio, the volume fraction of the aggregates, their grain size and their mechanical properties. The previous section has highlighted some of the tools that have been used to predict the strains of concretes : mean-field homogenization schemes and 3D numerical simulations.
In order to improve the prediction of the time-dependent strains of concrete, there is a need to extend the use of these upscaling methods to the ageing linear viscoelasticity[61]. Can we improve the quality of the predictions of the time-dependent strains by a better understanding of the particularities of the microstructure ?
Concrete as a matrix-inclusion composite is characterized by volume fractions of inclusions and an extended particle size. In addition, the transition from the elasticity to the viscoelasticity leads, in the case of concrete, to greater contrasts between the phases. In these delicate conditions, do homogenization schemes correctly account for the effect of the mechanical parameters or the microstructural parameters taken into account ? As for the elasticity, the estimates of the macroscopic behaviour produced by homogenization schemes should be verified by experimental results or by the results of 3D numerical simulations. Such verification would also make it possible to obtain an estimation of the influence of the particle properties on the time-dependent strains of concrete, with the condition of studying an elementary volume which is large enough to be representative and which has a fine enough resolution to describe the details of the microstructure.

0.6 Research objective

The thesis aims to build a basic ageing creep constitutive law of the VeRCoRs concrete, on the basis of physical arguments, by a micromechanical approach and which should be validated experimentally. The modeling part of the thesis has two main objectives : determine the ageing behaviour of VeRCoRs concrete from that of the cement paste and of the mortar, and estimate the ageing behaviour of the cement paste itself from information on the micro-mechanisms at the smaller scale. The first point composes an application tool already developed. The se-

cond point will begin by addressing the solidification mechanism (progressive precipitation of hydrates). It extends an approach developed in evolutionary morphological models of cement paste already developed and validated in elasticity. An analysis of the literature identifies appropriate mechanisms to consider. These micromechanical models are developed semi analytically (homogenization mean fields) and digitally (homogenization complete fields), to complete the field covered by modeling, or achieve the results of the comparison. Numerical homogenization uses the finite element method or methods introduced by CEA. This dual approach also helps to check the operation of the tools developed.
The experimental part has two goals :

- On the VeRCoRs concrete, to complete the experimental program with different ages of loading,
- To address the behaviour at lower scales (mortar and cement paste). These experiments serve as micromechanical model validation data.

To summarize

Part I introduces the mean-field homogenization of time-evolving microstructures with viscoelastic phases and performs the application to simplified micromechanical models of hydrating Cement Paste and C-S-H gel.

Part II details the creep experiment procedure on cement paste, mortar and the VeRCoRs concrete. This part also lists the raw and the post-processed experimental results.

Part III details the identification of the parameters of the ageing viscoelastic creep compliance models based on the experiments. This part describes the procedure of identification of parameters of the Logarithmic model, the general Kelvin model, the general Maxwell model and a hybrid model. In addition, the application of Part I and different confrontations model-experiment have been carried out.

Première partie

Mean-Field Homogenization of Time-Evolving Microstructures with Viscoelastic Phases : Application to a Simplified Micromechanical Model of Hydrating Cement Paste

Introduction

The creep response measured on a test at 3 months cannot be directly transposed to a structural calculation for a load at 3 years. It is also excluded to wait several years to perform a creep test on a specimen. To develop a model of material behaviour incorporating ageing creep, given the multi-scale and multi-physics nature of concrete, the micro-mechanical approach is attractive.
Homogenization of random media is a widely used, practical and efficient tool to estimate the effective mechanical behaviour of composite materials. However, when the microstructure evolves with respect to time, due to phase transformations, care should be taken to upscaling behaviours that themselves involve time, such as viscoelasticity. A natural assumption is to consider that the influence of microstructure evolution is negligible once the material is macroscopically loaded : it allows one to take advantage of the correspondence principle when the phases are linear viscoelastic. A new approach is proposed to overcome this limitation, building an equivalent composite replacing transforming phases by fictitious ageing viscoelastic phases. This equivalent composite has a constant microstructure but is made up of ageing linear viscoelastic phases. Then, its effective behaviour may be estimated taking advantage of recent approaches to homogenize such behaviours. Applications to cement paste are proposed, referring to a simplified morphological model. In particular, the approximation introduced when neglecting microstructure evolution is investigated. Qualitatively, compliance functions from evolving microstructure are found to be closer to the experimental ones.
This part is organized as follows. First, a time-evolving morphological model of hydrating cement paste is proposed. Anhydrous, hydrates, and capillary pores are considered, and a description of their spatial distribution as a function of time is proposed. This model is clearly a simplification of the genuine complexity of cement paste microstructure, but it allows for the illustration of developments presented in the next chapters without unnecessary technical complications. Moreover, a simplified method for modeling the hydration of cimentitious materials is proposed to improve the morphological model. The current state of knowledge of cement hydration mechanisms is reviewed [39].
Then, phases are considered as elastic, which allows for performing classic homogenization on snapshots of microstructure. Basics of mean-field homogenization in elasticity are recalled for the sake of completeness, and the effective Young's modulus of cement paste is estimated as a function of both the water-to-cement ratio and the hydration degree. Analyzing these results, limitations of the chosen simplified morphological model are pointed out, especially regarding prediction of setting. Here, two chapters are devoted to nonageing linear viscoelastic phases. Firstly, the microstructure is considered as frozen (i.e., it does not evolve any more) once the

macroscopic loading step has been applied. This allows for taking advantage of the correspondence principle, and the approach is recalled for the sake of completeness. However, applicability to cement pastes is restricted to late loading ages as in this case, hydration can be considered as nearly stabilized.
In addition, a chapter constituting the main originality of this part, describes the complete evolution of microstructure, combining micromechanical extensions of Bažant solidification theory and ageing linear viscoelastic mean-field homogenization.
One chapter is then dedicated to the application to polycrystalline microstructures with the methods of homogenization and the numerical simulations with academic test cases, with a consideration of the loads encountered on prestressed containment building of nuclear power plants. Eventually, several prospects are proposed to improve application of this new ageing approach to cement pastes.
In the end, the double scale microstructure of the cementitious materials and the volume fraction defined by the model are combined to better describe the microstructure. The modeling part of this chapter aims to estimate the ageing viscoelastic behaviour of cement paste from information on the chemical evolutions, extending an already developed approach to an evolving cement paste morphological model. These micromechanical models are derived semi-analytically. We discuss the suitability of the self-consistent homogenization scheme to describe the setting phase of cement paste. This approach helps to check the applicability of the tools.
The chapters 1,2,3,4 of this part are based on the paper published in the Journal of Nanomechanics and Micromechanics [166] and in the paper for the Sixth Biot Conference on Poromechanics [96] : DOI :10.1061/(ASCE)NM.2153-5477.0000116, DOI :10.1061/9780784480779.127.

Researches on Mean-Field Homogenization of Time-Evolving Microstructures

Some materials, such as concrete, exhibit a strong evolution of their microstructure along their life. During hydration of concrete, dissolution of anhydrous and precipitation of hydrates occur simultaneously, albeit more and more slowly. Evolution also occurs when concrete is exposed to ambient conditions, leading, for example, to leaching or carbonation. In all these cases, microstructure evolution is a key information to bridge the gap between physico-chemical processes occurring at smaller scales and macroscopic properties and behaviour of materials. Considering microstructure evolution is thus especially critical to build less empirical behaviour laws.
Homogenization techniques are widely used to upscale the mechanical behaviour of composite materials with constant microstructure. When microstructure evolves, elasticity can still be upscaled, straightforwardly working on snapshots of microstructure at given times [25][46][141][164]. However, care has to be taken for time-dependent elementary behaviours, such as nonageing linear viscoelasticity. Indeed, time appears in both morphological evolutions and behaviours of elementary phases. A common assumption is then to consider that microstructure does not evolve any more once the macroscopic loading has been applied [158][156][82][210]. This allows

for the reuse of the well-known correspondence principle [124], suitable for constant microstructures made up of nonageing linear viscoelastic phases. For cementitious materials, this approach is clearly restricted to loadings at late ages, once hydration is almost stabilized and assuming the absence of other mechanisms inducing microstructure changes. To overcome this limitation, new approaches have been proposed. As far as full-field homogenization is concerned, as the microstructure is explicitly described, its evolution can be taken into account by time-stepping methods. Using as input the time-evolving microstructure of a cement paste modeled as voxels, Li et al. [115][116] used a dedicated finite-element code to compute the overall response to given macroscopic strain paths. Microstructure evolution was explicitly taken into account through dissolution and precipitation of voxels. As far as mean-field homogenization is concerned, Scheiner and Hellmich [172] considered that during an infinitesimal time interval, microstructure evolves negligibly and estimated the effective creep rate of the evolving microstructure by the rate derived on the current microstructure, but subsequently kept constant, so that the correspondence principle can be used.

The ageing linear viscoelastic behaviour available in the code used in EDF is the Granger model [80]. In Mori-Tanaka homogenization scheme, the matrix ageing linear viscoelastic behaviour is thus defined by a constant Poisson ratio and the following uniaxial compliance function :

$$J_0^E(t,t') = \frac{1}{E_0} + f(t') \sum_{p=1}^{n} J_0^p (1 - e^{-\frac{t-t'}{\tau_0^p}}) \tag{8}$$

where E_0 is the Young's modulus ($1/E_0$ corresponding to the elastic part of the compliance function), J_0^p and τ_0^p for $p \in 1, ..., n$ are viscoelastic parameters, and $f(t')$ is the ageing function. The latter can take any form.

These approaches, numerical or semianalytical, to homogenize time-dependent microstructures whose phase behaviours are viscoelastic, are based on time-stepping algorithms and give the response to a specific loading path. A new simulation needs to be performed for each loading path investigated. This part of the thesis proposes an alternative, semianalytical approach, to estimate the effective ageing viscoelastic behaviour, fully characterized by the compliance or relaxation tensors as function of two time variables. This has recently been made possible thanks to a micromechanical extension [161][162] of Bažant solidification theory [18][16][146][41] and to mean-field homogenization of ageing linear viscoelastic behaviours [160][111]. These developments have recently been applied to cementitious materials [94].

The approach proposed in this part is general and could be applied to any composite material undergoing phase transformations (dissolution, precipitation, or conversion from solid to solid) that induce microstructure evolution. This microstructure evolution is assumed to be independent of the local stresses or strains. In other words, this evolution is known in advance. The application proposed in this section is restricted to ageing basic creep of a cement paste due to hydration, as ageing basic creep is an important feature of concrete behaviour [31].

Chapitre 1

Simplified Model for the Evolving microstruture of Hydrating Cement Paste

Sommaire

The microstructure of cement pastes is made up of more than 10 phases [118] categorized as either anhydrous, hydrates, or additives. Moreover, the morphology of hydrated phases, and especially of the main one for portland cements, calcium silicate hydrates (C-S-H), is highly complex (see [150][55][101][117] among others). This morphology is difficult to both observe and model. Addressing the question of microstructure of cement pastes and its evolution, is out of scope of this section. Thus, a simplified point of view is adopted here : both anhydrous and hydrates are not detailed but considered as single phases. In other words, only three phases coexist : anhydrous (subscript a, main types of minerals are normally present : alite, belite, aluminate (C3A) and a ferrite phase (C4AF)...), hydrates (subscript h, Calcium silicate hydrate, Calcium hydroxide, AFm and AFt phases...), and capillary porosity (subscript p). As the drained behaviour is sought, capillary water pressure is disregarded.
The aim of this section is to propose a mean-field homogenization method to take into account microstructure evolution. The three-phases configuration is simple enough to present the approach without unnecessary technical complications.

1.1 Volume Fractions Evolution : Hydration Model

During hydration, as a function of time, anhydrous progressively dissolve and hydrates precipitate. The well-known Powers model [145] is adopted to estimate the volume fractions as function of the hydration degree α (defined as the amount of anhydrous that has reacted over the amount

of initial anhydrous)

$$f_a(\alpha) = \frac{0.32(1-\alpha)}{w/c + 0.32} \tag{1.1a}$$

$$f_h(\alpha) = \frac{0.68\alpha}{w/c + 0.32} \tag{1.1b}$$

$$f_p(\alpha) = \frac{w/c - 0.36\alpha}{w/c + 0.32} \tag{1.1c}$$

where w/c = water-to-cement mass ratio. An empirical kinetic model is adopted to relate the hydration degree to time

$$\alpha(t) = \frac{(t/\tau_{kin})^{n_{kin}}}{1 + (t/\tau_{kin})^{n_{kin}}}\alpha_{max}, where\ \alpha_{max} = min(\frac{w/c}{0.42}, 1) \tag{1.2}$$

where τ_{kin} and n_{kin} = kinetics characteristic time and exponent. The theoretical maximum reachable hydration degree α_{max} is also estimated from the Powers model.
The volume fractions evolution is plotted in Fig.1.1, for $w/c = 0.5$ and $n_{kin} = 4$. As expected, the amount of anhydrous decreases with time, and the capillary porosity also decreases, as hydration is a space-filling process (the volume of hydrates produced is higher than the volume of anhydrous consumed).
A crude approximation of hydration and kinetics is adopted here for the sake of simplicity. More

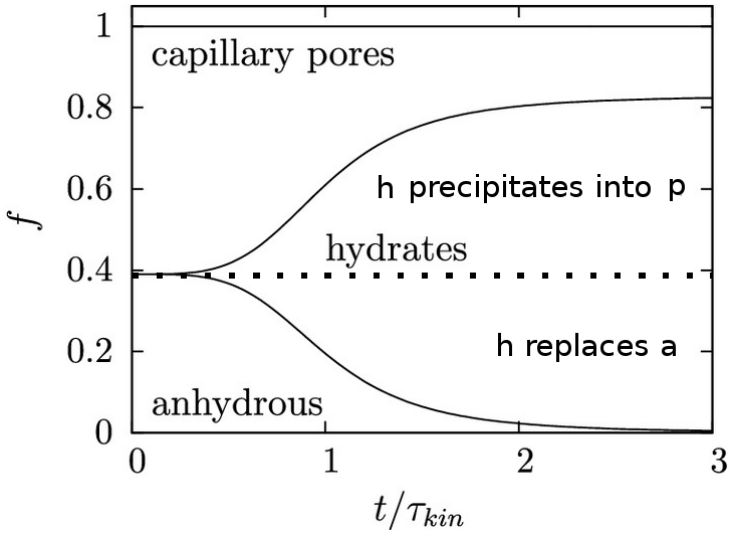

FIGURE 1.1 : Evolution of cumulative volume fractions of anhydrous, hydrates, and pores ($n_{kin} = 4, w/c = 0.5$).

advanced model is also used in this thesis in the third Part, which provides volume fractions of phases as a function of time.

1.2 Morphological Model and Its Evolution during Hydration

The volume fractions evolution being modeled, let us clarify the spatial distribution of the phases, that is the morphology of the composite material. The cement paste is described at any given time as a polycrystal-like assemblage. Each cell of the latter is thus occupied by either anhydrous, hydrates, or capillary porosity. Although simplified, this morphological model is rather commonly encountered [25][177].
The evolution of this morphology needs to be described. The volume of hydrates produced during an increment of time being higher than the volume of consumed anhydrous, the former is split in two subvolumes :

1. One part directly replaces the dissolved anhydrous (h replaces a) ;
2. The other part precipitates into capillary porosity (h precipitates into p).

The first part is assumed to occupy the same volume as that left by dissolved anhydrous, and the second part complements the first one, up to the total amount of hydrates produced. At the scale of cement paste, these phase transformations are assumed to affect random cells. At the scale of the individual cell, these transformations are assumed to occur instantly, so that each cell is homogeneous at any given time. A schematic representation of this evolving morphological model is depicted in Fig.1.2.

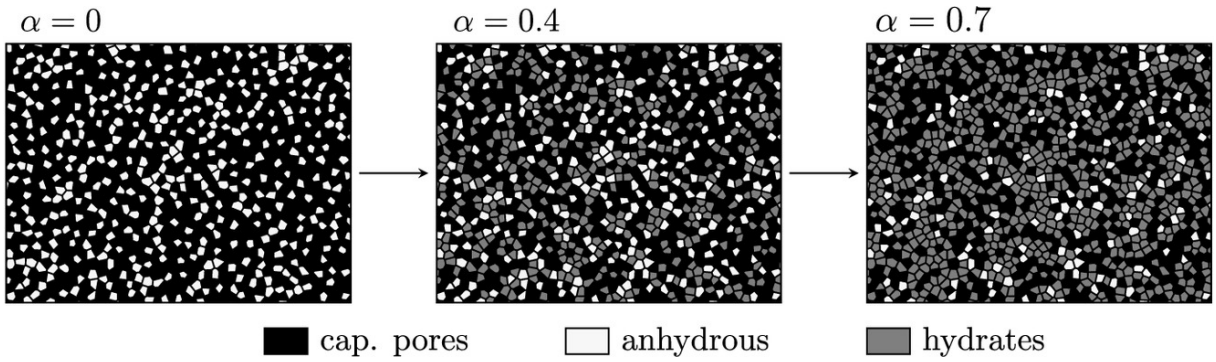

FIGURE 1.2 : Schematic two-dimensional representation of the evolving microstructure considered to model cement paste ($w/c = 0.6$).

Chapitre 2

Effective Elastic Stiffness of Evolving Microstructure

Sommaire

In this subsection, the behaviour of the phases is restricted to linear elasticity. As the elastic behaviour does not involve time, it is straightforward to estimate, at any given time, the effective stiffness of the composite material, from a snapshot of its morphology. The latter being constant, usual homogenization procedures can be used. The basic principle is briefly recalled here ; for more details see, for example, Zaoui [206] and Dormieux et al. [119].

2.1 Introduction to Mean-Field Homogenization in Elasticity

The general case of a n-phases composite is considered in this part. Phase i occupies the domain $\Omega_i(t)$, which depends on time t due to the evolving nature of the morphology. The volume fraction and stiffness tensor of phase i are respectively denoted by $f_i(t)$ and $\mathbb{C}_i$.
At any given time u (different notation from t, to emphasize that u is a given kinematic parameter), the set of equations to solve on the representative elementary volume (REV) Ω, with

kinetic uniform boundary conditions (macroscopic strain $\underline{\underline{E}}$), is

$$\underline{\underline{\epsilon}}(\underline{x}) = \underline{\underline{\underline{\underline{grad}}}}^s[\underline{\xi}(\underline{x})], \underline{x} \in \Omega \tag{2.1a}$$

$$\underline{div}[\underline{\underline{\sigma}}(\underline{x})] = \underline{0}, \underline{x} \in \Omega \tag{2.1b}$$

$$\underline{\underline{\sigma}}(\underline{x}) = \mathbb{C}(\underline{x}, u) : \underline{\underline{\epsilon}}(\underline{x}), \underline{x} \in \Omega \tag{2.1c}$$

$$\underline{\xi}(\underline{x}) = \underline{\underline{E}} \cdot \underline{x}, \underline{x} \in \partial\Omega \tag{2.1d}$$

where $\underline{\underline{\underline{\underline{grad}}}}^s()$ = symmetric part of the gradient operator, and the local stiffness is defined by

$$\mathbb{C}(\underline{x}, t) = \sum_{i=1}^{n} \mathbb{C}_i \chi_i(\underline{x}, t) \tag{2.2}$$

where $\chi_i(\underline{x}, t)$ = characteristic function of phase i : $\chi_i(\underline{x}, t) = 1$ when $\underline{x} \in \Omega_i(t)$, and 0 otherwise. Considering a snapshot of the evolving microstructure, that is at a fixed time u, the homogenization problem (Eq.(2.1)) is the same as a classic one with constant microstructure. The linear nature of this homogenization problem with respect to the loading parameter $\underline{\underline{E}}$ allows one to define the so-called strain localization tensor $\mathbb{A}_u$, relating the microscopic to the macroscopic strain

$$\underline{\underline{\epsilon}}(\underline{x}) = \mathbb{A}_u(\underline{x}) : \underline{\underline{E}} \tag{2.3}$$

the subscript indicates that $\mathbb{A}_u$ depends on u through the current morphology at this time. The effective stiffness then derives from the application of the local behaviour and from spatially average of the microscopic stress to get the macroscopic stress

$$\mathbb{C}^{eff}(u) = \langle \mathbb{C}(\underline{x}, u) : \mathbb{A}_u(\underline{x}) \rangle = \sum_{i=1}^{n} f_i(u) \mathbb{C}_i : \langle \mathbb{A}_u(\underline{x}) \rangle_{\Omega_i(u)} \tag{2.4}$$

where $\langle\rangle$ and $\langle\rangle_{\Omega_i(u)}$ denote the spatial average over Ω and $\Omega_i(u)$ respectively. The effective stiffness $\mathbb{C}^{eff}$ depends on u through volume fractions f_i, phase domains Ω_i, and the localization tensor $\mathbb{A}_u$.

The following subsection presents the calculation of the spherical part and the deviatoric part of the localization tensor.

2.1.1 Localization tensor of a spherical inclusion embedded in an infinite matrix.

Calculation case 1 : a spherical inclusion embedded in an infinite matrix subjected to an isotropic strain loading

We consider a strain field equal to e^∞ far away from the heterogeneity (that is to say, "infinitely far from the spherical inclusion"). The isotropic strain applied on the infinite matrix is :

$$\underline{\underline{E}} = \begin{pmatrix} e^\infty & 0 & 0 \\ 0 & e^\infty & 0 \\ 0 & 0 & e^\infty \end{pmatrix} \tag{2.5}$$

We assume that the form of displacement is :

$$\underline{\xi} = \xi(r)\underline{e_r} \tag{2.6}$$

According to Eq.(2.6) :

$$\varepsilon_{rr} = \frac{\partial \xi_r}{\partial r} = \frac{\partial \xi(r)}{\partial r} \tag{2.7}$$

$$\varepsilon_{\theta\theta} = \frac{1}{r}\frac{\partial \xi_\theta}{\partial \theta} + \frac{\partial \xi_r}{\partial r} = \frac{\xi(r)}{r} \tag{2.8}$$

$$\varepsilon_{\phi\phi} = \frac{1}{rsin\theta}\frac{\partial \xi_\phi}{\partial \phi} + \frac{\partial \xi_\theta}{\partial r}cot\theta + \frac{\xi_r}{\partial r} = \frac{\xi(r)}{r} \tag{2.9}$$

$$\varepsilon_{r\theta} = \frac{1}{2}(\frac{\partial \xi_\theta}{\partial r} - \frac{\xi_\theta}{r} + \frac{1}{r}\frac{\partial \xi_r}{\partial \theta}) = 0 \tag{2.10}$$

$$\varepsilon_{\theta\phi} = \frac{1}{2}(\frac{1}{rsin\theta}\frac{\partial \xi_\theta}{\partial \phi} + \frac{1}{r}\frac{\partial \xi_\phi}{\partial \theta} - \frac{cot\theta}{r}\xi_\phi) = 0 \tag{2.11}$$

$$\varepsilon_{r\phi} = \frac{1}{2}(\frac{1}{rsin\theta}\frac{\partial \xi_r}{\partial \phi} - \frac{\xi_\phi}{r} + \frac{\partial \xi_\phi}{\partial r}) = 0 \tag{2.12}$$

Specifically,

$$\underline{\underline{\sigma}} = ktr(\underline{\underline{\varepsilon}})\underline{\underline{I}} + 2\mu\underline{\underline{\varepsilon}}^{dev} \tag{2.13}$$

Here, the spherical (also called the hydrostatic) part of the strain tensor is the trace of the strain tensor (sum of the diagonals), and the deviatoric part of the strain tensor is marked as $\underline{\underline{\epsilon}}^{dev}$. The equation of equilibrium (2.1)(b) is written here :

$$\frac{\partial \sigma_{rr}}{\partial r} + \frac{1}{r}\frac{\partial \sigma_{r\theta}}{\partial \theta} + \frac{1}{rsin\theta}\frac{\partial \sigma_{r\phi}}{\partial \phi} + \frac{1}{r}(2\sigma_{rr} - \sigma_{\theta\theta} - \sigma_{\phi\phi} + \sigma_{r\theta}cos\theta) = 0 \tag{2.14}$$

$$\frac{\partial \sigma_{\theta r}}{\partial r} + \frac{1}{r}\frac{\partial \sigma_{\theta\theta}}{\partial \theta} + \frac{1}{rsin\theta}\frac{\partial \sigma_{r\phi}}{\partial \phi} + \frac{1}{r}((\sigma_{\theta\theta} - \sigma_{\phi\phi})cot\theta + 3\sigma_{r\theta}) = 0 \tag{2.15}$$

$$\frac{\partial \sigma_{\phi r}}{\partial r} + \frac{1}{r}\frac{\partial \sigma_{\phi\theta}}{\partial \theta} + \frac{1}{rsin\theta}\frac{\partial \sigma_{\phi\phi}}{\partial \phi} + \frac{1}{r}(3\sigma_{\phi r} + 2\sigma_{\phi\theta}cot\theta) = 0 \tag{2.16}$$

So, we can have :

$$\frac{\partial^2 \xi(r)}{\partial r^2} + \frac{2}{r}\frac{\partial \xi(r)}{\partial r} - \frac{2}{r^2}\xi(r) = 0 \tag{2.17}$$

Here we can verify that the form $\xi(r) = ar + \frac{b}{r^2}$ is appropriate.
The notation 0 represents the matrix and the notation 1 represents the inclusion.
So, we assume that for the inclusion :

$$\xi^1 = a_1 r + \frac{b_1}{r^2} \tag{2.18}$$

And for the matrix :

$$\xi^0 = a_0 r + \frac{b_0}{r^2} \tag{2.19}$$

The symmetries of the problem suggest to look for the displacement field by phase in the following radial form :

$$(\forall \alpha = 0, 1), \underline{\xi^\alpha} = \xi^\alpha(r)\underline{e_r} \tag{2.20}$$

The local equilibrium ($div\underline{\underline{\sigma}} = \underline{0}$) per phase imposes $\xi^\alpha = a_\alpha r + \frac{b_\alpha}{r^2}$. The singularity in r=0 imposes $b_1 = 0$ and the boundary condition gives $a_0 = e^\infty$.
We note that the stress field per phase is then in the form :

$$\sigma^\alpha_{rr} = 2\mu_\alpha(a_\alpha - 2\frac{b_\alpha}{r^3}) + (3k_\alpha - 2\mu_\alpha)a_\alpha, \sigma^\alpha_{\theta\theta} = \sigma^\alpha_{\phi\phi} = 2\mu_\alpha(a_\alpha + \frac{b_\alpha}{r^3}) + (3k_\alpha - 2\mu_\alpha)a_\alpha \tag{2.21}$$

Assuming a perfect adhesion at the "inclusion/solid matrix" interface ($r = R$), we have :

- Continuity of the displacement field :

$$\xi^1_r(r = R)\underline{e_r} = \xi^0_r(r = R)\underline{e_r} => a_1 R = e^\infty R + \frac{b_0}{R^2} \tag{2.22}$$

- Continuity of the stress vector :

$$\sigma^1_{rr}(r = R) = \sigma^0_{rr}(r = R) => 2\mu_1 a_1 + (3k_1 - 2\mu_1)a_1 = 2\mu_0(e^\infty - 2\frac{b_0}{R^3}) + (3k_0 - 2\mu_0)e^\infty \tag{2.23}$$

Yielding :

$$b_0 = \frac{R^3(2\mu_0 + (3k_0 - 2\mu_0) - 2\mu_1 - (3k_1 - 2\mu_1))e^\infty}{2\mu_1 + 4\mu_0 + (3k_1 - 2\mu_1)} \tag{2.24}$$

$$a_1 = \frac{(2\mu_0 + (3k_0 - 2\mu_0) - 2\mu_1 - (3k_1 - 2\mu_1))e^\infty}{2\mu_1 + 4\mu_0 + (3k_1 - 2\mu_1)} + e^\infty = A_j e^\infty \tag{2.25}$$

So the spherical part of the tensor of localization is obtained :

$$A_j = \frac{3k_0 + 4\mu_0}{4\mu_0 + 3k_1} \tag{2.26}$$

In addition, the parameters a_0, b_0, a_1, b_1 are obtained. According to (2.1)(d) :

$$\underline{\underline{\varepsilon_1}} = \overline{\underline{\underline{\varepsilon_1}}} = \mathbb{A}^0_1 : \underline{\underline{E^\infty}} \tag{2.27}$$

Calculation case 2 : a spherical inclusion embedded in an infinite matrix subjected to an deviatoric strain loading

Calculus for the elastic homogenization principles can be done in the software Maple, in applying the above principles. The equations of equilibrium, the linearized strain tensor and the behaviour law are entered in Maple. If the continuity conditions in displacement and the boundary conditions are added, Maple can solve the differential equations to define the shape of the equation of displacement.
In the simplified case of the isotropic strain loading conditions applied to an infinite matrix, the results can be calculated by hand directly because the polynomials in the equations are rather simple. But in the case of the deviatoric strain loading conditions, the equations become more complicated. So, it is easier to use Maple to define the coefficients in each equation.
The modules of Maple Tens3D [71] and Lociso (written by J. Sanahuja) are used during the calculation.
At first, we need to define a spherical coordinate system in Maple.
The deviatoric strain loading conditions applied to an infinite matrix is (in Cartesian coordinate system) is taken in the following form :

$$\underline{\underline{E}} = \begin{pmatrix} e^{\infty} & 0 & 0 \\ 0 & -e^{\infty} & 0 \\ 0 & 0 & 0 \end{pmatrix} \tag{2.28}$$

During the transformation from Cartesian coordinate system to spherical coordinate system, for each component of the displacement vector, there is the part of which "$e^{\infty}r$" is included. Here, the element with "$e^{\infty}r$" can be regarded as a function of r, which is denoted as $f(r)$. As a result, the functions of the form of the displacement $A_r f(r)$, $A_\theta f(r)$ and $A_\phi f(r)$ can be used here to represent this part in three coordinates (r, θ and ϕ). So we assume that the form of displacement is :

$$\underline{\xi} = \underline{\xi}(r, \theta, \phi) \; with \; \theta \in [0, pi] \; and \; \phi \in [0, 2\pi] \tag{2.29}$$

Then, the linearized strain tensor equation, the constitutive law equation and the equilibrium equation are entered in Maple.
The general solutions of the differential equations can be calculated in Maple according to the equations above.
And to find the particular solution, we must firstly add the boundary condition at infinity (Eq.(2.28)) and at $r = 0$ (that is, when $r = 0$, the displacement equals 0).
It is also necessary to add the conditions of continuity of the displacement field and the continuity of the stress vector :

$$\underline{\xi}^1(r = R) = \underline{\xi}^0(r = R) \tag{2.30}$$

$$\sigma^1_{rr}(r = R) = \sigma^0_{rr}(r = R) \tag{2.31}$$

So the deviatoric part of the localization tensor is :

$$A_k = \frac{5(4\mu_0 + 3k_0)\mu_0}{9k_0\mu_0 + 6k_0\mu_1 + 8\mu_0^2 + 12\mu_0\mu_1} \tag{2.32}$$

$$\mathbb{A}_1^0 = A_j\mathbb{J} + A_k\mathbb{K} \tag{2.33}$$

2.2 Micromechanical modeling with various homogenization schemes for cementitious materials

Simple homogenization estimates are obtained by assuming the same strain (Voigt) or stress (Reuss) in the phases in the REV. These assumptions respectively lead to overestimate and underestimate the overall stiffness of the multi-phase composite. More elaborated methods make up for these characteristics and base their foundations on Eshelby's result [62].
Homogenization procedures are mainly based on the definition of a local surrounding of a macroscopic material point with volume Ω and the boundary $\partial\Omega$. This volume Ω represents a characteristic part of the material which is sufficient to describe its structure and behaviour, respectively. This implies that the size of heterogeneities at the microlevel has to be one scale smaller than the size of the volume Ω of the macropoint. The Hill-Mandel condition is fulfilled by applying linear displacements, periodic boundary conditions or uniform tractions on $\partial\Omega$. Therefore the average strain in the volume Ω is equal to the macro strain.
for a multiphase composite consisting of n phases, $f_\alpha = \Omega_\alpha/\Omega$ denotes the volume fraction of each phase α with respect to the total volume Ω of the REV, which are subjected to the restriction $\sum_{\alpha=1}^{n} f_\alpha = 1$.
In the following, $\mathbb{A}_\alpha$ describes the volume average of $\mathbb{A}(x)$ in the phase α. As this average is done phase-wise, this results in phase wise constant localization tensors $\mathbb{A}_\alpha$. Hence, the effective stiffness tensor can be calculated via

$$\mathbb{C}^* = \sum_{\alpha=1}^{n} f_\alpha \mathbb{C}_\alpha : \mathbb{A}_\alpha \tag{2.34}$$

For the special case of an inclusion in an infinite matrix, the Eshelby solution can be used to determine the so far unknown localization tensors $\mathbb{A}_\alpha$. The strain in the inclusion can be calculated by

$$\underline{\underline{\epsilon}}^I = \mathbb{A}_I^0 : \underline{\underline{\epsilon}}^0 = [\mathbb{I} + \mathbb{S} : \mathbb{C}_M^{-1} : (\mathbb{C}_I - \mathbb{C}_M)]^{-1} : \underline{\underline{\epsilon}}^0 = const \tag{2.35}$$

where $\mathbb{I}$ designates the fourth-order symmetric identity tensor, $\mathbb{C}_M$ the stiffness tensor of the matrix, $\mathbb{C}_I$ the stiffness tensor of the inclusion and $\mathbb{S}$ the Eshelby tensor. In general, the Eshelby tensor $\mathbb{S}$ has both minor symmetries but no major symmetry. ϵ^0 is the strain at infinity in the location problem (inclusion in infinite medium, which is different from the strain applied to the bord of the REV.
In the following subsections some well-known homogenization schemes are depicted.

2.2.1 Dilute Eshelby scheme

The volume fraction of the inclusion phase is so low that the interaction in between these inclusions may be neglected. The corresponding volume fraction is defined as :

$$f_1 = 1 - f_0 \ll 1 \tag{2.36}$$

So that the matrix plays the role of the dominant phase.
Consequently, the homogenized elastic tensor reads :

$$\mathbb{C}_{dil}^{hom} = \mathbb{C}^0 + f_1(\mathbb{C}^1 - \mathbb{C}^0) : \mathbb{A}_1^0 \tag{2.37}$$

By inference, with isotropic assumptions, we have :

$$k_{dil}^{hom} = k^0 + f_1(k^1 - k^0)A_j \tag{2.38}$$

$$\mu_{dil}^{hom} = \mu^0 + f_1(\mu^1 - \mu^0)A_k \tag{2.39}$$

2.2.2 Mori-Tanaka scheme [132]

We have just treated a problem about a spherical inclusion embedded in an infinite homogeneous solid matrix with elastic moduli $\mathbb{C}^0$ subjected to an auxiliary strain $\underline{\underline{E_0}}$ applied at infinity of the matrix. It is noted as an auxiliary problem in the paragraph below.
The key assumption in Mori-Tanaka scheme is that the average strain in the matrix equals to the strain applied at infinity. And the average strain in the inclusion, is related to the average strain in the matrix ($\underline{\underline{E_0}}$) by a fourth order tensor. This fourth order tensor gives the relation between the uniform strain in the inclusion embedded in an all matrix material. Further, this material is subjected to uniform strain at infinity $\underline{\underline{E_0}}$.
We consider, the real volume average strain $\langle \underline{\underline{\varepsilon_{Rel}}} \rangle$ over Ω :

$$\langle \underline{\underline{\varepsilon_{Rel}}} \rangle = \underline{\underline{E}} \tag{2.40}$$

And the material of the matrix is subjected to uniform strain at infinity $\underline{\underline{E_0}}$:

$$\overline{\underline{\underline{\varepsilon_{Mat}}}} = \underline{\underline{E_0}} \tag{2.41}$$

The auxiliary problem with $\underline{\underline{E_0}}$ takes advantage of the results derived in the previous section, provided that $\underline{\underline{E}}$ be replaced by $\underline{\underline{E_0}}$. It makes use of the strain average rule to identify the link between $\underline{\underline{E}}$ be replaced by $\underline{\underline{E_0}}$.

That is to say :

$$(1-f_1)\overline{\underline{\underline{\varepsilon^0_{Rel}}}} + f_1\overline{\underline{\underline{\varepsilon^1_{Rel}}}} = \underline{\underline{E}} \tag{2.42}$$

According to Eq.(2.35), Eq.(2.36) and Eq.(2.42) :

$$[(1-f_1)\mathbb{I} + f_1\mathbb{A}^0_1] : \underline{\underline{E_0}} = \underline{\underline{E}} \tag{2.43}$$

As a result :

$$\underline{\underline{E}}^\infty = [(1-f_1)\mathbb{I} + f_1\mathbb{A}^0_1]^{-1} : \underline{\underline{E}} = \overline{\mathbb{A}}^{-1} : \underline{\underline{E}} \tag{2.44}$$

By inference :

$$\mathbb{C}^{hom}_{MT} = \mathbb{C}^0 + f_1(\mathbb{C}^1 - \mathbb{C}^0) : \mathbb{A}^0_1 : \overline{\mathbb{A}}^{-1} \tag{2.45}$$

For the spherical part :

$$k^{hom}_{MT} = k^0 + f_1(k^1 - k^0)A_j \frac{1}{(1-f_1) + f_1 A_j} \tag{2.46}$$

For the deviatoric part :

$$\mu^{hom}_{MT} = \mu^0 + f_1(\mu^1 - \mu^0)A_k \frac{1}{(1-f_1) + f_1 A_k} \tag{2.47}$$

2.2.3 Self-Consistent Scheme for Cement Paste

The morphology being assumed as polycrystalline at any given time, the self-consistent scheme [36][92] is the most adequate one to estimate the effective stiffness of cement paste, from the current volume fractions of anhydrous, hydrates, and pores. The behaviour of these phases is assumed to be isotropic, with bulk and shear moduli k_i, μ_i for phase $i \in a, h, p$. The derivation of the self-consistent scheme, with three families of spherical particles, is recalled here for the sake of completeness. The dependencies on the current time u are omitted to lighten notations.
The average strain in each phase i is estimated as the strain arising in a sphere made up of the same material, embedded in an infinite medium characterized by the sought effective stiffness $\mathbb{C}_{SC}$, with kinematic uniform ($\underline{\underline{E_0}}$) boundary conditions (Fig.2.1). This is an Eshelby inhomogeneity problem [63], whose solution is

$$\langle \underline{\underline{\epsilon}} \rangle_i = \mathbb{A}^{SC}_i : \underline{\underline{E_0}}, with\ \mathbb{A}^{SC}_i = [\mathbb{I} + \mathbb{P}^{sph}_{SC} : (\mathbb{C}_i - \mathbb{C}_{SC})]^{-1} \tag{2.48}$$

where $\mathbb{A}^{SC}_i$ = strain localization tensor in a sphere of stiffness $\mathbb{C}_i$ embedded in an infinite medium of stiffness $\mathbb{C}_{SC}$. It involves the Hill tensor $\mathbb{P}^{sph}_{SC}$ of a sphere in a medium of stiffness $\mathbb{C}_{SC}$. As both the elementary phases and the morphology are isotropic, the effective stiffness is expected to be isotropic. Consequently, the Hill tensor is also isotropic. It is also the case for the strain

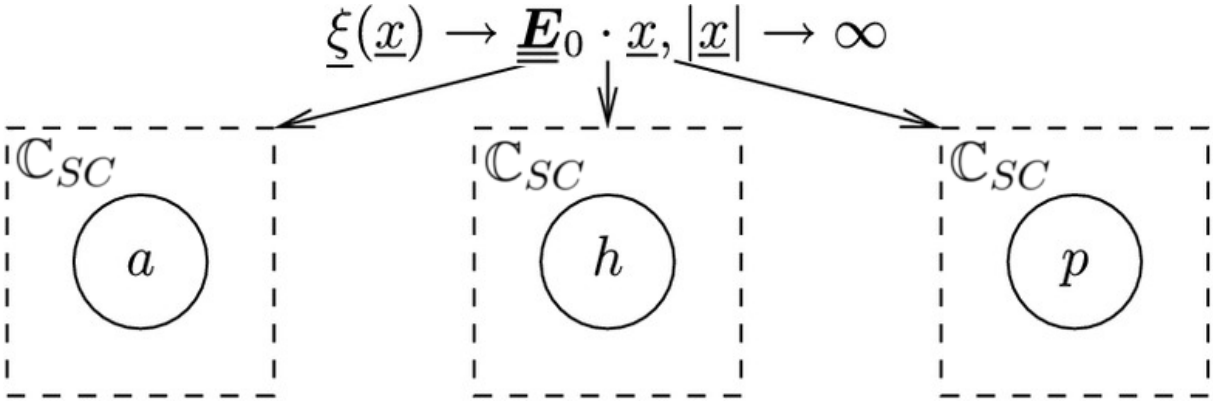

FIGURE 2.1 : Auxiliary problems to implement the self-consistent scheme ; anhydrous, hydrates, and pore space being represented by spherical shapes.

localization tensor, which can be written as $\mathbb{A}_i^{SC} = \mathbb{A}_{iJ}^{SC}\mathbb{J} + \mathbb{A}_{iK}^{SC}\mathbb{K}$, with

$$\mathbb{A}_{iJ}^{SC} = (1 + \frac{3k_{SC}}{3k_{SC} + 4\mu_{SC}} \frac{k_i - k_{SC}}{k_{SC}})^{-1} \tag{2.49a}$$

$$\mathbb{A}_{iK}^{SC} = (1 + \frac{6}{5} \frac{k_{SC} + 2\mu_{SC}}{3k_{SC} + 4\mu_{SC}} \frac{\mu_i - \mu_{SC}}{\mu_{SC}})^{-1} \tag{2.49b}$$

where k_{SC} and μ_{SC} = effective bulk and shear moduli.
The average strain in the whole REV is the weighted average of the average strains in each phase

$$\underline{\underline{E}} = \langle \underline{\underline{\epsilon}} \rangle = \sum_{i \in a,h,p} f_i \langle \underline{\underline{\epsilon}} \rangle_{\Omega_i} \tag{2.50}$$

the average stress in the whole REV can be written in a similar way. Eliminating the reference strain $\underline{\underline{E}}_0$ from the average stress and strain yields the implicit expression of the effective stiffness as estimated from the self-consistent scheme reads :

$$\mathbb{C}_{SC} = (\sum_{i \in a,h,p} f_i \mathbb{C}_i : \mathbb{A}_i^{SC}) : (\sum_{i \in a,h,p} f_i (\mathbb{A}_i^{SC}))^{-1} \tag{2.51}$$

The latter is a nonlinear equation on the effective stiffness $\mathbb{C}_{SC}$, as the strain tensor of localization $(\mathbb{A}_i^{SC})^{-1}$ itself depends on the latter through Eq.(2.49). Recalling the considered assumptions, this tensorial equation only involves isotropic tensors. It can thus be projected on $\mathbb{J}$ and $\mathbb{K}$ respectively, yielding a system of two nonlinear equations on the effective bulk and shear moduli

$$k_{SC} = \frac{\sum\limits_{i\in a,h,p} f_i k_i \mathbb{A}_{iJ}^{SC}}{\sum\limits_{i\in a,h,p} f_i \mathbb{A}_{iJ}^{SC}} \tag{2.52a}$$

$$\mu_{SC} = \frac{\sum\limits_{i\in a,h,p} f_i \mu_i \mathbb{A}_{iK}^{SC}}{\sum\limits_{i\in a,h,p} f_i \mathbb{A}_{iK}^{SC}} \tag{2.52b}$$

2.3 Application for different schemes

The numerical parameters used in the simulations are collated in Table 2.1 (for the self-consistent scheme, the material parameters of Phase 1 take those of the matrix, and the material parameters of Phase 2 take those of the inclusion). The stiffness is defined by the bulk modulus k (GPa) and the shear modulus μ (GPa). The material parameters in Table 2.1 is given for the academic example, and is not referred to a certain cemetitious material.

The modulus homogenized by different schemes are drawn in simple lines in Fig.2.2.

TABLE 2.1 : Material parameters used in the application.

	Bulk modulus k (GPa)	Shear modulus μ (GPa)
Matrix	2	1
Inclusion	15	4

In the Fig.2.2, the spherical and deviatoric part of stiffness are marked with the continuous lines

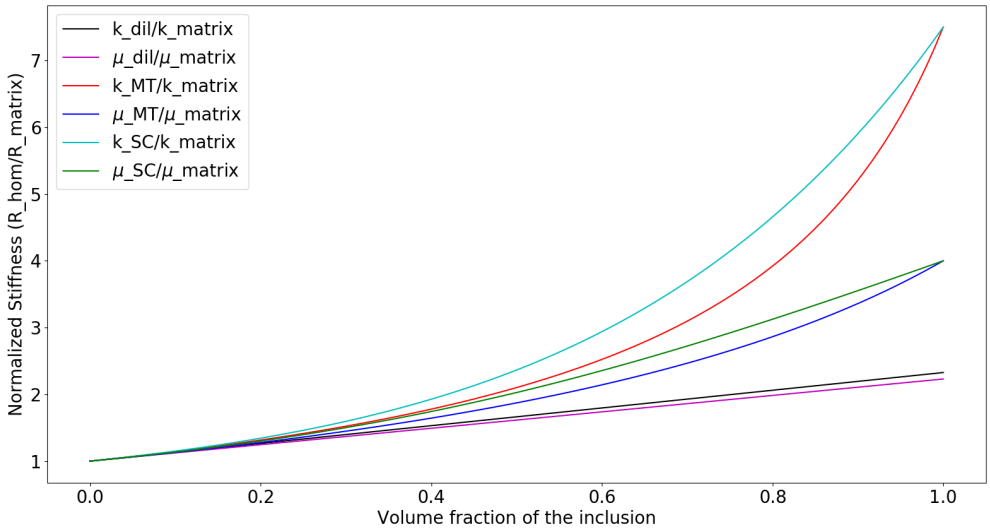

FIGURE 2.2 : Homogenized moduli derived by different schemes.

with different colors (k_{dil} and μ_{dil} for the spherical and deviatoric part of stiffness calculated by the dilute scheme, k_{MT} and μ_{MT} for the spherical and deviatoric part of stiffness calculated by the Mori-Tanaka scheme, k_{SC} and μ_{SC} for the spherical and deviatoric part of stiffness calculated by the self-consistent scheme).
Finally, in Fig.2.2, we compare the stiffness moduli estimated by three homogenization schemes. Note that the dilute scheme is relevant only when the volume fraction of the inclusion phase is sufficiently low.
Moreover, we see that the self-consistent scheme predicts stiffer moduli than does the Mori-Tanaka scheme. In fact, it is known that, although the Mori-Tanaka scheme involves the interaction between particles, when any particle is added, the matrix is always considered as the original one without taking into account the existing reinforcement by other particles already added. Thus, in mathematics, the effective stiffness homogenized is smaller. However, in the self-consistent scheme, the property of the reference media is assumed to be that after all the particle phases are added, which implies sufficiently large number of sufficiently small added phases in the REV and take into account the interaction of all the phases.

2.4 Evolution of Cement Paste Elasticity

Two kinds of input data are required in Eq.(2.52) : the current values of the volume fractions f_i and the bulk and shear moduli k_i, μ_i. Volume fractions are provided by the Powers model in Eq.1.1. The elastic properties of the elementary phases come from nano-indentation measurements [194][195] and are gathered in Table 2.2. The effective Young's modulus of hydrating cement paste homogenized by the self-consistent scheme is plotted as a function of the degree of hydration for various w/c ratios in Fig.2.3(a).
As expected, the effective Young's modulus of paste increases with the hydration degree, and is

TABLE 2.2 : Material and Kinetics Parameters Used in Applications.

Phase	E(GPa)	ν	τ/τ_{kin}	ν^v	n_{kin}
Anhydrous	135 [194]	0.3 [194]	N/A	N/A	-
Hydrates	31 [195]	0.24 [195]	3	0.2	4
Capillary pores	0	N/A	N/A	N/A	-

higher for lower w/c ratios. Moreover, the micromechanical model is able to describe the setting mechanism : below a critical degree of hydration α^c, the effective stiffness is 0, and for $\alpha \geq \alpha^c$, it increases from 0. This feature comes from a well-known property of the underlying self-consistent scheme : to get a solid effective behaviour (the percolation threshold), the total solid volume fraction $f_a + f_h$ has to reach 1/2 with spherical inclusions, which is the result of culstering of pores. And the behaviour of a system close to its critical porosity is percolatin theory. This condition can be translated to the expression of the critical degree of hydration as a function of the w/c

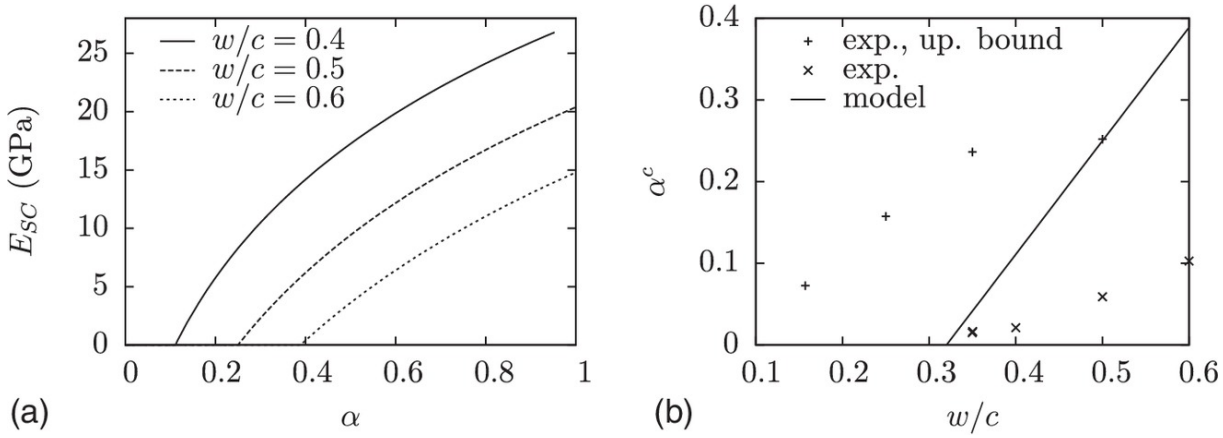

FIGURE 2.3 : (a) Effective Young's modulus of cement paste homogenized by the self-consistent scheme, estimated as a function of hydration degree for various w/c ratios ; (b) critical degree of hydration, at setting, estimated from the Powers model and experimentally (experimental results from [186]).

ratio, referring to the Powers model in Eq.1.1

$$\alpha^c = \frac{w/c - 0.32}{0.72} \tag{2.53}$$

2.5 Discussion on the Critical Degree of Hydration

The setting degree of hydration can be difficult to directly measure experimentally, due to difficulties to perform classical mechanical tests on cementitious materials at very early ages. Torrenti and Benboudjema [189] proposed an approach to estimate it, from compressive strength measurements for various hydration degrees, reported by Taplin [187] and Byfors [40]. Namely, the strength dependence with respect to the hydration degree is approximated by an affine function, whose intersection with the 0-strength axis provides an estimate of the setting hydration degree. However, this estimate can be considered as an upper bound, as a few data points indicate non-zero strength (a couple of MPa) for hydration degrees lower than this estimate. Thus, at early age, strength does not increase with respect to the hydration degree according to an affine law, but rather in a smoother way, according to a concave upward curve. Pichler et al. [141] reported experimental setting degrees of hydration from Boumiz et al.[30] and Sun et al. [183], which are much lower than those from Torrenti and Benboudjema[189].
This is further confirmed by more recent experimental works. Still regarding compressive strength, Pichler et al. [142] measured a few MPa for a $w/c = 0.42$ paste at $\alpha \approx 0.1$. Classical mechanical tests can only, by nature, be performed on already set samples. To overcome this limitation, Azenha et al. [8] developed the elasticity modulus measurement based on ambient response method (EMM-ARM) technique, which allows one to continuously monitor the Young's modulus of cementitious materials, from the fluid state. This technique has been used to estimate the setting time of cement pastes [121], and combined with estimates of the degree of hydration through chemical shrinkage measurements [122], to relate the Young's modulus to the hydration degree.

Nonzero stiffness ($E \approx 0.2GPa$) has been measured for hydration degrees as low as $\alpha \approx 0.05$ on pastes prepared with w/c ratios ranging in between 0.4 and 0.5.
These experimental results allow for assessing the critical hydration degree estimated by the morphological model adopted here, and to highlight its limitations [Fig.2.3(b) : experimental results from Torrenti and Benboudjema [189] and Pichler et al. [141] are reported using respectively, $+$ and $\times$ dots] :

1. Instantaneous setting (at $\alpha = 0$, before even starting hydration) occurs for $w/c < 0.32$; in this case the initial volume fraction of anhydrous is higher than $1/2$. This limitation has already been pointed out by Bernard et al. [25] ;

2. At $w/c > 0.35$, the setting degree of hydration is overestimated, and at $w/c = 0.5$ it happens to correspond to the upper bound proposed by Torrenti and Benboudjema [189] ;

3. The predicted stiffness evolution does not follow a concave upward curve just after setting.

These limitations mainly come from the simplified nature of the adopted morphological model.

2.6 Discussion on the Morphological Model

The aim of this section was to propose a mean-field homogenization approach to estimate the effective ageing viscoelastic behaviour of time-evolving microstructures. To focus on the presentation of the approach rather than on technical complications, the morphological model has been deliberately chosen as a simplified representation of cement pastes. Future works may include improvements of this microstructure description. A few possibilities are recalled here, based on cement paste morphological models that have proven realistic enough to provide relevant estimates of other effective mechanical properties, such as stiffness, strength, and (nonageing) creep. From the proposed model, which considers spherical particles and every phase at the same scale, several improvements are possible :

1. Considering non spherical shapes for hydrate particles, such as needles [181][141][140][142][188] or platelets [164][181]. As shown on stiffness predictions [141], considering C-S-H solid particles as needles (prolates of infinite aspect ratio) allowed to predict $\alpha_c = 0$ for $w/c > 0.32$, thus underestimating the critical hydration degree rather than overestimating it (case of spherical particles). Still, for $w/c < 0.32$, these models predict a positive Young's modulus even before starting hydration ($\alpha = 0$).

2. Considering a multiscale microstructure, that is introducing a scale separation between C-S-H particles and clinker grains (and possibly other hydrate particles such as portlandite) [164][46][181][140][82][142][188]. Combined with spherical C-S-H solid particles, this allowed one to overcome the past instantaneous setting time [$E(\alpha = 0) > 0$], irrespective of the w/c ratio [164][140] and to get a Young's modulus evolution starting with upward concavity [140]. Furthermore, considering hydrate particles as oblates [164] or prolates [165] of finite

aspect ratio allowed to predict a nonzero critical hydration degree, whose dependence on w/c is parametrized by the particles aspect ratio. Still, the onset of Young's modulus evolution is rather affine, but this can be improved considering a multiscale pore space in the hydrates matrix [164].

3. Considering two types of C-S-H, namely high-density and low-density, either homogenized to provide a matrix embedding cement grains [46] or respectively considered as inner (surrounding cement grains) and outer products (acting as a matrix embedding cement grains surrounded by inner products)[164].

4. Considering a double scale structure to describe the matrix phase in the morphological model.

Going back to the scope of this section, as the adopted model is not able to predict a concave upward onset of Young's modulus, its α_c predictions are still compared to the experimental estimates of [189] [see + dots in Fig.2.3(b)]. At $w/c \approx 0.5$, both approaches happen to be consistent : viscoelastic simulations will focus on this specific water-to-cement ratio.

Chapitre 3

Effective Viscoelastic Behavior of Evolving Microstructure : "Frozen Microstructure" Approximation

Sommaire

The phases behaviour is now considered as nonageing linear viscoelastic. Contrary to the elastic case, this behaviour now explicitely involves time. Upscaling is no longer as straightforward as considering a snapshot of the microstructure at a given time and performing homogenization on this snapshot. As the domains occupied by phases evolve with respect to time, a specific procedure will be proposed in the next chapter.
For now, a usual simplification [see [158][112][82] for mean-field homogenization or [210] for full-field homogenization] is that : to estimate the effective response of the evolving composite, the microstructure is considered as frozen once the strain step has been applied. As microstructure becomes constant, classical homogenization of nonageing linear viscoelastic behaviours becomes relevant. The latter is briefly recalled in the next subsection.

3.1 Introduction to Nonageing Linear Viscoelasticity Homogenization of Constant Microstructures

In this subsection, the REV is considered to be made up of n nonageing linear viscoelastic phases, without any evolution of its microstructure. The set of equations to solve on the REV,

with kinematic uniform boundary conditions (macroscopic strain $\underline{\underline{E}}(t)$, now depending on time), is

$$\underline{\underline{\epsilon}}(\underline{x},t) = grad^s[\underline{\xi}(\underline{x},t)], \underline{x} \in \Omega \tag{3.1a}$$

$$\underline{div}[\underline{\underline{\sigma}}(\underline{x},t)] = \underline{0}, \underline{x} \in \Omega \tag{3.1b}$$

$$\underline{\underline{\sigma}}(\underline{x},t) = \int_{t'=-\infty}^{t} \mathbb{C}(\underline{x},t-t') : d\underline{\underline{\epsilon}}(\underline{x},t'), \underline{x} \in \Omega \tag{3.1c}$$

$$\underline{\xi}(\underline{x},t) = \underline{\underline{E}}(t) \cdot \underline{x}, \underline{x} \in \partial\Omega \tag{3.1d}$$

where the local relaxation tensor is defined as

$$\mathbb{C}(\underline{x},t-t') = \sum_{i=1}^{n} \mathbb{C}_i(t-t')\chi_i(\underline{x}) \tag{3.2}$$

where $\chi_i(\underline{x})$ = characteristic function of phase i.
The classical approach to solve this problem is to take advantage of the correspondence principle [124] : The Laplace-Carson transform changes nonageing linear viscoelastic behaviours into elastic ones. The Laplace-Carson transform of function $f(t)$ is $f^*(p) = p\mathcal{L}f(p)$ with the Laplace transform $\mathcal{L}f(p) = \int_{-\infty}^{\infty} f(t)e^{-pt}dt$.
Applying the Laplace-Carson transform to the set of Eq.3.1 yields, taking advantage of the main properties of this transform (linearity and transformation of convolutions into products)

$$\underline{\underline{\epsilon}}^*(\underline{x},p) = \underline{\underline{grad}}^s[\underline{\xi}^*(\underline{x},p)], \underline{x} \in \Omega \tag{3.3a}$$

$$\underline{div}[\underline{\underline{\sigma}}^*(\underline{x},p)] = \underline{0}, \underline{x} \in \Omega \tag{3.3b}$$

$$\underline{\underline{\sigma}}^*(\underline{x},p) = \mathbb{C}^*(\underline{x},p) : \underline{\underline{\epsilon}}^*(\underline{x},p), \underline{x} \in \Omega \tag{3.3c}$$

$$\underline{\xi}^*(\underline{x},p) = \underline{\underline{E}}^*(p) \cdot \underline{x}, \underline{x} \in \partial\Omega \tag{3.3d}$$

and where the Laplace-Carson transform of the local relaxation tensor is

$$\mathbb{C}^*(\underline{x},p) = \sum_{i=1}^{n} \mathbb{C}_i^*(p)\chi_i(\underline{x}) \tag{3.4}$$

For each value of the Laplace variable p, in the Laplace-Carson domain, this problem is equivalent to the elastic one (Eq.(2.1)).
Consequently, estimates from elastic homogenization schemes can be directly reused, formally replacing stiffness tensors by the Laplace-Carson transforms of the relaxation tensors. This yields the effective relaxation tensor in the Laplace-Carson domain $\mathbb{C}^{eff*}(p)$. The effective nonageing relaxation tensor in the time domain $\mathbb{C}^{eff}(t)$ is then obtained by inversion of the Laplace transform. The latter can be performed analytically only in the simplest cases (in terms of both morphology and phase behaviours). In the general case, inversion can be performed numerically,

for instance using the Stehfest algorithm [3][72][179]

$$f(t) \approx \frac{ln2}{t} \sum_{k=1}^{2M} \zeta_k \mathcal{L}_f(k\frac{ln2}{t}) \tag{3.5}$$

Here, $ln2$ means the natural logarithm $log_e 2$.
with the weights

$$\zeta_k = \frac{(-1)^{M+k}}{M!} \sum_{j=floor[(k+1)/2]}^{min(k,M)} j^{M+1} \begin{pmatrix} M \\ j \end{pmatrix} \begin{pmatrix} 2j \\ j \end{pmatrix} \begin{pmatrix} j \\ k-j \end{pmatrix} \tag{3.6}$$

where $floor(x)$ = floor function, giving the highest integer lower or equal to x; and $\begin{pmatrix} n \\ k \end{pmatrix}$ = binomial coefficient. Further computations are performed with $M = 10$, which has been found to be a good compromise with respect to the accuracy required for evaluation in the Laplace domain of the function to be inverted.

3.2 "Frozen Microstructure" Homogenization

The evolving microstructure with nonageing linear viscoelastic phases is now considered. The "frozen microstructure" simplification consists in assuming that microstructure does not evolve any more after a given time u. The average stress response to a macroscopic strain starting at time u is sought. The macroscopic strain $\underline{\underline{E}}$ is thus equal to 0 for $t < u$. The microscopic strain and stress fields are then also equal to 0 for $t < u$. The frozen microstructure assumption can be expressed as : for $t \geq u, \Omega_i(t) = \Omega_i(u)$. Consequently, the relaxation tensor field across the REV can be written as

$$\mathbb{C}(\underline{x}, t-t') = \sum_{i=1}^{n} \mathbb{C}_i(t-t')\chi_i(\underline{x}, u), \quad t \geq t' \geq u \tag{3.7}$$

u being fixed, this local relaxation tensor has the same expression as Eq.3.2. As $\epsilon(t) = \sigma(t) = 0$ for $t < u$, the fact that the microstructure still evolves for $t < u$ does not matter. In other words, Eqs.3.1 and 3.2 still apply here, quantities starting to be non-0 from time $t = u$ instead of from time $t = 0$.
The homogenization process, using the correspondence principle, as recalled previously, can then be taken advantage of to estimate the nonageing effective stiffness tensor $\mathbb{C}_u^{eff,frozen}(t-u)$. The latter has been indexed by u to emphasize the fact that it depends on the given time u through the distribution of the phases at time u. Repeating this process for various values of u yields approximations of the effective relaxation and compliance tensors, as

$$\mathbb{C}^{eff}(t,u) \approx \mathbb{C}_u^{eff,frozen}(t-u) \; and \; \mathbb{S}^{eff}(t,u) \approx \mathbb{S}_u^{eff,frozen}(t-u) \tag{3.8}$$

where $\mathbb{S}_u^{eff,frozen} = (\mathbb{C}_u^{eff,frozen})^{-1}$ in the sense of nonageing linear viscoelasticity. This inversion can be straightforwardly performed in the Laplace-Carson domain. Note that one nonageing linear viscoelastic homogenization computation is required for each value of u.

3.3 Application to the homogenization scheme

The numerical processings between the Laplace-Carson (LC) transform space and the temporal dimension is carried out in Python. The script written by Y. El Assami [60] is applied and modified.
The principles of the transformation of spaces in Python are the same as in Maple.

Application to the Mori-Tanaka scheme

The spherical and the deviatoric part of the relaxation function in the Laplace-Carson dimension are as follows :

$$k_{MT}^* = k_0^* + f(k_1^* - k_0^*)\mathbb{A}_j^* \frac{1}{(1-f) + f\mathbb{A}_j^*} \tag{3.9}$$

$$\mu_{MT}^* = \mu_0^* + f(\mu_1^* - \mu_0^*)\mathbb{A}_k^* \frac{1}{(1-f) + f\mathbb{A}_k^*} \tag{3.10}$$

The spherical and the deviatoric part of the relaxation function in the temporal dimension are obtained afterwards by the inverse transform.

Application to the Self-Consistent Scheme for Cement Paste

At a given time u, the morphology of the cement paste is characterized by the volume fractions $f_i(u)$. As previously recalled, the equations on the effective bulk and shear moduli established in elasticity in Eq.2.52 can be reused here, replacing elastic moduli by Laplace-Carson transforms of the nonageing linear viscoelastic relaxation functions

$$k_{SC}^*(p) = \frac{\sum\limits_{i\in(a,h,p)} f_i(u) k_i^*(p) A_{iJ}^{SC*}(p)}{\sum\limits_{i\in(a,h,p)} f_i(u) A_{iJ}^{SC*}(p)} \tag{3.11a}$$

$$\mu_{SC}^*(p) = \frac{\sum\limits_{i\in(a,h,p)} f_i(u) g_i^*(p) A_{iJ}^{SC*}(p)}{\sum\limits_{i\in(a,h,p)} f_i(u) A_{iJ}^{SC*}(p)} \tag{3.11b}$$

Note that as u is fixed parameter. $f_i(u)$ remains constant and it is not affected by the Laplace-Carson transform. With this condition, the components of the strain localization tensor are obtained similarly from Eq.2.49.

$$\mathbb{A}_{iJ}^{SC*}(p) = (1 + \frac{3k_{SC}^*(p)}{3k_{SC}^*(p) + 4\mu_{SC}^*(p)} \frac{k_i^*(p) - k_{SC}^*(p)}{k_{SC}^*(p)})^{-1} \tag{3.12a}$$

$$\mathbb{A}_{iK}^{SC*}(p) = (1 + \frac{6}{5} \frac{k_{SC}^*(p) + 2\mu_{SC}^*(p)}{3k_{SC}^*(p) + 4\mu_{SC}^*(p)} \frac{\mu_i^*(p) - \mu_{SC}^*(p)}{\mu_{SC}^*(p)})^{-1} \tag{3.12b}$$

Resolution of Eq.3.4 and Laplace-Carson inversion yield the nonageing effective bulk $k_u^{SC,frozen}(t-u)$ and shear $\mu_u^{SC,frozen}(t-u)$ relaxation functions of the frozen microstructure when $t > u$. Repeating the process for various times u allows for deriving approximations of the ageing bulk and shear relaxation and compliance functions, as in Eq.3.8.

3.3.1 Application for different schemes

The numerical parameters used in the simulations are summarized in Table 3.1. The stiffness is defined by the bulk modulus k (GPa) and the shear modulus μ (GPa), and the time is normalized by the characteristic time τ, which is identified by the experimental results on the cement paste for the VeRCoRs concrete.

Here, the behaviour of the matrix is represented by the Maxwell viscoelastic model with one

TABLE 3.1 : Material parameters used in the application

	k (GPa)	μ (GPa)	$\frac{\eta/k}{\tau}$	$\frac{\gamma/\mu}{\tau}$	Volume fraction
Matrix	2	1	0.2	0.133	0.9
Inclusion	15	4			0.1

viscoelastic chain, and the behaviour of the inclusion is represented by the elastic model.
The stress relaxation modulus and the creep compliance modulus homogenized by different schemes are drawn as simple lines in Fig.3.1, Fig.3.2, Fig.3.3 and Fig.3.4.

The results show, as a function of time, the evolution of the stress relaxation and the creep compliance function for the spherical part (k) and the deviatoric part (μ) with the analytical Laplace-Carson transform and the numerical Laplace-Carson inversion.

3.4 "Frozen Microstructure" Approximation for Effective Creep of Cement Paste

The elementary behaviour of anhydrous phase is elastic. For the sake of simplicity, both bulk and shear behaviours of hydrates are represented by the Maxwell model (hydrates' viscoelastic behaviour is discussed in the next part)

$$\mathbb{C}_h(t) = 3k_h(t)\mathbb{J} + 2\mu_h(t)\mathbb{K} \tag{3.13}$$

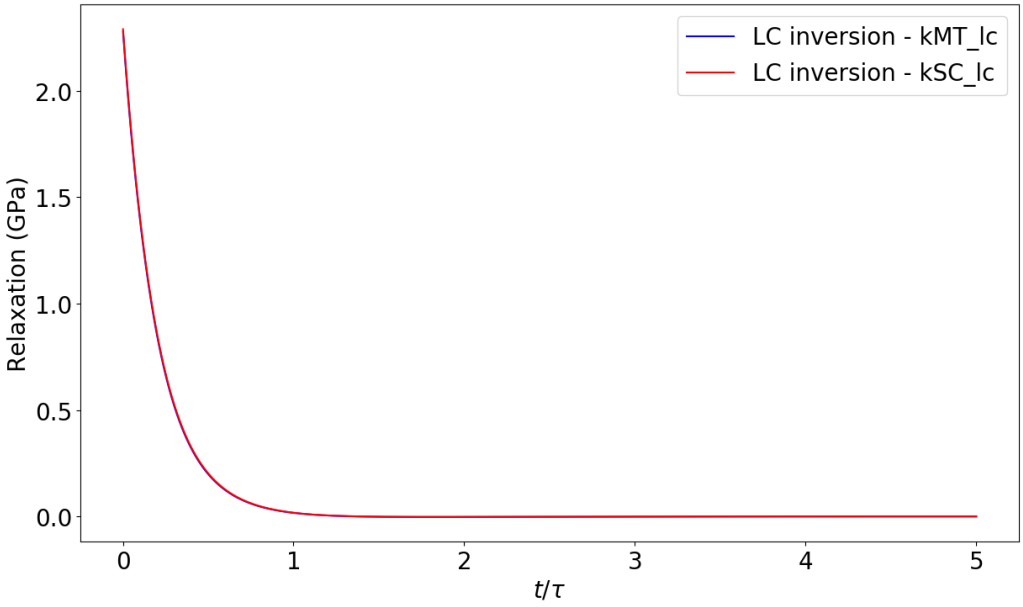

FIGURE 3.1 : The homogenized relaxation function k (GPa) calculated with the Laplace-Carson transform.

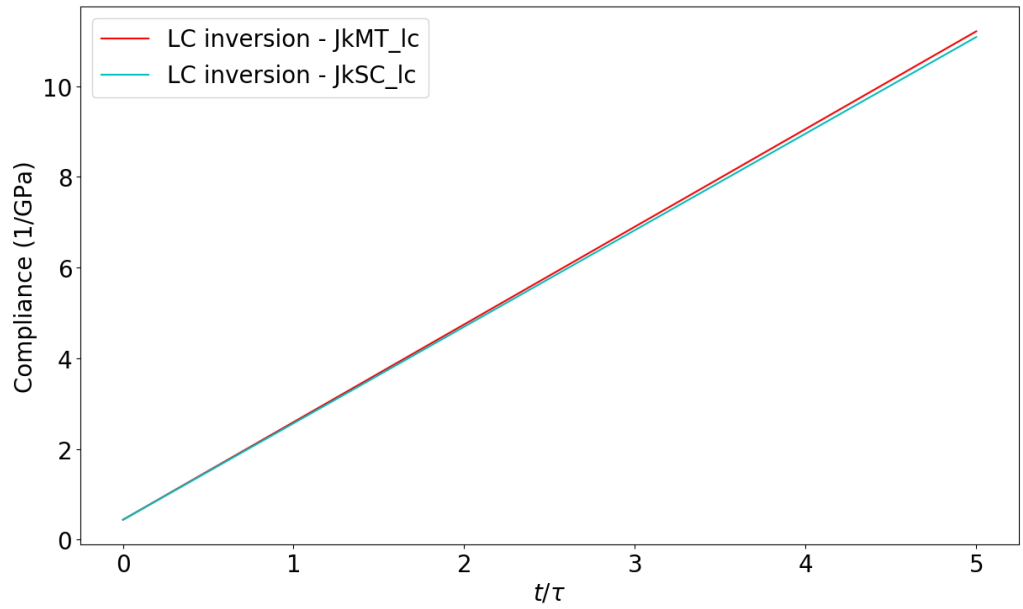

FIGURE 3.2 : The homogenized creep compliance J_k calculated with the Laplace-Carson transform.

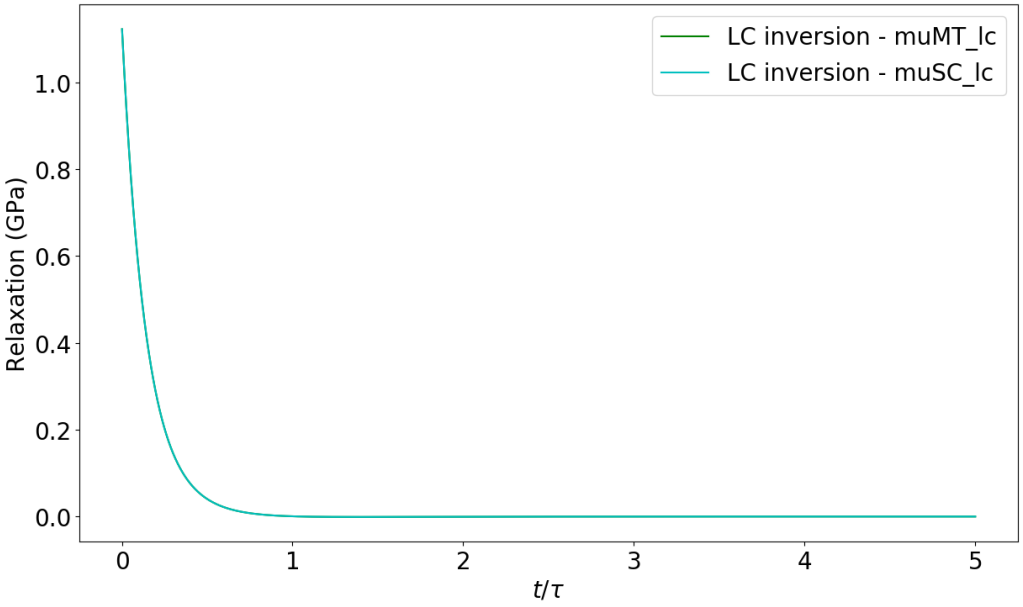

FIGURE 3.3 : The homogenized relaxation function μ (GPa) calculated with the Laplace-Carson transform.

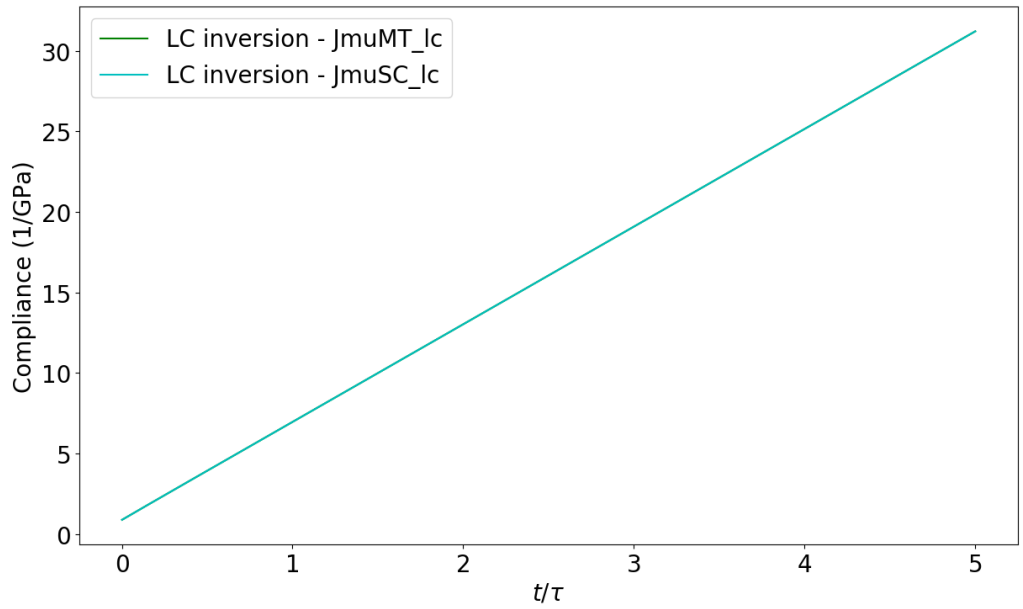

FIGURE 3.4 : The homogenized creep compliance J_μ calculated with the Laplace-Carson transform.

with the bulk and shear relaxation functions

$$k_h(t) = K_h e^{-K_h t/\eta_h} H(t) \tag{3.14a}$$

$$\mu_h(t) = M_h e^{-M_h t/\gamma_h} H(t) \tag{3.14b}$$

where $H(t)$ = Heaviside function. The constants $K_h,\ M_h$, respectively. $\eta_h,\ \gamma_h$ are the bulk and shear stiffness and viscosities, respectively. This behaviour can be alternatively defined from the elastic Young's modulus E_h and the Poisson ratio ν_h and from the viscous characteristic time τ_h and the Poisson ratio ν_h^v

$$k_h = \frac{E_h}{3(1-2\nu_h)} \tag{3.15a}$$

$$\mu_h = \frac{E_h}{2(1+\nu_h)} \tag{3.15b}$$

$$\eta_h = \frac{\tau_h E_h}{3(1-2\nu_h^v)} \tag{3.15c}$$

$$\gamma_h = \frac{\tau_h E_h}{2(1+\nu_h^v)} \tag{3.15d}$$

$$\tag{3.15e}$$

The Laplace-Carson transform of Eq.3.14 yields the bulk and shear relaxations in the Laplace-Carson domain

$$k_h^*(p) = \frac{1}{1/k_h + 1/(\eta_h p)} \tag{3.16a}$$

$$\mu_h^*(p) = \frac{1}{1/\mu_h + 1/(\gamma_h p)} \tag{3.16b}$$

Numerical values of material parameters are gathered in Table 2.2 ; the viscous characteristics of hydrates are arbitrarily chosen for this preliminary application. Times are scaled by the kinetics characteristic time τ_{kin}.

The effective uniaxial compliance functions, obtained for various loading times u, are plotted in Fig.3.5 as continuous lines. The evolution of the initial elastic strain, obtained as the inverse of the effective Young's modulus (see the chapter dedicated to elasticity), is also plotted as a dotted line. The latter is consistent with the effective uniaxial compliance functions.

Taking into account the particular microstructure at the loading time u allows for the derivation of an ageing effective behaviour. However, the latter is approximated as microstructure is assumed to be frozen for $t \geq u$. To evaluate the amount of approximation induced by this assumption, microstructure evolution is completely taken into account in the next chapter.

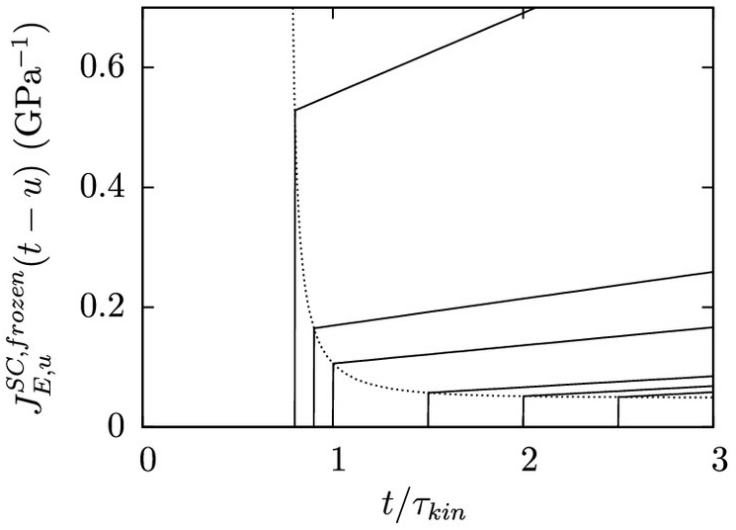

FIGURE 3.5 : Plain lines : effective uniaxial compliance functions of cement paste, approximated from frozen microstructure, plotted for various stress loading times u ($w/c = 0.5$) ; dotted line : initial elastic strain estimated from elasticity homogenization.

3.5 Discussion on Hydrates Elementary Viscoelastic Behaviour

For the sake of simplicity, the elementary viscoelastic behaviour of the hydrates has been represented by a Maxwell model. However, any nonageing linear viscoelastic behaviour can be used, provided that the relaxation moduli are known in the Laplace-Carson domain. Regarding the relevant behaviour to use, it can be derived following a bottom-up approach, taking advantage of micromechanics, starting from the creep mechanism at the microscale or nano-scale. Consensus on the latter seems not to be reached yet, and many hypotheses can be found in the literature [21], among which are transfers between capillary and adsorbed water [203], water transfers to newly created microcracks [154], and viscous sliding between C-S-H sheets [185]. Discussing the relevance of these micromechanisms is far beyond the scope of this chapter.
Still, if the viscous sliding mechanism is chosen, recent works would allow for estimating the appropriate nonageing linear viscoelastic behaviour to use at the scale of the hydrates (instead of the simplified Maxwell model considered in this section) :

1. Considering that C-S-H solid particles are made up of a stack of elementary sheets sliding one onto the other, with a Maxwell behaviour, the effective bulk and shear creep functions of a porous gel made up of such particles can be estimated from a self-consistent scheme [163]. The asymptotic behaviour (finite strain or asymptotic strain rate) is found to be dependent on both porosity and aspect ratio of solid particles.

2. Considering viscous sliding surfaces embedded into an elastic matrix, Shahidi et al.[176] derived the effective viscoelastic behaviour of such a material. Equivalent stiffness and viscosities of simple rheological models have also been derived as functions of the matrix stiffness and interfaces viscosity, size, and density [143]. Then, Eq.3.16 can be replaced by the latter.

Indeed, classical basic creep tests on cement pastes provide the compliance of cement paste when loaded at a given age, see, for example, Tamtsia and Beaudoin [185], Tamtsia et al. [186], and Le Roy [156]. The appropriate hydrate behaviour can then be back-analyzed using a micromechanical model (see Sanahuja et al. [158] where the sliding characteristic time of C-S-H sheets has been fit on cement paste creep measurements from Le Roy [156]). However, these classical tests only provide the compliance function at a given loading age. More precisely, one sample and one test are required for each loading age, prohibiting extensive characterization of ageing creep. Recently, Irfan-ul-Hassan et al. [87] proposed a new technique to characterize the ageing viscoelastic behaviour of cement pastes from short creep tests repeated on the same sample. Parameters of a power-law creep function are calibrated on experimental results and are given as a function of either time or hydration degree. These results could be back-analyzed to estimate the elementary behaviour of hydrates.

Chapitre 4

Effective Viscoelastic Behavior of Evolving Microstructure : Taking into Account the Complete Evolution

Sommaire

The aim of this section is to propose an approach that does not rely on a frozen microstructure, that is, to consider the complete evolution of microstructure as the composite material is loaded. For the sake of simplicity, the approach is not illustrated on a generic n phases composite, but directly on cement paste.

4.1 Homogenization of Evolving Microstructure with Viscoelastic Phases

As microstructure evolves with respect to time, classic homogenization of random media (based on the correspondence principle with the Laplace-Carson transform) cannot be straightforwardly used in the framework of viscoelasticity. Still, the solidification theory from Bažant [18][16], Bažant and Prasannan [146], and Carol and Bažant [41] represents a promising source of inspiration, as it allows for deriving the effective ageing linear viscoelastic behaviour arising from the progressive precipitation of parallel layers of nonageing viscoelastic material. To be applied to cement paste, this theory needs to be extended in two directions :

- To consider more general precipitation mechanisms than the parallel arrangement of layers ; and
- To also consider the solid (anhydrous) to solid (hydrates) phase transformation.

In this subsection, no particular morphology of the cement paste is assumed.
As described in the first chapter, dedicated to morphology, depending on the position of this point, one of these phenomena may occur :

- Material at this point stays anhydrous ($\Omega_{a\to a}$) ;
- Transformation from anhydrous to hydrates (solid-to-solid transformation, $\Omega_{a\to h}$) ;
- Transformation from pore space to hydrates (precipitation, ($\Omega_{p\to h}$) ;
- Material at this point stays as pore space (($\Omega_{p\to p}$)).

Instead of considering a snapshot of the evolving morphology at a given time t, the phase transformations occurring at a point ($\underline{x}$) of the cement paste REV are investigated. In $\Omega_{p\to h}$, precipitation occurs. As in Bažant solidification theory, hydrates are assumed to precipitate in a zero-stress state. The equivalent mechanical behaviour at point $\underline{x}$ is identified through the stress response to strain steps starting at various times (Fig.4.1). The subdomains affected by the transformations listed below are respectively denoted by $\Omega_{a\to a}$, $\Omega_{a\to h}$, $\Omega_{p\to h}$, $\Omega_{p\to p}$; they constitute a partition of the REV Ω.
The idea of the proposed extension of Bažant solidification theory is to affect an equivalent ageing linear viscoelastic behaviour to each point in the REV. In the subdomain $\Omega_{a\to h}$, the field $t_{a\to h}(\underline{x})$ is introduced to represent the time at which transformation from anhydrous to hydrates occurs at point $\underline{x}$. This field is supposed to be known as it can be derived from the description of the evolving morphology. The field $t_{p\to h}(\underline{x})$ is similarly defined as the precipitation time at $\underline{x}$ in $\Omega_{p\to h}$.
If the strain step occurs before precipitation time $t_{p\to h}(\underline{x})$, the point $\underline{x}$ behaves as pore space :

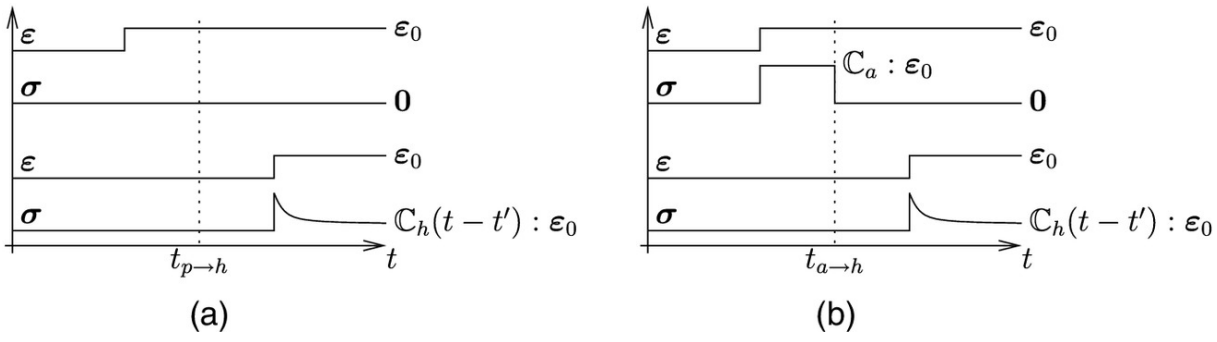

FIGURE 4.1 : Definition of equivalent ageing linear viscoelastic behaviour to represent (a) precipitation and (b) dissolution-precipitation phase transformation processes occurring at a given time, through stress responses to strain steps starting before or after transformation time

stress stays at 0 even after precipitation, as hydrates are assumed to precipitate in a stress-free state. If the strain step occurs after precipitation time, the nonageing viscoelastic behaviour of hydrates is obviously retrieved. Thus, the equivalent ageing behaviour is a tensorial generalization of the one that can be used for one layer of Bažant's solidifying composite.

$$\mathbb{C}_{p\to h}(\underline{x},t,t') = \mathbb{C}_h(t-t')H[t'-t_{p\to h}(\underline{x})] \tag{4.1}$$

Here, the hydrate behaviour is nonageing linear viscoelastic [relaxation $\mathbb{C}_h(t-t')$], but note that no technical reason limits the approach to nonageing behaviours.
In $\Omega_{a\to h}$, a solid (anhydrous)-to-solid (hydrates) transformation occurs. This dissolution-precipitation process has not been considered by the original Bažant solidification theory. As adopted by Li et al. [116] for full-field simulations of cement paste creep, a instantaneous phase transform process is assumed, involving dissolution shortly followed by precipitation. That is, anhydrous are first dissolved, then, after a short time, hydrates precipitate to occupy the domain left by anhydrous. This short time separating dissolution and precipitation is assumed to be negligible with respect to other characteristic times of the model (related to global hydration kinetics and to the hydrates viscoelastic behaviour). As the volume of hydrates replacing anhydrous is here assumed to be equal to the volume of dissolved anhydrous (the complement volume precipitating in pore space), hydrates are considered to precipitate in a zero-stress state. This is clearly a simplifying assumption ; in reality, hydrates precipitating in place of anhydrous may be subjected to stress, as crystals growing in pores [173] and due to confinement effects related to the expansive nature of the transformation from anhydrous to hydrates [174]. Also, the current stress state may affect both dissolution [47] and precipitation [7] processes and their kinetics. These effects (growing hydrates subjected to stress and influence of the stress state on dissolution and precipitation processes) are neglected in this simplified first approach and constitute sources of improvement for future works.
If the strain step occurs before dissolution-precipitation time $t_{a\to h}(\underline{x})$, the stress is first equal to the elastic stress (stiffness $\mathbb{C}_a$) in the anhydrous phase, then drops to 0 at transformation time, as anhydrous are dissolved and, shortly after, replaced by hydrates that precipitate in a zero-stress state [Fig.4.1(b)]. If the strain step occurs after dissolution-precipitation time, the nonageing viscoelastic behaviour of hydrates is obviously retrieved. The fictitious ageing relaxation tensor is thus completely defined from these relaxation tests

$$\mathbb{C}_{a\to h}(\underline{x},t,t') = \mathbb{C}_a H(t-t')H[t_{a\to h}(\underline{x})-t]H[t_{a\to h}(\underline{x})-t'] + \mathbb{C}_h(t-t')H[t'-t_{a\to h}(\underline{x})] \tag{4.2}$$

Thus, an equivalent composite is built, affecting to each point $\underline{x}$ a fictitious ageing viscoelastic behaviour equivalent to the behaviour at the same point $\underline{x}$ in the real composite undergoing microstructure evolution

$$\mathbb{C}(\underline{x},t,t') = \begin{cases} \mathbb{C}_a H(t-t'), \underline{x}\in\Omega_{a\to a} \\ \mathbb{C}_{a\to h}(\underline{x},t,t'), \underline{x}\in\Omega_{a\to h} \\ \mathbb{C}_{p\to h}(\underline{x},t,t'), \underline{x}\in\Omega_{p\to h} \\ 0, \underline{x}\in\Omega_{p\to p} \end{cases} \tag{4.3}$$

The equivalent composite has a constant microstructure, and its microscopic behaviour is ageing

linear viscoelastic. The constant nature of microstructure now allows for taking advantage of mean-field homogenization. Still, in $\Omega_{a\to h}$ and $\Omega_{p\to h}$, the relaxation tensor continuously depends on position $\underline{x}$, through the transformation time. As this prevents homogenization, it is necessary to replace this continuum by a finite number of phases. The idea is to gather points into equal-volume subdomains, according to their transformation times.

The proposed approach is illustrated on $\Omega_{p\to h}$. Fig.4.2 shows the volume fraction evolution of hydrates precipitating into pore space, as a continuous line. The dashed line shows the discretized volume fraction of hydrates precipitating considered with $N = 3$ subdomains. The subdomain $\Omega^i_{p\to h}, i = 1, \ldots, N$ contains the points precipitating during the time interval corresponding to $(i-1)/N f^{max}_{p\to h} \leq f_{p\to h}(t) < \frac{i}{N} f^{max}_{p\to h}$, where $f^{max}_{p\to h}$ is the maximum, final value of $f_{p\to h}(t)$ over the time interval of the entire simulation. The discretization consists in considering that this whole subdomain precipitates at time $t^i_{p\to h}$ such that $f_{p\to h}(t^i_{p\to h}) = f^{max}_{p\to h}(i-1/2)/N$. The same process is repeated to subdivide the domain $\Omega_{a\to h}$ into N subdomains $\Omega^i_{a\to h}$.

Thus, the equivalent composite is subdivided into $2N + 2$ phases :

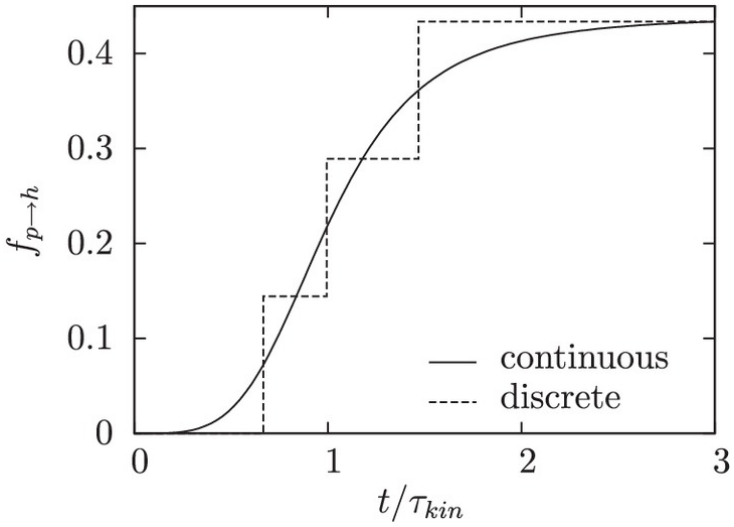

FIGURE 4.2 : Volume fraction of hydrates precipitating into pores : continuous and discretized for $N = 3$ ($w/c = 0.5$)

- One phase for $\Omega_{a\to a}$;
- N phases for $\Omega^i_{a\to h}, i = 1...N$;
- N phases for $\Omega^i_{p\to h}, i = 1...N$; and
- One phase for $\Omega_{p\to p}$.

The phases associated to $\Omega_{a\to a}$ and $\Omega_{p\to p}$ are also qualified as fictitious so that the $2N+2$ phases of the equivalent composite can be collectively described as fictitious phases. The effective behaviour of this multiphasic equivalent composite is expected, when $N \to \infty$, to converge towards the effective behaviour of the continuous equivalent composite. The latter has the same local behaviour, at any point $\underline{x}$, as the evolving composite REV.

The multiphasic equivalent composite, having a constant microstructure, can now be homogenized, taking advantage of recent approaches to upscale ageing linear viscoelastic behaviours.

4.2 Introduction to Homogenization of Aging Linear Viscoelastic Composites

Among the recent approaches [149][127][160] to homogenize ageing linear viscoelastic composites, [160] is flexible enough to directly use as inputs the fictitious behaviours introduced to represent phase transformations (relaxation tensors in Eqs.4.1 and 4.3).
The morphology of the equivalent composite suggests resorting to a self-consistent scheme to homogenize its $2N+2$ fictitious phases, using spherical shapes. Only the main expressions, useful for implementation, are reproduced here ; for more details see [160].
The homogenization problem to solve is the same as Eq.3.1, except that the microscopic behaviour is now ageing linear viscoelastic

$$\underline{\underline{\sigma}}(\underline{x},t) = \int_{t'=-\infty}^{t} \mathbb{C}(\underline{x},t,t') : d\underline{\underline{\epsilon}}(\underline{x},t') \tag{4.4}$$

where the relaxation tensor field is homogeneous per fictitious phase

$$\mathbb{C}(\underline{x},t,t') = \sum_{i=1}^{2N+2} \mathbb{C}(t,t')\chi_i(\underline{x}) \tag{4.5}$$

where $\chi_i(\underline{x})$ =characteristic function of fictitious phase i in the equivalent composite. As shown in [160], elastic homogenization can be extended to ageing linear viscoelasticity when the inclusions are spherical. The equations to solve to get the self-consistent estimates of the effective bulk and shear relaxations have the same structure as Eq.2.52

$$k^{SC} = (\sum_{i=1}^{2N+2} f_i k_i \circ A_{iJ}^{SC}) \circ (\sum_{i=1}^{2N+2} f_i A_{iJ}^{SC})^{-1} \tag{4.6a}$$

$$\mu^{SC} = (\sum_{i=1}^{2N+2} f_i \mu_i \circ A_{iK}^{SC}) \circ (\sum_{i=1}^{2N+2} f_i A_{iK}^{SC})^{-1} \tag{4.6b}$$

where $\circ$ =Volterra integral product $f(t,.) \circ x(.) = \int_{t'=-\infty}^{t} f(t,t')dx(t')$ [196][197], "-1" marks the inverse calculation, i iterates over the fictitious phases, k_i and μ_i which depend on times t and t' are the bulk and shear relaxation functions of fictitious phase i, and f_i is the constant (as the equivalent composite has a constant morphology) volume fraction of phase i. The components A_{iJ}^{SC} and A_{iK}^{SC} of the strain tensor of localization are also functions of t and t' and have to be carefully derived solving the Eshelby inhomogeneity problem with ageing linear viscoelastic phases (compared to the chapters describing the elastic and the nonageing viscoelastic phases),

resorting to a displacement approach [160].

$$A_{iJ}^{SC} = (3k_i + 4\mu_{SC})^{-1} \circ (3k_{SC} + 4\mu_{SC}) \tag{4.7}$$

$$A_{iK}^{SC} = H + 2(2H + 3D_{SC}) \circ [2\mu_i \circ (2H + 3D_{SC}) + \mu_{SC} \circ (6H - D_{SC})]^{-1} \circ (\mu_{SC} - \mu_i) \tag{4.8}$$

Where H still denotes the identity element of the Volterra integral operator.
And

$$D_{SC} = (k_{SC} + \mu_{SC})^{-1} \circ \frac{2}{3}\mu_{SC} \tag{4.9}$$

These expressions involve the Volterra integral product $\circ$ and its inverse. To evaluate them in practice, the integral is approximated using the trapezoidal rule following [20], so that relaxation functions are converted to matrices, whose components are defined as

$$2f_{i,j} = \begin{cases} f(t_0,0) + f(t_0,t_0), i = j = 0 \\ f(t_i,0) - f(t_i,t_1), i \geq 1, j = 0 \\ f(t_i,t_{j-1}) - f(t_i,t_{j+1}), i \geq 2, 1 \leq j \leq i-1 \\ f(t_i,t_{j-1}) + f(t_i,t_i), i \geq 1, j = i \\ 0, 1 \leq i+1 \leq j \leq n \end{cases} \tag{4.10}$$

The Volterra product becomes a straightforward product between square matrices, and its inverse becomes matrix inversion. Solving the matrix equations obtained from Eq.4.6 yields the matrix representation (as defined by Eq.4.10) of the effective bulk and shear relaxation functions. The latter define the complete effective behaviour. The response to any loading path can then be postprocessed from these matrices and the time discretization of this loading path [160].

4.3 Application to Aging Creep of Cement Paste due to Hydration

The effective ageing uniaxial compliance function is plotted in Fig.4.3(a) as continuous lines. The mix design parameters of the cement paste for the VeRCoRs concrete are applied as the conditions of the simulations. Compliance functions obtained from the frozen microstructure approximation are also reported as dashed lines. The initial elastic strain is plotted as a dotted line. Before the critical degree of hydration is reached at t^c, the effective Young's modulus is 0, so there is no point plotting the compliance function for loading times $t' < t^c$.

Both approaches (frozen and evolving microstructure) are consistent with the initial elastic strain as estimated from elastic homogenization. Both compliance functions are very close when loading occurs at late ages, as the microstructure does not evolve much once loaded.
However, even though Scheiner and Hellmich [172] considered that during an infinitesimal time interval, microstructure evolves negligibly and estimated the effective creep rate of the evolving

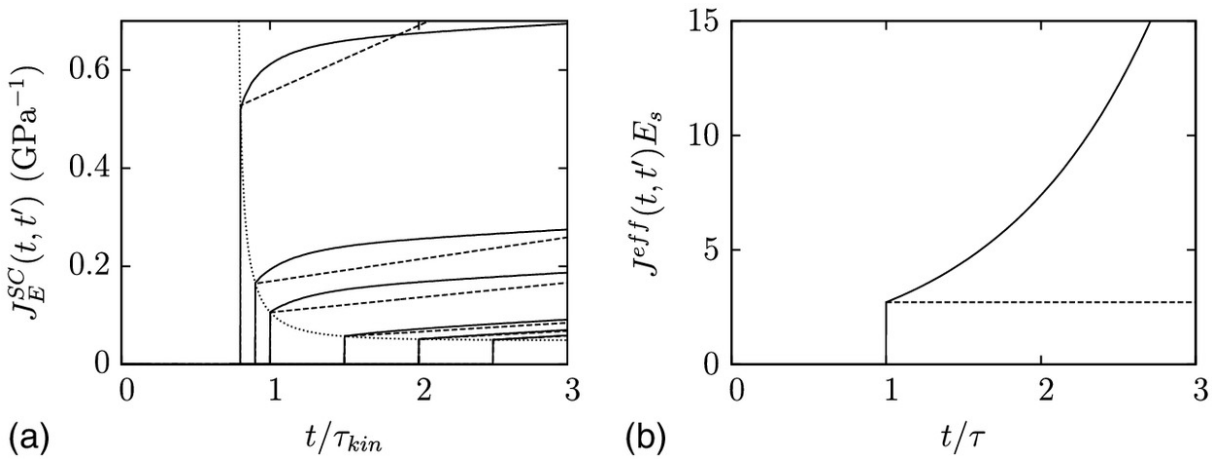

FIGURE 4.3 : (a) Effective uniaxial compliance functions of cement paste (w/c=0.5), plotted for various stress loading times t' : considering full evolution of microstructure with $N = 100$ fictitious phases (continuous lines), and assuming a frozen microstructure (dashed lines) ; dotted line represents the initial elastic strain ; (b) effective compliance function of dissolving parallel elastic layers, when $f_s(t) = e^{-t/\tau}$, plotted for stress loading time $t'/\tau = 1$ considering full evolution of microstructure (continuous line) or a frozen microstructure (dashed line)

microstructure by the rate derived on the current microstructure, according to Fig.4.3, at early ages, once creep starts, the strain evolution is different : the compliance functions do not even share the same tangent. This a priori nonintuitive result (for several examples of composites exhibiting only solidification, both compliance functions are found to have the same initial tangent [161]) seems to be the consequence of the anhydrous dissolution process. Li et al.[116] noticed the same effect on full-field simulations and called it apparent viscoelastic relaxation.

A simple one-dimensional (1D) model, inspired by the solidification theory, can help to get an idea of the influence of dissolution. A parallel arrangement of elastic (Young's modulus E_s) dissolving layers is considered. The solid volume fraction is thus a decreasing function of time t, denoted by $f_s(t)$. The applied uniaxial stress is a step, as $\Sigma(t) = \Sigma_0 H(t - t')$, the loading time t' being a parameter. The stress in the remaining solid phase is thus $\sigma(t) = \Sigma(t)/f_s(t)$. The strain in the solid phase is also the macroscopic strain, due to the parallel arrangement : $E(t) = \epsilon(t) = \Sigma_0 H(t - t')/[E_s f_s(t)]$. As $f_s(t)$ decreases, the macroscopic strain E(t) increases for t>t', while the macroscopic strain for a frozen microstructure stays at $E^{frozen}(t) = \Sigma_0 H(t - t')/[E_s f_s(t')]$ [Fig.4.3(b)]. Note that the strain rates at loading ($t'/\tau = 1$) are clearly different.

The approach proposed to homogenize evolving microstructures is illustrated on a representation of cement paste, which is too simplified to allow a quantitative comparison of ageing creep functions to experimental results. Still, for future reference, bibliographic sources providing creep behaviour of cement pastes aforementioned in the subsection regarding hydrates behaviour, are recalled here. Le Roy [156] measured basic creep of cement pastes at 28 days and of concretes at various loading ages. Use of the latter data for validation would require an additional upscaling step, from cement paste to concrete. As morphology does not evolve at the concrete scale, this upscaling is straightforward following [160], once a concrete morphological model (which may in-

clude interfacial transition zones) has been defined. Briffaut et al. [31] also provide creep results at concrete scale. Tamtsia et al. [186] provide basic creep curves of cement pastes loaded at 18, 24, and 30 h. Irfan-ul-Hassan et al. [87] propose an extensive characterization of the first minutes of creep functions of cement pastes through repeated short tests on the same sample.

Qualitatively, the creep functions estimated considering microstructure evolution [continuous lines in Fig.4.3(a)] are closer to the experimental results of Tamtsia et al.[186] (Fig. 6 on the referenced paper) than those estimated considering frozen microstructure [dashed lines in Fig.4.3(a)]. Indeed, the experimental creep strain rate is high at the onset, then decreases as a function of time (creep functions show a significant downward concavity).

As a conclusion of this chapter, there are two aspects to improve the study in this field. On one hand, the model presented in this chapter is one first trial of ageing viscoelastic cement paste model and there are more details to add in to make this model more realistic. On the other hand, there is little study in the literature to connect the creep experiments results with the ageing viscoelastic behaviour of cementitious materials, so it is a meaningful work to carry out the basic creep experiments of cementitious materials for the VeRCoRs concrete to offer the physical parameters for the ageing viscoelastic creep model. The experimental results and the improved micro-macro models will be presented in the second and the third part of this thesis.

Chapitre 5

Numerical and analytical solutions and comparisons of effective creep model

Sommaire

5.1 Morphology of composite and solidifying mechanisms investigated

This section is devoted to a first application over a simplified microstructure : a polycrystalline microstructure where a solid material progressively solidifies into other phases (modelled as polycrystalline phases in the analytical solution and modelled as 32 discretized families of precipitating polycrystalline phase in the numerical solution). As information about morphology can be integrated thanks to homogenization of random media, it is possible to investigate the influence of the precipitation mechanism on the effective ageing behaviour. A solidifying scenario is investigated : precipitation in whole phases, one after the other, in random order.
The matrix and the solidified material are respectively denoted by subscripts 0 and s. The volume fraction f_0 of matrix is constant. In this case, the initial volume fraction of solid phase is 50% (then the volume fraction for the phases to be precipitated is 50%). As pores are progressively invaded by solidified materials, the volume fraction f_s of the latter increases up to f_s^∞, while porosity $\phi = 1 - f_0 - f_s$ decreases down to $\phi_\infty = 1 - f_0 - f_s$ ($f_s^\infty \leq 1 - f_0$). For the sake of simplicity, the kinetics of the precipitating process is modelled through an "S-shaped" curve (Fig.5.1) :

$$f_s(t) = f_s^\infty (t/\tau)^\alpha / (1 + (t/\tau)^\alpha) \tag{5.1}$$

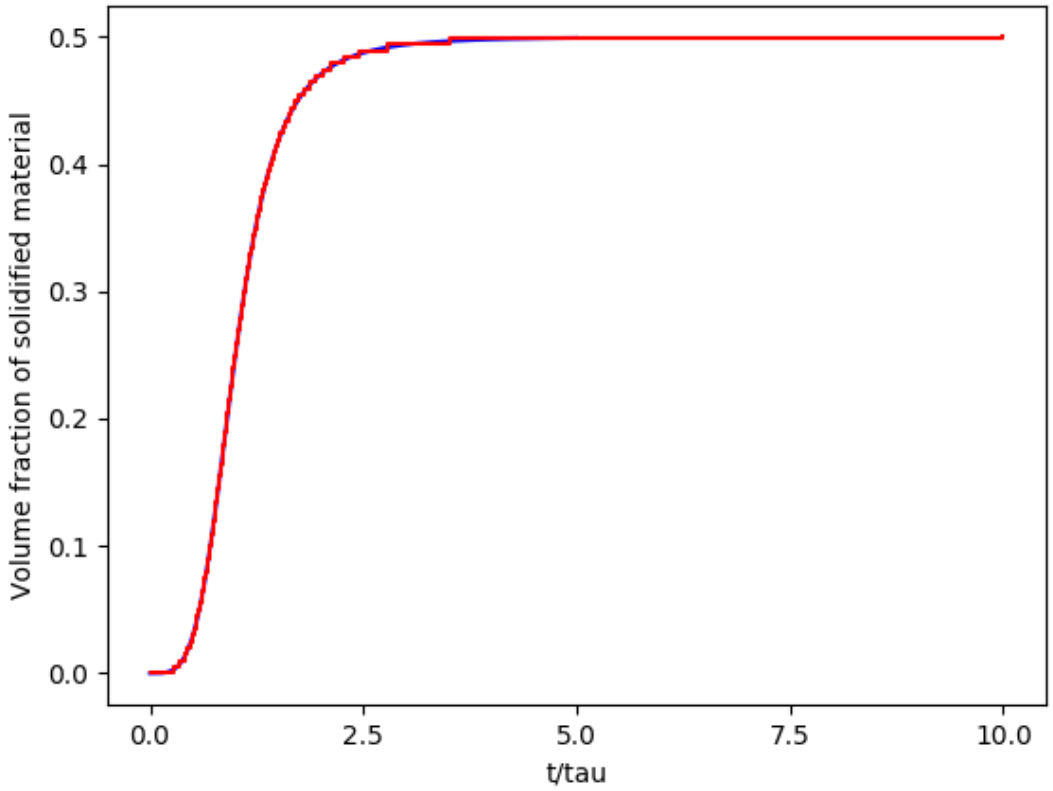

FIGURE 5.1 : Volume fraction of precipitate, and as a red line the discretized volume fraction as considered by the homogenization model, with $\alpha = 4$ and for $N = 100$ fictitious phases ($f_0 = 0.5$).

where τ and α are the characteristic ageing time and a kinetic parameter.

5.2 Behaviour of the different phases

The spherical and deviatoric behaviours of solidified material are represented by a generalized Maxwell rheological model (also named as Maxwell–Wiechert model) for the sake of simplicity, even if any linear viscoelastic behaviour (including ageing) could be used.

In this generalized Maxwell model, 2 Maxwell elements are assembled in parallel with a spring.

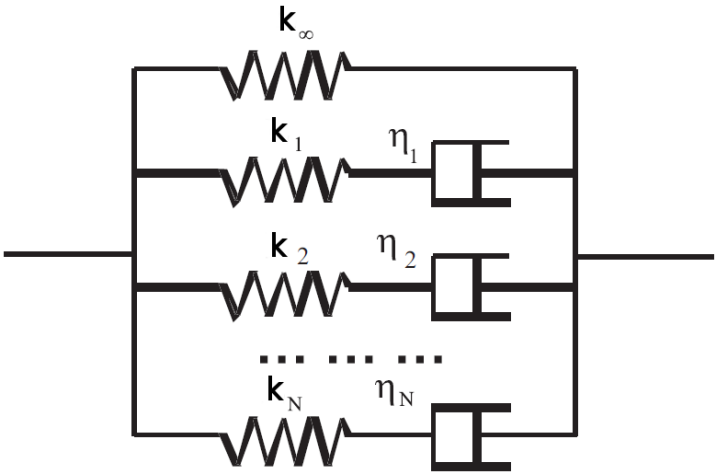

FIGURE 5.2 : Schematic of Maxwell–Wiechert model.

The stiffness and viscosity of the spherical (resp. deviatoric) part of the Maxwell behaviour are denoted by k and η (resp. μ and γ). The numerical parameters used in the simulations are gathered on table 5.1. The stiffness is defined by the Young's modulus E and the Poisson ratio ν, instead of k and μ.

TABLE 5.1 : Material parameters used in the application (stresses are normalized by the Young's modulus E_0 of the initial solid phase, and times are normalized by the characteristic ageing time τ).

	Elastic branch		Stiffness		Stiffness		Characteristic time				Volume fraction	Kinetic parameter
	$\frac{E_\infty}{E_0}$	ν	k_1	k_2	μ_1	μ_2	$\frac{\eta_1/k_1}{\tau}$	$\frac{\gamma_1/\mu_1}{\tau}$	$\frac{\eta_2/k_2}{\tau}$	$\frac{\gamma_2/\mu_2}{\tau}$	f	α
Initial solid phase	1	0.3	1.67	0.83	1.00	0.18	1.25	0.45	2.00	8.52	0.5	n/a
Precipitate	1	0.3	1.67	0.83	1.00	0.18	1.25	0.45	2.00	8.52	From 0 to $f_s^\infty = 0.5$	4

5.3 Numerical modeling of the microstructure with solidifying mechanism

The comparisons between the analytical Mori-Tanaka estimates and FEM 3D simulations are provided by [95]. This chapter focuses on the comparisons with the analytical self-consistent es-

timates and FEM 3D simulations between the polycrystalline morphology corresponding to the self-consistent homogenization method.

A periodic polycrystalline microstructure is generated via the Computer-Aided Design code Salome (http ://www.salome-platform.org). The corresponding procedure relies on the open-source python library Combs implemented in Salome [12]. The latter consists in inserting particles of prescribed sizes and shapes in a box. The placement follows a random process where points are arbitrarily determined in the box, and verifications are made that the current inclusion to insert does not overlap the already embedded ones. Unstructured periodic meshes are then generated with triangles for surfaces and tetrahedral elements for volumes with the help of the automatic meshing softwares developed by Distene (http ://www.meshgems.com). The procedure has been applied in the context of materials exhibiting a matrix-inclusion morphology to various problems regarding mesoscale concrete behaviour, as corrosion [138] and analysis of matrix/aggregate interface effects [11] among others.

Here, the polycrystalline geometry is generated by making use of the Neper software (http ://neper.sourceforge.net/), which allows obtaining periodic microstructures. The geometry is then imported in Salome and the specimen is subsequently constructed with parallel opposite surfaces constrained with periodic features (in the original geometry created by Neper, the grains overlapping the surfaces are not cut). The meshing procedure follows then straightforwardly.

For the simulations, a microstructure with 5000 grains is studied, see figure 5.3. It was decided to set the initial volume fraction of the solid phase at t=0 to 50%, meaning that the volume fraction of precipitated phase is also 50% (figure 5.4). To describe the progressive hydration process, the precipitated phase is discretized in 32 families of very similar volume fraction. This discretization procedure, together with the partition of all grains into either initial solid phase or precipitate one, is fully random and performed in Mathematica ; it requires as input the index and volume fraction of each grain. Thus, on average each family of the precipitated phase comprises 78 grains, depending of their volume fraction. The number of tetrahedrons in the generated mesh is 2.82x106. The simulations are performed in the finite element code Cast3M (www-cast3m.cea.fr), with the material parameters indicated in Table 5.1, and with 40 time steps. Note that the hydration process is simply reproduced by switching the mechanical properties of the family which is precipitating at a certain time from very small values (in practice they are set to 10^{-8} times lower) to the values indicated in Table 5.1. Finally, the boundary conditions applied to the surfaces of the specimen are as follows : homogeneous stresses for the compliance properties, and homogeneous strains for the relaxation ones. One calculation is performed to obtain either the bulk (spherical loading) or the shear (deviatoric loading) properties, and for one time of loading. The number of fictitious phases used in the analytical modeling is 100.

The self-consistent homogenization scheme is applied on the analytical calculation. To evaluate the Volterra integral product in practice, the integral is approximated using the trapezoidal rule, so that relaxation functions are converted to matrices, whose components are defined as Eq.(4.10). The Volterra product becomes a straightforward product between square matrices, and its inverse becomes matrix inversion. The response to any loading path can then be post-processed from these matrices and the time discretization of the loading path.

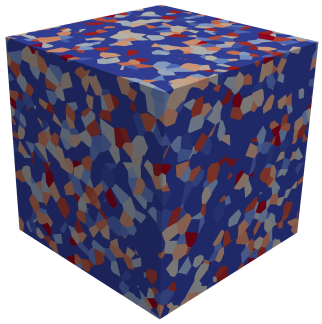

FIGURE 5.3 : Microstructure of the REV with solidifying mechanism.

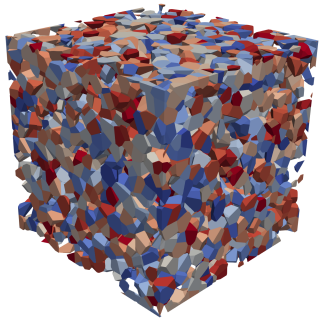

FIGURE 5.4 : Microstructure of the phases of precipitate discretized in 32 families with solidifying mechanism.

5.4 Analytical and numerical results on a solidification mechanism

We analyse the spherical and the deviatoric part of the global behaviour for the age of loading $t_0 = 0.5,\quad 1.0,\quad 1.5,\quad 2.0,\quad 2.5,\quad 3.0$ days.
Considering the mechanism of precipitation in the whole crystal space, one crystal after the other (the model on Fig.1.2), the effect of precipitation kinetics is now described through the parameter α, and results are presented as follows :

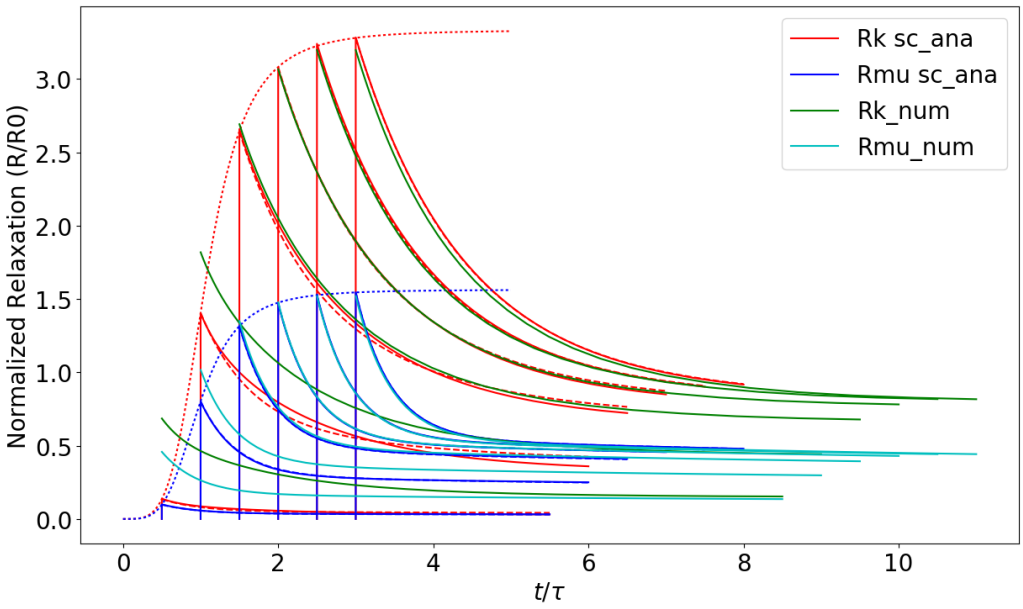

FIGURE 5.5 : Ageing effective relaxation functions, for the solidifying mechanisms, with $\alpha = 4$.

Effective relaxation functions are plotted as continuous lines on Fig.5.5, with $\alpha = 4$ and for the solidifying mechanisms. Dotted lines represent the evolution of the instantaneous elastic stiffness (the bulk modulus and the shear modulus), estimated from self-consistent homogenization schemes, taking into account the current morphology at time t. Dashed lines represent the effective relaxation functions estimated assuming a frozen microstructure (i.e. which does not evolve any more) once the loading strain step has started, which allows to take advantage of the correspondence principle. Clearly enough, when the microstructure is expected to evolve once the loading step has been applied, an deviation can be found between the nonageing relaxation functions (dashed lines) and the ageing relaxation functions (continuous lines) marked by the same color.
In Fig.5.5, the continuous lines are mostly focused.

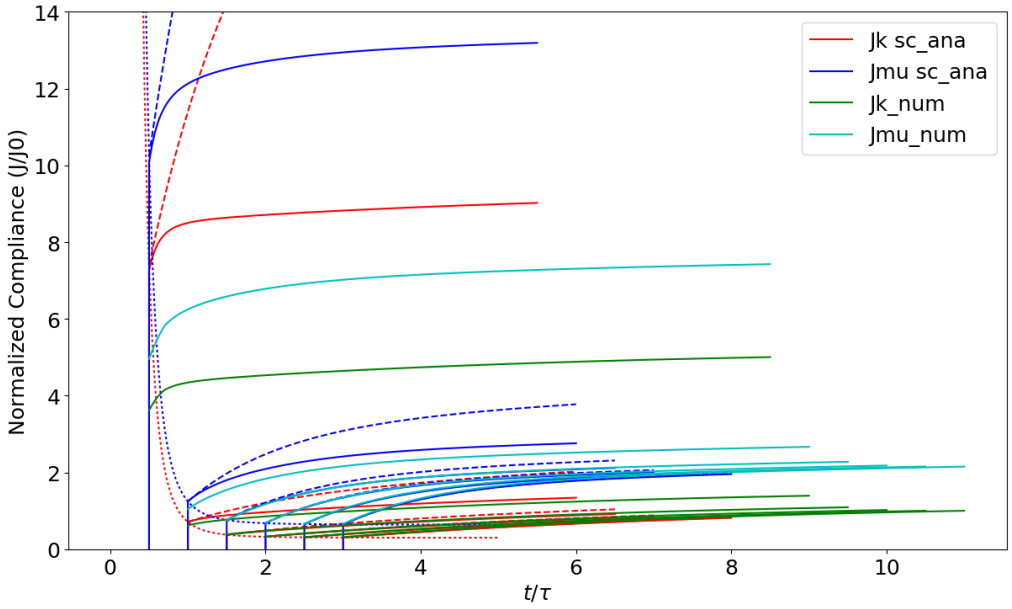

FIGURE 5.6 : Ageing effective compliance functions, for the solidifying mechanisms, with $\alpha = 4$.

- The red continuous lines (the analytical solution for $N = 100$ fictitious ageing phases, indicated as "Rk sc ana") ;
- The green continuous lines (the numerical simulation solution calculated by Cast3M) are the spherical part of the evolution of the ageing viscoelastic stress relaxation of the REV (indicated as "Rk num") ;
- The deep blue continuous lines (the analytical solution for $N = 100$ fictitious ageing phases, indicated as "Rmu sc ana") ;
- The light blue continuous lines (the numerical simulation solution calculated by Cast3M) are the deviatoric part of the evolution of the ageing viscoelastic stress relaxation of the REV (indicated as "Rmu num").

Effective compliance functions are plotted as continuous lines on Fig.5.6, with $\alpha = 4$ and for the solidifying mechanisms. Dotted lines represent the evolution of the instantaneous elastic compliance (inverse of the bulk modulus and the shear modulus), estimated from the self-consistent homogenization schemes, taking into account the current morphology at t. When the microstructure is expected to evolve once the loading step has been applied, an important deviation can be found between both creep functions.
In Fig.5.6, the evolution of compliance shows the same coherence between the numerical results and the analytical results as the evolution of relaxation.
Comparing the numerical simulation results with the analytical results, there are differences especially for $t_0 = 0.5$ day ; for $t_0 > 1$ day, the numerical simulation result and the analytical result

are close.

In fact, for $t_0 = 0.5$ day, there is a volume fraction of the solid phase close to 50%. With this condition, the initial solid phases in the numerical simulation are in fact totally connected, as shown in Fig.5.7, whereas the self-consistent homogenization scheme predicts a percolation threshold at exactly 50%.

This difference could be clearer when the evolution of elastic stiffness is drawn as a function of

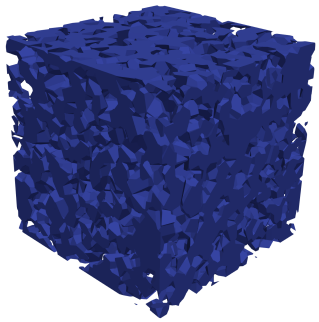

FIGURE 5.7 : Initial microstructure of the connected matrix with solidifying mechanism.

the volume fraction of the solid phase, as shown in Fig.5.8. The continuous lines (the analytical solution by the self-consistent homogenization scheme) and the dots (the numerical simulation calculated by Cast3M) are quite different when the volume fraction of the solid phase is close to 0.5, but the numerical simulation results and the analytical results are close when the volume fraction of the solid phase is larger than 0.8. Precisely, there is always a good correlation between the numerical simulation results and the analytical results when $t_0 > 1$ day.

Then, it seems that even when considering a polycristalline microstructure whose morphology is theoretically close to the one of the self-consistent scheme, important differences are observed in particular in the vicinity of the percolation threshold. It should also be mentioned that the analytical self-consistent results assume that the particles are spherical, whereas in the simulations they are polyhedral.

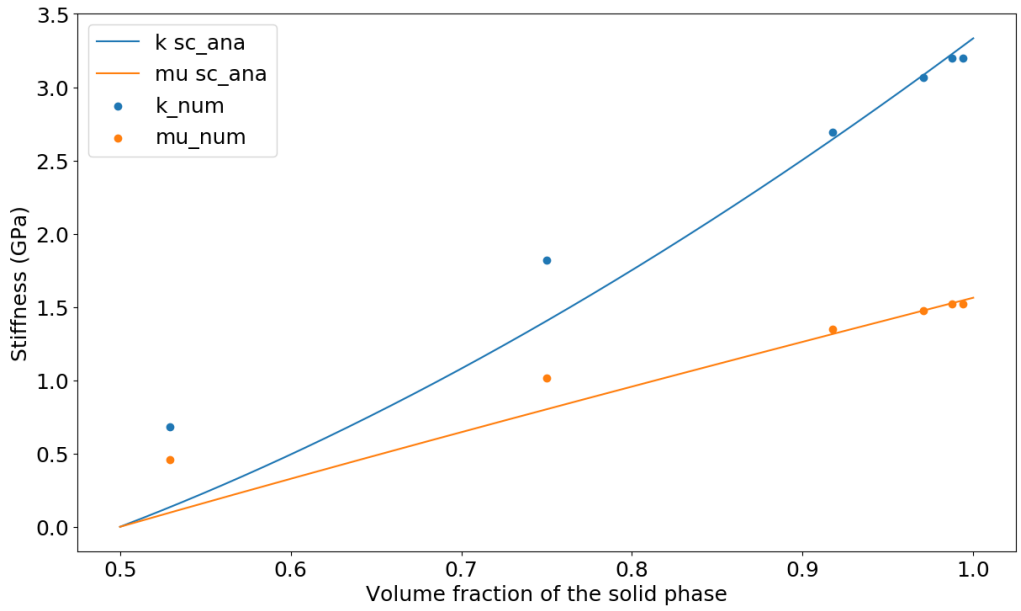

FIGURE 5.8 : Ageing effective relaxation evolution in function of the volume fraction of the solid phase, for the solidifying mechanisms.

Chapitre 6

Double Scale Model of the Aging Creep of Low Density Hydrates of Cement Paste

Sommaire

6.1 Introduction of the multi-scale microstructural model

To consider creep during microstructure evolution, the Bažant solidification theory [18], has been recently extended to more general evolving microstructures and phase transformations [166], taking advantage of mean-field homogenization of ageing linear viscoelastic behaviours [160]. This method can be used on a multi-scale microstructural model of cement paste, and this chapter proposes a first application to ageing basic creep of the low-density hydrates matrix of a cement paste since it is this part in the cement paste that indicates the ageing viscoelastic behaviour.
The chapter is organized as follows. Firstly, a time evolving multi-scale morphological model of hydrating cement paste is proposed. Anhydrous, hydrates and capillary pores are considered. This model is a simplification of the genuine complexity of cement paste microstructure to illustrate developments without unnecessary technical complications. Then, focusing on the outer hydrates,

ageing basic creep is estimated. Eventually, several prospects are proposed to further apply this new ageing approach to cement pastes and concrete.

6.2 Microstructure model

The observation of a polished section of a hydrated cement paste reveals several zones :

- The remaining anhydrous grains ;
- Around the anhydrous grains, "high density" hydrates ;
- "Low density" hydrates (having a higher porosity than "high density" hydrates) ;
- Portlandite (which is not taken into account in this simplified approach).

It is now necessary to construct a microstructure representation that accounts for the observed morphological characteristics.
Following ([164], see also Figure 6.1), within a macroscopic REV (where hydrates appear as a continuous phase), spherical composite inclusions (an anhydrous core surrounded by a layer of high density hydrates) are immersed in a low density hydrate matrix. On the mesoscopic scale, we distinguish the solid phase from the pore space of high and low density hydrates. The two materials are differentiated by their porosity and morphology. During the hydration, the anhydrous core is progressively dissolved and the diameter of the core is thus reduced. Simultaneously, the layer of high density hydrates becomes thicker and the low density hydrates matrix becomes denser.

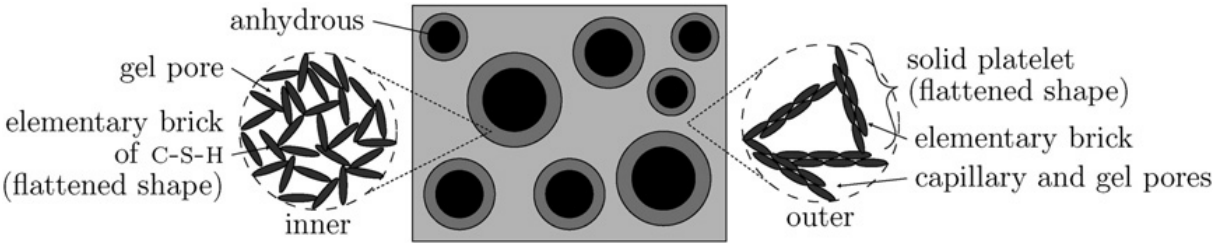

FIGURE 6.1 : Schematic representation of the proposed morphological model of cement paste, with the model of outer hydrates [164].

6.2.1 Overcoming a too late hydration degree

Setting of paste directly follows setting of low density hydrates. Modeling low density hydrates solid phase by spherical particles, in the context of a self-consistent scheme, yields an overestimate of the setting hydration degree, as the amount of the critical solid volume fraction of solids to precipitate is too high ($f_s^{cri} = 0.5$). To avoid this shortcoming, it is possible to use :

- A non-spherical shape to model the solid phase of low density hydrates [164]. The extension of this method to ellipsoidal particles has been realized and validated by M. Di Ciaccio

during his internship at the Department MMC of *EDF R&D* in 2014. But this method (anisotropic shape and behaviour) brings great technical difficulties from the point of view of the implementation of homogenization methods in the context of ageing viscoelasticity. There was the result of Eshelby problem by J-F. Barthelemy during this thesis [10], but this part of the work has been finished before the result in [10] was available.

- A multi-scale description, that is, in a REV of low-density hydrates, a first self-consistent scheme to homogenize bigger pores and C-S-H gel clusters (small mixture on the large scale). These gel clusters are described on the lower scale by a second self-consistent scheme with solid particles and smaller pores. The critical volume fraction of solid phase could decrease with this multi-scale morphological treatment. Thus, late setting hydration degree can be improved not by modifying the shape of the particles but with their multi-scale arrangement, which is currently technically accessible. [97] shows that the multi-scale structure is more realistic for the C-S-H gel and it intensifies the problem of the setting hydration degree for the mechanical properties. As a result, the multi-scale arrangement becomes more necessary.

6.2.2 Modelling outer microstructure evolution

We now focus on the outer or low-density hydrates. To estimate the effective ageing creep due to microstructure evolution, it is required to finely describe the latter. Zooming on a given cluster of the outer microstructure reveals, at the small scale, pores and solid. The local volume fraction of solid phase on the small scale is $f_s(t, t')$, where t' is the time at which this cluster starts to densify, and t is the current time. This function $f_s(t, t')$ is 0 for $t < t'$, is increasing with t for all t' and can follow any kinetics curve.
At the outer scale, the volume fraction of clusters which have started to densify is $f_m^{REV}(t)$. This function increases with t and can also apply to any kinetics curve.
On Figure 6.2, in each small mixture (cluster) phase that can be distinguished on a large scale, the evolution of the cluster density (or solid volume fraction) is represented by the gray level of each phase : the darker the denser. In addition, during hydration, there are more and more clusters that start to densify. Simultaneously, zooming on each small mixture, more and more solid phase is precipitating at the small scale.
For example, in Fig.6.3, the evolution of the solid phase volume fraction in the REV at the local scale is shown as a function of time. The four arrows indicate the volume fraction of the solid phase in the four schemes at the small scale, demonstrating that more and more solid phase is precipitating.
To precise the mechanical properties of each phase at different scales, we pick one phase at each scale and the subordinate relationship at different scales is marked by arrows in Fig.6.4. The equivalent mechanical behaviour at point $\underline{x}$ is identified through the stress response to strain steps starting at various times (See Fig.4.1 (a)).
In one elementary solid phase (the black phase in the circle in Fig.6.4), if the strain step occurs

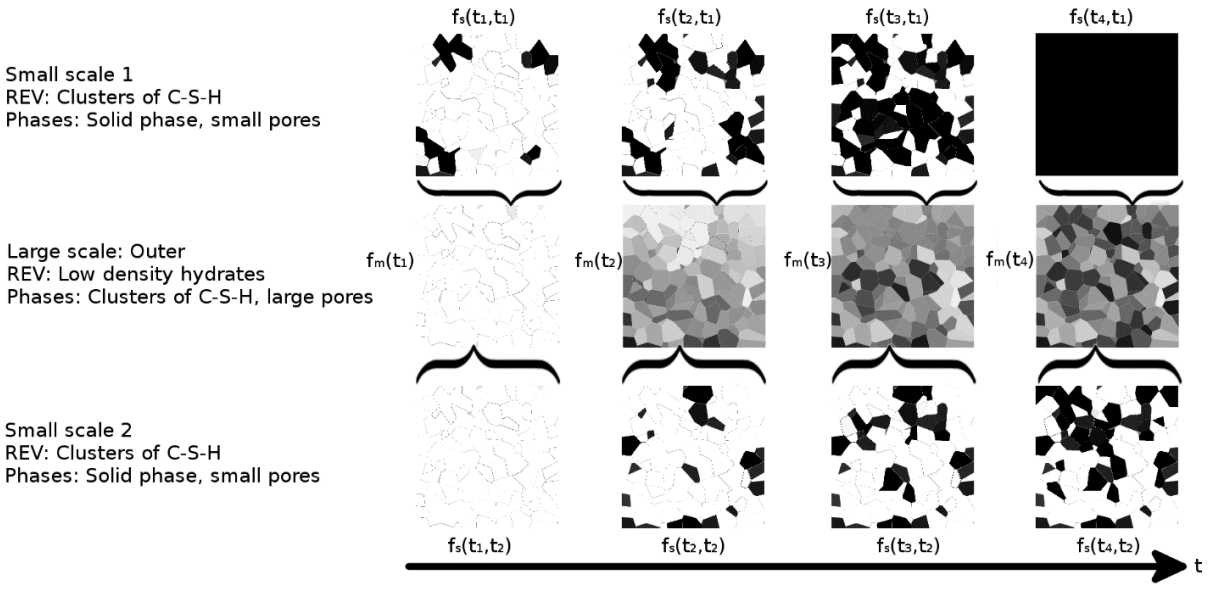

FIGURE 6.2 : Outer hydrates : schematization of the precipitation on two scales.

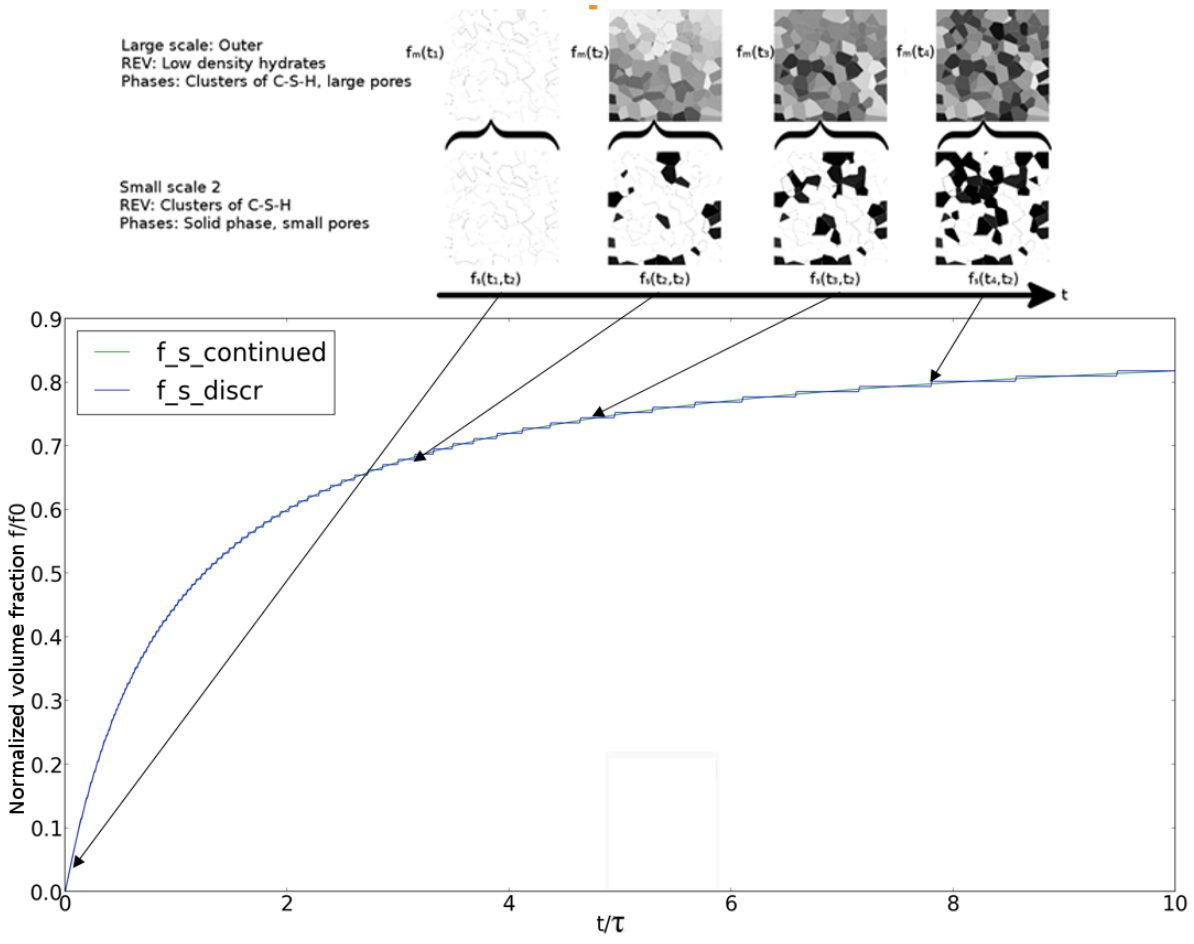

FIGURE 6.3 : Evolution of the solid phase volume fraction in the REV at the small scale 2.

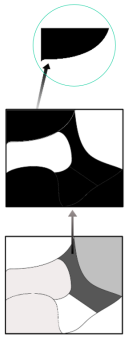

FIGURE 6.4 : Elemental solid phase and the subordinate relationship at different scales.

before precipitation time $t_{p\to h}(\underline{x})$, the point $\underline{x}$ behaves as pore space : stress stays at 0 even after precipitation, as hydrates are assumed to precipitate in a stress-free state. If the strain step occurs after precipitation time, the nonageing viscoelastic behaviour of hydrates is obviously retrieved. Thus, the equivalent ageing behaviour is a tensorial generalization of the one that can be used for one layer of Bažant's solidifying composite [160]. In this case, a Maxwell model is applied to describe the viscoelastic behaviour of the elementary solid phase.
Then we study the scale composed by the elementary solid phase and the small pore space. Each phase at this scale has its own time of the beginning of precipitation t_i, as shown in Fig.6.5.
The phase marked t_e in Fig.6.5 is picked out as an example here. The time of the beginning

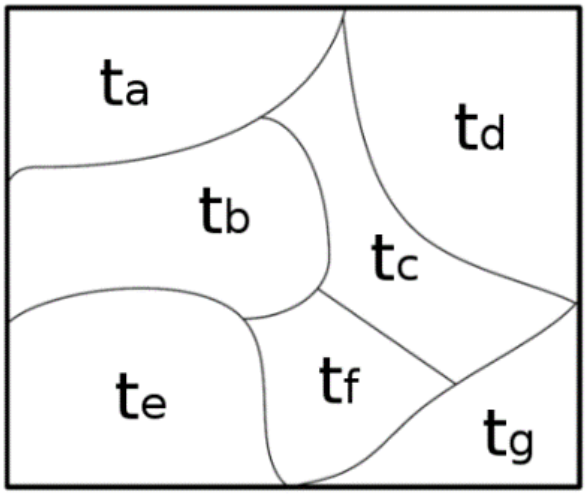

FIGURE 6.5 : Time of the beginning of precipitation in one REV composed by the elementary solid phase and the small pore space.

of precipitation is t_e. As shown in Fig.6.6, after precipitation time t_e, the nonageing viscoelastic behaviour of hydrates is described by a stiffness behaviour that is presented in Fig.6.6.
After this step, we study the scale composed by the clusters described in Fig.6.5. Each phase at this scale has its own time of the beginning of densification t_I, as shown in Fig.6.7. It means that, for example, in the phase marked t_E, the small phases at the smaller scale begin to precipitate

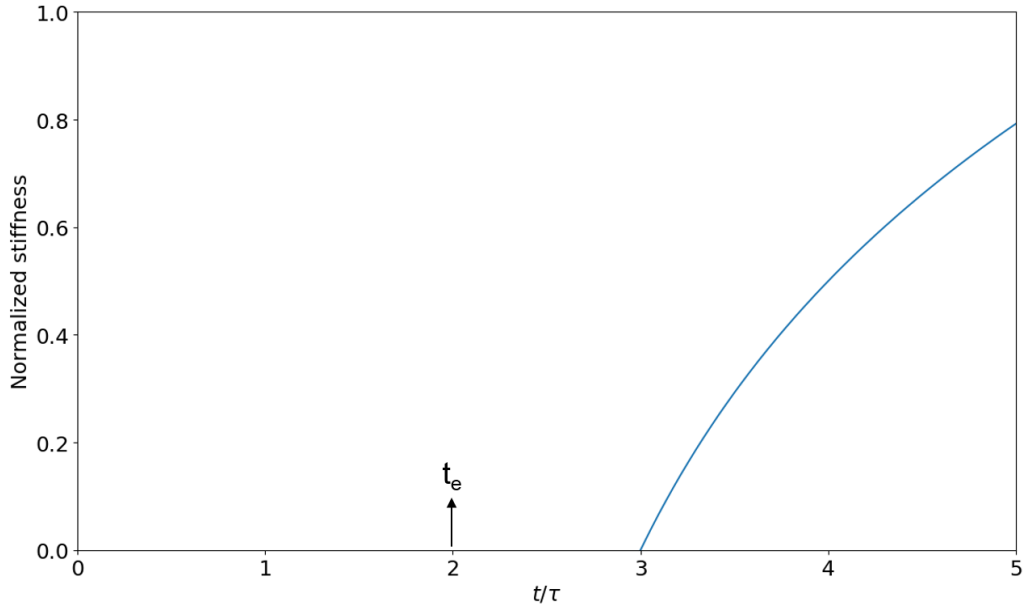

FIGURE 6.6 : Evolution of the stiffness of the phase marked t_e.

at time t_E. At this scale, as different phases have different time of beginning of densification, different phases have different volume fraction of the elementary solid phase. A representative scheme is shown in Fig.6.8. We focus on the phase marked with the arrows indicating the volume fraction of the elementary solid phase in this cluster phase. The volume fraction of the elementary solid phase for each cluster phase in the image is represented by a degree of grey : black or dark grey for high volume fraction and light grey or white for low volume fraction. During hydration, there are more and more clusters that start to densify. Simultaneously, zooming on each small cluster phase, more and more solid phase is precipitating at the small scale, so the degree of grey rises from light grey to dark grey in the rang of time $[t_1, ..., t_i, t_{i+1}, ..., t_n]$.

On the other hand, the evolution of the overall volume fraction of the solid phase in outer scale is written, cluster by cluster, as a function of the evolution of the local volume fraction of the solid phase at the local scale ($f_s(t, t')$), and as a function of the derivative of the evolution of the volume fraction of already densifying small mixtures of the solid phases and the capillary pores ($\dot{f}_m^{REV}(t'_i)$) :

$$f_s^{REV}(t) = \sum_{i=1}^{N_{smallmixture}} f_s(t, t')\Delta V_i \tag{6.1}$$

$$\Delta V_i = \dot{f}_m^{REV}(t'_i)\Delta t'_i \tag{6.2}$$

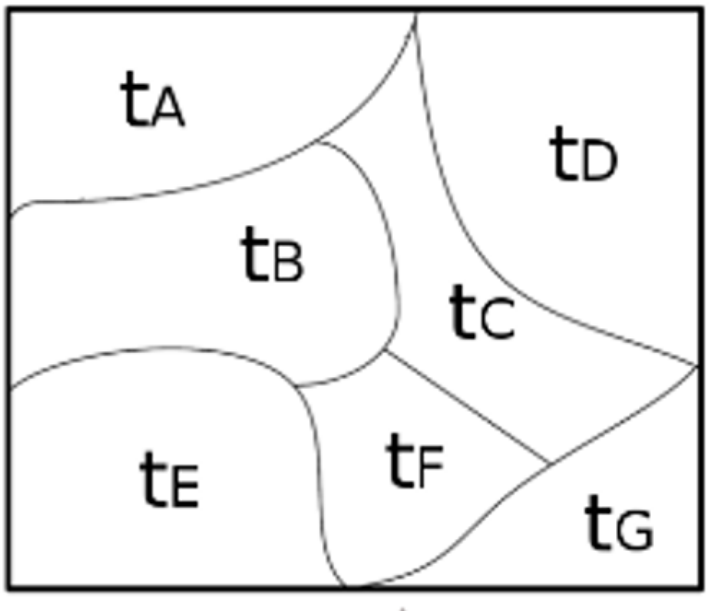

FIGURE 6.7 : Time of the beginning of densification in one REV composed by the clusters.

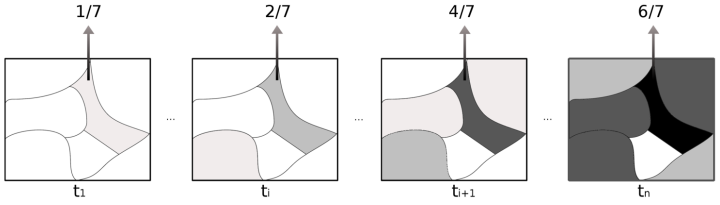

FIGURE 6.8 : Evolution of the degree of densification calibrated by the degree of grey.

ΔV_i is the volume occupied by small mixture phase i. Then the evolution of the overall volume fraction of the solid phase on a large scale $f_s^{REV}(t)$ can be written as the integral equation :

$$f_s^{REV}(t) = \int_0^t f_s(t,t')\dot{f}_m^{REV}(t')dt_i' \tag{6.3}$$

For example, the evolution of the local volume fraction of the solid phase at the local scale $f_s(t,t')$ could be written as :

$$f_s(t,t') = f_s^{\infty} * \frac{(((t-t')/\tau)^{\alpha})}{(1.+((t-t')/\tau)^{\alpha})} H(t-t') \tag{6.4}$$

where, the volume fraction $f_s(t,t')$ increases up to f_s^{∞}, τ and α are the characteristic ageing time and a kinetic parameter.
And the evolution of the volume fraction of already densifying small mixtures of the solid phases and the capillary pores could be written as :

$$f_m^{REV}(t) = f_m^{\infty} * \frac{(((t)/\tau)^{\alpha})}{(1.+((t)/\tau)^{\alpha})} \tag{6.5}$$

where, the volume fraction $f_m^{REV}(t)$ increases up to f_m^{∞}.
If the parameter $\alpha = 1$, $f_m^{\infty} = 0.9$ and $f_s^{\infty} = 0.9$, the evolution of the volume fraction of each phase is as follows :
In the Fig.6.9, the fm_REV curve indicates the evolution of the volume fraction of already

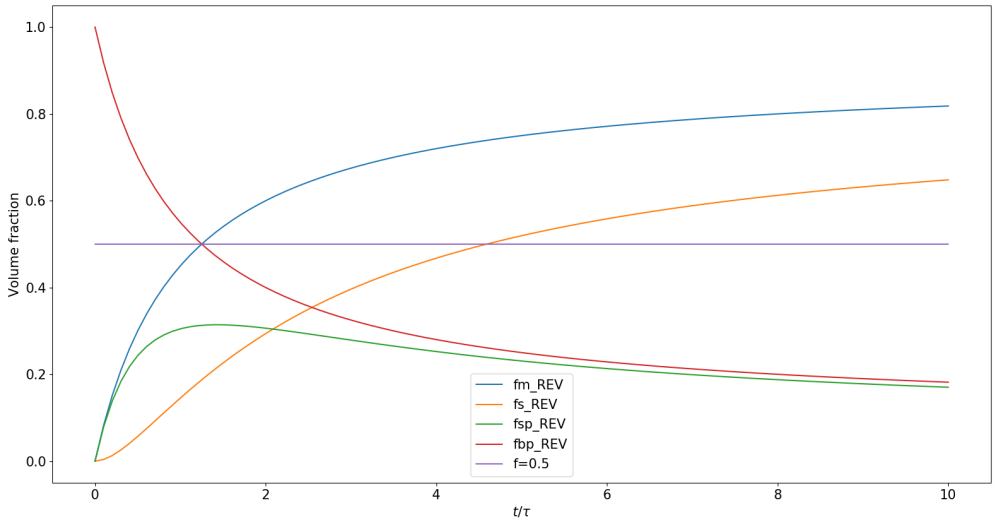

FIGURE 6.9 : Example : Evolution of the volume fraction of each phase in a double-scale microstructure.

densifying small mixtures of the solid phases and the capillary pores $f_m^{REV}(t)$, and the fs_REV curve indicates the evolution of the global volume fraction of the solid phase. So the evolution

of the capillary pores fsp_REV could be calculated by subtracting the fs_REV curve from the fm_REV curve. And the evolution of the big pores at the big scale fbp_REV could be calculated by subtracting the fm_REV curve from the whole volume.

6.2.3 Hydration Model

For the sake of simplicity, the evolution of cement paste phases is modelled through the Powers Model [145] and simplified kinetics (the development of the hydration model will also be studied in this thesis). Powers model provides the volume fractions in anhydrous cement paste, hydrates, capillary pores and water in the form of very simple functions of the water to cement mass ratio w/c and degree of hydration α. The Figure 6.10 presents the comparison of the setting hydration degree between the single scale sphere-based model, the spheroid model and the multi-scale sphere-based model, all the models being based on the self-consistent homogenization scheme.

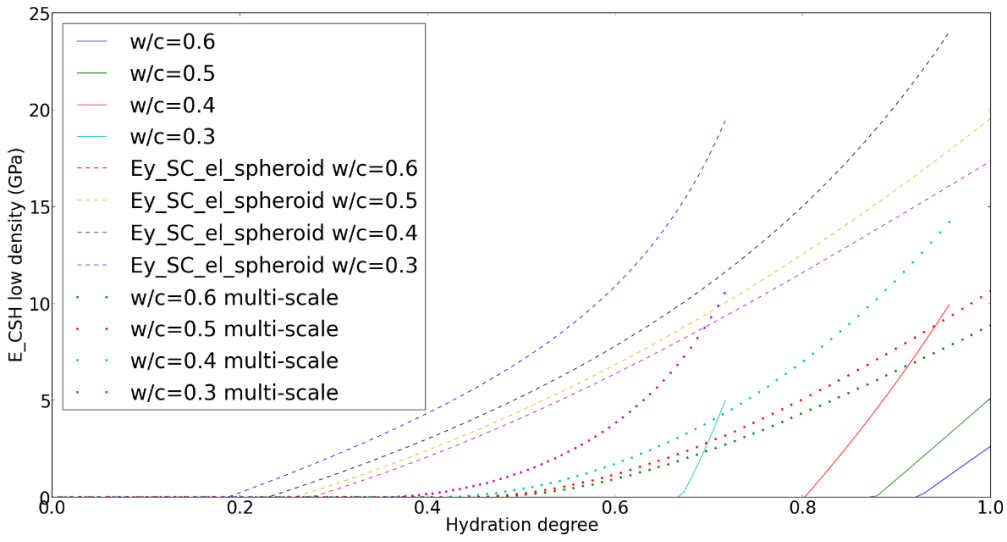

FIGURE 6.10 : Comparison of the setting hydration degree between the single scale model, the spheroid model and the multi-scale model.

In conclusion, on one hand, the multi-scale model (dotted line) and the spheroid model (dashed line) correct the late setting hydration degree, and the multi-scale model is more technically tractable in the ageing viscoelastic context. On the other hand, over the long term, there are differences on the effective Young's modulus among different modeling method.

6.3 Estimate for the Effective viscoelastic behaviour of outer hydrates

6.3.1 From a tensorial extension of solidification theory to fictitious ageing phases

Effective ageing behaviours can arise from non ageing ones at the lower scale with the elementary phases, because the underlying morphology of the composite material evolves with time. As mentioned before, we here refer to the solidification theory from Bažant [15] : some phases are expected to precipitate at given times.
For the 2-scales outer hydrates, the inputs are :

- The functions describing the microstructure evolution, $f_s(t,t')$ and $f_m^{REV}(t)$;
- A discretization of time, to build up the fictitious phases at each scale : each fictitious phase is characterized by a precipitating time and a volume fraction ;
- The viscoelastic behaviour of hydrate solids, assumed to be represented by a Maxwell model for the sake of simplicity (any other viscoelastic model can be considered, including ageing) : parameters are the bulk and shear elastic moduli and the bulk and shear viscosities.

Each cluster, depending on its densification starting time, is first homogenized using a self-consistent scheme. Then, all the clusters are homogenized using another self-consistent scheme, to get the outer effective behaviour.

TABLE 6.1 : Material parameters used in the application [161] (stresses are normalized by the referenced Young's modulus E_0, and times are normalized by the characteristic ageing time τ).

	Stiffness		Characteristic time		Volume fraction	Kinetic parameter
	$\frac{E}{E_0}$	ν	$\frac{\eta_1/E_1}{\tau}$	$\frac{\eta_2/E_2}{\tau}$	f	α
Existed solid phase	10	0.25	5	0.67	0.1	n/a
Precipitate	10	0.25	5	0.67	From 0 to $f_s^\infty = 0.9$	4

6.3.2 Effective behaviour of a small mixture phase

Bulk (solid lines) and shear (dashed lines) effective relaxation functions of a small mixture phase, starting precipitation at time $t'/\tau = 0$, are plotted in red on Fig.6.11 (τ is the characteristic ageing time). As a means of (partial) validation, the effective elastic moduli are also plotted in green as a function of time : they must correspond to the initial step of the relaxation functions.

However, the ageing creep of evolving microstructure homogenization technique considers a discretized evolution of the solid volume fraction, due to the introduction of the N fictitious phases

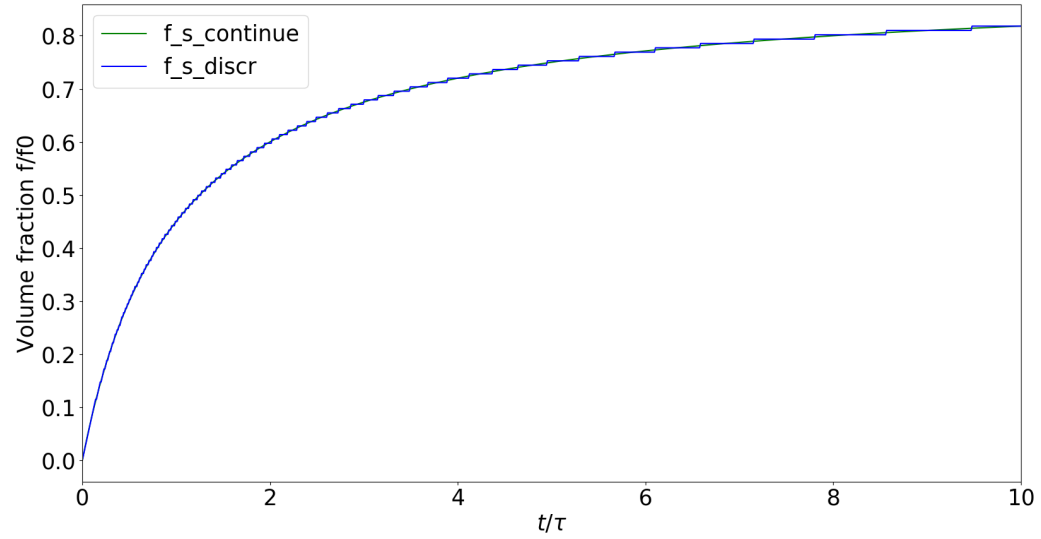

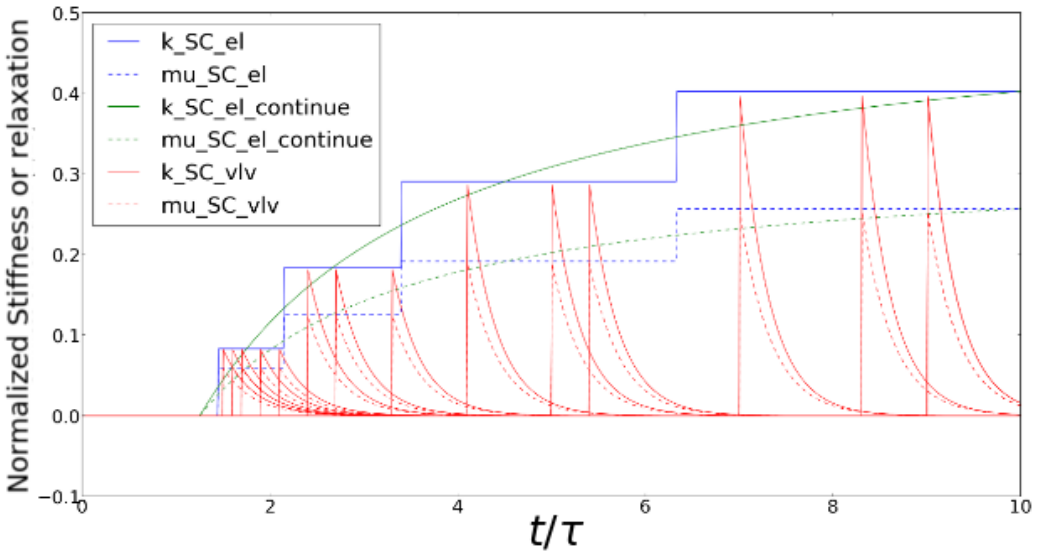

FIGURE 6.11 : (a) Volume fraction evolution of the solid phases ($f\_s\_continue$ and f_s_discr) in a small mixture REV (blue : discrete volume fraction evolution ; green : continuous volume fraction evolution) ; (b) Relaxation functions (red curves) and elastic moduli (blue : discrete volume fraction evolution ; green : continuous volume fraction evolution) of a small mixture.

(Fig.6.11(a)). Using this discretized volume fraction evolution, the effective elastic moduli are plotted in blue on Fig.6.11(b) (stresses are normalized by the solid phase Young's modulus E_0, and times are normalized by the characteristic ageing time τ). The latter are successfully compared to the relaxation functions.

6.3.3 Effective behaviour of outer hydrates

At the outer scale, a number of clusters are considered, starting densification at instants $t' = u_0^1, u_0^2, ...$, and the cumulated volume fractions of small mixture phases being densified are $f_m(u_0^1),\ f_m(u_0^2), ...$ Each cluster is homogenized using the aforementioned procedure. Then these clusters are homogenized using a self-consistent scheme.
Results are plotted on Fig.6.12. When considering the discrete evolution of volume fractions, the effective moduli are consistent with the relaxation functions. The differences are influenced by the convergence threshold of the self-consistent scheme and the number of time discretization points. If the value of the convergence threshold is too big, the calculation with the self-consistent scheme might not give a precise enough result, which causes the difference. On the other way, if the number of time discretization is not enough, the continuity of the result might be influenced and the difference might be caused.

In addition, if the Fig.6.12(b) and the Fig.6.12(c) are examined together, it could be concluded that the rigidity of your the Fig.6.12(c) starts on a moment corresponding to a solid volume fraction well below 0.5 (shown in the Fig.6.12(b)).
Based on the comparison results, the multi-scale modeling begins to establish the stiffness in earlier hydration period than the single scale modeling, which means that the multi-scale modeling corrects the unreal late setting phase and efficiently simplifies the calculation. Moreover, several scales can be added to modify the late setting phase to a value tending towards reality, which avoids the defect of the self-consistent scheme when dealing with the problem of porous materials with single scale morphological model. Other results also show that the higher the initial water to cement ratio, the latter is the setting phase, regardless of model style.

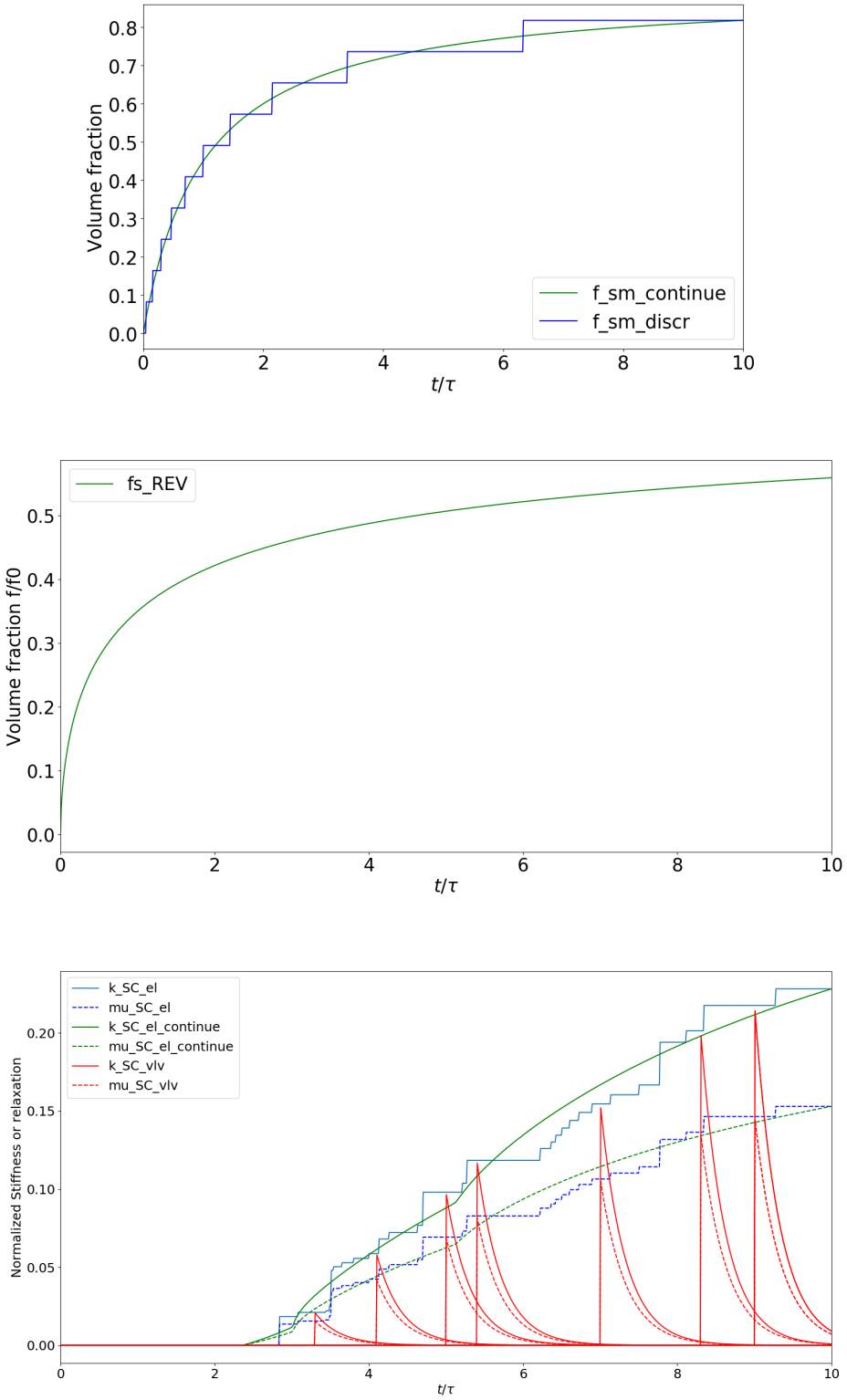

FIGURE 6.12 : (a) Volume fraction evolution of the small mixture phases ($f\_sm\_continue$ and f_sm_discr) in the "Low density" hydrates REV (blue : discrete volume fraction evolution ; green : continuous volume fraction evolution) ; (b) Volume fraction evolution of the solid phases in the "Low density" hydrates REV ; (c) Relaxation functions (red curves) and elastic moduli (blue : discrete volume fraction evolution ; green : continuous volume fraction evolution) of outer hydrates.

Chapitre 7

Conclusion and Prospects

An approach to upscale the mechanical behaviour of composite materials undergoing geometrical evolutions of their microstructure is proposed, with preliminary applications to cement pastes. Mean-field homogenization is considered. Both elastic and nonageing viscoelastic behaviours are considered for the different phases. While the evolving nature of microstructure does not prevent the use of mean-field homogenization in the case of elastic phases, special care has to be taken for viscoelastic phases. Indeed, time appears both in the elementary behaviours and in the evolution of microstructure. Even if the phases are nonageing, the effective behaviour is ageing viscoelastic.

A common approach, considering microstructure as frozen once the macroscopic loading step has been applied, allows for approximating the effective ageing behaviour using readily available tools (namely the correspondence principle with the Laplace-Carson transform), when phases are nonageing. The originality of this chapter resides in the approach proposed to overcome this assumption. Extending Bažant's solidification theory, an equivalent composite is built, whose microstructure is constant but made up of ageing linear viscoelastic fictitious phases. Taking advantage of recent advances in ageing linear viscoelastic homogenization, the effective behaviour of this equivalent composite can then be estimated. Note that this approach is not restricted to nonageing phases in the evolving microstructure : ageing phases are more straightforward to consider. As expected, the frozen microstructure assumption is, found to be valid only for late-age loadings, once the microstructure evolution becomes negligible. When loaded at early age, compliance functions from both techniques (with and without this frozen assumption) only share the initial elastic strain. Even the initial strain rate is different. This is attributed to the dissolution process. Qualitatively, compliance functions from evolving microstructure are closer to the experimental ones reported in Tamtsia et al. [186].

A multi-scale morphological model has been designed to model outer hydrates, avoiding the late setting issue. It is used in an ageing viscoelastic homogenization technique considering microstructure evolution [168]. Even if this first application focuses on simplified inputs, the technique is flexible enough to be able to use any kinetics curve and any isotropic linear viscoelastic behaviour.

The proposed application to cement paste is deliberately crude to focus on the description of the homogenization approach rather than on unnecessary technical details. However, with the

further comparisons to experimental data in the third part in this thesis, the model has been and could be improved in several aspects :

- Hydration kinetics : More realistic hydration kinetics should be used, either coming from experimental measurements or from hydration models. Moreover, the various anhydrous and hydrated phases could be detailed (e.g. C_3S, C_2S, C_3A, C_4AF...) ;
- Morphological model : Morphologies that have been successfully used to estimate other mechanical properties (stiffness, strength, nonageing creep) can be adapted in the ageing viscoelastic context proposed here. Some of these models include features (multiscale representation, aspherical shapes) that have proven to reduce shortcomings on prediction of the setting hydration degree ;
- Elementary viscoelastic behaviour of C-S-H : More realistic behaviours could be used, for example, obtained from the scale where sliding interfaces can be explicitly described ;
- Stress state of anhydrous and hydrates : A study of the influence of the stress state over dissolution and precipitation processes could be performed, and also the zero-stress assumption for hydrates precipitating in confined spaces should be overcome ;
- Aging mechanisms : As cementitious materials experimentally shows ageing creep even for loadings at long term (typically several years, see e.g., data reported by Bažant [207][17]), mechanisms other than hydration could be taken into account.
- Make the evolving microstructure more realistic and less random, taking into account an organization of precipitation around the anhydrous grains. The basic hydration model considering dissolution and precipitation around an anhydrous particle is being currently coupled ;
- Continue upscaling, up to the cement paste, including high density hydrates, portlandite and anhydrous grains, then up to the VeRCoRs concrete, considering interface effects around the aggregates.

Among these prospects, modifications of hydration kinetics or viscoelastic behaviour of hydrates can be straightforwardly taken into account by the proposed approach. And the application of more realistic viscoelastic behaviour could be carried out with experimental results. Indeed, it is modular enough to use as inputs any kinetics curve and any linear viscoelastic behaviour, defined by compliance or relaxation functions, for elementary phases. Improving the morphological model requires the extension of a apherical inhomogeneity [160] to a spheroidal inhomogeneity (see [111][10] in the case of a constant Poisson ratio for the matrix) and to a multilayered composite sphere.
Aging viscoelastic estimates are consistent with the effective elastic moduli.
Further improvements of the approach proposed here and applications to concrete are already promising.

Deuxième partie

Creep experiment procedure on cement paste, mortar and the VeRCoRs concrete

Chapitre 8

Manufacturing process of cementitious materials in the laboratory

Sommaire

8.1 Introduction

In the framework of studies on cementitious materials at EDF $R\&D$, it is necessary to produce representative specimens of different scales of cementitious materials for VeRCoRs concrete, such as cement pastes, mortars and concretes.

The aim of this chapter is to describe the procedure for manufacturing cement paste, mortar and concrete up to the demolding stage in the laboratory because there is the need for this thesis to manufacture mortar that is as close as possible to the matrix surrounding the aggregates in the REV of the VeRCoRs concrete and to manufacture cement paste that is as close as possible to the matrix surrounding the sands in the REV of mortar.

The mix design of the cementitious materials for the VeRCoRs concretes are the same as that of the 1 :3-scale experimental mock-up of a reactor containment-building (the VeRCoRs mock-up).

The mix design of the cimentitious materials of the VeRCoRs concrete is indicated in Table 8.1, Table 8.2 and Table 8.3 (G=aggregates, S=sable, C=cement, W=water).

Cement Paste						
Volume (L)	m Cement (kg)	V Cement (L)	m Admixture (kg)	V Water with admixture (L)	V Added Water (L)	W/C
14	16.495	5.321	0.134	0.102	8.552	0.525

FIGURE 8.1 : Mix design of cement paste.

Mortar (0 - 4 mm)								
Volume (L)	m Cement (kg)	V Cement (L)	m G1 (0 - 4 mm) (kg)	V G1 (L)	m Admixture (kg)	V Added Water (L)	W/C	S/C
10	5.956	1.921	12.668	4.872	0.048	3.160	0.525	2.127

FIGURE 8.2 : Mix design of mortar.

The VeRCoRs Concrete											
Volume (L)	m Cement (kg)	V Cement (L)	m G1 (0 - 4 mm) (kg)	m G2 (4 - 11 mm) (kg)	m G3 (8 - 16 mm) (kg)	m Admixture (kg)	V Admixture (L)	V Added Water (L)	W/C	G/S	S/C
76	24.031	7.752	62.331	33.419	41.304	0.195	0.184	14.684	0.525	1.199	2.594

FIGURE 8.3 : Mix design of the VeRCoRs concrete.

- A "cement paste" is considered here as a mixture of cement and water in quantities fixed by a mix design.
- A "mortar" uses the same constituents as the cement paste, but with the addition of sand.
- Finally, a "concrete" is a set of cement, water, sand and aggregates of various sizes.

The addition of admixtures to modify the mechanical properties and/or workability is effected during this manufacture of VeRCoRs concrete.
The cylindrical specimens with the dimension of $3.6cm \times 18cm$ (called small dimension, for cement paste and mortar) or of $8cm \times 30cm$ (called large dimension, for concrete) were obtained according to the manufacturing procedure for the creep experiments and the shrinkage experiments described in the following chapters. In addition, the prisms with the size of $4cm \times 4cm \times 16cm$ are manufactured for the compressive strength test at cement paste and mortar scale according to the standard NF EN 196-1 and the cylindrical specimens with the dimension of $11cm \times 22cm$ are manufactured for the compressive strength test at the VeRCoRs concrete scale according to the standard NF EN 12390-3.

8.2 Preparation

8.2.1 Preparation of the components

The cement has been placed in waterproof bags, themselves stored in waterproof cans as soon as possible after the reception. Silica gel was added to the cans to absorb as much water as possible.

On the day of manufacture, the texture of the cement was tested by the touch of the hand. A very rough cement (which the cement clusters are difficult to crush) indicates a water absorption that could adversely affect the physical properties of the cured product.
The sand and the coarse aggregates were dried beforehand in an oven, at a temperature of 105°C, for several hours. Once the drying was finished, the material was stored in waterproof cans. The addition of water for the saturation of the sand and of the coarse aggregates is taken into account in the calculation of the quantities of the manufacture.
The water chosen to maximize the reproducibility of the manufacture between different laboratories was the demineralized water, available via the water supply network of the laboratory. The total water represents the water needed for the hydration of the cement (also called the effective water), the water for the absorption in the aggregates and the water included in the liquid admixtures.

FIGURE 8.4 : Preparation of the components.

8.2.2 Preparation of the molds

In the case of parallelepipedic metal molds ($4cm \times 4cm \times 16cm$), it was checked that the removable parts are properly cleaned, assembled and tightened, that the holes for plots of shrinkage have been blocked by a stud (attention to the direction of the stud) or by a piece of tape, and that the mold has been properly coated with formwork oil.
In the case of plastic molds designed in the laboratory, we have checked the correct cleaning of the bottom of the mold, then have put a piece of electrical tape on the hole (the pump for the demolding was connected to the hole of mold via a flexible, compression-proof hose and then the mold was pumped until the specimen was released, Fig.8.13) to check the water tightness by filling the mold with water and noting that there was no drop under the mold.
Finally, the cardboard molds was verified that there was no deformations or signs of deterioration (cuts, holes, humidity influence...).

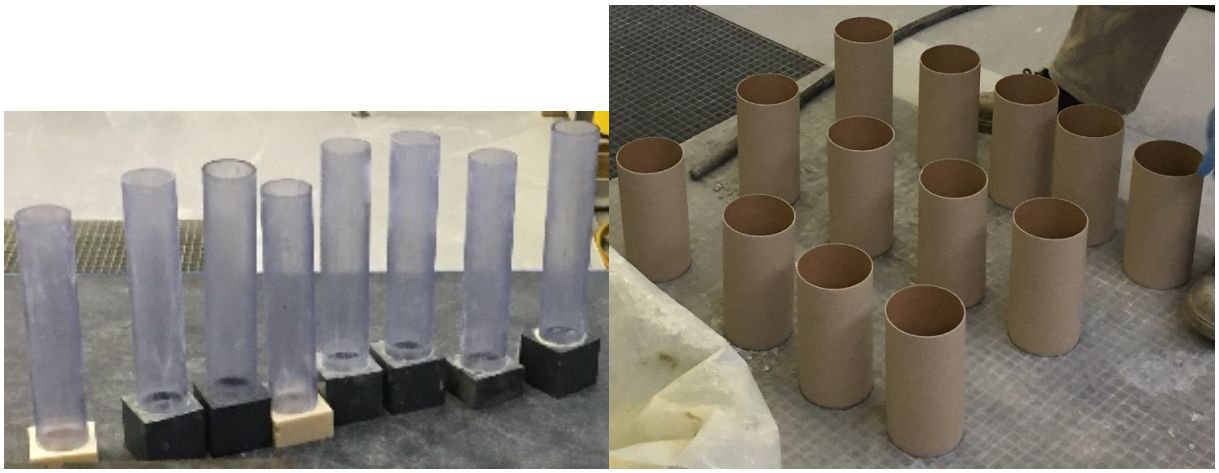

FIGURE 8.5 : Photos of the molds (Left : plastic molds with the diameter of 3.6cm ; Right : cardboard molds with the diameter of 8cm).

FIGURE 8.6 : Photos of the parallelepipedic metal molds ($4cm \times 4cm \times 16cm$) (Left : empty molds ; Right : molds during the manufacture of specimens).

8.3 Manufacturing of specimens

8.3.1 Preparation

The preparation phase during the day of the manufacture consisted first of all to validate each point of the preceding section. Once done, the constituents were weighed precisely according to the mass calculated in the table of mix design (Table 8.1, Table 8.2 and Table 8.3) and the molds to be used were arranged at the height of the manufacture work.

8.3.2 Mixing

FIGURE 8.7 : Hobart Stainless Steel Wire Whip.

Cement paste

1. Dilute the admixture in the demineralized water.
2. Introduce the cement and mix with the wire loop whip of Hobart for 1 minute.
3. introduce the water into the bowl, taking care to avoid any loss of water or cement.
4. time=t0 : As soon as the demineralized water and cement was in contact, immediately turn on the mixer with the whip of Hobart at low speed while starting the timing the mixing steps.
5. time=t0+1min30s : Turn off the mixer for 30 sec and scrape.

FIGURE 8.8 : Mixer with the whip of Hobart.

6. Turn on the mixer with the whip of Hobart again at low speed for 90 sec.

Mortar

1. Separate the demineralized water into the parts of a quarter and three quarters.
2. Dilute the admixture in the part of three quarters of the demineralized water.
3. Place the sand in the mixer and mix it with 1/4 of the demineralized water for 1 minute at low speed.
4. time=t0 : As soon as the 1/4 of the demineralized water and sand was in contact, immediately start the timing of the mixing steps.
5. time=t0+30s : Add the cement.
6. time=t0+1min30s : Add the part of three quarters of the demineralized water.
7. time=t0+5min30s : Turn off the mixer with the whip of Hobart.

VeRCoRs concrete

1. Weigh the absorbed water and the added water separately.
2. time=t0, Place the aggregates in the mixer and mix it with absorbed water.
3. time=t0+30s, Turn off the mixer and wait (5 to 10 min if there is no problem of leaks).

4. Mix the admixture and add water.
5. time=t0+10min30s : Add cement and turn on the mixer.
6. time=t0+11min30s : Add the water with the admixture.
7. time=t0+15min30s : Turn of the mixer.

8.3.3 Test on fresh batch

The different tests were carried out during pouring. The possibility of reusing the material was concerned. In some cases the material tested is reusable (but it is not reused in reality) because some tests do not change at all the mechanical and chemical properties of material, and in other cases it is reused to make the full exploitation of the manufactured material.

Tests on fresh cement paste

- Density : The material tested was reusable.
- Aerometer test (1 liter) : The material was not reusable.
- Slump Cone test : The material was reused and was re-mixed with the rest of the material.
- Marsh Cone Fluidity (EN445) Lab Test : The material was not reused because air has got into the material.

Tests on fresh mortar

- Density : The material tested was reusable.
- Aerometer test (1 liter) : The material was not reusable.
- Slump Cone test : The material was reused and was re-mixed with the rest of the material.
- Marsh Cone Fluidity (EN445) Lab Test : The material was not reused because air has got into the material.

Tests on fresh concrete

- Density : The material tested was reusable.
- Aerometer test (8 liters) : The material was not reusable.
- Slump Cone test : The material was reused and was re-mixed with the rest of the material.

FIGURE 8.9 : Equipment to measure the density of manufactured material.

8.3.4 Casting and vibration

To vibrate the metal prismatic molds, we have used the spatula.
To vibrate the plastic cylindrical molds, we deposited them on the deck gratings, then contacted them between the deck gratings with a vibrating needle until all the bubbles disappear.
To vibrate the cardboard molds, we vibrate any diameter greater than or equal to 110mm with a vibrating needle (Fig.8.12). The molds with the size of $8cm \times 30cm$ were vibrated by pricking. In both cases, the maximum height of a layer to be vibrated was 110mm. The surface of the section of vibrating needle does not exceed one quarter of the surface of the section of the mold.

8.4 Conservation during curing period (24h)

Once poured, the samples underwent a curing period of 24 hours.
The cylindrical and prismatic molds were equipped with plastic stretch film (parafilm).
The prismatic molds were placed in a waterproof box containing a container filled with water.
This curing period aims at avoiding the evaporation of water and the drying of the specimens.

8.5 Demolding

The demolding stage began at the end of the 24 hours of curing.
The cardboard molds were submerged in water to aid in demolding.
The metal molds were disassembled, scraped, re-oiled, and then reassembled.
A manual water pump was used (Fig.8.13) to demold the sample in the plastic cylindrical molds. The pump was connected to the mold via a flexible, compression-proof hose and then was pumped until the specimen was released. The most effective method was to go up to about 30 bar and to maintain this pressure until the specimen was released.

FIGURE 8.10 : Equipment to carry out the Marsh Cone Fluidity (EN445) Lab Test.

FIGURE 8.11 : Equipment to carry out the Aerometer test (1 liter).

FIGURE 8.12 : Vibration of the cardboard molds.

The water level of the pump was checked regularly, as it might compress air instead of water, which leaded to the projection of the specimen.

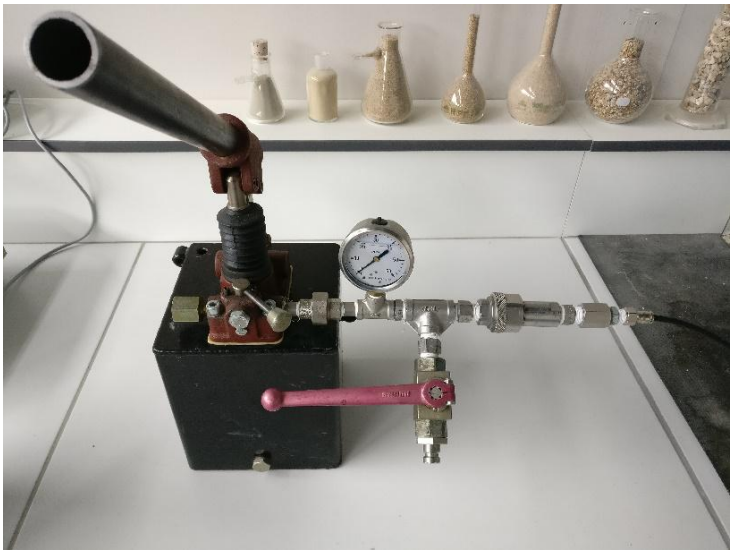

FIGURE 8.13 : Manual water pump.

8.6 Conservation of specimens

There is important conservation work for the specimens during the period between the demolding and the creep test. Especially, there are some test specimens stored for 1 year before the start of the creep tests. For this reason, the specimens have been placed in waterproof bags, themselves stored in waterproof cans as soon as possible after the demolding. And the checks (the weighings) have been carried out to ensure the autogenous storage conditions for the specimens. The weighings results showed that the maximum mass loss during the conservation after 385 days is less than 2 grammes, which confirmed that the autogenous storage conditions was achieved.

Chapitre 9

Creep experiment procedure on cement paste, mortar and concrete

Sommaire

9.1 Introduction

The civil engineering laboratory of the MMC department in EDF $R\&D$ has laboratory equipments enabling the characterization of macroscopic concrete creep strains (shrinkage, creep, relaxation), in support of the understanding and modeling of the ageing behavior of the VeRCoRs concrete. These equipments are installed in one special room of the laboratory for creep experiment.
The origin of these equipments dates back to the early 2000s, with the installation of a series of the first generation creep test benches. They were then equipments carrying out tests of bending on concrete beams subjected to aggressive environments. In 2002, these benches were assigned to a new activity : the study of the relaxation of concrete beams. In 2008, a new experimental program proposed the use of these benches for cylinder relaxation tests. These tests proved unusable because of difficulties mainly related to the sealing.
During the move of the laboratory and the investments in EDF $R\&D$, three new benches of high capacity are acquired and installed. The management and acquisition system has been completely revised.
In the framework of the CiWAP2 project in EDF $R\&D$ and more particularly in this thesis, these benches are used in 2017-2018 for the performation of creep experiments on concrete, mortar and cement paste.
This chapter details the general procedure for carrying out the experiments.

9.2 Overall description of the experiments

The purpose of the experiments described in this chapter is the characterization of autogenous shrinkage, and basic creep under uniaxial compression at 20 °C. These characterizations were carried out on two geometries : small cylindrical specimens with the dimension of $3.6cm \times 18cm$, and big cylindrical specimens with the dimension of $8cm \times 29cm$.
These dimensions make it possible to carry out the experiments on cement paste, mortar, and concrete (for concrete with small aggregates, typically less than 2 cm).
In addition to the creep under load of cementitious materials, the protocol described in this chapter allows the characterization of the recovery of creep.
The present protocol therefore describes the performation of the experiments collected in the Table 9.1. The acronyms presented in the same table will be used in the chapter for clarity.

TABLE 9.1 : Denomination of the experiments described and their acronyms.

Experiment	Acronym
Non-drying shrinkage	NDS
Non-drying creep	NDC

The tests that were carried out are listed in a synthetic way in Fig.9.1, Fig.9.2 and Fig.9.3 as well

as a timeline of the tests on each of the bench groupe (every 2 benches form 1 bench group), the preparation phases are included in the first day of every creep test. These timelines were planned to optimize the occupation of the benches (as well as the preparation phase). They explain why the test at the age of loading at 1 day did not last more than 6 days, and the test at 7 days did not last more than 21 days, etc ...
This organization has also made it possible to make only one batch per material and thus making the most of the time for experiments from one batch to another.

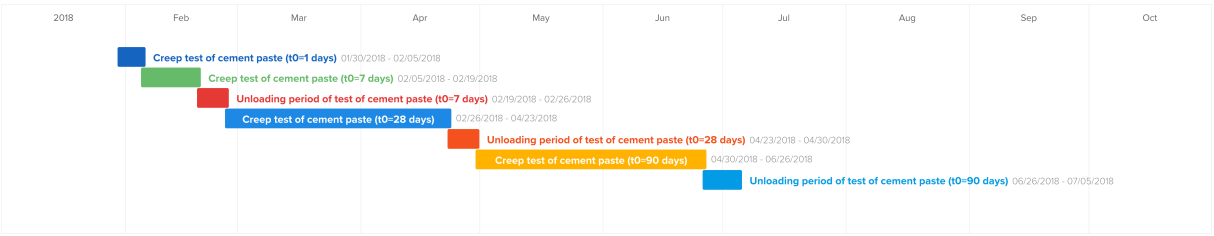

FIGURE 9.1 : Timeline of tests on Bench 1 and Bench 2.

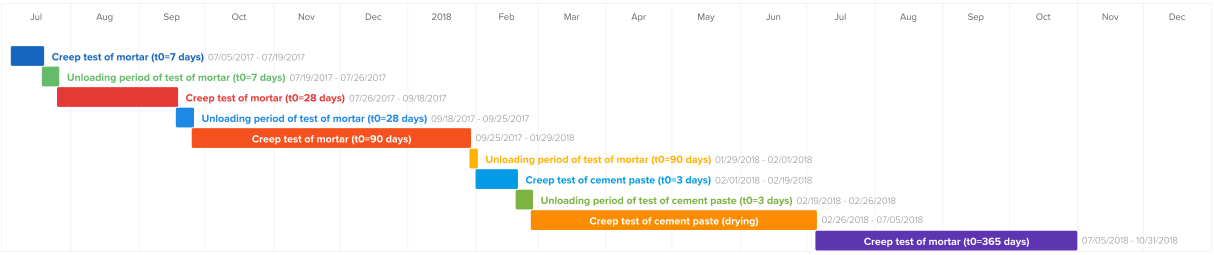

FIGURE 9.2 : Timeline of tests on Bench 3 and Bench 4.

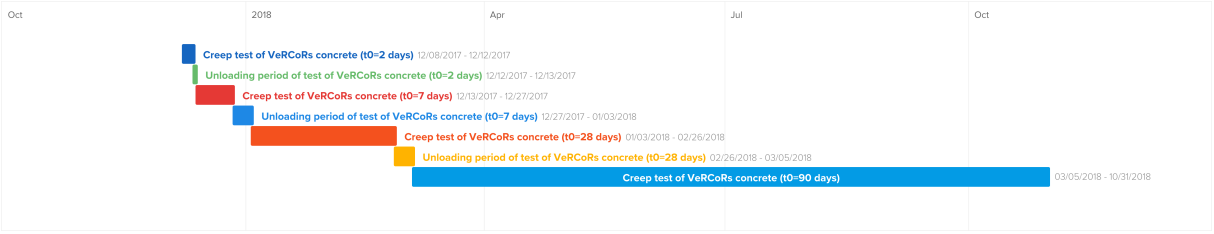

FIGURE 9.3 : Timeline of tests on Bench 5 and Bench 6.

9.3 Porosity measurements on each batch

This section follows the report of $EDF R\&D$ in which the context of the porosity measurements is presented, and the measurements of the porosity of cement paste, mortar and the VeRCoRs concrete are presented. The reflection on the cementitious materials manufacturing procedure is continued based on the porosity measurements of each material.
The specimens were kept under the demineralized water until the start of the porosity measurements. The porosity measurements were carried out during the summer of 2017. In particular, it could be ensured that the specimens were tested at the same age of curing.
It was decided to take three samples at the bottom, middle and the top of each test specimen. The cell usually reserved for the vacuum cooling of the samples was used to achieve the saturation (see Figure 9.4).

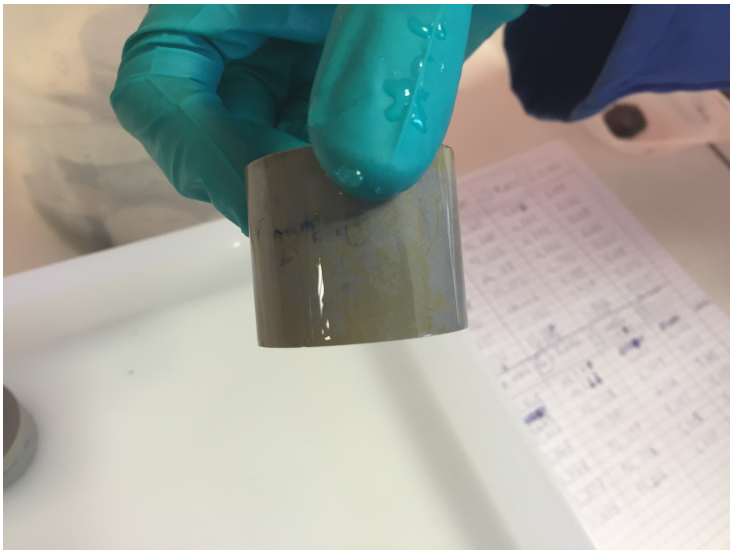

FIGURE 9.4 : A sample used for the porosity measurements.

The porosity results of the samples are shown in Table 9.2, Table 9.3 and Table 9.4. An average value of porosity of 47.04% for the cement paste samples, 23.06% for the mortar samples and 15.38% for the VeRCoRs concrete samples is obtained.

TABLE 9.2 : Average porosity of the samples of cement paste.

Porosity (%)	Bottom	Middle	Top	Average
Sample 1	45.12	47.65	47.63	46.80
Sample 2	46.14	47.10	47.70	46.98
Sample 3	46.29	47.67	48.10	47.35
Average	45.85	47.47	47.81	47.04

TABLE 9.3 : Average porosity of the samples of mortar.

Porosity (%)	Bottom	Middle	Top	Average
Sample 1	22.79	23.32	23.13	23.08
Sample 2	22.92	23.22	23.00	23.05
Sample 3	22.83	23.14	23.19	23.05
Average	22.85	23.23	23.11	23.06

TABLE 9.4 : Average porosity of the samples of the VeRCoRs concrete.

Porosity (%)	Bottom	Middle	Top	Average
Sample 1	13.98	15.61	16.35	15.31
Sample 2	14.01	15.66	16.90	15.53
Sample 3	13.77	15.51	16.60	15.29
Average	13.92	15.59	16.62	15.38

The porosity measurements of the cement paste samples, the mortar samples and the VeRCoRs concrete samples show that the sample homogeneity is generally considered to be satisfactory. The maximum difference between the top and the bottom of the test samples is 2.89%. The difference is due to the concrete mix design (bleeding and settlement of the heavy elements in cementitious materials). There is also the repeatability of the experimental results among these three sample (there are similar values from one sample to another).
In addition, the calculation of the porosity of cement paste could be carried out based on the mix design of mortar and the measured porosity of mortar. With the same principle, the calculation of the porosity of mortar could be carried out based on the mix design of the VeRCoRs concrete and the measured porosity of the VeRCoRs concrete.
To realize this calculation, the volume of water should be calculated firstly :

$$V_w = V_{batch}\phi_{ex} \tag{9.1}$$

where V_w is the volume of water, V_{batch} is the volume of the manufactured batch (10L for mortar, 76L for the VeRCoRs concrete), and ϕ_{ex} is the measured average porosity of the REV material (23.06% for mortar and 15.38% for the VeRCoRs concrete).
Then the volume of the matrix phase in one manufactured batch could be calculated :

$$V_{mat} = V_{batch} - V_G \tag{9.2}$$

where, V_{mat} is the volume of the matrix phase, V_G is the volume of the aggregates (sand for mortar and coarse aggregates for the VeRCoRs concrete).

So the porosity of the matrix phase could be calculated as :

$$\phi_{mat} = \frac{V_w}{V_{mat}} \tag{9.3}$$

Cement paste is the matrix phase of mortar, and mortar is the matrix phase of the VeRCoRs concrete. ϕ_{ex} could be obtained by Table 9.3 and Table 9.4. V_{batch} and V_G could be obtained by the mix design parameters. According the calculation, the porosity of cement paste phase in the REV of mortar equals to 44.97%, which is close to the measured cement paste porosity 47.04%. And the porosity of mortar phase in the REV of the VeRCoRs concrete equals to 25.09%, which is also close to the measured cement paste porosity 23.06%. This verification confirms that the manufacture has respected the mix design of the VeRCoRs concrete materials and the fabricated samples are reliable.

9.4 Preparation and instrumentation of the specimens for creep experiments

This protocol describes the organisation of the shrinkage and the creep experiments on specimens manufactured in the civil engineering laboratory of the MMC department at EDF *R&D*. The cylindrical specimens of the dimension of $3.6cm \times 18cm$ (called small dimension, for cement paste and mortar) or of $8cm \times 30cm$ (called large dimension, for concrete) were obtained according to the manufacturing procedure described in the previous chapter.
The preparation and instrumentation phase of the specimens meet three objectives :

- Ensure flat and parallel faces to apply the loading (for creep experiments) and thus ensuring a state of uniform and uniaxial stress on the test specimen.
- Ensure a very tight seal for all the experiments carried out under autogenous conditions (autogenous shrinkage and basic creep).
- Ensure good transmission of the axial strains of the specimens to the strain measurement system.

The installation of the instrumentation supports is considered inseparable from the seal because of the choice made in this protocol of a direct contact between the instrumentation supports and the specimen.
To meet the three objectives stated above, two main phases were performed : the cutting or the grinding on one hand, the instrumentation and the sealing on the other hand.

9.4.1 Choice of the specimens

The specimens were not tested in their order of manufacture, which would induce the bias, given the possibility that there is a systematic difference in the properties between the specimens at the beginning of the batch and those at the end of the batch.

A random permutation was applied to the numbering of the specimens with a python script (for the random permutation of N specimens).

9.4.2 Cutting and grinding

Unloaded specimens

For the experiments of NDS that do not require the application of a load, the specimens were neither ground nor cut to the right dimensions. The criterion of acceptability of a specimen is the existence of a sufficiently perpendicular face for the cylinder to allow to lay the specimen stably vertical.
For these specimens, the pieces of the excess material likely to come off are removed by means of a brush, a file or cutter. Some specimens of cement paste were also cut by a saw under water, which has the disadvantage of bringing extra water to autogenous tests.

Loaded specimens

For the loaded specimens, the dimensional accuracy requirements are more important. The perpendicularity of the loaded faces with respect to the cylindrical shaft of the specimens conditions the possibility of establishing a state of uniaxial stress in the specimen.
Two methods were used : the cutting with a wet saw under water (for small specimens) and the grinding in the laboratory LECBA of the CEA (for large specimens).

Sawing For sawing the small specimens with the small wet saw (see Fig.9.5). The sawing procedure is as follows :

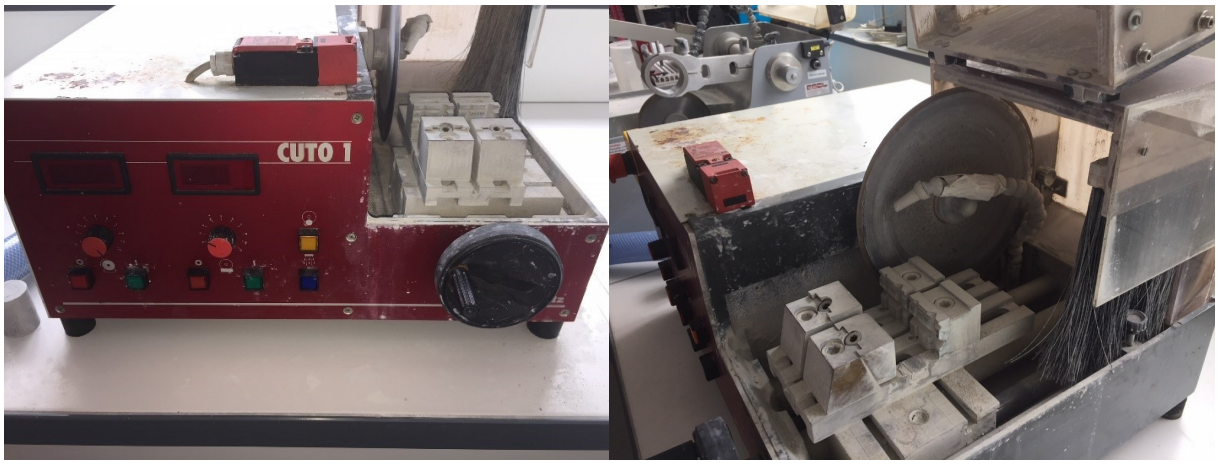

FIGURE 9.5 : Sawing equipment of cement paste and mortar specimens.

- the specimens were maintained by the two clamping systems ;

- the perpendicularity of the specimen with respect to the blade at a standstill was checked with an angle square ruler ;
- the position of the specimen was marked (so as to locate the top face of the specimen) ;
- one side of the specimen was cut ;
- the perpendicularity of the cut with respect to the cylindrical shaft of the specimens was verified on a flat support ;
- when the perpendicularity was too bad (typically greater than 1 mm on the height of the specimen) : the specimen was placed back on the saw correcting its position according to the perpendicularity defect detected with the angle square ruler, then the defect side of the specimen was recut.

As the final size of the specimen should be 18 cm and the above procedure was repeated on both sides, a margin was left at each cut, and to make the final cut to fix the length of the specimen at 18 cm only in a well-functioning saw system. Once the cut was completed, the selfpropelled undercarriage was manually returned to its original position (Figure 9.6), and the specimen was removed. The operator verifies that there has been no blade jump during the cutting which would deteriorate the flatness of the cut. The cut not flat was slightly repaired by the polisher.

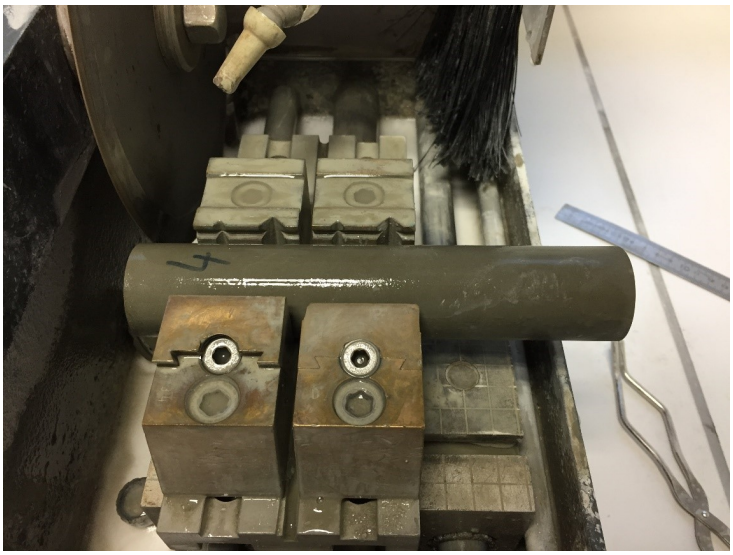

FIGURE 9.6 : Specimen after the cutting.

The important parameters for a good cut are :

- Blade size : 200 mm in diameter
- Blade thickness : 0.5mm
- Advancement speed of the selfpropelled undercarriage : about 2mm/min
- Speed of the rotation of the blade : 3000 rpm

Grinding The grinding of the $8cm \times 30cm$ specimens was performed at CEA LECBA (see Figure 9.7). The final size of the specimen is $8cm \times 29cm$. The parameters of the surfacing machine are :

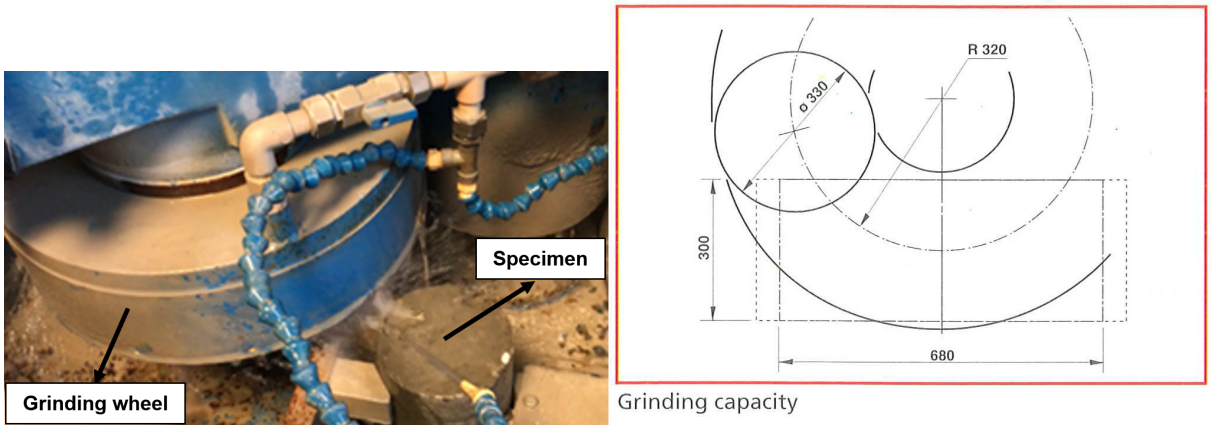

FIGURE 9.7 : Grinding of a cylinder specimen at CEA LECBA.

- Model of the surfacing machine : Esacta PMD
- Surface of the table to put the specimen : $680mm \times 300mm$
- Distance from center of grinding wheel to center of column : 320 mm
- Grinding wheel diameter : 330 mm
- Min. and max. distance from grinding wheel to table : 145-375 mm
- Vertical travel of grinding wheel : 230 mm
- Grinding wheel speed : 700 – 1400 RPM
- Grinding wheel motor : 1-2 hp
- Feed motor hp 0.25 hp

9.4.3 Sealing and installation of the instrumentation supports

The procedure for sealing the specimens has been started in 2017. In fact, the internal and the external creep experiments are frequently impacted by the air leakage in the experiment system for the sealing of the specimens [44].
The work carried out consisted of the tests of different sealing solutions. This work concluded that the best technique is based on the use of a self-adhesive aluminum (with the brand of Yelloz components, ref. ADAT506, SCAPA Tapes) for the common parts, and the X60 gauge glue (the method of preparation of the X60 glue is detailed in the following subsection) with the brand of HBM for the parts of singularities.
The procedure for the sealing and the installation of the instrumentation supports differs according to the type of experiment :

- NDS : self-adhesive aluminum on the cylindrical shaft and the ends of the specimens, treatment of the holes on the cylindrical shaft linked to the instrumentation supports.
- NDC : self-adhesive aluminum on the cylindrical shaft, treatment of the holes on the cylindrical shaft linked to the instrumentation supports, gluing of the ends to the load plates.

These different situations are described separately in the following paragraphs. During the experiments carried out in 2017, it was decided to use 3 layers of SCAPA tapes for the experiments at the age of loading of 1 year, and 2 layers for the experiments at the age of loading not greater than 3 months.

Case of NDS experimental pieces

SCAPA Tapes Non-drying shrinkage experiments are the longest experiments since they are ideally started as soon as 24 hours after the manufacture and must last in parallel with all the creep experiments with the same material, which can be carried out at different time of loading. For this reason, it was decided to use 3 layers of self-adhesive aluminum on the shaft and the ends of the specimens. This requires for each specimen the preparation of different pieces of SCAPA tapes.
For the small specimens :

- 1 rectangular pieces ($18cm \times 45cm$) or 3 rectangular pieces ($18cm \times 15cm$)
- 6 discs with the diameter of 8cm

For the big specimens :

- 3 rectangular piece ($29cm \times 30cm$)
- 6 discs with the diameter of 15cm

The preferred technique for the cylindrical shaft is the use of a separate piece per turn, because it facilitates the establishment of the "hats" used at the ends of the specimens. The elements were set up by repeating the following sequence three times :

- Set up the rectangular piece for the cylindrical shaft.
- If necessary, cut with the cutter the SCAPA tapes exceeding the length of the specimen.
- Place the "hat" at both ends of the specimen.
- Flatten the SCAPA tapes with a hard but not sharp object such as the handle of a marker.

This procedure makes it possible to obtain a very tight specimen.

Instrumentation support and glue After the sealing step, the instrumentation support was positioned as in Fig. 9.8, and tightened so as to mark the SCAPA tape. The support was then removed to take out the specimen and to allow the cutting of the "windows" at the sharp screw marks left on the SCAPA tape (approximately $2mm \times 2mm$). These six windows were cut with a cutter as precisely as possible.

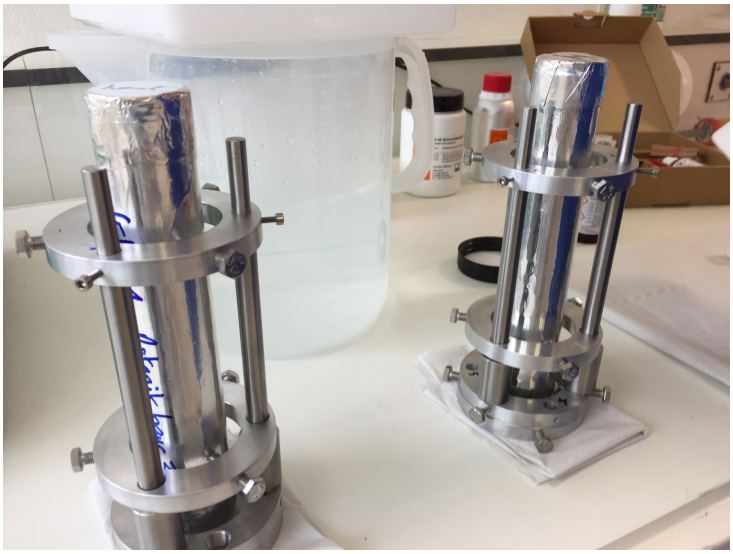

FIGURE 9.8 : Instrumentation stand with the mounting brackets.

Finally, the specimen was brought under the fume hood (turned on) in order to be carried out with the placement of X60 glue to seal the windows. The operators wore a mask (Type FFP3), a pair of glasses and protective gloves.
The instrumentation support was then put back in place using the supports provided for this purpose and was tightened with a wrench. Finally, the X60 glue was prepared with the method of preparation as follows :

FIGURE 9.9 : Scope of delivery for Glue X60 (SG).

1. Add a sufficient quantity of the powder component A to one of the cups supplied in the package. A measuring spoon filled level to the edge is sufficient for an SG with up to 30mm active length.

2. Add component B (approx. 6 to 7 drops for 1 spoon of powder) and mix thoroughly with a stirrer or spatula.

Then the glue prepared was drawn into a Pasteur pipette and injected around the pointed screws so as to block the windows (Figure 9.10).

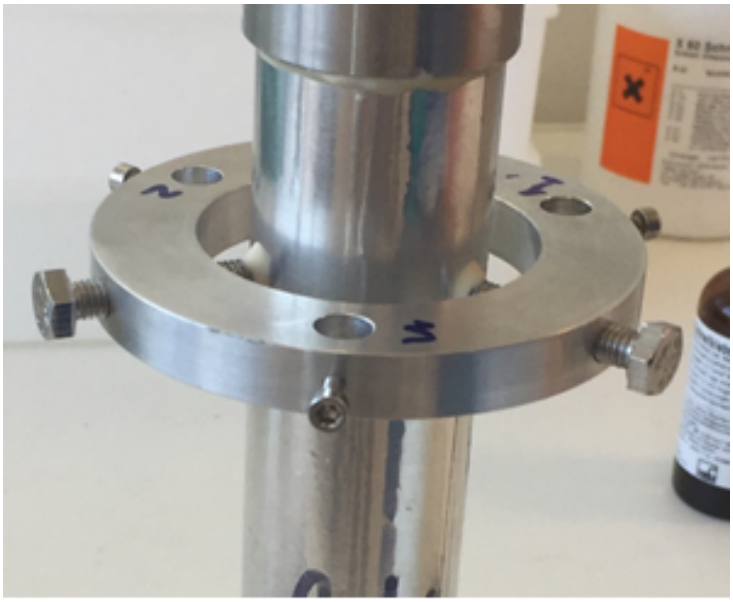

FIGURE 9.10 : Re-sealing the windows with the X60 glue.

In this last step, if the specimen was prepared at a young age of hydration, a gas release of an unknown origin (hydration of the cement paste or interaction with SCAPA tapes) has been observed which made it difficult to place the glue. When this occured, several same gluing steps were carried out to plug the small holes created by the gas in the glue during the setting of the material.

Case of NDC experimental pieces

SCAPA Tapes Given the generally shorter duration of creep experiments (with multiple ages of loading), it was decided to use 2 layers of self-adhesive aluminum (SCAPA tapes) on the shaft of the specimens. This requires for each specimen the preparation of different pieces of SCAPA tapes.
For the small specimens :

- 1 rectangular piece ($19cm \times 30cm$) or 2 rectangular pieces ($19cm \times 15cm$)

For the big specimens :

- 2 rectangular pieces ($30cm \times 30cm$)

The cylindrical shaft was thus sealed, the SCAPA tape that exceeds the length of the specimenis was cut. The SCAPA tape was finally flattened.

Instrumentation support, load plate and glue In a second step, the instrumentation support was tightened so as to mark the SCAPA tape.
Finally, the load plates was stuck to the specimen. This specific step of the NDC experiment is now described in detail.
The load plate of the experiment for small specimen is shown in Figure 9.11. On the left the upper load plate is presented with a collar formed by a wire in its insulating sheath and by stretch film. On the right, the pad used as the lower load plate is shown.

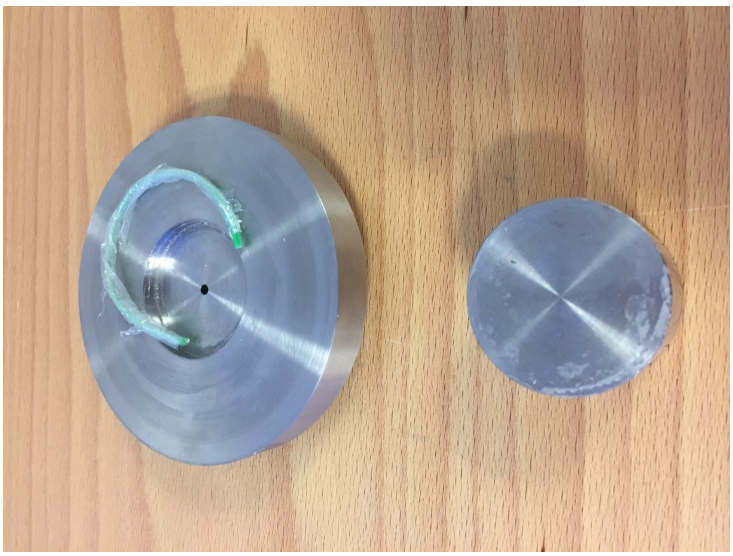

FIGURE 9.11 : Creep Load Trays for small specimens. Left : upper plate (with the ball joint at the back). Right : lower plate.

Regarding the experiments for big specimens, it was not necessary to use a lower plate as for small specimens, the instrumentation support having the objective of allowing to place the LVDTs without kinking the cables for the LVDTs.
As previously mentioned, the instrumentation support ring with small holes was downside in the final configuration of the specimen. For small specimens, the stud was glued to the specimen (or more precisely to the end of the SCAPA tape) by an ring-shaped bead of X60 glue. For large specimens, a plate was used and glued in the same way to the specimen.
For the upper plate, a centering hole was present, with a margin of a few millimeters relative to the diameter of the specimen. A collar formed by a wire in its insulating sheath and by the stretch film was placed in this space to center the specimen and to block this space with the X60 glue without filling it completely, to limit the glue used. The X60 glue sealing was then

performed between the SCAPA tape and the load plate (see Figure 9.12).

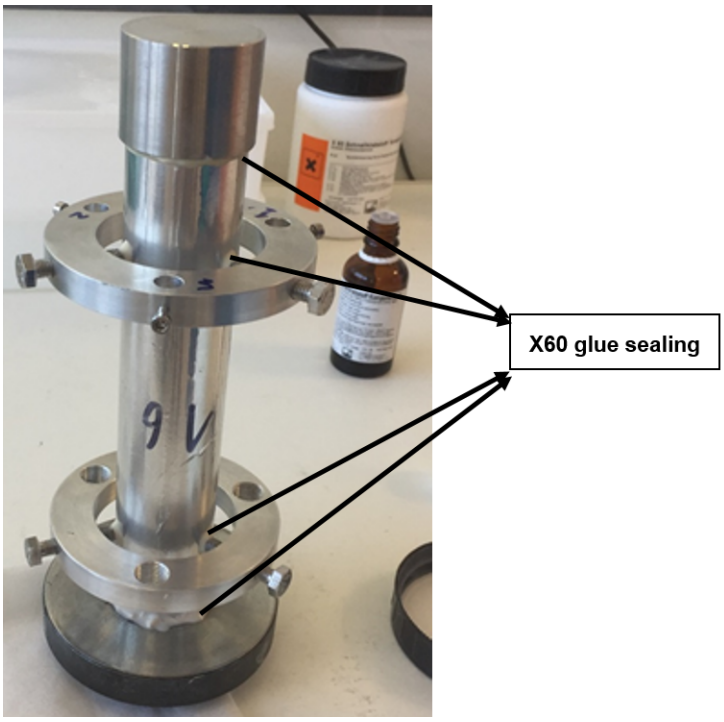

FIGURE 9.12 : Small size NDC specimen completely sealed.

After the end of the gluing operation, a waiting time was respected before moving the specimens to ensure the finalization of the curing of the adhesive (about a few minutes of waiting).

9.5 Determination of the loading level to be applied

In the experimental creep programs, it is important to choose the loading level in relation to the compressive strength of the tested material at the age of loading. It is therefore necessary to measure the compressive strength of cement paste, mortar and concrete at the same time as the time for the start of the creep experiment. For these three materials, the standard methods were used.
Like the main experimental program (shrinkage, creep), a random specimen permutation was applied to avoid the effects due to the production order.

9.5.1 Cement paste and mortar

For cement paste and mortar, the compressive strength test carried out is the $4cm \times 4cm \times 16cm$ specimen test of the standard NF EN 196-1, which was the subject of an internal qualification at the laboratory on the press MTS and on the creep benches (see Fig. 9.13).

FIGURE 9.13 : Compressive strength test on cement paste on the MTS press of the laboratory.

9.5.2 VeRCoRs Concrete

For the VeRCoRs concrete, the test carried out is the $11cm \times 22cm$ test of the standard NF EN 12390-3. This test has been conducted at CEA LECBA (see Fig.9.14).

9.5.3 Choice of load level of creep experiments and measurements of the Young's modulus

The compressive strengths of the samples at different ages of loading are in Table 9.5, Table 9.6, Table 9.7, Table 9.8, Table 9.9, Table 9.10, Table 9.11, Table 9.12, Table 9.13, Table 9.14, Table 9.15 :

TABLE 9.5 : Compressive strengths of the cement paste samples at the age of loading=1 day.

Sample number	BL28-1a	BL28-1b	BL28-2a	BL28-2b	BL28-3a	BL28-3b
Force (kN)	27.75	27.14	29.38	28.58	27.11	26.29
Stress (MPa)	17.3	17.0	18.4	17.9	16.9	16.4

FIGURE 9.14 : Compressive strength test on the VeRCoRs concrete at CEA LECBA.

TABLE 9.6 : Compressive strengths of the cement paste samples at the age of loading=3 days.

Sample number	BL28-4a	BL28-4b	BL28-5a	BL28-5b	BL28-6a	BL28-6b
Force (kN)	57.69	57.32	54.78	53.99	58.49	55.69
Stress (MPa)	36.1	35.8	34.2	33.7	36.6	34.8

TABLE 9.7 : Compressive strengths of the cement paste samples at the age of loading=7 days.

Sample number	BL28-7a	BL28-7b	BL28-8a	BL28-8b	BL28-9a	BL28-9b
Force (kN)	69.15	63.65	66.79	66.63	68.52	65.21
Stress (MPa)	46.7	43.0	46.4	46.3	48.9	46.6

TABLE 9.8 : Compressive strengths of the cement paste samples at the age of loading=28 days.

Sample number	BL28-10a	BL28-10b	BL28-11a	BL28-11b	BL28-12a	BL28-12b
Force (kN)	86.36	88.11	80.98	81.61	87.71	87.83
Stress (MPa)	58.4	59.5	56.2	56.7	59.3	59.3

TABLE 9.9 : Compressive strengths of the cement paste samples at the age of loading=90 days.

Sample number	BL28-13a	BL28-13b	BL28-14a	BL28-14b	BL28-15a	BL28-15b
Force (kN)	100.89	95.78	89.67	88.46	90.12	95.19
Stress (MPa)	68.2	64.7	59.0	58.2	60.9	64.3

TABLE 9.10 : Compressive strengths of the mortar samples at the age of loading=7 days.

Sample number	BL25-16a	BL25-16b	BL25-17a	BL25-17b	BL25-18a	BL25-18b
Force (kN)	88.43	86.80	90.20	89.01	88.75	89.06
Stress (MPa)	55.3	54.3	56.4	55.6	55.5	55.7

TABLE 9.11 : Compressive strengths of the mortar samples at the age of loading=28 days.

Sample number	BL25-4a	BL25-4b	BL25-5a	BL25-5b	BL25-6a	BL25-6b
Force (kN)	106.95	103.57	108.04	105.26	108.82	106.75
Stress (MPa)	66.8	64.7	67.5	65.8	68.0	66.7

TABLE 9.12 : Compressive strengths of the mortar samples at the age of loading=90 days.

Sample number	BL25-7a	BL25-7b	BL25-8a	BL25-8b	BL25-9a	BL25-9b
Force (kN)	114.05	115.10	115.23	108.85	111.46	112.13
Stress (MPa)	71.3	71.9	72.0	68.0	69.7	70.1

TABLE 9.13 : Compressive strengths of the VeRCoRs concrete samples at the age of loading=7 days.

Sample number	BL27-7	BL27-16	BL27-17
Force (kN)	390.77	400.30	414.85
Stress (MPa)	39.0	39.9	41.4

TABLE 9.14 : Compressive strengths of the VeRCoRs concrete samples at the age of loading=28 days.

Sample number	BL27-6	BL27-18	BL27-20
Force (kN)	454.15	470.13	459.42
Stress (MPa)	45.3	49.5	48.3

TABLE 9.15 : Compressive strengths of the VeRCoRs concrete samples at the age of loading=90 days.

Sample number	BL27-4	BL27-8	BL27-9
Force (kN)	528.66	530.04	498.08
Stress (MPa)	55.6	55.8	52.4

In the context of the experiments carried out so far, the maximum load level is 30% of the compressive strength, so that the creep behavior remains in the linear range. Given the capacities of the creep benches (which are 25kN for the low capacity benches and 100kN for the high capacity benches) and a habit related to the context of the concrete containment building to load at 12 MPa, a force of less than 30% of the compressive strength has often been used.
The evolution of the Young's modulus $E(t_0)$ with $t_0 = 1, \quad 2, \quad 3, \quad 7, \quad 28, \quad 90$ days could be calculated with the experimental results of the loaded force variation ΔF and the average displacement variation $\Delta\bar{\xi}$ during the loading and unloading period with ages of loading

$t_0 = 1, \quad 2, \quad 3, \quad 7, \quad 28, \quad 90$ days and ages of unloading $t'_0 = 6, \quad 21, \quad 82, \quad 84, \quad 195$ days (marked as "Measured by bench" at the scale of cement paste and as "Bench A", "Bench B" at the scale of the VeRCoRs concrete).
Moreover, at the scale of the VeRCoRs concrete, we have also carried out the simple compression test to determine Young's modulus directly in EDF, in CEA and in CEBTP (marked as "measured by press" and "CEBTP").
The evolution of the Young's modulus of the samples at different ages of loading are presented too (Fig.9.15, Fig.9.16, Fig.9.17).

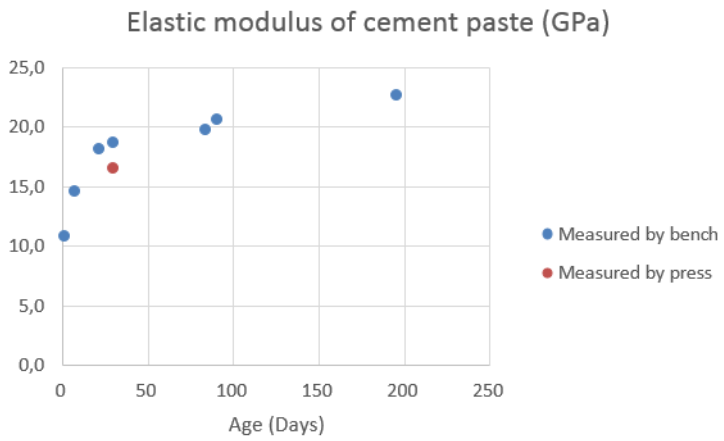

FIGURE 9.15 : Evolution of the Young's modulus of the samples of cement paste.

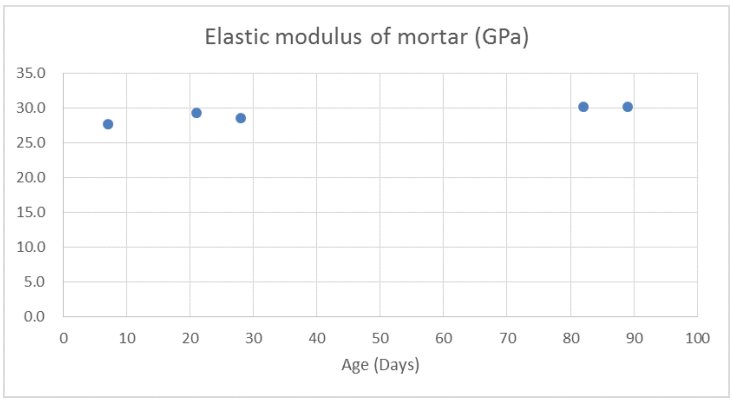

FIGURE 9.16 : Evolution of the Young's modulus of the samples of mortar.

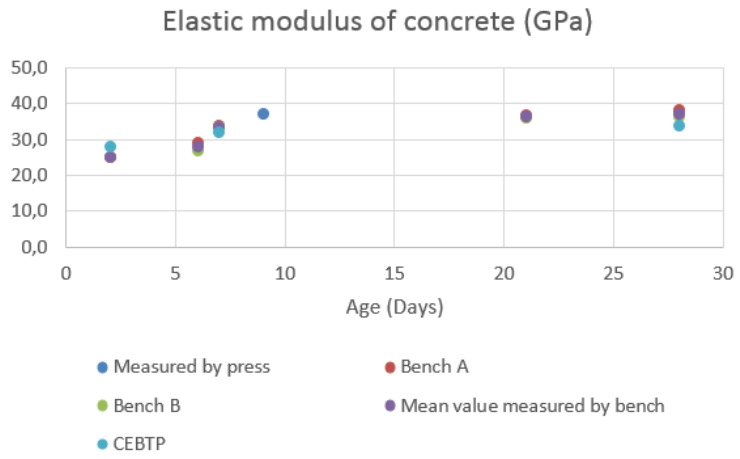

FIGURE 9.17 : Evolution of the Young's modulus of the samples of the VeRCoRs concrete.

9.6 Setting up the specimens on the benches

The specimens of shrinkage and creep started simultaneously were placed on the benches grouped by the age of loading. This allows the specimens, whose results were post-processed together, to have the ambient conditions as close as possible. For example, the subtraction of the autogenous shrinkage from a creep result made it possible to limit the thermal fluctuations when both specimens were subjected to the same temperature evolution (Fig.9.18).

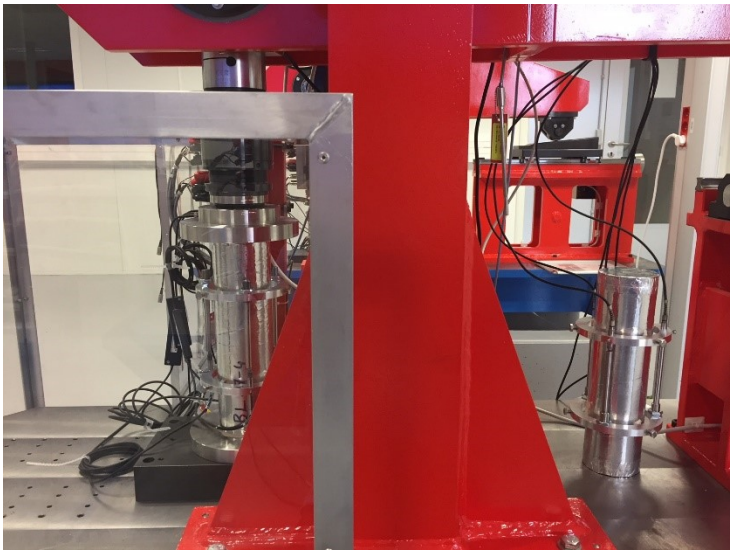

FIGURE 9.18 : Autogenous shrinkage and creep specimens on a big test bench.

9.6.1 Weigh-in

Before any experiment start, the specimen is weighed in a well-defined configuration to make it possible to know the variation of its mass during the experiment.

TABLE 9.16 : weighing for the different experiments.

Experiment	Weighing configuration
NDS	Specimen+SCAPA tapes+X60 glue+rings+big screws+small screws
NDC	Specimen+load plates glued+SCAPA tapes+X60 glue+rings+big screws+small screws

9.6.2 Instrumentation of the specimens

The specimens for the mechanical experiments were instrumented. The installation of the instrumentation supports was described in the previous section, so we focus here on the installation of the sensors to the supports.
The instrumentation of the specimens was carried out by the installation of 3 LVDT type sensors at 120 °, which was facilitated by the prior installation of the instrumentation supports.
The adjustment screws for the sensors and the associated nut (Figure 9.19) were first placed in the 3 big threaded holes. Then, the sensors were put in place and tightened by small screws. Particular attention is paid to screw neither too hard nor too close to the head of sensor, as this causes the internal friction to the sensor and limits its movements, which strongly impacts the displacement measurement.

FIGURE 9.19 : Screw/nut system used to adjust the range of the displacement sensors.

Once the sensors were installed, the adjustment of their range was achieved by measuring either directly transducer's output signal voltage by the multimeter, or the displacement by the acqui-

sition system. In all cases, special care was taken to place the sensor in the center of its range by screwing more or less the thread. When its position was good, it was fixed by tightening the associated nut on the ring with the wrench.
For the shrinkage experiments of which the cables of the sensors extend upward, special care was taken in securing the cables to verify that the overall flexibility of the instrumentation support system was sufficient to avoid the potential cable stresses to influence the measurement performed (Figure 9.20).

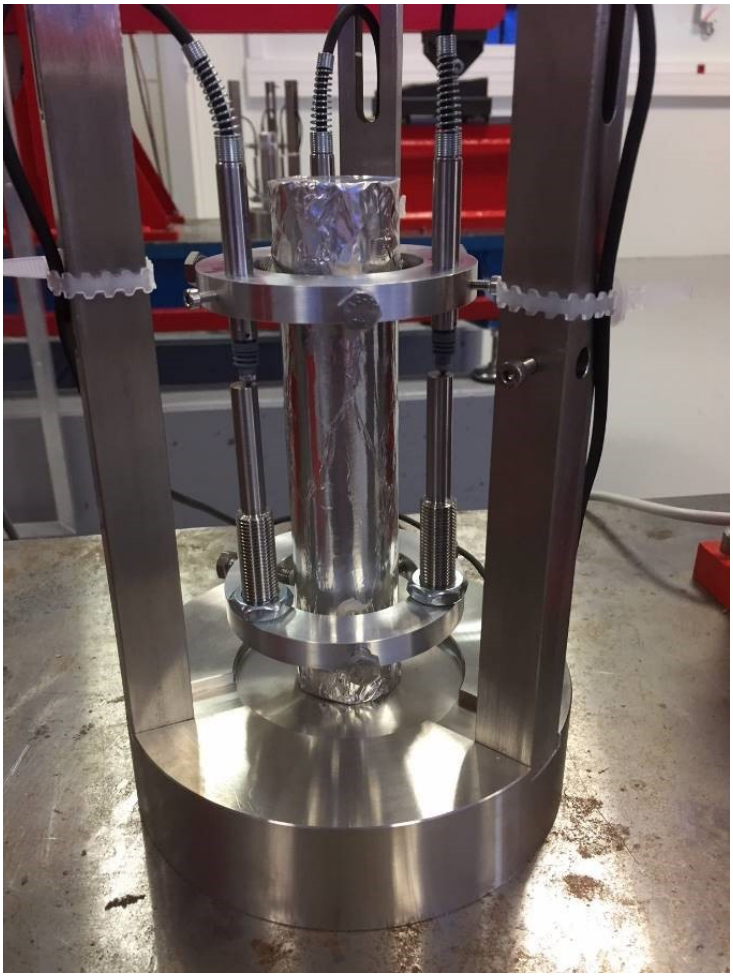

FIGURE 9.20 : Final configuration of a small NDS specimen.

For the creep specimens, the sensor cables were stabilized by the use of the tape or the wire bundle clamps for the same reason.
The references of the LVDT sensors used was noted in the experiment rapport.
The number of each channel is noted on the ring of the support to facilitate the following centering procedure.

9.6.3 Centering of creep specimens

For the creep experiments, a final installation step was carried out : the centering of the specimens. This operation aims to ensure a state of stress as homogeneous as possible on the cylindrical specimens tested.
The centering is achieved by the following steps :

- The specimen is placed geometrically.
- A preload at 50 daN is carried out.
- The displacements of the 3 LVDTs are noted.
- A load at about 1/3 of the final load (typically 500daN was used for a final load of 1200 daN) is applied (using the manual control box "pocket" of the bench).
- The displacements of the 3 LVDTs are noted.
- The relative deviation to the average increment of displacement of the LVDTs between the loads of 50 daN and 500 daN was calculated for each LVDT. When one of the relative deviations was greater than 20%, the sample was unloaded and its positioning was modified (in the difficult cases, the placement of a prop under the load plate is applied), then the procedure was carried out afresh.

This procedure aims to compensate for the geometrical defects (in particular of perpendicularity) of the specimens. Sometimes it is very difficult to lead. Several defects can prevent from carrying it out :

- The lock ring is insufficiently tightened to the specimen.
- One of the LVDTs shows inconsistent results due to the excessive tightening or too close distance between the head of the sensor and the screw of maintenance.
- A flexible material is interposed between the specimen and the load plate.

In addition to an instantaneous gap lower than 20%, it is important that the 3 LVDTs move in the same direction when the load is maintained. Otherwise, this means that the specimen flexes more and more.
Once the procedure of the centering was successful, the load was decreased at the 50daN preload level to maintain the sample while limiting the creep and waiting for the start of the experiment. In the chapters of the analysis of the experimental results that follows, this preload is always considered.

9.6.4 Manual load cycles on creep experiments

Consistent with the practice of measuring the stabilized Young's modulus, two cycles of manual charging until the full load were made just before starting the load from the supervision software.

These are loading-unloading cycles and the order of magnitude of the time that a cycle takes is about 20 seconds.

9.7 Configuration and start of the experiment

The tests were carried out on 6 benches installed in the creep room of the laboratory. The conditions of the temperature and the relative humidity of this room are controlled at 20°C and 50% of the relative humidity.

9.7.1 Case of mechanical tests

The final start of the test required the configuration of the supervision software (which manages the control) and the configuration of the acquisition software.

Configuration of the supervision

For the configuration of the supervision, a preload level equal to the desired load was chosen. A constant force profile at that same load was created and selected. Two benches were grouped by one supervision tab, because of the impossibility for the software to manage six tabs simultaneously.
The configuration design uses PID to control a constant power pulse. One sensor measures voltage and controls those measurements to a power setpoint to carry out the creep experiments. The PID values was entered in the central software platform for each bench, taking into account the type of the material loaded. The values used during the experiments are :

- Cement paste on small bench : 0.90 ; 0 ; 0
- Mortar on small bench : 0,75 ; 0 ; 0
- Cement paste on big bench : 0,50 ; 0 ; 0
- Mortar on big bench : 0,65 ; 0 ; 0
- Concrete on big bench : 0,80 ; 0 ; 0

When the PID values were changed, the central software platform was restarted.
The loaded force for each material and for each age of loading is listed in Table 9.18.

The loading time for each experiment is different and depends on the PID values of the experiment. It is controlled between 10 seconds to 12 seconds.

TABLE 9.17 : Loaded force for each material and age of loading.

Material	Age of loading (days)	Loaded force (N)	Loading stress (MPa)
Cement paste	1	5000	4.91
Cement paste	3	10000	9.82
Cement paste	7	12000	11.79
Cement paste	28	12000	11.79
Cement paste	90	12000	11.79
Mortar	7	12000	11.79
Mortar	28	12000	11.79
Mortar	90	12000	11.79
Mortar	365	12000	11.79
VeRCoRs concrete	2	44000	8.75
VeRCoRs concrete	7	76000	15.12
VeRCoRs concrete	28	76000	15.12
VeRCoRs concrete	90	76000	15.12

Configuration of the acquisition

In the acquisition software, a tab was configured for each group of sensors which was then saved in the same file. The ideal situation would be to have one file per experiment, this option was not possible due to the limit of the maximum number of tabs, which is 10.
For this reason, the shrinkage and creep tests positioned on the same bench were configured in the same tab and thus saved in the same file.
For each channel, a measure scale was configured beforehand, integrating the actual calibration that had been performed on the sensor concerned. A particular point of vigilance was the fact of differentiating LVDTs with the base of 1 mm and those with the base of 0.5 mm.
The file names mentioned the starting date, the name of the experiment, the type of the experiment and the bench concerned.
The acquisition frequency was set at 1 point per second at the start of the experiment.
In addition, the acquisition of the two values of the room temperature in a separate tab was configured.

Beginning of the experiment

Once the supervision and the acquisition software were configured, the following steps were performed :

- The acquisition was started on the tabs concerned by each bench (1 point per second).
- The modes of the control of the benches were passed in the "remote" mode.
- The load cycle was started on the relevant piloting software tabs.

Once the kinetics of creep slowed down, the acquisition went into 1 point per minute, then 1 point per hour, in order to limit the amount of the data acquired.
With regard to the shrinkage experiments, the acquisition was carried out simultaneously and linked to that of the creep experiments, because of the limitation of the number of the tabs which imposed to group in a single tab the shrinkage and the creep experiments started on the same bench.

Ambient measurements

During the experiments between 2017 and 2018, the ambient measurement was limited to two temperature values measured by the PT100 (3 wire) temperature transducers placed respectively next to the row of the small benches and the row of the big benches.

9.7.2 Exceptional events

Pilot loss during the experiment

A frequent event during the creep experiments was the loss of the control of the load. This loss of control was due to different sources :

- Loss of electrical power.
- The voluntary shutdown of the control to isolate a bench during the restart operations of the central software platform or the supervision software.

In these different cases the benches remained in the situation of the relaxion of the load during the absence of control (the control boxes were then in the "local" mode).
To restart the regulation, the control boxes were put back into the "remote" mode and the supervision software was restarted in the same way as it was used for the initial start, even if the actual force seen on the conditioners during the experiment or following the shutdown period differed from the setpoint.

Particular vigilance on the big benches These benches suffered from a design defect that influenced the load when the concrete specimen was under load. When the regulation was no longer active, the force exerted by the concrete specimen on the bench induced a rotation of the worm and a displacement of the plate (in the case where the motor was no longer supplied, the displacement of the plate was much more important). When the regulation was stopped, the plates of these benches were locked with the clamps (Figure 9.21).

Problem with air-conditioning

During the period 2017-2018 the air conditioning system was still quite new, several failures have occurred. During these failures, it seemed that it was only the problem of the humidifier, the system then suffering from the hot air in the test rooms. The temperature then rose to about 33°C during one day.

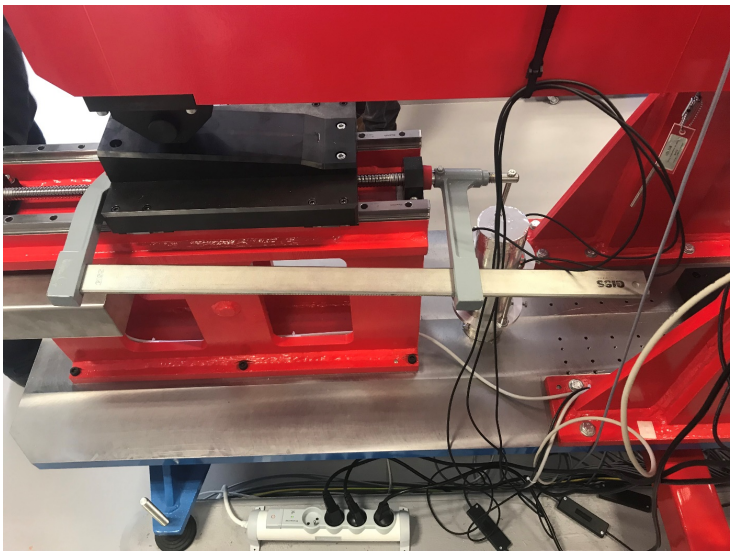

FIGURE 9.21 : Blocking a big bench with a clamp when the power was interrupted.

Software Bugs

Since the software was not designed by our laboratory and the sources of the software were not at all allowed to be modified by us, there were some software bugs. The bugs are listed as follows : The piloting software :

- There was a tab number limit because of the "LabView memory" problem. The piloting software was started with 2 benches in the same tab for each experiments which made it possible to limit the total number of the tabs to 3.
- The setpoint of the force droped to 0 for 2s during the ramp part of the loading phase, so the loaded force droped to 0. This setpoint bug was resolved by changing a new version of the central software platform and therefore no longer occured.

The acquisition software :

- There was the graphical bug on the demonstration of the current curves.

The central software platform :

- The central software platform frequently crashed because of a memory problem. The current procedure to recover this bug was the restart of the central software platform and the 'Piloting-Acquisition' software regularly (every 2 weeks).
- At the beginning of the experiment, there were frequent brownouts between the central software platform and the benches. There was interruption of ethernet link between the piloting software and each arduino card for the bench and and damage of the coax carrying an analog signal between each sensor and the acquisition software. The ethernet link and the coax were arranged at the level of the central software platform. This bug has been

hunted down by the use of a new version of the central software platform, and did not occur anymore.

- The power supply failed one time. The power supply was standard to tower type PCs. The loan of a power supply by the computer correspondent in EDF allowed the computer to reboot normally.

9.7.3 End of the experiment

Recovery

When the loading period was over, the recovery evolution of the strain was measured. The acquisition frequency on the benches to be unloaded was set at 1 point per second, then the benches were switched to the "local" mode and the complete unloading was performed manually. Once the recovery kinetics slowed down, the acquisition frequency was increased to 1 point per minute, then 1 point per hour.

Final weigh-in

The specimen was finally weighed in a configuration identical to that described in 9.6.1 according to the test considered, which made it possible to quantify the parasitic mass loss that has occurred on the non-drying specimens.

TABLE 9.18 : Mass evolution for each material and age of loading.

Material	Age of loading (days)	Sample 1 Mass loss (g)	Sample 1 Mass loss (%)	Sample 2 Mass loss (g)	Sample 2 Mass loss (%)
Cement paste	1	0.01	0.001	0.05	0.003
Cement paste	3	0.00	0.000	0.09	0.005
Cement paste	7	0.06	0.003	0.07	0.004
Cement paste	28	0.15	0.008	0.17	0.010
Cement paste	90	0.23	0.012	0.14	0.007
Mortar	7	0.04	0.002	0.12	0.007
Mortar	28	0.05	0.003	0.10	0.006
Mortar	90	0.11	0.007	0.10	0.006
VeRCoRs concrete	2	0.20	0.002	0.30	0.003
VeRCoRs concrete	7	3.30	0.030	0.00	0.000
VeRCoRs concrete	28	0.30	0.003	0.20	0.002

The maximum relative mass loss is 0.03% of the total sample mass, which indicates the effectiveness of the sealing in the experiments.

9.7.4 Exploitation of the results

Conversion

The raw files produced by the acquisition software were in the TDMS format and were converted to the text format by the conversion software. In case of bug, they were read by the Python module npTDMS.

Separation of the experiments and concatenation

A script for the post-processing of the raw files produced by the conversion software has been developed and was capitalized.

Capitalization and exploitation

The files processed by the previous script were capitalized in the CADEEX platform in $EDF\ R\&D$, where a processing script specific for the creep behavior was developed.

Chapitre 10

Experimental results

This chapter displays the raw experimental results obtained directly from the LVDT displacement sensors, the temperature sensors and the force sensors. Then the additional post-processing is required for the calculation of the equivalent time, the strain of all the types of the experiments, the stress and the evolution of the basic creep compliance.

Sommaire

10.1 Raw experimental results

10.1.1 Temperature

The temperature evolution in the lab is controlled around 20°C. But with the continuous monitoring with the sample temperature, done during the measurements in order to take into account the effect of temperature on the hydration process, several abrupt temperature changes caused by the air conditioner problems were registered (e.g. :Fig.10.1).

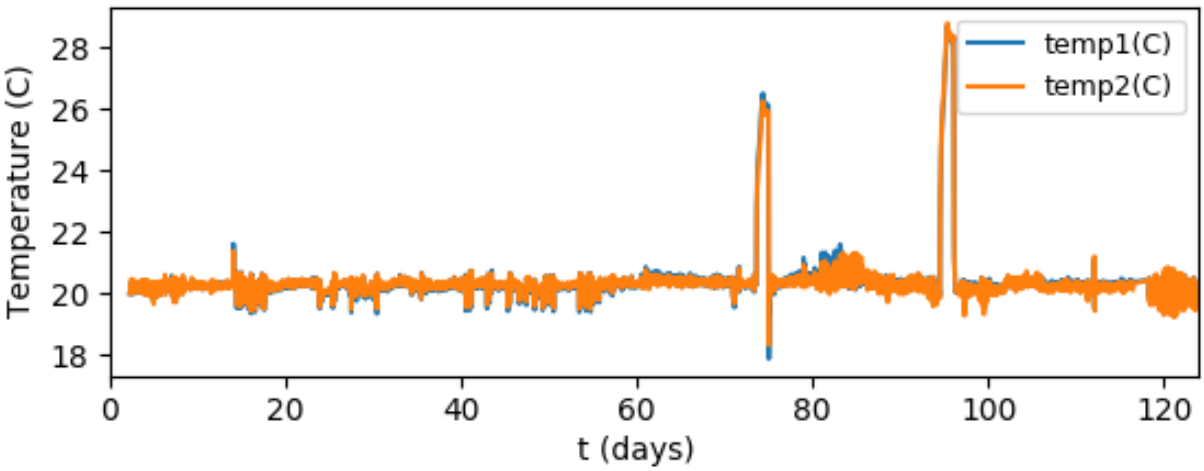

FIGURE 10.1 : Example : temperature evolution of the environment of the creep experiment (the VeRCoRs concrete with the age of loading = 90 days).

10.1.2 Displacement

The 3 LVDTs measured the longitudinal displacement evolution of the specimens during the whole period of each experiment. So the displacement evolution of the specimen at each scale (from cement paste to mortar, then to the VeRCoRs concrete) and at each age of loading (1 day, 2 days, 3 days, 7 days, 28 days, 90 days and 365 days) was saved as the raw experimental result.

An example of the evolution of longitudinal displacement is presented in Fig.10.2. The displacement is separated in the under load period and the unload period. The three curves in each figure describe the evolution of displacement of the three LVDT displacement sensors for each specimen.

10.2 Post-processed experimental results

10.2.1 Equivalent time

As written in the previous section, several abrupt temperature changes caused by the air conditioner problems were registered. For example, in Fig.10.3, there is a fluctuation of the temperature

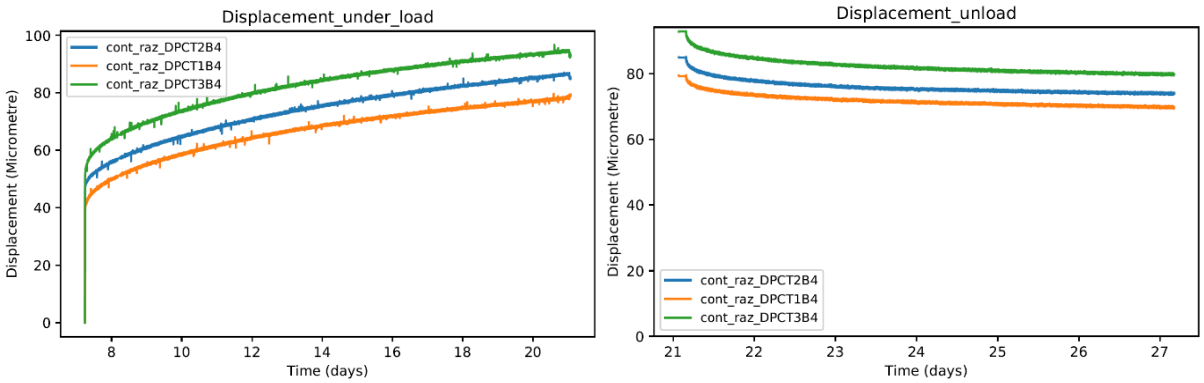

FIGURE 10.2 : Example : longitudinal displacement evolution of the specimen (Left : under load period, Right : unload period, mortar with the age of loading = 7 days).

from 20°C to 28°C at $t = 95$ days. An equivalent time is thus necessary and feasible to be computed with the Eq.10.1 proposed by Freiesleben Hansen and Pedersen [54].

$$t_{eq}(t,T) = \sum_{i=0}^{t} exp(\frac{-U}{R}(\frac{1}{273+T(i)} - \frac{1}{273+T_{ref}}))\Delta t \tag{10.1}$$

Where :

- T is the temperature, in °C,
- T_{ref} is the reference temperature, generally 20°C,
- R is the universal gas constant, 8.314J/mol/K,
- U is the apparent activation energy, in J/mol.

Equation 10.1 defines the equivalent time which is based on the Arrhenius equation. This equation shows the accelerating effect of a given temperature history T in comparison with a reference temperature T_{ref} (when $T > T_{ref}$). The apparent activation energy E_a is determined from the post-processing of the experimental data with the nonlinear optimization of the compliance model for basic creep described in this section. The equivalent time is sequensely calculated with the fixed activation energy. So the ageing viscoelastic behavior in the real experiment ambient as a function of the equivalent time is the same as the theoretical ageing viscoelastic behavior as a function of the reference temperature, 20°C in the case of this thesis. An example of the comparison of the evolution of the temperature as a function of the real time and as a function of the reference temperature is in Fig.10.3.

Once the equivalent time is calculated, all the post-processed data results are results as a function of the equivalent time, not as a function of the real time.

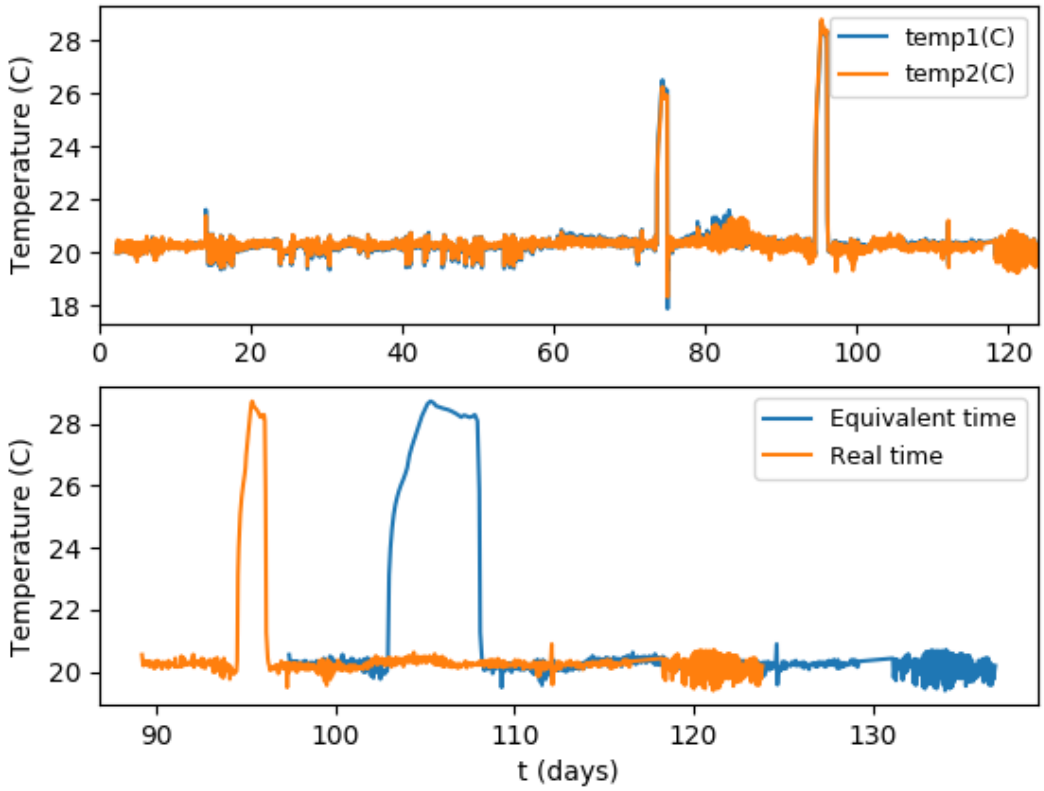

FIGURE 10.3 : Example : comparison of the evolution of the temperature as a function of the real time and as a function of the reference temperature (the VeRCoRs concrete with the age of loading = 90 days).

10.2.2 Strain

The values of the axial measurement base is decided by the distance between the two rings of the metal instrumentaion for each specimen. As a result, the values of the axial measurement base are : $0.108m = 1.08 \times 10^5 \mu m$ for the small test specimens for cement paste and mortar, and $0.130m = 1.30 \times 10^5 \mu m$ for the big test specimens for the VeRCoRs concrete. At first, the average longitudinal displacement of each specimen was calculated. The average displacement was then divided by the measurement base to calculate the strain evolution for the creep experiments and the shrinkage experiments (Eq.10.2) :

$$\epsilon = \frac{\Delta L_i}{L_i} \tag{10.2}$$

Here :

- ΔL is the evolution of the average longitudinal displacement of the specimen i,
- L_i is the axial measurement base of the specimen i.

Examples of the evolution of the shrinkage strain and the creep strain is presented in Fig.10.4.

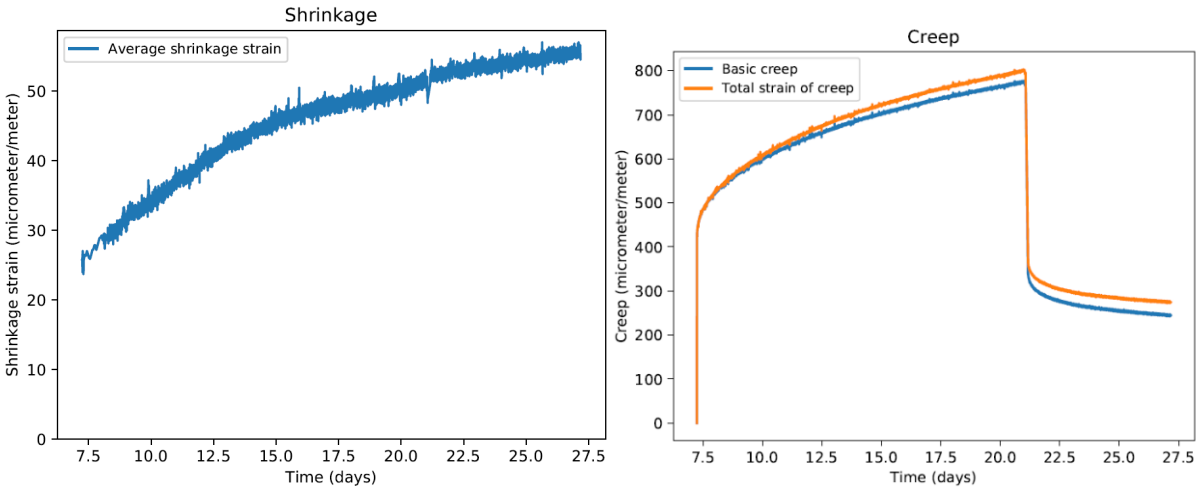

FIGURE 10.4 : Example : strain evolution of the specimen (Left : the shrinkage strain, Right : the total strain of the creep and the basic creep, mortar with the age of loading = 7 days).

Here, the time-dependent deformations of cementitious materials at constant temperature was subdivided into a load independent part, called shrinkage, and a load dependent part, called basic creep. The autogenous shrinkage strains have been subtracted from the total strain of the creep to calculate the basic creep of each specimen. The application of the experimental results is restricted to ageing basic creep of cement paste, mortar and the VeRCoRs concrete due to hydration, as ageing basic creep is an important feature of concrete behavior [166].

10.2.3 Compliance

The creep compliance here is the basic creep strain per unit of stress ($10^{-6}/MPa$)[157]. In the post-processing procedure, the basic creep values were divided by the constant stress of the load for each experiment to calculate the compliance evolution of cement paste, mortar and the VeRCoRs concrete.

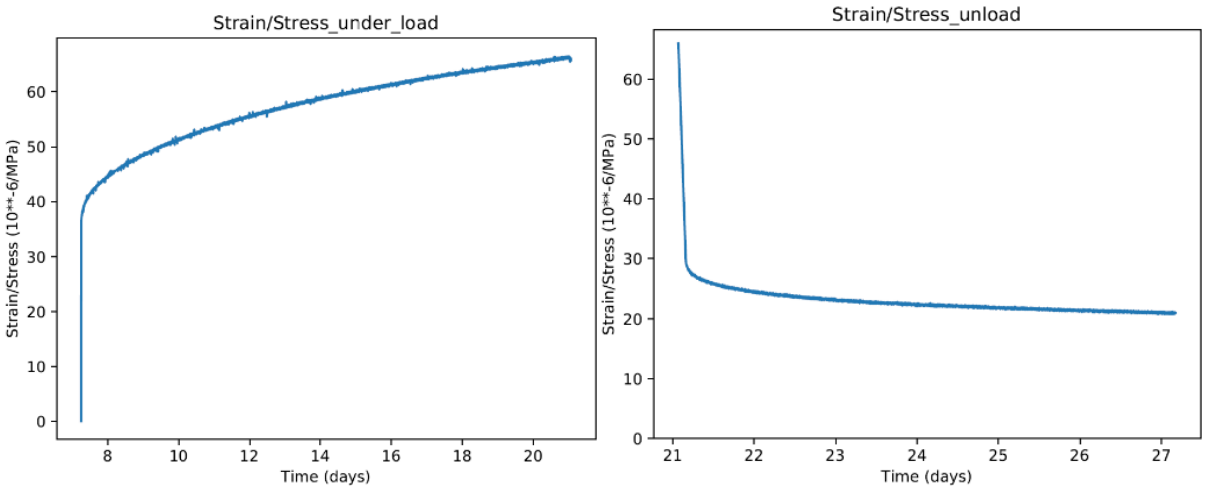

FIGURE 10.5 : Example : strain/stress evolution of the specimen (Left : under load period, Right : recovery period, mortar with the age of loading = 7 days).

In addition, the equivalent time corrects the accelerating effect of a period of the evident temperature rise. For example, in Fig.10.6.

As presented in the Fig.10.6, before the correction of time, there is a abrupt acceleration of the evolution of strain/stress during the period of the evident temperature rise, which is incoherent with the ageing viscoelastic behavior in a stable ambient, but the reconstruction of the evolution in the equivalent time dimension tends to correct this incoherence.

With this principle to post-process the raw experimental results from the longitudinal displacement data of each LVDT sensor, the evolution of the strain of basic creep and the compliance of basic creep at each scale (from cement paste to mortar, then to the VeRCoRs concrete) and at each age of loading (1 day, 2 days, 3 days, 7 days, 28 days and 90 days) was calculated and assembled in the same figure (Fig.10.7). To zoom in the viscoelastic behavior at early age on one hand and the long term ageing behavior with the more evident general perspective, the evolution of compliance could be featured in making the x-axis on a logarithmic scale.

The experimental evolution of the compliance of basic creep strain is presented in Fig.10.7 (autogenous strains have been subtracted). During the experiments, for each sample loaded, a complete unloading is performed to highlight the effect of creep recovery, which will be presented in the following chapter. As expected, from the scale of cement paste to that of mortar, then to that of concrete, the compliance of basic creep is lower and lower. Moreover, the basic creep strain

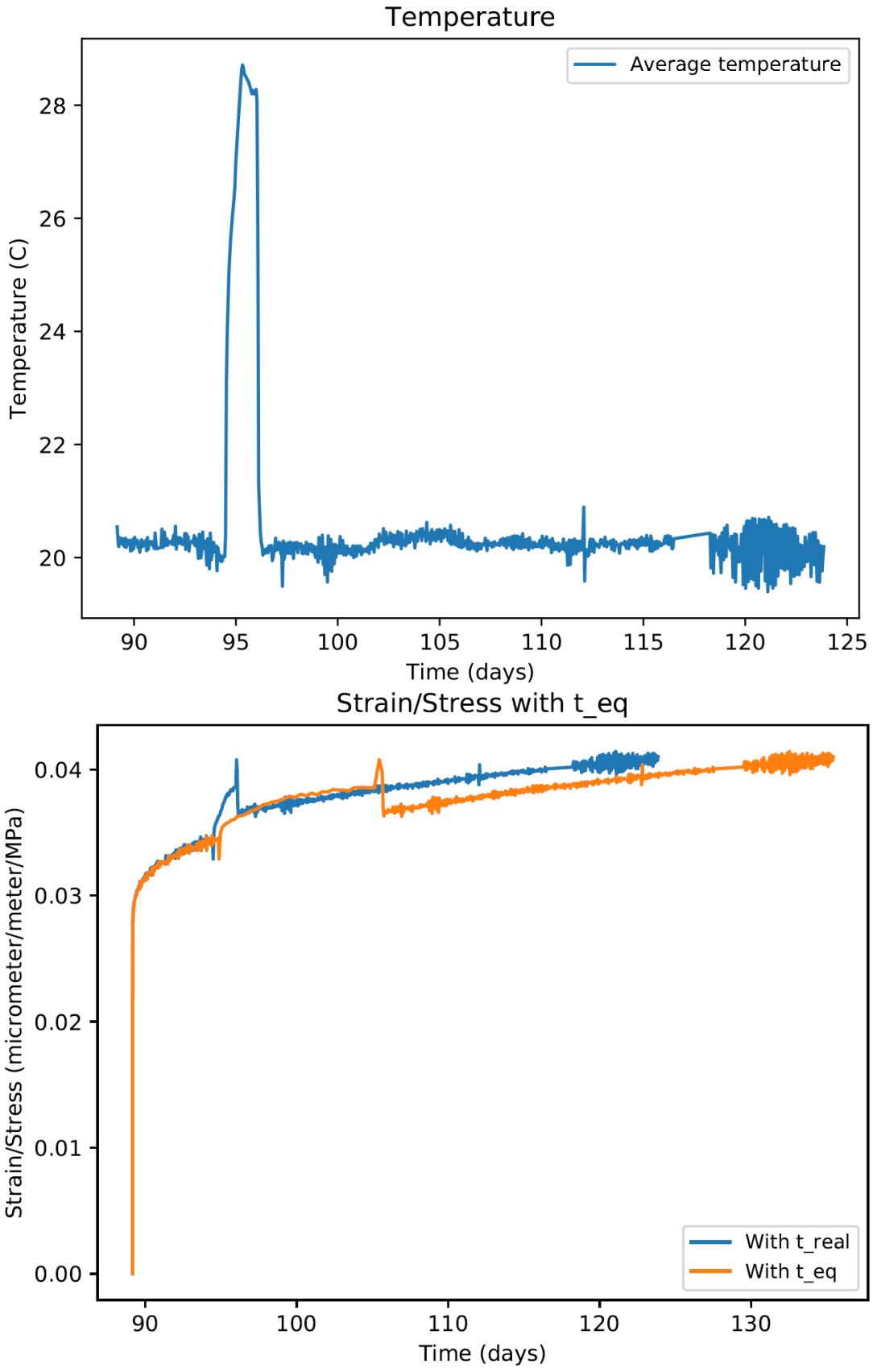

FIGURE 10.6 : Example : Comparison of the strain/stress evolution with and without the correction of time, the VeRCoRs concrete with the age of loading = 90 days).

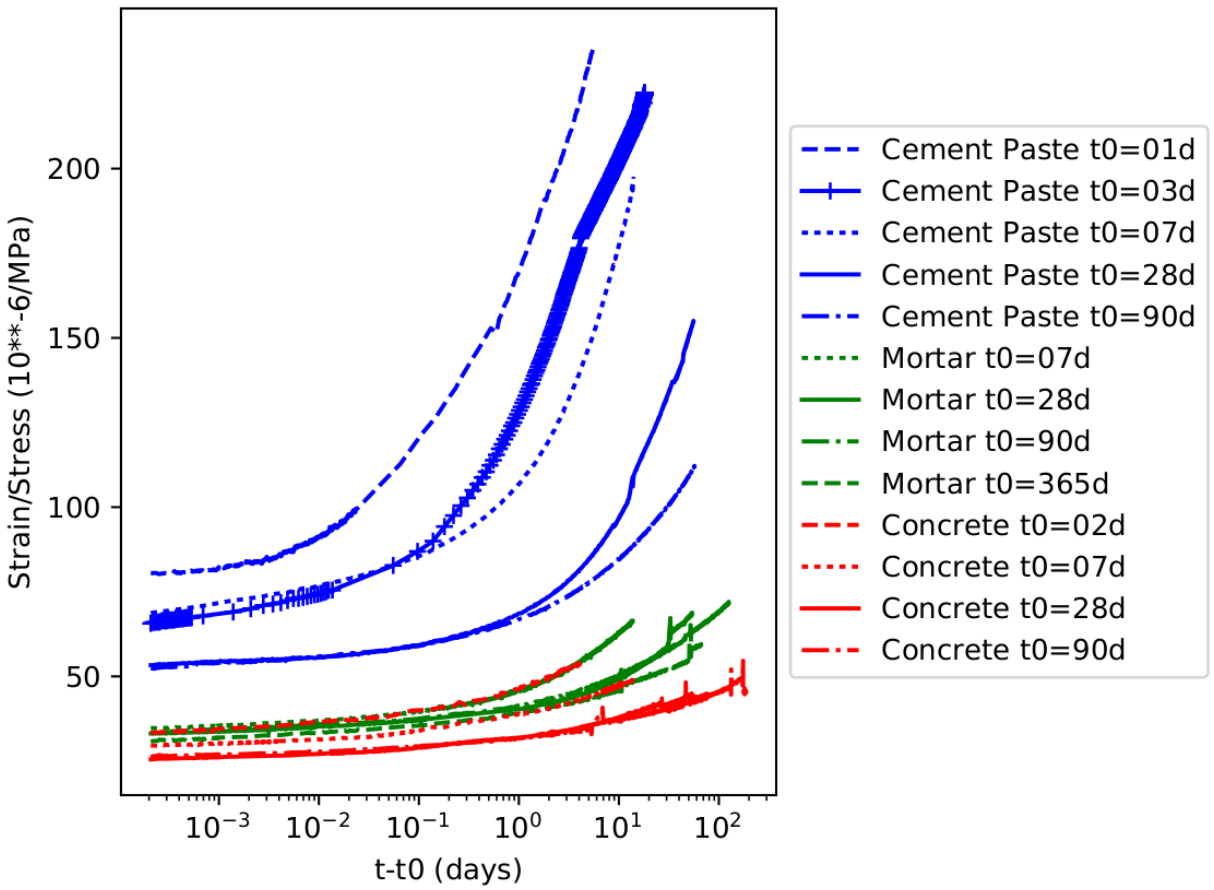

FIGURE 10.7 : Compliance evolution : loading age effect (t0 = age at the end of loading ramp).

rate decreases with the increase of the age of loading (which corresponds to an increase of the hydration degree). As demonstrated in the Fig.10.7, the long term ageing viscoelastic behavior of the cementitious materials at each scale is evident and could be applied to identify the parameters of the ageing viscoelastic models. The curves are then used to compare with the modelling behavior results.

Troisième partie

Expoitation of experimental data, comparisons between cement paste model and basic creep experimental results, and improvement of hydration model

Chapitre 11

Identification of parameters for the ageing viscoelastic behaviour model and Upscaling using homogenization

Identification of the parameters for the ageing viscoelastic model based on the experimental results are carried out and the validation of the model shows the coherence between the modeling results and the experimental results.
With the parameters identified from the experiments, micromechanical model can be developed to perform the multi-scale homogenization model of the VeRCoRs concrete.

Sommaire

11.1 Compliance model based on a logarithmic function of time

11.1.1 Identification of parameters

From a theoretical point of view, in the light of recent developments, the compliance data can be fitted using a creep law reworked by [113] based on ideas arising from an analysis of experimental tests. Indeed, [113] shows that the derivative of the compliance dJ/dt tends to $1/(Ct)$ when t was large. Based on the compliance data from the experiments on VeRCoRs materials, the value of C for a given material depends on the age of loading t_0. The compliance model for basic creep is thus the Eq.11.1 :

$$J(t,t_0) = \frac{1}{E(t_0)} + \frac{1}{C(t_0)} Log(1 + \frac{t-t_0}{\tau(t_0)}) \tag{11.1}$$

Where :

- $E(t_0)$ is the Young's modulus at the age of loading, in GPa,
- $C(t_0)$ is a variable depending on mix design and the age of loading, describing the long term creep, in GPa,
- $\tau(t_0)$ is a kinetic constant depending on the age of loading, in day.

The Eq.11.1 describes only the strain after the loading period (about 20 seconds). To consider the loading period, the Eq.11.1 is improved to the Eq.11.2 (the strain obtained under a constant stress load ramp) with the application of the Laplace-Carson transform :

$$\begin{aligned} J(t,t_0) = & \\ & (\frac{t_{load} - (t-t_0)}{E(t_0)t_{load}} - \frac{\frac{(t-t_0+\tau(t_0))ln(\frac{t-t_0+\tau(t_0)}{\tau(t_0)})}{C(t_0)t_{load}} + \frac{t_{load}-t}{C(t_0)t_{load}}}{ln(10)}) Heaviside(t-t_{load}) \\ & + \frac{t}{t_{load}} + \frac{\frac{(t+\tau(t_0))ln(\frac{t+\tau(t_0)}{\tau(t_0)})}{C(t_0)t_{load}} - \frac{t}{C(t_0)t_{load}}}{ln(10)} \end{aligned} \tag{11.2}$$

Where t_{load} is the loading period in day.
With the nonlinear optimization of the Eq.10.1 and the Eq.11.2, the value of $E(t_0)$, $C(t_0)$, $\tau(t_0)$ and $U(t0)$ can be identified for each experiment with a certain age of loading and a certain material.
There are 4 steps to finish the processes of the identification of parameters.

1. Firstly, the experimental results of compliance J_{ex} is obtained. The Eq.10.1 and the Eq.11.2 are applied, the sum $\sum_t (J_{ex}(t) - J(t,t_0))^2$ (the cost function) is then calculated. Afterwards the method of least squares is applied by the nonlinear optimization to calculate the correct apparent activation energy $U(t_0)$ considering the effect of temperature on the hydration process, with which the equivalent time $t_{eq}(t_0)$ can be calculated for each experiment. The

flowchart of the Nonlinear Least Squares Optimization of $U(t_0)$ is precised in Fig.11.1.

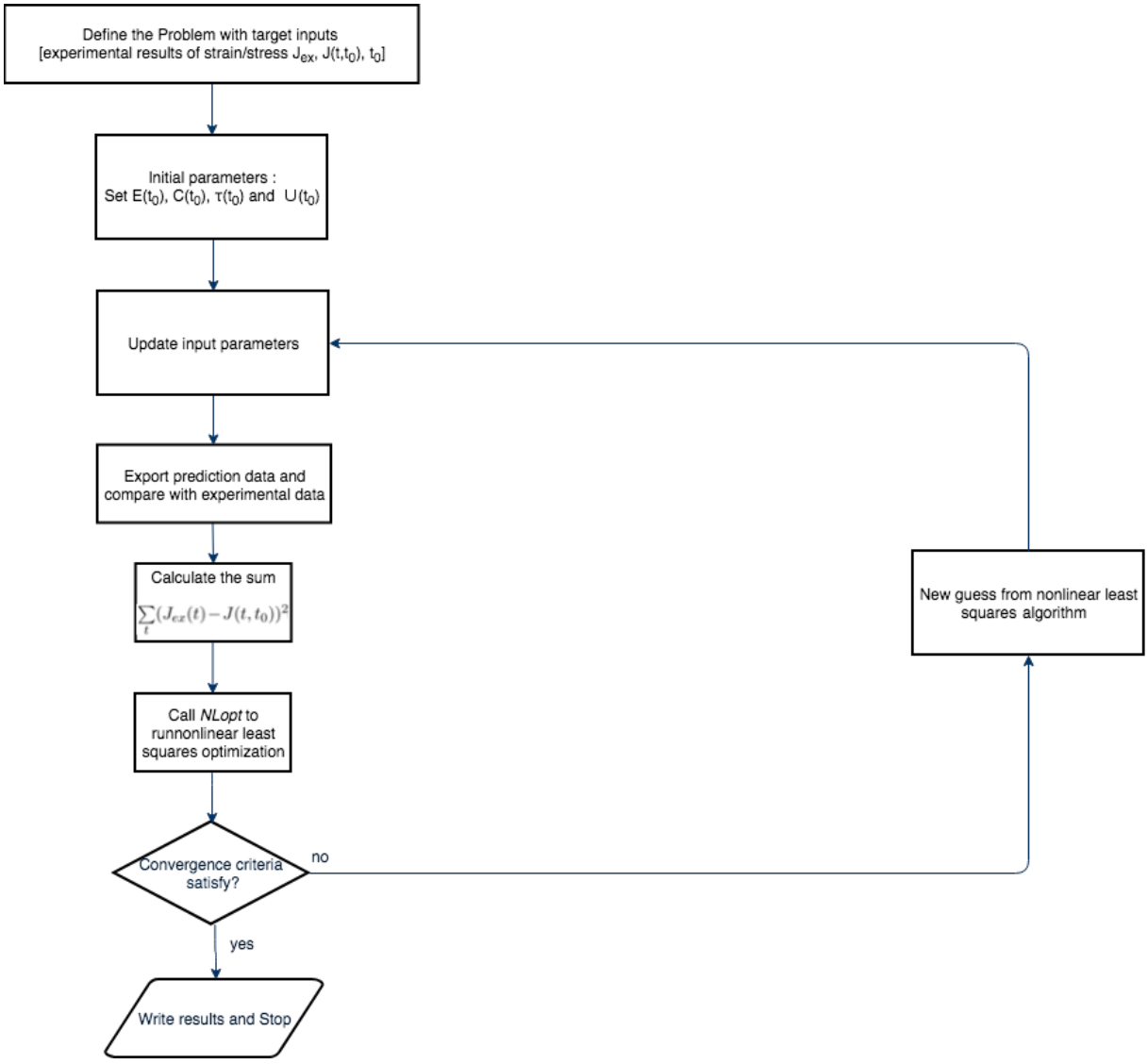

FIGURE 11.1 : Flowchart of the Nonlinear Least Squares Optimization.

2. Secondly, the strain/stress evolution during the loading period (about 20 seconds) in the equivalent time t_{eq} passes to the nonlinear optimization with the Eq.11.2 to define the correct Young's modulus at the age of loading $E(t_0)$. Here, the cost function is always the sum of $\sum_t (J_{ex}(t) - J(t,t_0))^2$ but the parameter t is only the loading period (about 20 seconds).

3. Thirdly, with the correct $E(t_0)$, a least squares polynomial fit process is performed with the compliance results after the ramp with the same principe of Fig.11.1. The derivative of the compliance dJ/dt tends to $1/(C(t_0)t)$ when t is large, which aides to calculate $C(t_0)$.

4. Fourthly, the correct $E(t_0)$ and the least squares polynomial fit line aide to calculate $\tau(t_0)$.

With this method, the analytical solution of the compliance for each material and each time of loading is calculated with the form of the Eq.11.2. An example is presented in the Figure 11.3 : $E(t_0)$, $C(t_0)$, $\tau(t_0)$, $U(t_0)$ and $t_{eq}(t_0)$ for each age of loading can be calculated with this method.

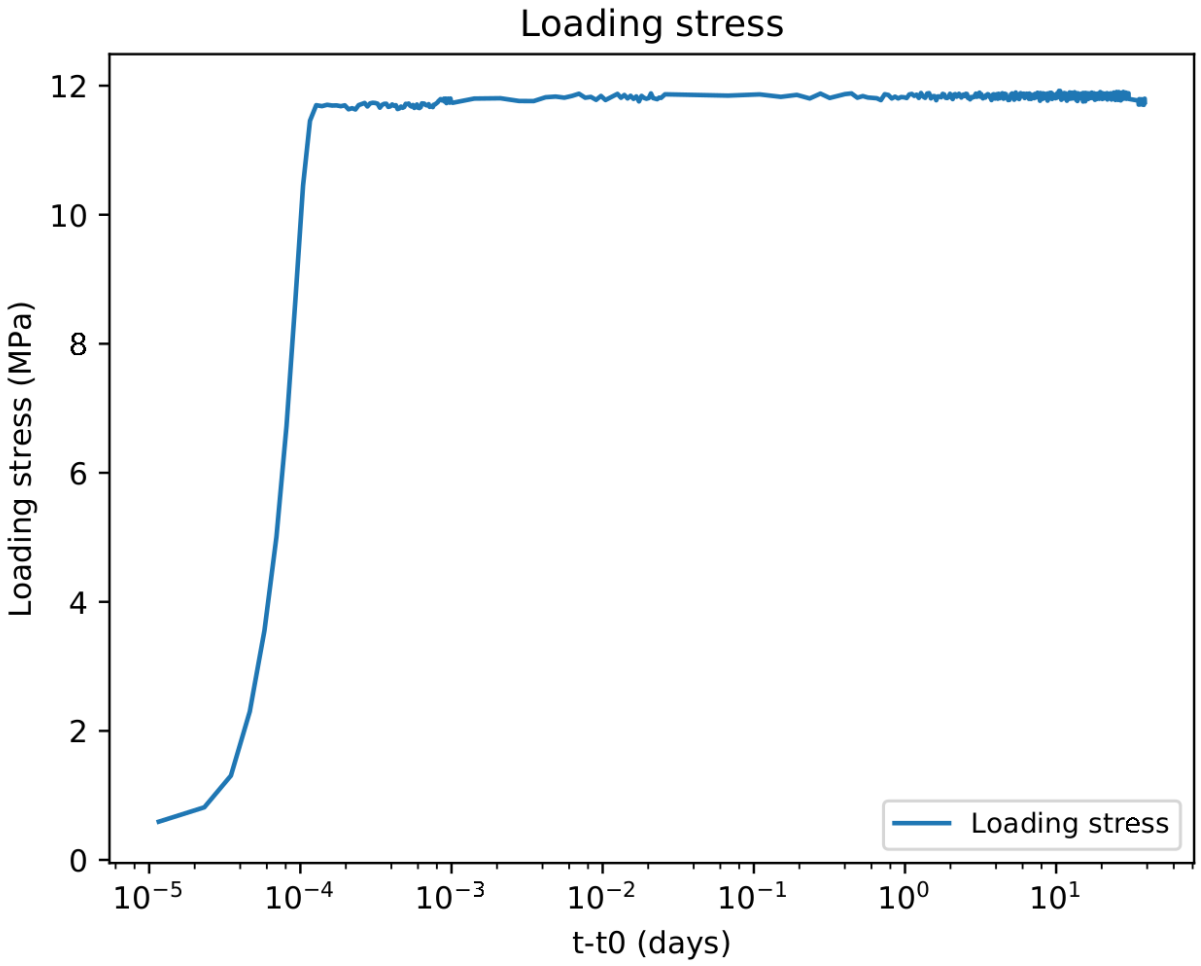

FIGURE 11.2 : Evolution of loading stress.

Nevertheless, $E(t_0)$, $C(t_0)$ and $\tau(t_0)$ can be described as three function types :

$$f(t_0) = A + B(1 - e^{\frac{-t_0}{D}}) \tag{11.3}$$

$$f(t_0) = A + Bt_0 + Dt_0^2 \tag{11.4}$$

$$f(t_0) = (A - D)/[1 + (t_0/G)^B] + D \tag{11.5}$$

The method of nonlinear optimization is also applied with the Eq.11.3, Eq.11.4 and Eq.11.5 to calculate the proper parameters A, B, D and G for $E(t_0)$, $C(t_0)$ and $\tau(t_0)$.
Here, the parameters A, B, D and G are optimized to each function for $E(t_0)$, $C(t_0)$ and $\tau(t_0)$ with the obtained experimental data for $t_0 = 1, \quad 2, \quad 3, \quad 7, \quad 28, \quad 90$ days. Then with the

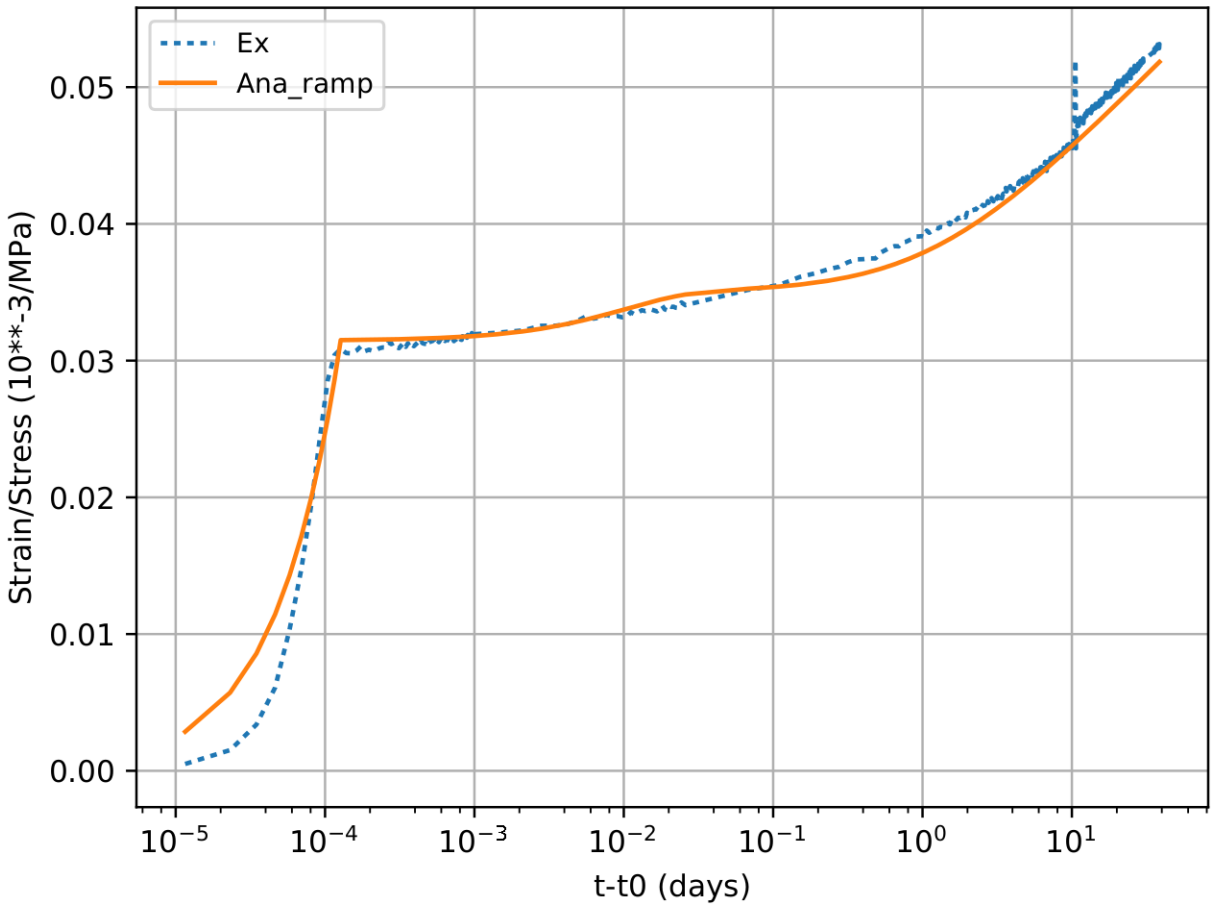

FIGURE 11.3 : Response of a stress ramp followed by a constraint stress load : experimental result (dotted line) and analytical result (continuous line).

deducted function $E(t_0)$, $C(t_0)$, and $\tau(t_0)$ for $t_0 = 1, \quad 2, \quad 3, \quad 7, \quad 28, \quad 90$ days, the values of $E(t_0)$, $C(t_0)$ and $\tau(t_0)$ with other age of loading t_0 could be calculated. Fig.11.4, Fig.11.5 and Fig.11.6 show the evolution of $E(t_0)$, $C(t_0)$ and $\tau(t_0)$ as functions of t_0. In this figures, the axe X is the axe for the time t_0, and the axe Y is the axe for $E(t_0)$, $C(t_0)$ and $\tau(t_0)$. The average experimental results of two benches are marked as circles in the figures and the function results are the curves in the figures.

In addition, even the function values of $E(t_0)$ and $\tau(t_0)$ are close to the identified experimental

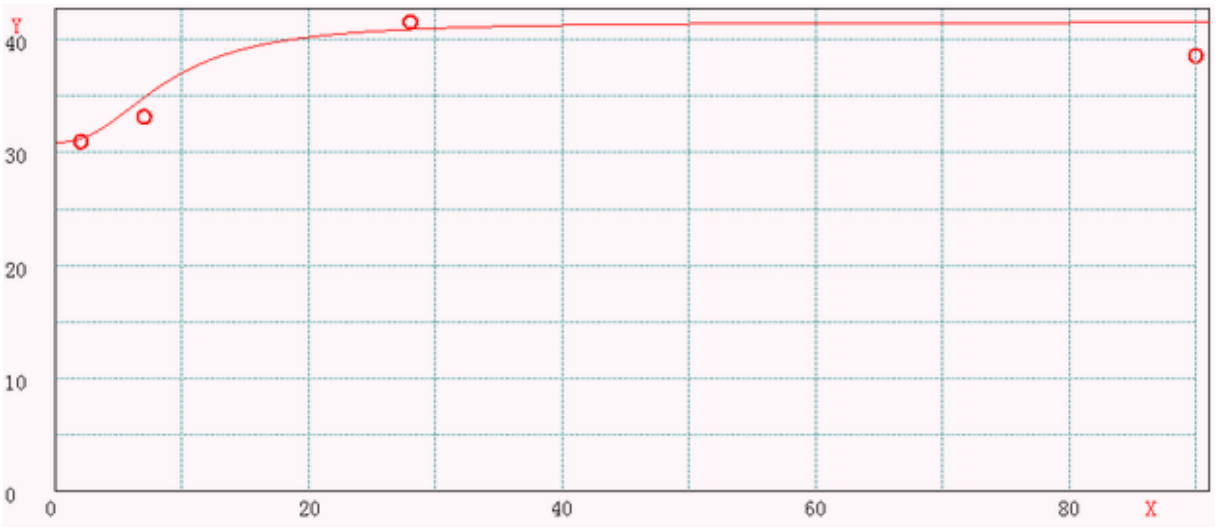

FIGURE 11.4 : Example : evolution of $E(t_0)$ as functions of t_0, scale of VeRCoRs concrete.

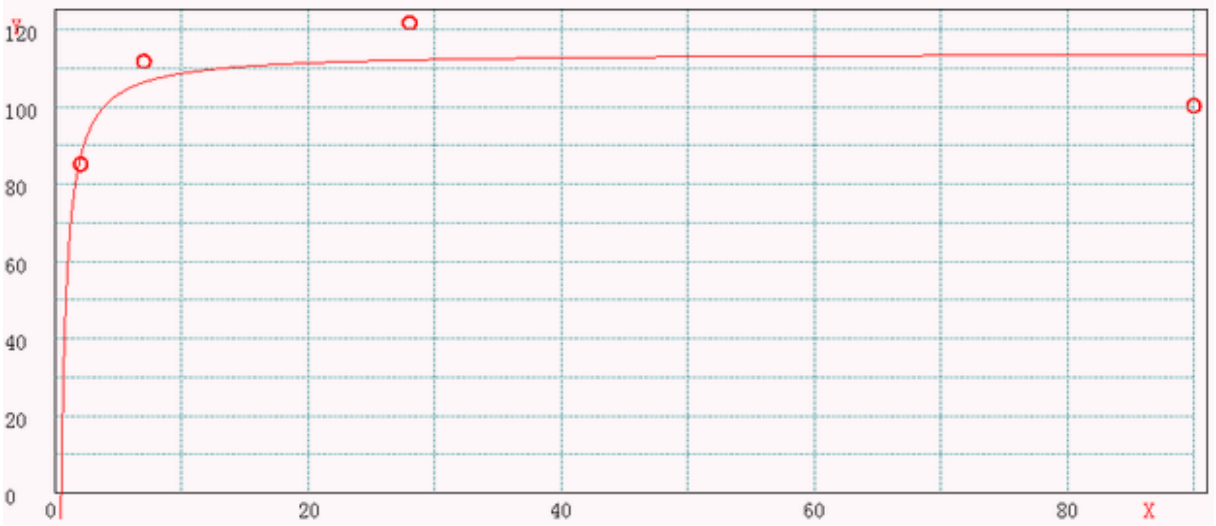

FIGURE 11.5 : Example : evolution of $C(t_0)$ as functions of t_0, scale of VeRCoRs concrete.

values, there are still identified experimental values far from the function values for $C(t_0)$, for example, $C(t_0 = 90 \quad days)$ is far from the identified experimental value C at the age of loading for 90 days. In this situation, the interpolation and the extrapolation are carried out to propose

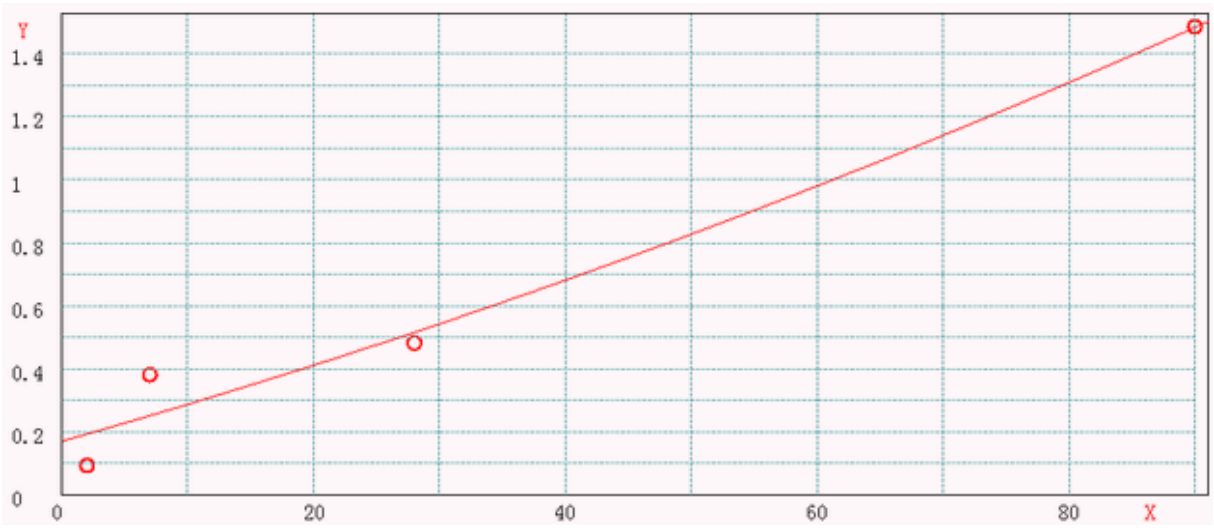

FIGURE 11.6 : Example : evolution of $\tau(t_0)$ as functions of t_0, scale of VeRCoRs concrete.

another method to obtain the values of $E(t_0)$, $C(t_0)$ and $\tau(t_0)$ with other age of loading t_0. At first, the varification of the ageing viscoelastic model with the parameters $E(t_0)$, $C(t_0)$ and $\tau(t_0)$ identified is carried out at the scale of cement paste, of mortar and of the VeRCoRs concrete. The model is applied to recalculate the evolution of the basic creep compliance and to compare the modeling results with the experimental results, the results at the scale of the VeRCoRs concrete are shown in Fig.11.7, Fig.11.8 and Fig.11.9 with different ages of loading for example.

According to Fig.11.7, Fig.11.8 and Fig.11.9, the continuous lines are close to the dotted lines.

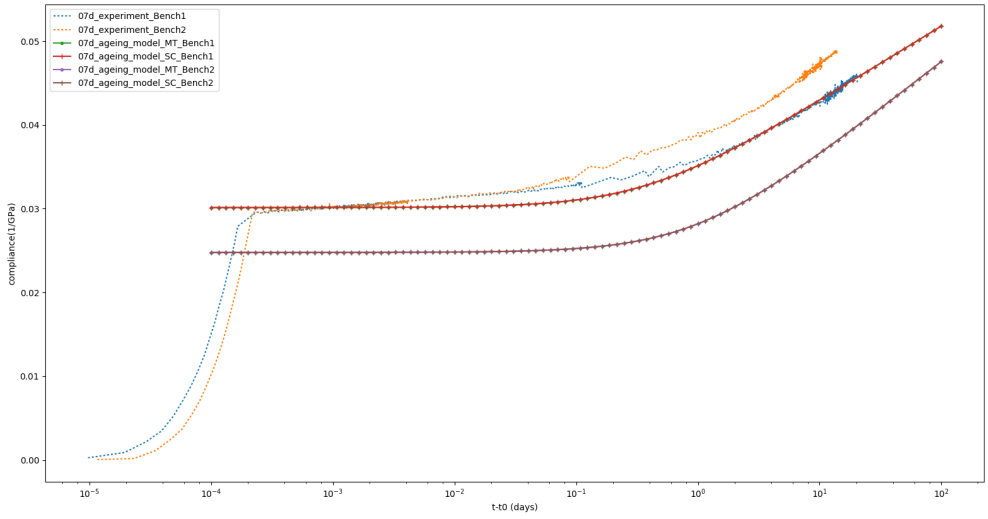

FIGURE 11.7 : Example : evolution of the basic creep compliance and comparison of the modeling results with the experimental results, scale of VeRCoRs concrete, $t_0 = 7$ days.

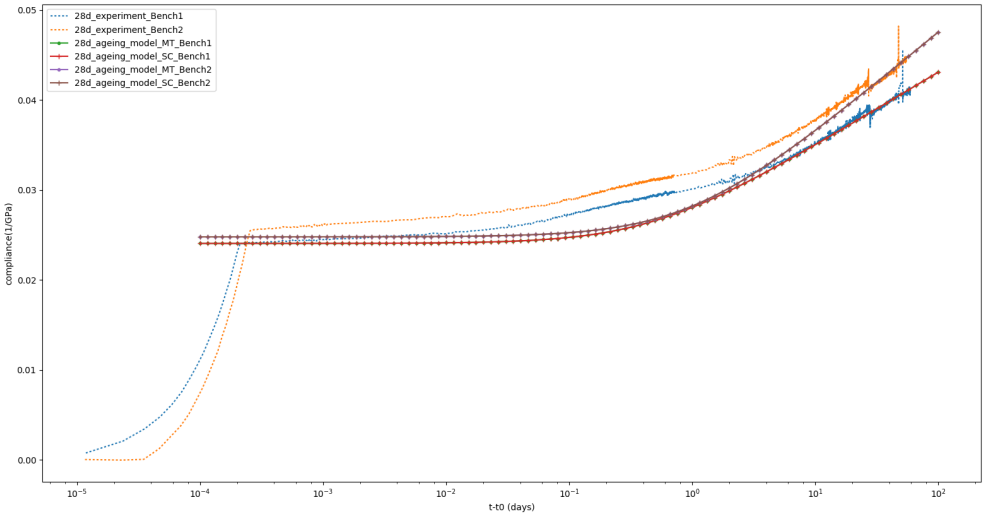

FIGURE 11.8 : Example : evolution of the basic creep compliance and comparison of the modeling results with the experimental results, scale of VeRCoRs concrete, $t_0 = 28$ days.

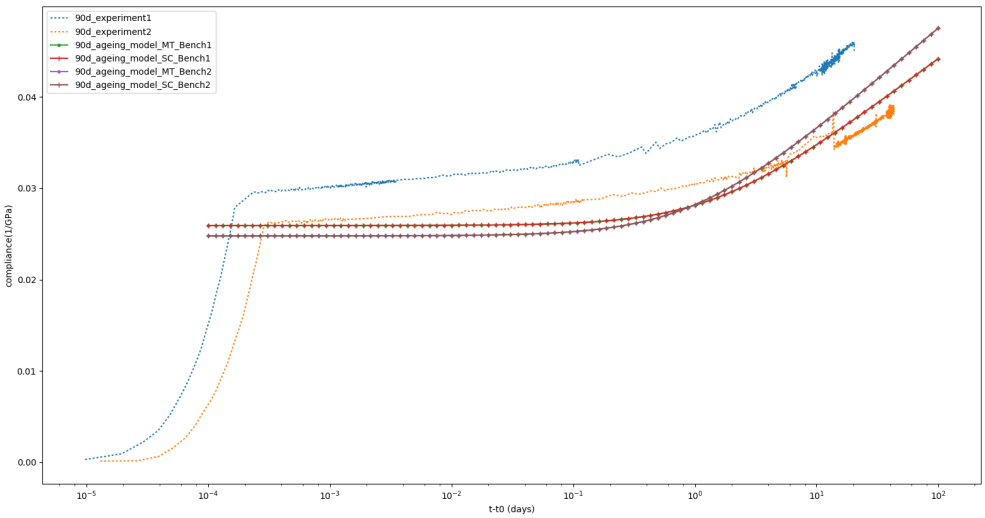

FIGURE 11.9 : Example : evolution of the basic creep compliance and comparison of the modeling results with the experimental results, scale of VeRCoRs concrete, $t_0 = 90$ days.

So the modeling results are close to the experimental results, which justify the applicability of the model. However, it is also evident that the divergence of the modeling results between the Bench 1 and the Bench 2 for the age of loading $t_0 = 7$ days should not be neglected. The study of the parameters of $E(t_0)$, $C(t_0)$ and $\tau(t_0)$ for this 2 benches are carried out and it proves that there is more oscillation on the parameter $E(t_0 = 7\ days)$ identified in Bench 2 at the scale of the VeRCoRs concrete.
Moreover, the figures show that the modeled compliance function underestimate the compliance value in the range of $10^{-2} - 10^{0}$ days, which is a default of the identification procedure. There could have been a larger given weight to the short-term fitting part in the cost function.

11.1.2 Upscaling using homogenization

This part proposes a semi-analytical approach to estimate the effective ageing viscoelastic behaviour characterized by the compliance tensors as functions of two time variables (t, t_0)[161]. The spherical and deviatoric behaviours of cementitious material are represented by the creep compliance models based on the creep experiments with the constant Poisson's ratio given by the code $Vi(CA)_2T$ in EDF.
The Mori–Tanaka and self-consistent homogenization schemes is then applied to upscale the ageing viscoelastic behaviour from the scale of cement paste to the scale of mortar (with cement paste as the ageing viscoelastic matrix and sand as the inclusion), and from the scale of mortar to the scale of concrete (with mortar as the ageing viscoelastic matrix and coarse aggregate as the inclusion). The mechanical properties of sand and aggregate are supposed to be elastic. In the VeRCoRs concrete, the mechanical properties of sand and coarse aggregate are listed in Table 11.1. The data for the Young's Modulus E at the scale of cement paste is identified by the experimental results as shown in the previous subsection.

TABLE 11.1 : Constant mechanical properties of materials at different scales for the VeRCoRs concrete.

	Sand	Coarse aggregate	Cement paste	Mortar
Young's Modulus (GPa)	72	62		
Poisson's ratio	0.27	0.27	0.23	0.24

The effective ageing uniaxial compliance function is plotted in Fig.11.10 as continuous lines with the method mentioned in [166].
The comparison results demonstrate that the ageing compliance model is not perfectly adapted to the experimental results. This logarithmic creep compliance model underestimate the creep compliance in the short term and overestimate the creep compliance in the long term.

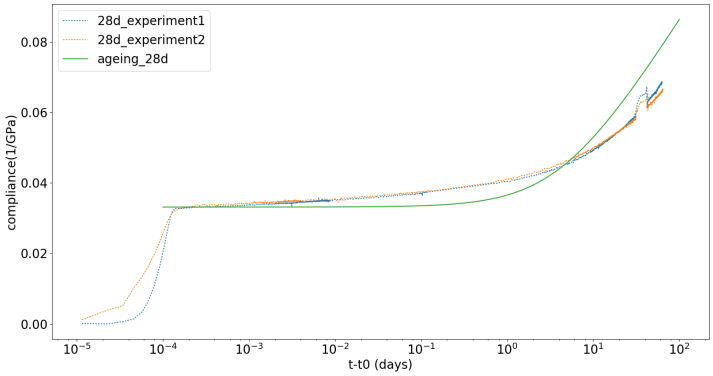

FIGURE 11.10 : Example : Effective uniaxial compliance [157] functions of mortar ($w/c = 0.525$), plotted for age of loading t_0 =28 days. Comparison between the experimental results on mortar (2 dotted lines) and the upscaling using the Mori–Tanaka homogenization scheme (green continuous line based on the parameters as functions of t_0.

11.2 Optimization based on a Generalized Maxwell model

11.2.1 Generalized Maxwell model

The Generalized Maxwell model, also known as the Maxwell–Wiechert model (after James Clerk Maxwell and E. Wiechert[200][201]), is the most general form of the linear model for viscoelasticity. In the Generalized Maxwell model for these experimental results, 7 Maxwell elements are assembled in parallel. It takes into account that the relaxation does not occur at a single time, but in a set of times. Due to the presence of Maxwell elements of different lengths, with shorter ones contributing less than longer ones, there is a varying time distribution. The Maxwell model shows this by having spring–dashpot Maxwell elements which are necessary to accurately represent the distribution. The Fig.11.11 shows the generalized Maxwell model (this is the similar figure as in the Chapter 5).[190]

11.2.2 General model form for relaxation function

We present here the classical method allowing to determine the relaxation function of the generalized Maxwell model by Laplace-Carson transformation. For simplicity, the method is detailed below in the one-dimensional (1D) case.
Given $N+1$ elements with moduli E_i, viscosities η_i, and relaxation times $\tau_i = \frac{\eta_i}{E_i}$
The system of the equations associated with the generalized Maxwell model (Figure 11.11) is

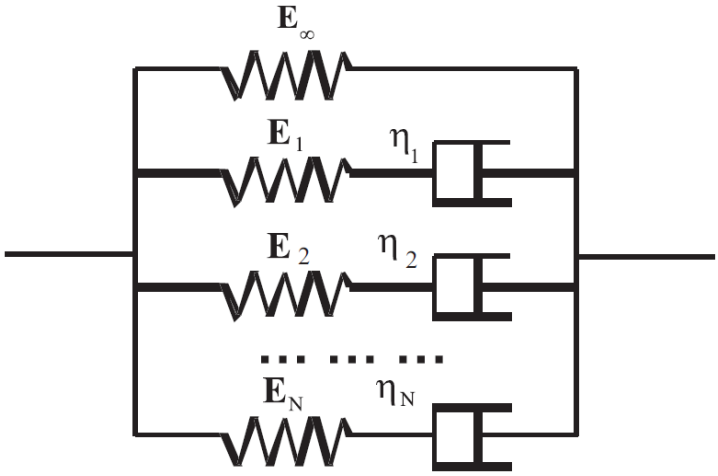

FIGURE 11.11 : Schematic of Maxwell–Wiechert model.

expressed by

$$\begin{cases} \sigma_\infty(t) = E_\infty \epsilon(t), \\ \sigma_i(t) = E_i(\epsilon(t) - \alpha_i(t)) = \eta_i \dot{\alpha_i}, \\ \sigma(t) = \sigma_\infty(t) + \sum_{i=1}^{N} \sigma_i(t). \end{cases} \tag{11.6}$$

In Eq.(11.6), σ_i is the stress in the spring-dashpot element i, α_i is the strain related to the dashpot i ; the index $i = 1, 2, .., N$ with N as the number of the parallel spring-dashpot elements, E_∞ and E_i are Young's moduli ; η_i characterizes the dashpot of the element i ; σ and ϵ indicate the total stress and the total strain of the system ; $\dot{x}$ is the time derivative of x. To aide the calculation with the time derivative, by applying the Laplace-Carson transform to the system of equations 11.6, we obtain

$$\begin{cases} \sigma^*_\infty(p) = E_\infty \epsilon^*(p), \\ \sigma^*_i(p) = E_i(\epsilon^*(p) - \alpha^*_i(p)) = \eta_i p \alpha^*_i(p), \\ \sigma^*(p) = \sigma^*_\infty(p) + \sum_{i=1}^{N} \sigma^*_i(p). \end{cases} \tag{11.7}$$

where p is a complex variable. From Eq.(11.7) :

$$\alpha^*_i(p) = \frac{E_i \epsilon^*(p)}{\eta_i p + E_i} \tag{11.8}$$

and the stress in the spring-dashpot element i of the generalized Maxwell model is expressed by

$$\sigma^*_i(p) = \frac{\eta_i p E_i \epsilon^*(p)}{\eta_i p + E_i} \tag{11.9}$$

By substituting $\sigma_i^*(p)$ and $\sigma_\infty^*(p)$ in Eq.(11.7), we arrive at

$$\sigma^*(p) = (E_\infty + \sum_{i=1}^{N} \frac{\eta_i p E_i}{\eta_i p + E_i})\epsilon^*(p). \tag{11.10}$$

In order to obtain the relaxation function of the model, we apply a macroscopic deformation strain $\epsilon(t) = \epsilon_0 H(t)$ where $H(t)$ is the Heaviside function and ϵ_0 is a constant. We have $\epsilon^*(p) = L\epsilon(t) = \epsilon_0 \frac{1}{p}$ with $L\{.\}$ as the Laplace-Carson transform operator. By substituting the expression of $\epsilon^*(p)$ in Eq.(11.10), the total stress in the Laplace space is expressed by :

$$\sigma^*(p) = \frac{1}{p}(E_\infty + \sum_{i=1}^{N} \frac{\eta_i p E_i}{\eta_i p + E_i})\epsilon_0. \tag{11.11}$$

The total stress is obtained in the time domain by applying Laplace-Carson inverse transform to Eq.11.11 :

$$\sigma(t) = R(t)\epsilon_0. \tag{11.12}$$

where the relaxation function $R(t)$ is defined by :

$$R(t) = L^{-1}\frac{1}{p}(E_\infty + \sum_{i=1}^{N} \frac{\eta_i p E_i}{\eta_i p + E_i}) = E_\infty + \sum_{i=1}^{N} E_i e^{-t/\tau_i}, \tag{11.13}$$

τ_i is the relaxation time of the spring-dashpot element i, defined by $\tau_i = \eta_i / E_i$.
In the case of the identification of parameters in this section, $N = 7$ and relaxation times $\tau_i = 10^{-3}, 10^{-2}, 10^{-1}, 10^{0}, 10^{1}, 10^{2}, 10^{3}$ (days).

3D linear viscoelasticity In the three-dimensional isotropic case where the deviatoric and spherical parts of the stress tensor can be expressed separately, the fourth-order tensors associated with the elements of the generalized Maxwell model are given by

$$\mathbb{C}_\infty = 3k_\infty \mathbb{J} + 2\mu_\infty \mathbb{K}, \tag{11.14}$$

$$\mathbb{C}_i^e = 3k_i^e \mathbb{J} + 2\mu_i^e \mathbb{K}, \tag{11.15}$$

$$\mathbb{C}_i^v = 3k_i^v \mathbb{J} + 2\mu_i^v \mathbb{K}, \tag{11.16}$$

where $\mathbb{C}_\infty$ corresponds to the elastic element of the first branch of the model, $\mathbb{C}_i^e$ and $\mathbb{C}_i^v$ characterize the properties of the elastic element and the viscous element of the viscoelastic branch i. k_∞, k_i^e, μ_∞ and μ_i^e are the corresponding elastic bulk modulus and elastic shear modulus, k_i^v

and μ_i^v are the corresponding viscous bulk modulus and viscous shear modulus.
For a linear viscoelastic material described by the generalized Maxwell model, we have the bulk and shear relaxation functions in the case of 3D linear viscoelasticity :

$$\begin{cases} R_k(t) = 3k_\infty + \sum_{i=1}^{N} 3k_i^e e^{-t/\tau_i^k}, \\ R_\mu(t) = 2\mu_\infty + \sum_{i=1}^{N} 2\mu_i^e e^{-t/\tau_i^\mu}, \end{cases} \tag{11.17}$$

where τ_i^k and τ_i^μ are defined by

$$\tau_i^k = \frac{k_i^v}{k_i^e}, \quad \tau_i^\mu = \frac{\mu_i^v}{\mu_i^e}. \tag{11.18}$$

The ageing version of this relaxation function could be written as :

$$\begin{cases} R_k(t,t_0) = 3k_\infty(t_0) + \sum_{i=1}^{N} 3k_i^e(t_0) e^{-t/\tau_i^k(t_0)}, \\ R_\mu(t,t_0) = 2\mu_\infty(t_0) + \sum_{i=1}^{N} 2\mu_i^e(t_0) e^{-t/\tau_i^\mu(t_0)}, \end{cases} \tag{11.19}$$

where $k_\infty(t_0)$, $k_i^e(t_0)$, $\mu_\infty(t_0)$ and $\mu_i^e(t_0)$ are identified by the experimental results and t_0 indicates the age of loading.

11.2.3 Numerical evaluation of the Volterra integral operator and its inverse

The mechanical behaviour considered in this thesis is linear viscoelasticity with ageing. This behaviour is written as a Stieltjes integral relating the stress tensor evolution to the strain tensor history (see [157] for example) :

$$\sigma(t) = \int_{-\infty}^{t} \mathbb{C}(t,t') : d\epsilon(t') \tag{11.20}$$

where $\mathbb{C}(t,t')$ is the relaxation tensor.
According to the principle show in the Chapter 4, the corresponding creep compliance function can be obtained from numerically inverting the relation $\sigma = R \circ \epsilon$ where $R(t,t_0) = R_b(t-t_0)$ to get $\epsilon = J \circ \sigma$ (using the matrix equivalence described before), then evaluating $J_b(t) = J(t,t_0) = J(t,.) \circ H(.)$.

11.2.4 Identification of parameters

With the nonlinear optimization following the flowchart of principle in Fig.11.15, the values of $E_i(t_0)$ and $U(t_0)$ can be identified for each experiment with a certain age of loading and a certain material.

Firstly, the generalized Maxwell model is applied by the nonlinear optimization to calculate the correct apparent activation energy $U(t_0)$ considering the effect of temperature on the hydration process, with which the equivalent time $t_{eq}(t_0)$ can be calculated for each experiment.
Then based on the compliance data from the experiments on VeRCoRs materials, the values of E_i for a given material depend on the age of loading t_0. The compliance model for basic creep is thus optimized with the experimental data of different t_0. Here, the cost function is always the sum $\sum_t (J_{ex}(t) - J(t, t_0))^2$.
With this method, the analytical solution of the compliance for each material and each time of loading is calculated with the expression of the generalized Maxwell model. An example is presented in the Figure 11.12.

In the Figure 11.12, there is a different evolution between the experiment results and the

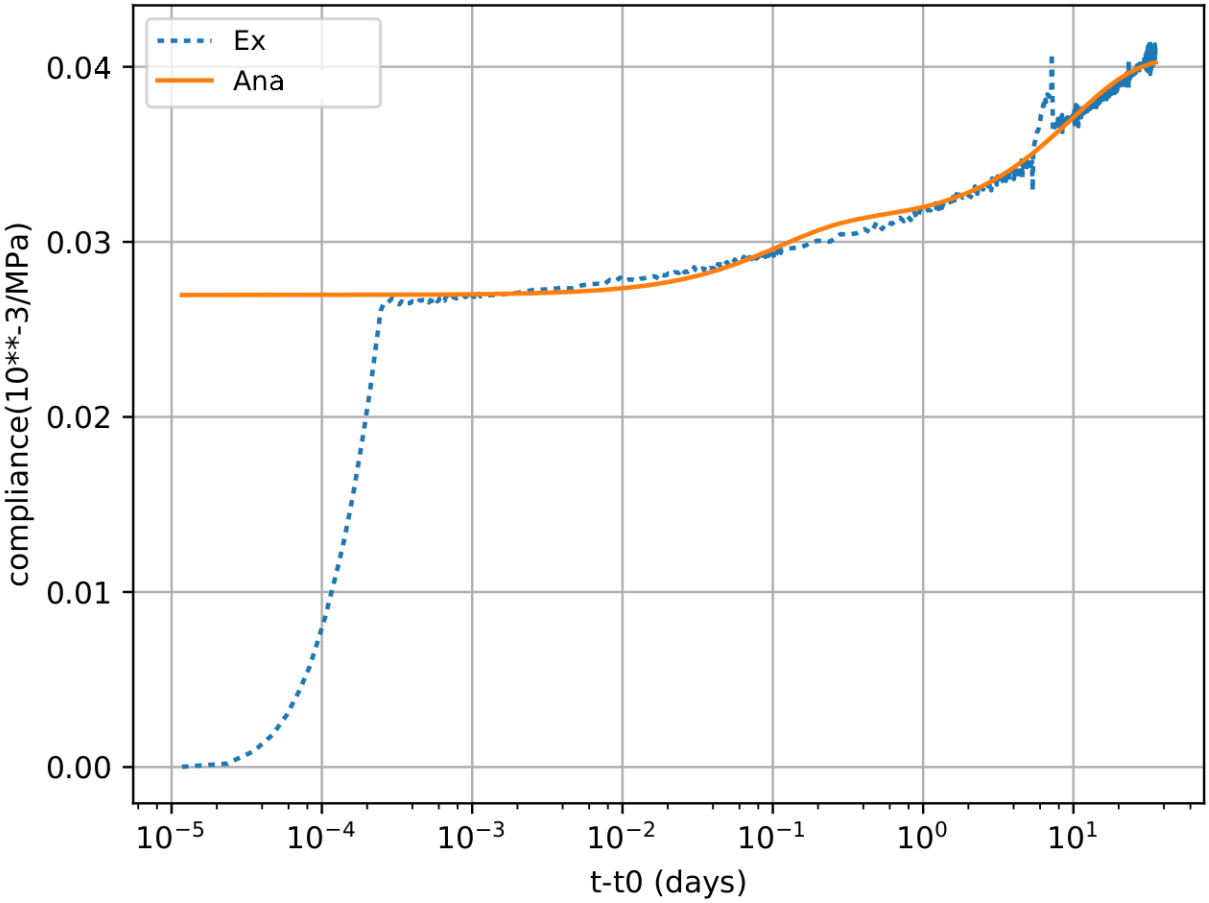

FIGURE 11.12 : Evolution of Strain/Stress for compressive basic creep : experimental result (dotted line) and analytical result (continuous line, compliance calculated by generalized Maxwell model).

analytical results for small $t - t_0$. It is because the strain/stress evolution during the loading period (about 20 seconds) is not shown in the analytical compliance results.
$E_i(t_0)$, $U(t_0)$ and $t_{eq}(t_0)$ for each age of loading can be calculated with this method. Nevertheless, $E_i(t_0)$ can be described as three function types : Eq.11.3, Eq.11.4 and Eq.11.5.

The method of nonlinear optimization is also applied with the Eq.11.3, Eq.11.4 and Eq.11.5 to calculate the proper parameters A, B and D and G for $E_i(t_0)$.

11.2.5 Upscaling using homogenization

This part proposes a semianalytical approach to estimate the effective ageing viscoelastic behaviour characterized by the compliance tensors as functions of two time variables (t, t_0)[161]. The Mori–Tanaka and self-consistent homogenization schemes is then applied to upscale the ageing viscoelastic behaviour from the scale of cement paste to the scale of mortar (with cement paste as the ageing viscoelastic matrix and sand as the inclusion), and from the scale of mortar to the scale of concrete (with mortar as the ageing viscoelastic matrix and coarse aggregate as the inclusion). The mechanical properties of sand and aggregate are supposed to be elastic. In the VeRCoRs concrete, the mechanical properties of sand and coarse aggregate are listed in Table 11.1.
With the same upscaling principe, the effective ageing compliance function is than calculated and shown in Fig.11.13. The comparison results demonstrate that the ageing compliance model

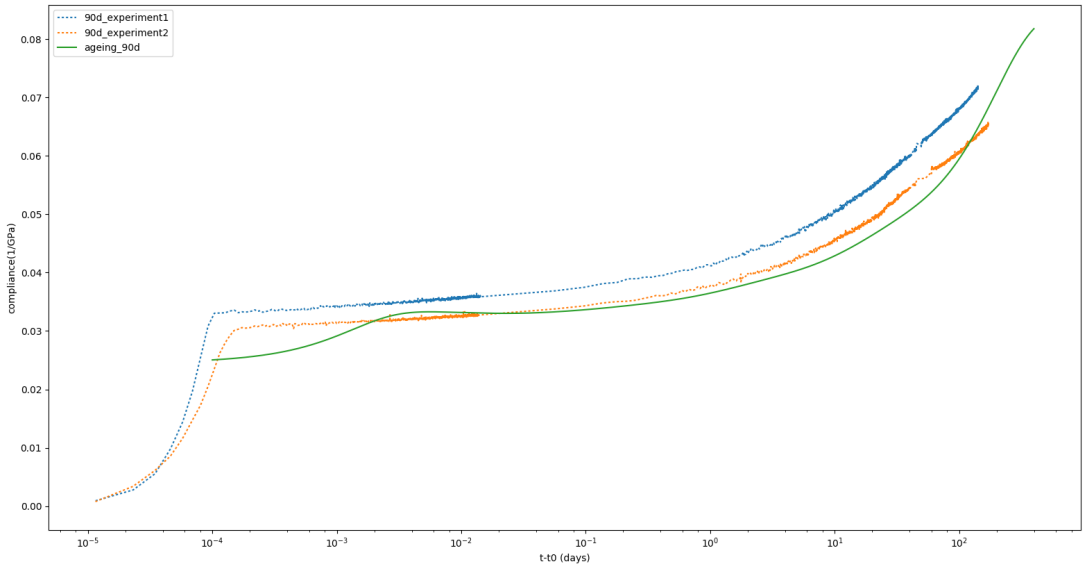

FIGURE 11.13 : Example : Effective uniaxial compliance [157] functions of mortar ($w/c = 0.525$) based on the generalized Maxwell model, plotted for age of loading t_0 =90 days. Comparison between the experimental results on mortar (2 dotted lines) and the upscaling using the Mori–Tanaka homogenization scheme (green continuous line based on the parameters as functions of t_0.

based on the generalized Maxwell model is not yet perfectly adapted to the experimental results either. This creep compliance model also underestimate the creep compliance in the short term and overestimate the creep compliance in the long term.

11.3 Optimization based on a Generalized Kelvin model

11.3.1 Generalized Kelvin model

The generalized Kelvin model is composed of n Kelvin units in series plus an isolated spring. The stress at each unit is the same external stress $\sigma(t)$ while the total (observable) strain $\epsilon(t)$ is the sum of the internal strains in each element. Given 1 Kelvin unit with moduli E_i and viscosities η_i, for a generic Kelvin element i :

$$\sigma_i(t) = (E_i + \eta_i \partial/\partial t)\epsilon_i(t) \tag{11.21}$$

We have for the model in Fig.11.14

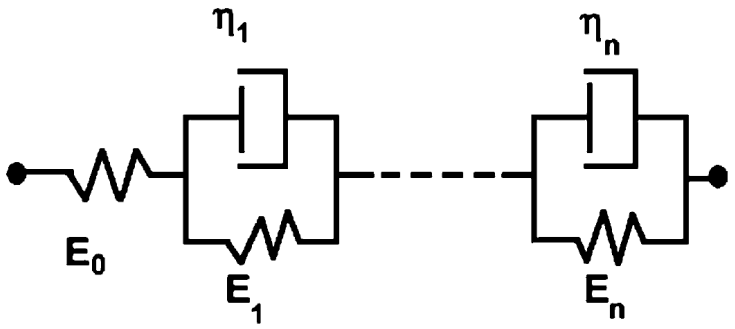

FIGURE 11.14 : Kelvin chains with instantaneous elasticity.

$$\epsilon(t) = (\frac{1}{E_0} + \sum_{i=1}^{n}(E_i + \eta_i \partial/\partial t)^{-1})\sigma(t) \tag{11.22}$$

When the functional relation $\epsilon(t)$ is linear it has a simple and useful representation given by the Riesz theorem [151] : if the creep compliance function J is linear and continuous, it can be written

$$\epsilon(t) = \int_{\tau_0}^{t} J(t-\tau)\dot{\sigma}(\tau)d\tau \tag{11.23}$$

Here, τ_0 should be chosen in a way that for $\tau < \tau_0$ the material is at rest, without stress and strain.
With this principle, the creep compliance function for the generalized Kelvin model is gathered, for a generic value of t_0,

$$J(t,t_0) = J_b(t-t_0) = \frac{1}{E_0} + \sum_{i=1}^{n}\frac{1}{E_i}[1 - e^{-\frac{t-t_0}{\tau_i}}]; \quad \tau_i = \eta_i/E_i \tag{11.24}$$

In the case of the identification of parameters in this section, $n = 7$ and retardation time $\tau_i = 10^{-3}, 10^{-2}, 10^{-1}, 10^{0}, 10^{1}, 10^{2}, 10^{3}$ (days).

11.3.2 Identification of parameters and upscaling using homogenization

Like the generalized Maxwell model, with the nonlinear optimization following the flowchart of principle in Fig.11.15, the values of $E_i(t_0)$ and $U(t0)$ can be identified for each experiment with a certain age of loading and a certain material.
$E_i(t_0)$, $U(t_0)$ and $t_{eq}(t_0)$ for each age of loading can be calculated with this method. Nevertheless, $E_i(t_0)$ can be described as three function types : Eq.11.3, Eq.11.4 and Eq.11.5.
The method of nonlinear optimization is also applied with the Eq.11.3, Eq.11.4 and Eq.11.5 to calculate the proper parameters A, B and D and G for $E_i(t_0)$.
With the same principles shown in the upscaling work with the generalized Maxwell model, the Mori–Tanaka and self-consistent homogenization schemes is then applied to upscale the ageing viscoelastic behaviour from the scale of cement paste to the scale of mortar (with cement paste as the ageing viscoelastic matrix and sand as the inclusion), and from the scale of mortar to the scale of concrete (with mortar as the ageing viscoelastic matrix and coarse aggregate as the inclusion). The effective ageing compliance function is therefore calculated with the method mentioned in [166].
In general, the generalized Maxwell model of and the generalized Kelvin model are chosen for the identification of the spherical and deviatoric behaviours of cementitious material represented by the creep compliance models based on the creep experiments with the constant Poisson's ratio given by the code $Vi(CA)_2T$ in EDF. The identified generalized Maxwell model is applied in the numerical simulation with the developed generalized Maxwell behaviour Mfront script. The identified generalized Kelvin model is applied to validate the reliability of the experimental results because, for the creep results, the ageing compliance function could be developed more directly with the generalized Kelvin model than in the generalized Maxwell model.

11.4 Hybrid compliance model

11.4.1 Identification of parameters

Basic creep compliance could be expressed as a logarithmic function in which the age of loading affects only the term $t - t_0$. But this compliance function underestimate the compliance value in the range of $10^{-2} - 10^{0}$ day. So a Kelvin unit with the retardation time $\tau_{Kelvin} = 10^{-2}$ day is added in the compliance function to correct the error value in the range of $10^{-2} - 10^{0}$ day.
The compliance model for basic creep is thus the Eq.11.25 :

$$J(t,t_0) = \frac{1}{E(t_0)} + \frac{1}{C(t_0)} Log(1 + \frac{t-t_0}{\tau(t_0)}) + \frac{1}{E_{Kelvin}(t_0)}[1 - e^{-\frac{t-t_0}{\tau_{Kelvin}}}] \tag{11.25}$$

With the nonlinear optimization of the Eq.10.1 and the Eq.11.25, the value of $E(t_0)$, $C(t_0)$, $\tau(t_0)$, $E_{Kelvin}(t_0)$ and $U(t0)$ can be identified for each experiment with a certain age of loading and a certain material.
Like the principle for the logarithmic model, there are 4 steps to finish the processes of the identification of parameters.

1. Firstly, the experimental results of compliance J_{ex} is obtained. The Eq.10.1 and the Eq.11.25 are applied, the sum $\sum_t (J_{ex}(t) - J(t,t_0))^2$ (the cost function) is then calculated. Afterwards the method of least squares is applied by the nonlinear optimization to calculate the correct apparent activation energy $U(t_0)$ considering the effect of temperature on the hydration process, with which the equivalent time $t_{eq}(t_0)$ can be calculated for each experiment. The flowchart of the Nonlinear Least Squares Optimization of $U(t_0)$ is precised in Fig.11.15.

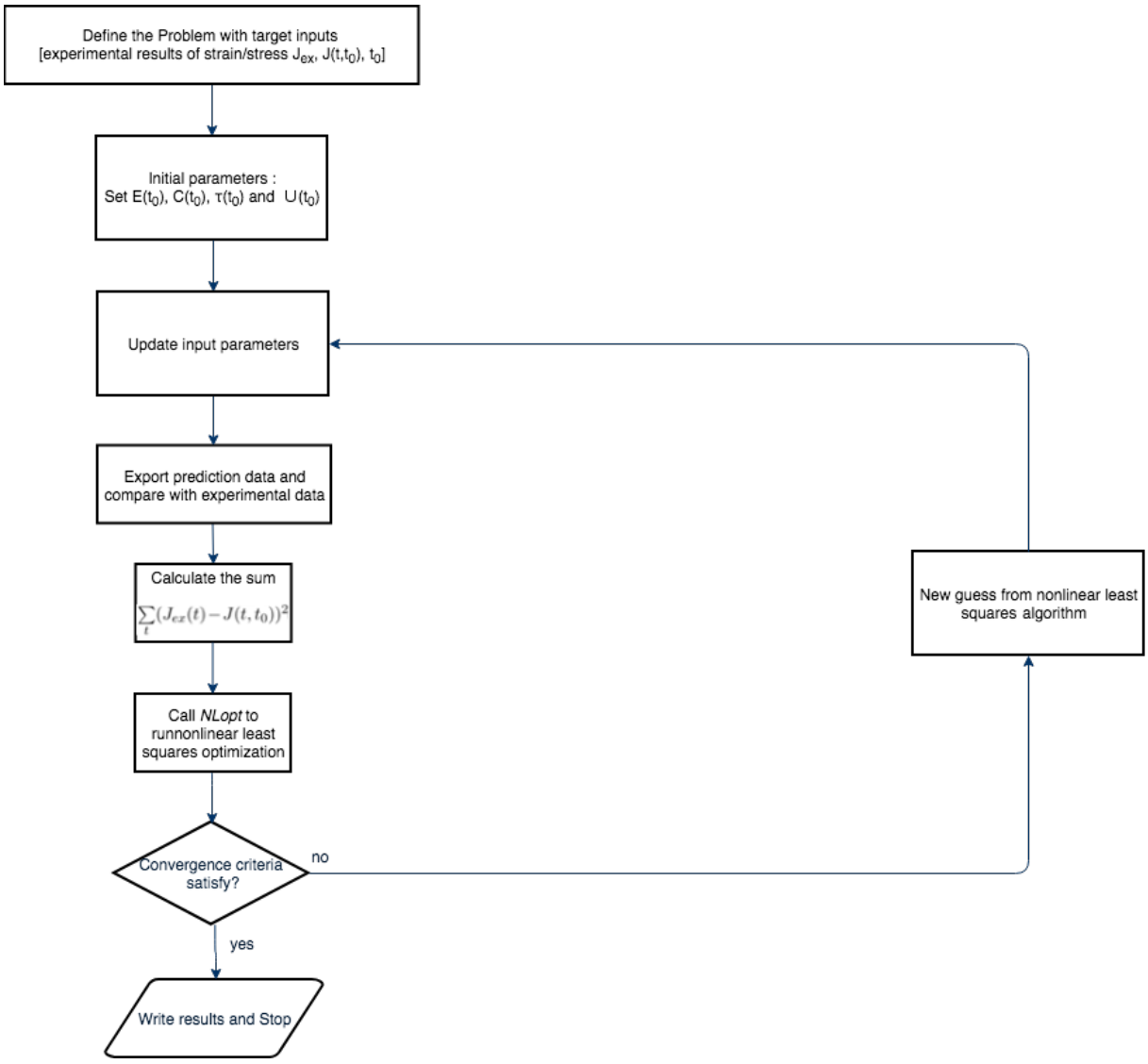

FIGURE 11.15 : Flowchart of the Nonlinear Least Squares Optimization.

2. Secondely, the strain/stress evolution during the loading period (about 20 seconds) in the equivalent time t_{eq} passes to the nonlinear optimization with the Eq.11.2 to define the correct Young's modulus at the age of loading $E(t_0)$. Here, the cost function is always the sum of $\sum_t (J_{ex}(t) - J(t,t_0))^2$ but the parameter t is only the loading period (about 20

seconds).

3. Thirdly, with the correct $E(t_0)$, a least squares polynomial fit process is performed with the compliance results after the ramp with the same principe of Fig.11.15. The derivative of the compliance dJ/dt tends to $1/(C(t_0)t)$ when t was large, which aides to calculate $C(t_0)$.

4. Fourthly, the correct $E(t_0)$ and the least squares polynomial fit line aide to calculate $\tau(t_0)$.

With this method, the analytical solution of the compliance for each material and each time of loading is calculated with the form of the Eq.11.25. An example is presented in the Figure 11.16 : $E(t_0)$, $C(t_0)$, $\tau(t_0)$, $E_{Kelvin}(t_0)$, $U(t_0)$ and $t_{eq}(t_0)$ for each age of loading can be calculated with

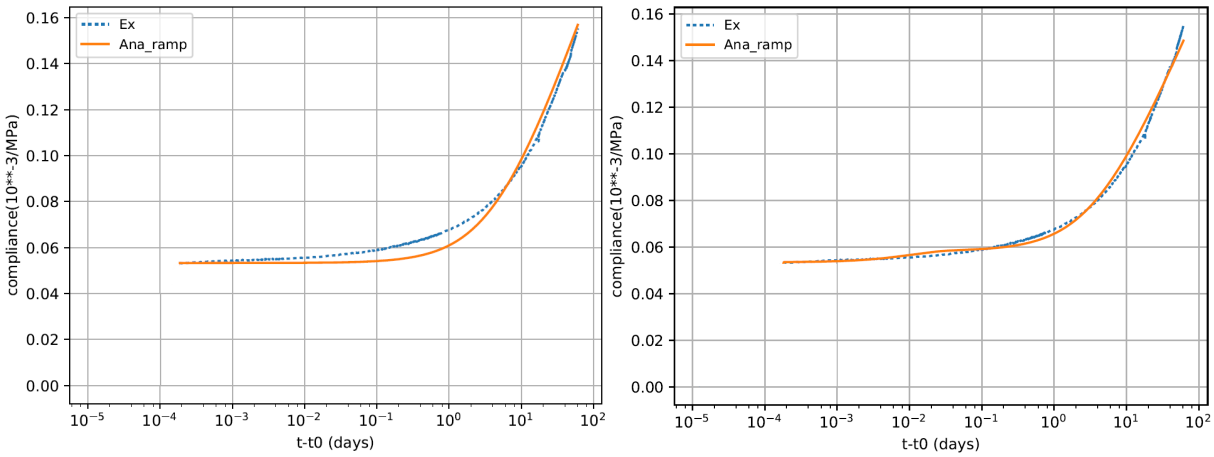

FIGURE 11.16 : Example : Basic creep compliance evolution of the specimen. Left : logarithmic function result (solid line), Right : hybrid model result (solid line), cement paste with the age of loading = 28 days).

this method. Nevertheless, $E(t_0)$, $C(t_0)$, $\tau(t_0)$ and $E_{Kelvin}(t_0)$ can be described as three function types : Eq.11.3, Eq.11.4 and Eq.11.5.

The method of nonlinear optimization is also applied with the Eq.11.3, Eq.11.4 and Eq.11.5 to calculate the proper parameters A, B, D and G for $E(t_0)$, $C(t_0)$, $\tau(t_0)$ and $E_{Kelvin}(t_0)$. Here, the parameters A, B, D and G are optimized to each function for $E(t_0)$, $C(t_0)$, $\tau(t_0)$ and $E_{Kelvin}(t_0)$ with the obtained experimental data for $t_0 = 1, \quad 3, \quad 7, \quad 28, \quad 90$ days. Then with the deducted function $E(t_0)$, $C(t_0)$, $\tau(t_0)$ and $E_{Kelvin}(t_0)$ for $t_0 = 1, \quad 3, \quad 7, \quad 28, \quad 90$ days, the values of $E(t_0)$, $C(t_0)$, $\tau(t_0)$ and $E_{Kelvin}(t_0)$ with other age of loading t_0 could be calculated. Fig.11.17, Fig.11.18, Fig.11.19 and Fig.11.20 show the evolution of $E(t_0)$, $C(t_0)$, $\tau(t_0)$ and $E_{Kelvin}(t_0)$ as functions of t_0. For $t > 100$ days, conjecture is developed to estimate the evolution of the parameters.

In addition, even the function values of $E(t_0)$ and $C(t_0)$ are close to the identified experimental values, there are still identified experimental values far from the function values for $\tau(t_0)$ and $E_{Kelvin}(t_0)$, for example, $\tau(t_0 = 90 \quad days)$ is far from the identified experimental value τ at the age of loading for 90 days, and $E_{Kelvin}(t_0 = 3 \quad days)$ is far from the identified experimental value E_{Kelvin} at the age of loading of 3 days. In this situation, the interpolation and the

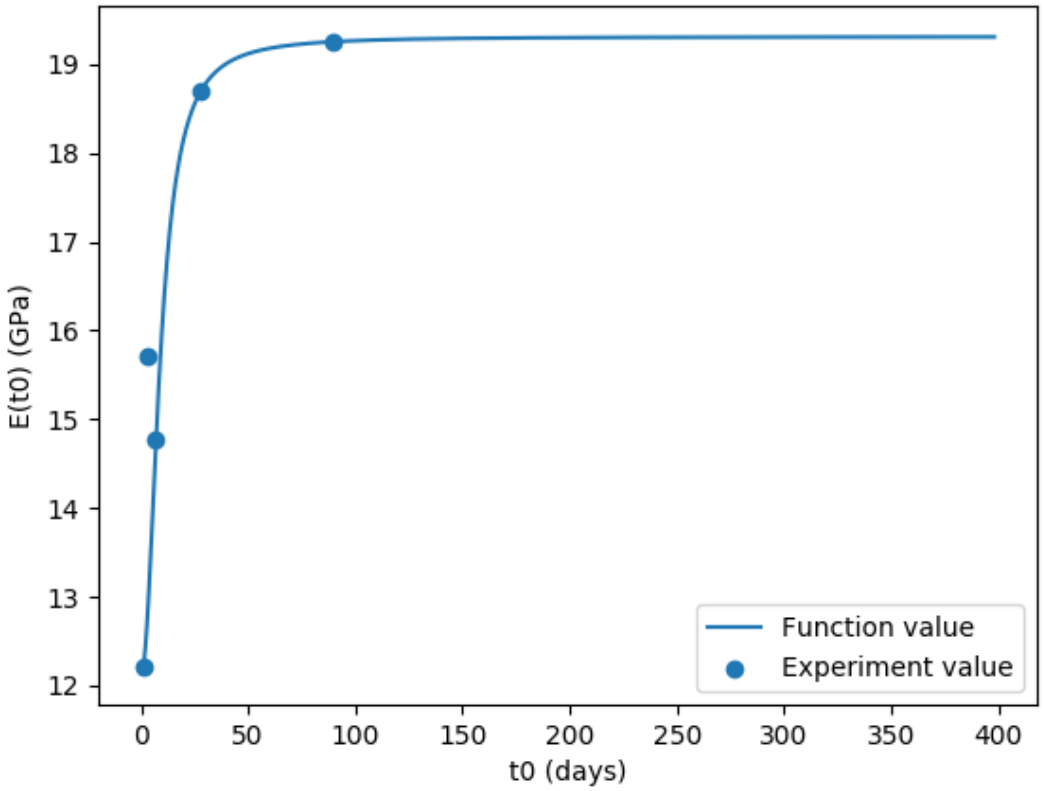

FIGURE 11.17 : Example : evolution of $E(t_0)$ as function of t_0, cement paste scale.

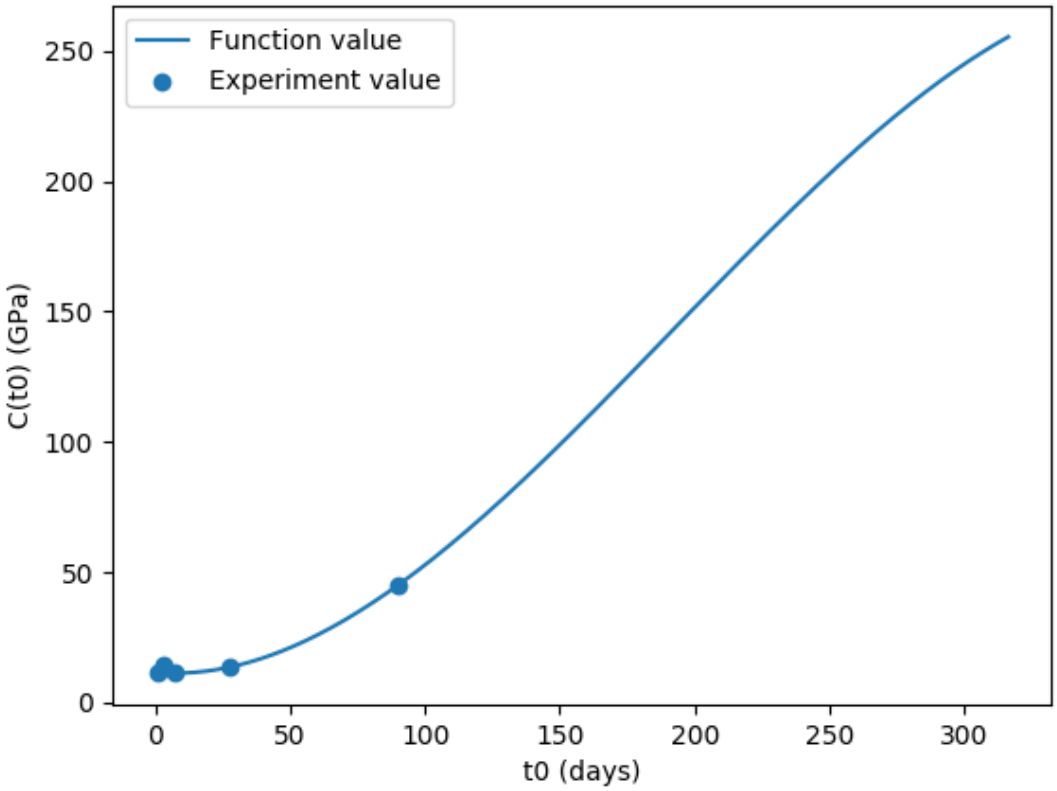

FIGURE 11.18 : Example : evolution of $C(t_0)$ as function of t_0, cement paste scale.

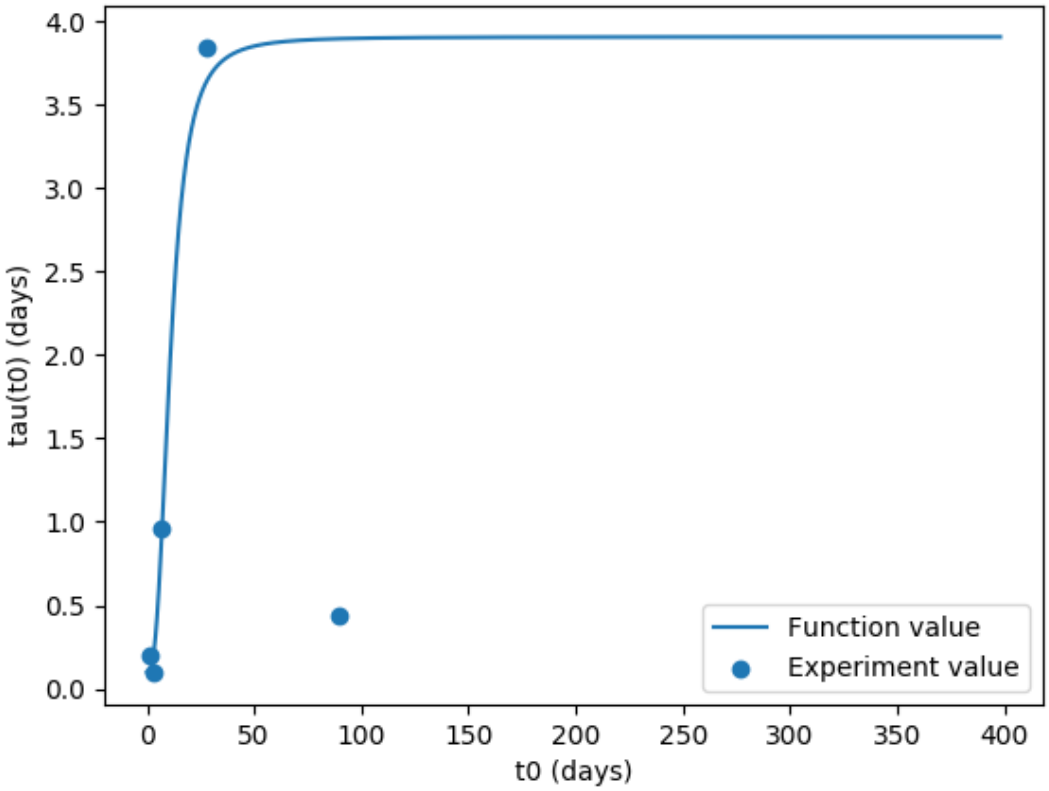

FIGURE 11.19 : Example : evolution of $\tau(t_0)$ as function of t_0, cement paste scale.

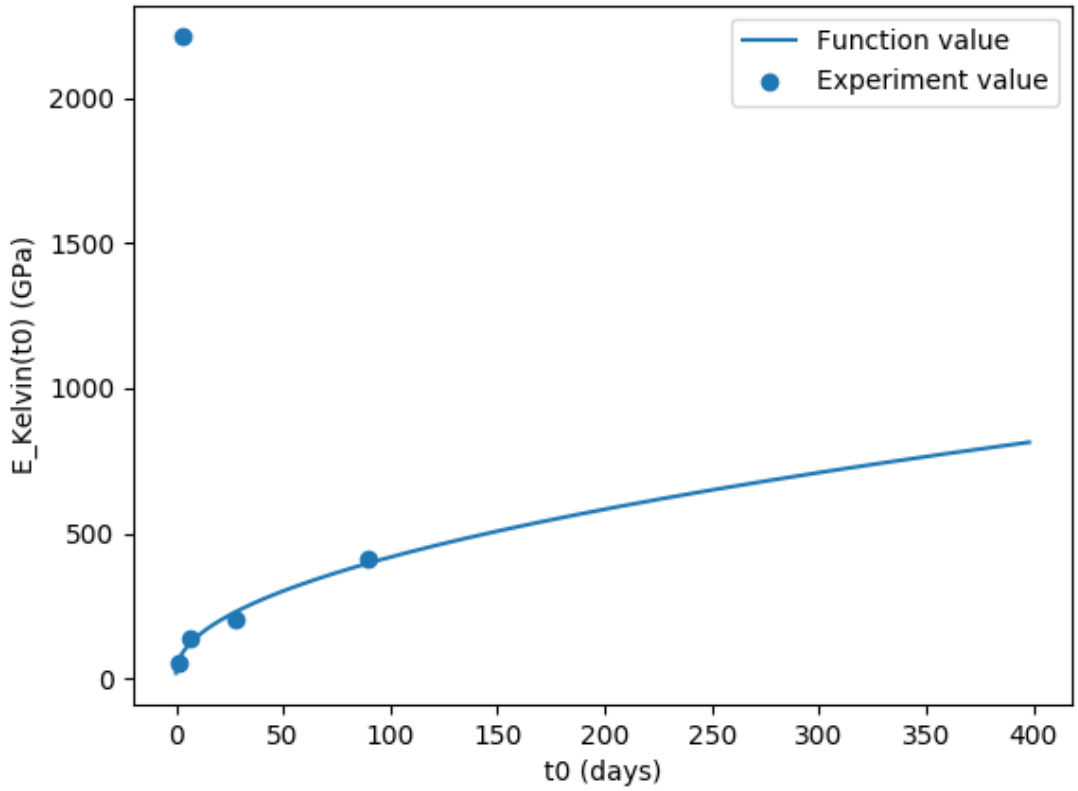

FIGURE 11.20 : Example : evolution of $E_{Kelvin}(t_0)$ as function of t_0, cement paste scale.

extrapolation are carried out to propose another method to obtain the values of $E(t_0)$, $C(t_0)$, $\tau(t_0)$ and $E_{Kelvin}(t_0)$ with other age of loading t_0. The comparison between the function results and the interpolation-extrapolation results during the upscaling phase is also performed to verify if the functions of $E(t_0)$, $C(t_0)$, $\tau(t_0)$ and $E_{Kelvin}(t_0)$ can always give reasonable results when there is at most one identified experimental value far from the function value (just as the case of $\tau(t_0 = 90 \quad days)$ and $E_{Kelvin}(t_0 = 3 \quad days)$ at the cement paste scale).
At first, the verification of the ageing viscoelastic model with the parameters $E(t_0)$, $C(t_0)$, $\tau(t_0)$ and $E_{Kelvin}(t_0)$ identified is carried out at the scale of cement paste. The model is applied to recalculate the evolution of the basic creep compliance and to compare the modeling results with the experimental results, as shown in Fig.11.21 and Fig.11.22 with different ages of loading for example.

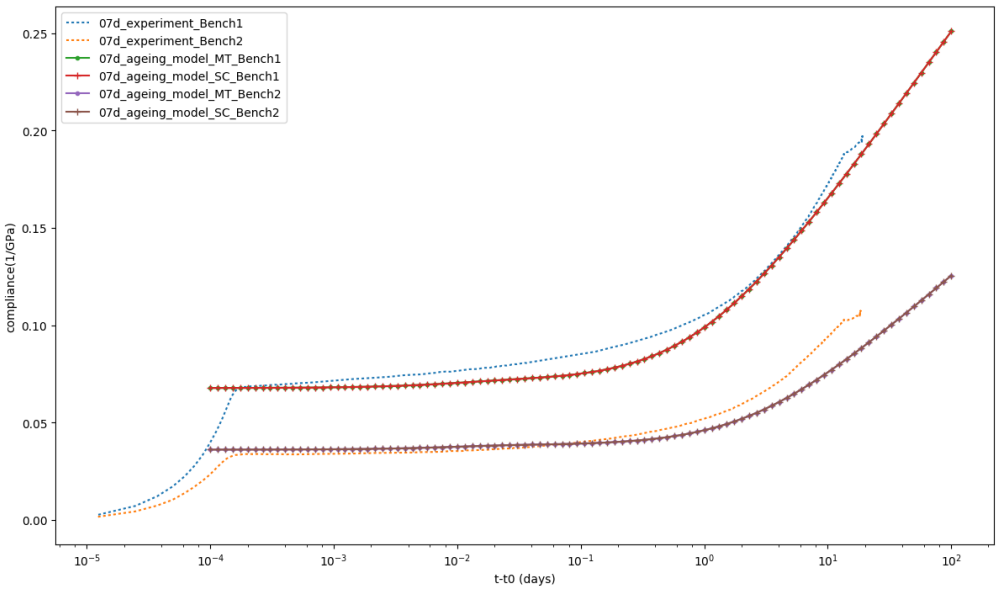

FIGURE 11.21 : Example : evolution of the basic creep compliance and comparison of the modeling results with the experimental results, cement paste scale, $t_0 = 7$ days.

According to Fig.11.21 and Fig.11.22, the continuous lines are close to the dotted lines. So the modeling results are close to the experimental results, which justify the applicability of the model. However, it is also evident that the divergence of the experimental results between the 2 benches should not be neglected. The study of the parameters of $E(t_0)$, $C(t_0)$, $\tau(t_0)$ and $E_{Kelvin}(t_0)$ for these 2 benches are carried out and it proves that there is more oscillation on the parameters identified in Bench 2 than that in Bench 1 at the cement paste scale. So the experimental data of the Bench 1 are more reliable at the cement paste scale.

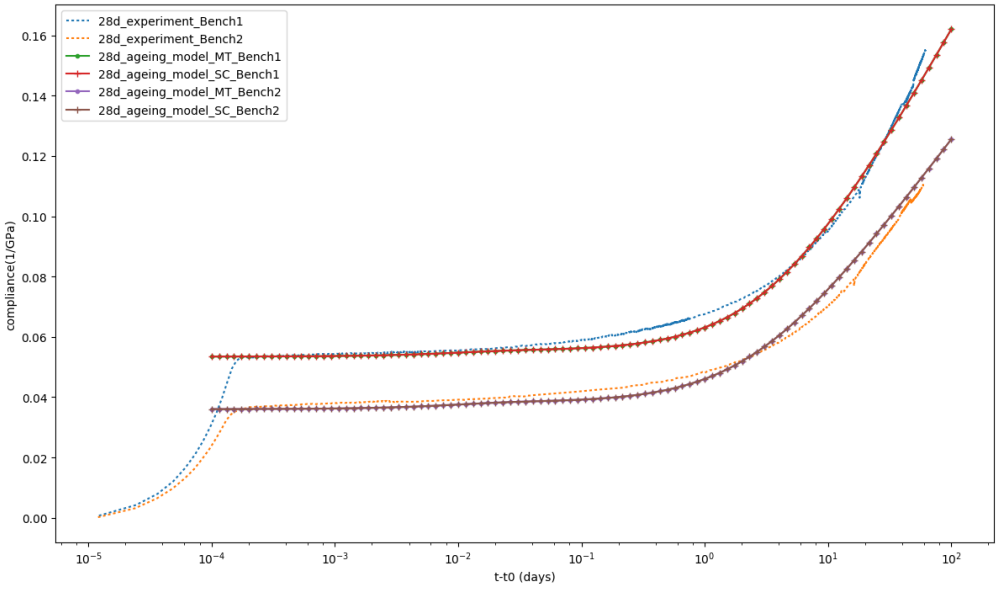

FIGURE 11.22 : Example : evolution of the basic creep compliance and comparison of the modeling results with the experimental results, cement paste scale, $t_0 = 28$ days.

11.4.2 Physical submodel for identified parameters at scale of cement paste

The method of nonlinear optimization applied with the Eq.11.3, Eq.11.4 and Eq.11.5 to calculate the proper parameters A, B, D and G gives a pure mathematical approach to define $E(t_0)$, $C(t_0)$, $\tau(t_0)$ and $E_{Kelvin}(t_0)$. In addition, physical submodel could be defined to describe the parameters as a function of age of loading t_0, as in Eq.11.26 :

$$f(t_0) = A_{ini} + (1 - e^{-\frac{t_0 - t_{ini}}{\tau_f}})A_\infty \tag{11.26}$$

Where :

- t_{ini} is the initial moment that starts the plot of the evolution of a chosen parameter ;
- A_{ini} is the value of the chosen parameter when $t_0 = t_{ini}$;
- A_∞ is the value of the chosen parameter when $t_0 \to \infty$;
- τ_f is the caracteristic time of the evolution of the chosen parameter.

The method of nonlinear optimization is then applied with the Eq.11.26 to calculate the proper parameters t_{ini}, A_{ini}, A_∞ and τ_f for $E(t_0)$, $C(t_0)$ and $\tau(t_0)$. Here, the parameters t_{ini}, A_{ini}, A_∞ and τ_f are optimized to each function for $E(t_0)$, $C(t_0)$ and $\tau(t_0)$ with the obtained experimental data from the two creep test benches for $t_0 = 1,\quad 3,\quad 7,\quad 28,\quad 90$ days. Then with the deducted

function $E(t_0)$, $C(t_0)$ and $\tau(t_0)$ for $t_0 = 1,\quad 3,\quad 7,\quad 28,\quad 90$ days, the values of $E(t_0)$, $C(t_0)$ and $\tau(t_0)$ with other age of loading t_0 could be calculated. Fig.11.23, Fig.11.24 and Fig.11.25 show the evolution of $E(t_0)$, $C(t_0)$ and $\tau(t_0)$ of the two creep test benches as functions of t_0.

An evident difference could be identified from the comparison of the same parameter between

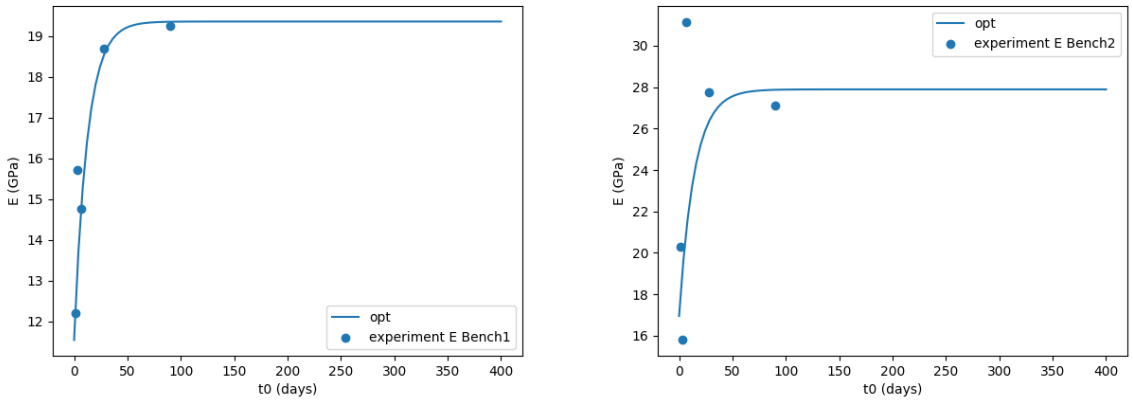

FIGURE 11.23 : Example : evolution of $E(t_0)$ of the two creep test benches as functions of t_0, cement paste scale.

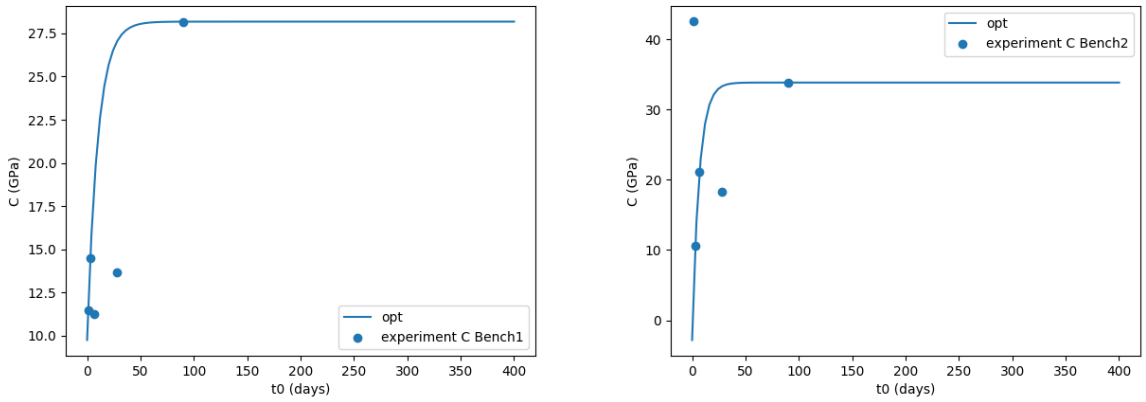

FIGURE 11.24 : Example : evolution of $C(t_0)$ of the two creep test benches as functions of t_0, cement paste scale.

the two different benches. It is more difficult to maintain the regularity of the evolution as a function of t_0 for the parameters identified from the Bench 2. The cause may be that there is some oscillation of the registered data in one LVDT displacement sensor on the speciment on the Bench 2. As shown in Fig.11.26, one displacement measured by the 3 LVDT displacement sensors installed on the Bench 2 (the orange line) demonstrates evident oscillation. Even during the post-processing this influenced displacement date is deleted, the lack of one group of the LVDT data cause the underestimation of the eccentricity ratio when the average displacement is calculated, and there are also notable differences between the remaining 2 LVDT sensors, which

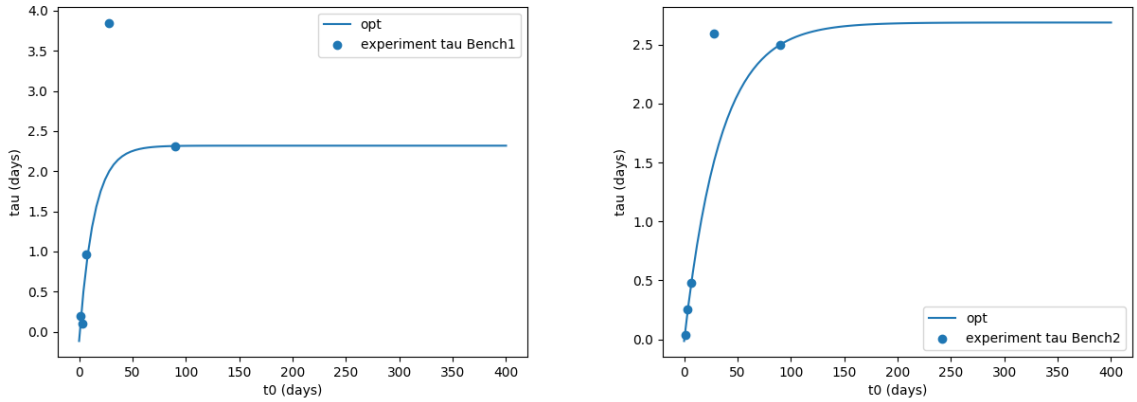

FIGURE 11.25 : Example : evolution of $\tau(t_0)$ of the two creep test benches as functions of t_0, cement paste scale.

makes the data of the Bench 2 at cement paste scale with the age of loading $t_0 = 90$ days less reliable than that of the Bench 1.

11.4.3 Identified Young's modulus at scale of cement paste

In addition, another comparison is carried out on Young's modulus $E(t_0)$ identified by different methods.

On one hand, the method of nonlinear optimization is then applied with the Eq.11.26 to calculate the proper parameters t_{ini}, A_{ini}, A_∞ and τ_f for $E(t_0)$ with t_0 as any age of loading from the identified parameters $E(t_0)$ with $t_0 = 1,\quad 3,\quad 7,\quad 28,\quad 90$ days (Method 1).

On the other hand, the parameters $E(t_0)$ with $t_0 = 1,\quad 3,\quad 7,\quad 21,\quad 28,\quad 84,\quad 90\quad 148$ days could also be calculated with the experimental results of the loaded force variation ΔF and the average displacement variation $\overline{\Delta\xi}$ during the loading and unloading period with ages of loading $t_0 = 1,\quad 3,\quad 7,\quad 28,\quad 90$ days and ages of unloading $t_0' = 21,\quad 84,\quad 148$ days (Method 2).

Fig.11.27 shows the comparison of these two methods.

Fig.11.27 shows that the experimental results of $E(t_0)$ identified by the Method 2 are less than those identified by the Method 1. In fact, the evolution of strain/stress (ϵ/σ) is ploted in a semi-log graph (as in Fig.11.16), which forms the plot with the pure elastic behaviour period and the long-term viscoelastic behaviour period. The well defined elastic behaviour period in the semi-log graph helps to avoid the influence of the viscoelastic behaviour of the material and calculate the elastic $E(t_0)$ precisely. However, during the application of the Method 2, the loaded force variation ΔF and the average displacement variation $\overline{\Delta\xi}$ are calculated as Eq.11.27 and Eq.11.28 :

$$\Delta F = F_{end} - F_{ini} \tag{11.27}$$

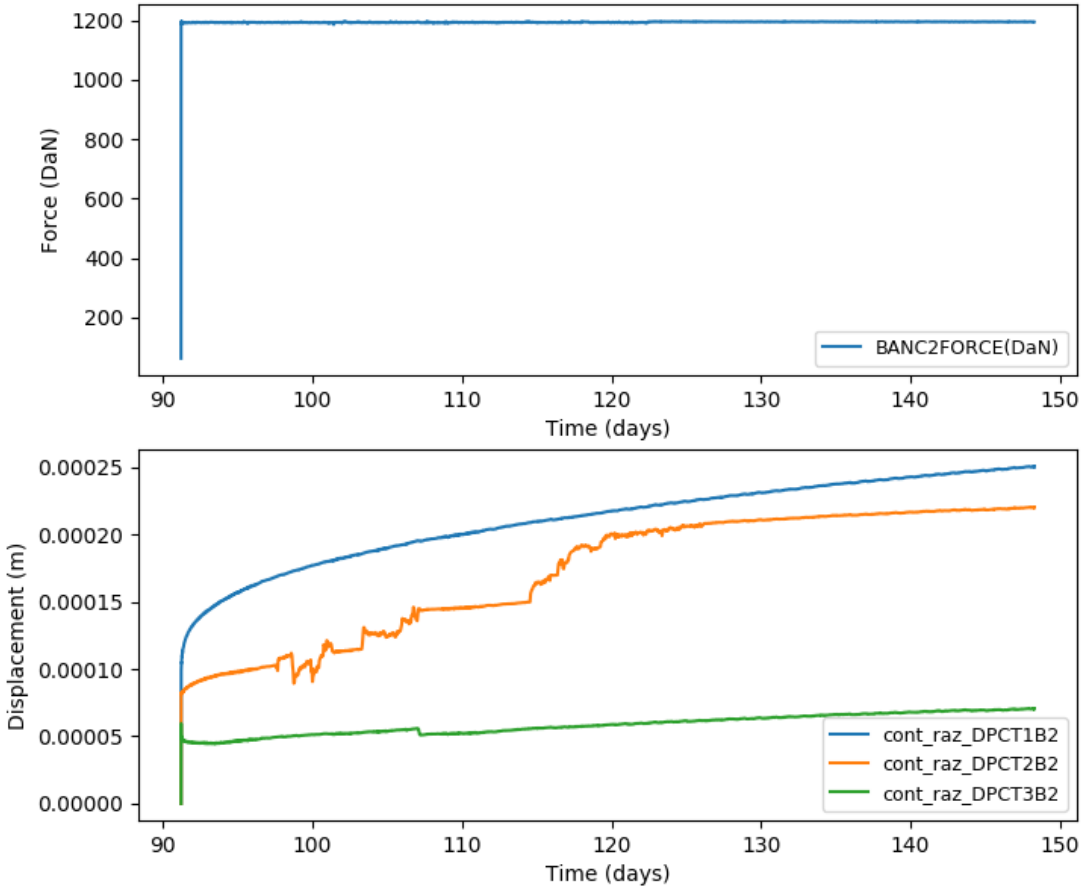

FIGURE 11.26 : Evolution of displacement measured by the 3 LVDT displacement sensors installed on the Bench 2 for the creep experiment at cement paste scale with the age of loading $t_0 = 90$ days.

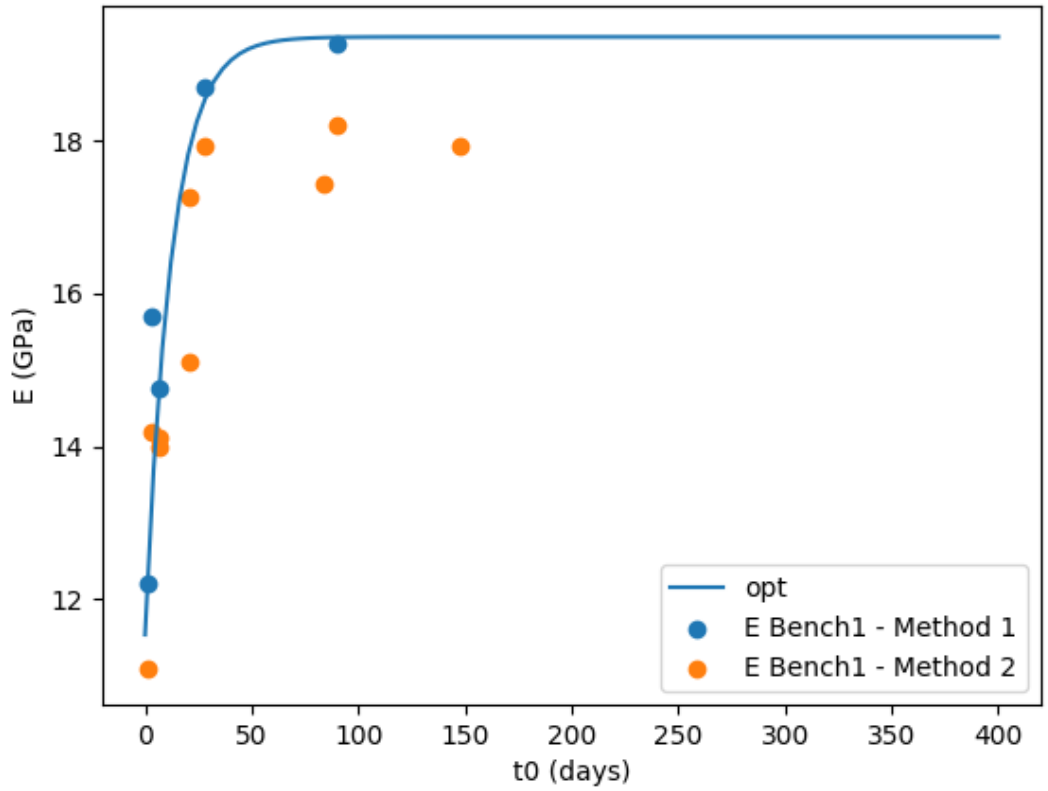

FIGURE 11.27 : Example : evolution of $E(t_0)$ of the Creep test Benche 1 as functions of t_0 with comparison of two methods to identify the experimental value $E(t_0)$, cement paste scale.

$$\overline{\Delta\xi} = \bar{\xi}_{end} - \bar{\xi}_{ini} \tag{11.28}$$

Here, the values of F_{end} is measured as the last value of the loaded force during the loading step or the first value of the loaded force during the unloading step (which is certainly the maximum force in the loading ou unloading step). But during the last moment of the loading step or the first moment of the unloading step, material loaded enters already in the viscoelastic period. So the Method 1 measures the initial tangent modulus and the Method 2 measurs the secant modulus (Fig.11.28). This is the reason why the Method 2 underestimate $E(t_0)$.

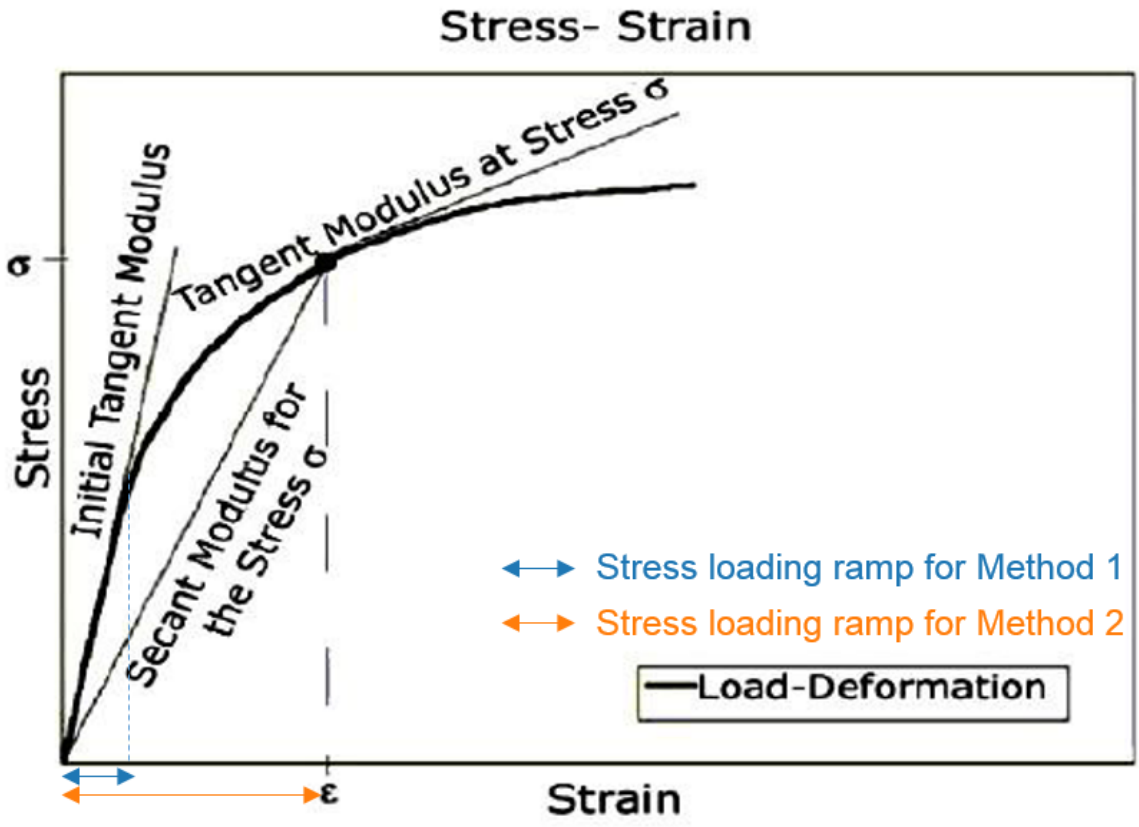

FIGURE 11.28 : Difference between the initial tangent modulus and the secant modulus.

11.4.4 Physical submodel for identified parameters at scale of mortar

The same form of the physical submodel could be defined to describe the parameters as a function of age of loading t_0 at the scale of the mortar, as in Eq.11.26.

The method of nonlinear optimization is applied with the Eq.11.26 to calculate the proper parameters t_{ini}, A_{ini}, A_∞ and τ_f for $E(t_0)$ and $C(t_0)$. Here, the parameters t_{ini}, A_{ini}, A_∞ and τ_f are optimized to each function for $E(t_0)$ and $C(t_0)$ with the obtained experimental data from the two creep test benches for $t_0 = 7,\quad 28,\quad 90\quad 365$ days. Then with the deducted function $E(t_0)$ and $C(t_0)$ for $t_0 = 7,\quad 28,\quad 90\quad 365$ days, the values of $E(t_0)$ and $C(t_0)$ with other age

of loading t_0 could be calculated. The two curves in the Fig.11.29 show the evolution of $E(t_0)$ and $C(t_0)$ of the creep test benche as functions of t_0.

The verification of the ageing viscoelastic model with the parameters $E(t_0)$, $C(t_0)$, $\tau(t_0)$ and $E_{Kelvin}(t_0)$ identified is also carried out at the scale of mortar. The model is applied to recalculate the evolution of the basic creep compliance and to compare the modeling results with the experimental results, as shown in Fig.11.30, Fig.11.31, Fig.11.32 and Fig.11.33 with different ages of loading for example.

According to Fig.11.30, Fig.11.31 and Fig.11.33, the continuous lines are close to the dotted lines. So the modeling results are close to the experimental results, which justify the applicability of the model. However, it is also evident that the divergence between the experimental results and the modeling results in Fig.11.32 should not be neglected.

11.4.5 Identified Young's modulus at scale of mortar

In addition, another comparison is carried out on Young's modulus $E(t_0)$ identified by different methods.

On one hand, the method of nonlinear optimization is then applied with the Eq.11.26 to calculate the proper parameters t_{ini}, A_{ini}, A_∞ and τ_f for $E(t_0)$ with t_0 as any age of loading from the identified parameters $E(t_0)$ with $t_0 = 7, \quad 28, \quad 90 \quad 365$ days (Method 1).

On the other hand, the parameters $E(t_0)$ with $t_0 = 7, \quad 21, \quad 28, \quad 82, \quad 90, \quad 210, \quad 365$ days could also be calculated with the experimental results of the loaded force variation ΔF and the average displacement variation $\overline{\Delta\xi}$ during the loading and unloading period with ages of loading $t_0 = 7, \quad 28, \quad 90 \quad 365$ days and ages of unloading $t_0' = 21, \quad 82, \quad 210$ days (Method 2).

Fig.11.34 shows the comparison of these two methods.

Fig.11.34 shows that the experimental results of $E(t_0)$ identified by the Method 2 are less than those identified by the Method 1.

The reason indicates the same principe. the evolution of strain/stress ϵ/σ is ploted in a semi-log graph (as in Fig.11.16), which forms the plot with the pure elastic behaviour period and the long-term viscoelastic behaviour period. The well defined elastic behaviour period in the semi-log graph helps to avoid the influence of the viscoelastic behaviour of the material and calculate the elastic $E(t_0)$ precisely. However, during the application of the Method 2, the loaded force variation ΔF and the average displacement variation $\overline{\Delta\xi}$ are calculated as Eq.11.27 and Eq.11.28. So the values of F_{end} is measured as the last value of the loaded force during the loading step or the first value of the loaded force during the unloading step (which is certainly the maximum force in the loading ou unloading step). But during the last moment of the loading step or the first moment of the unloading step, material loaded enters already in the viscoelastic period. So the Method 1 measures the initial tangent modulus and the Method 2 measurs the secant modulus (Fig.11.28). This is the reason why the Method 2 underestimate $E(t_0)$.

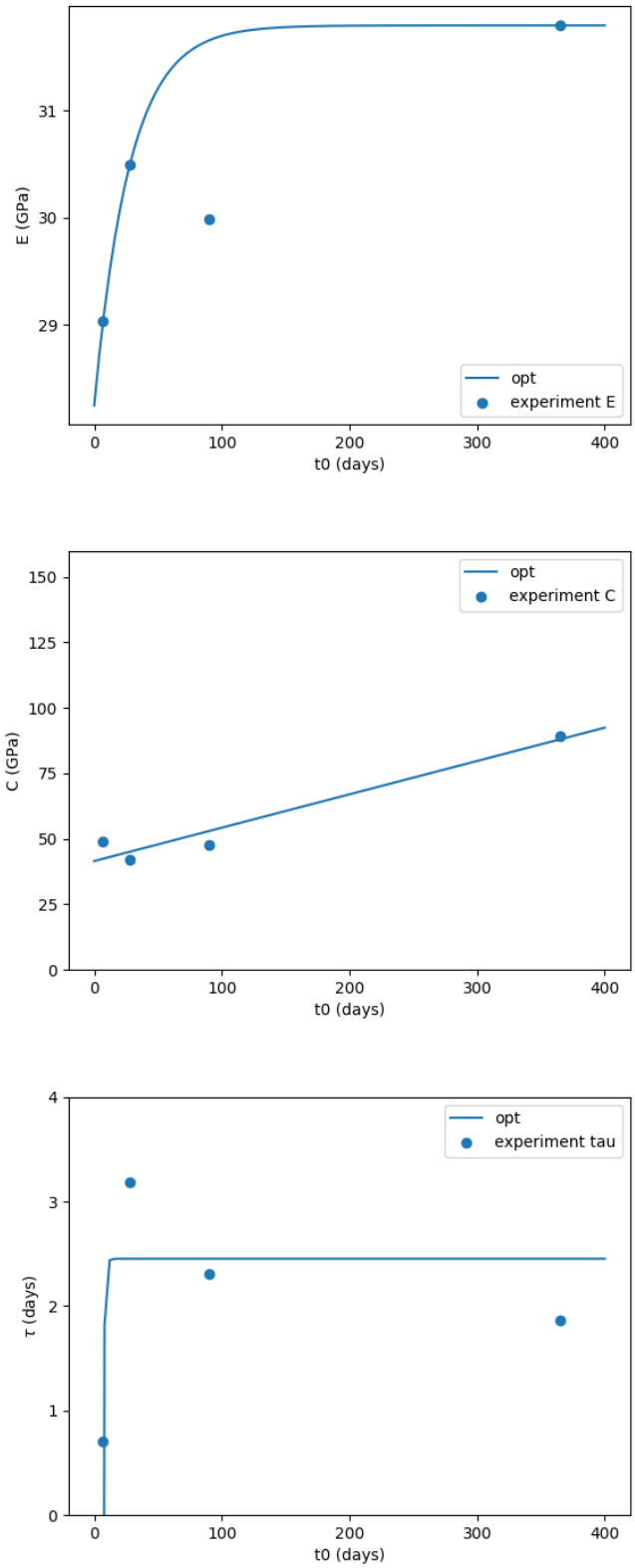

FIGURE 11.29 : Example : evolution of $E(t_0)$ (Top), $C(t_0)$ (Middle) and $\tau(t_0)$ of the creep test bench as functions of t_0, mortar scale.

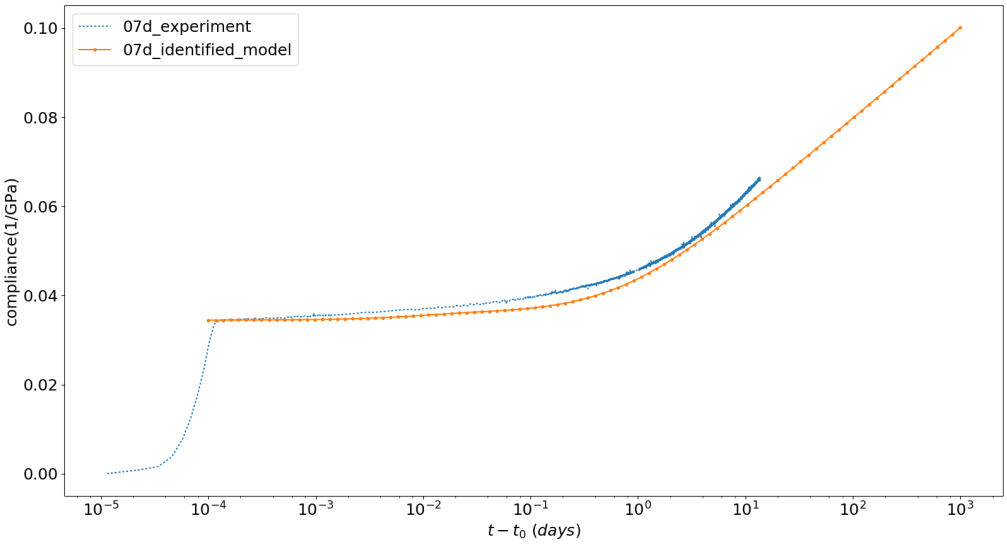

FIGURE 11.30 : Example : evolution of the basic creep compliance and comparison of the modeling results with the experimental results, mortar scale, $t_0 = 7$ days.

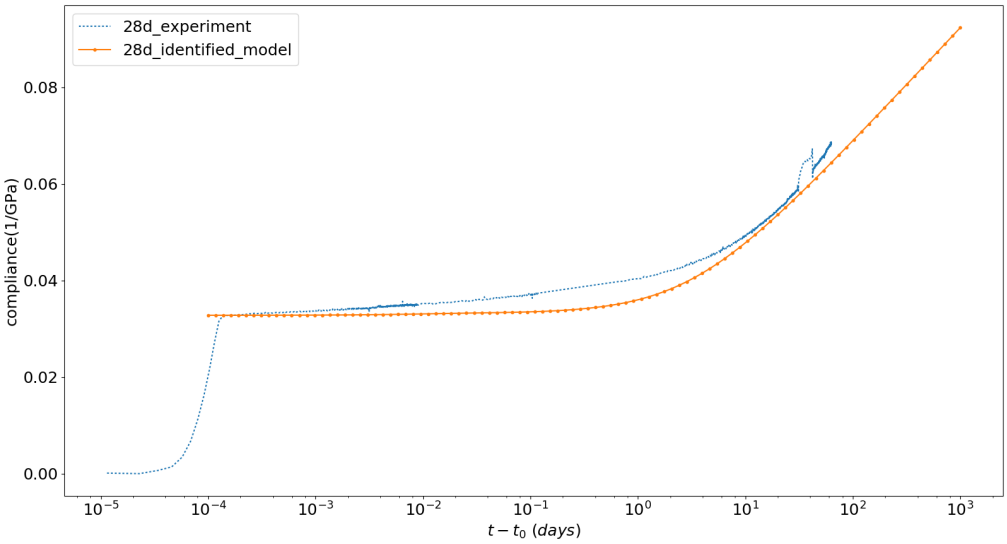

FIGURE 11.31 : Example : evolution of the basic creep compliance and comparison of the modeling results with the experimental results, mortar scale, $t_0 = 28$ days.

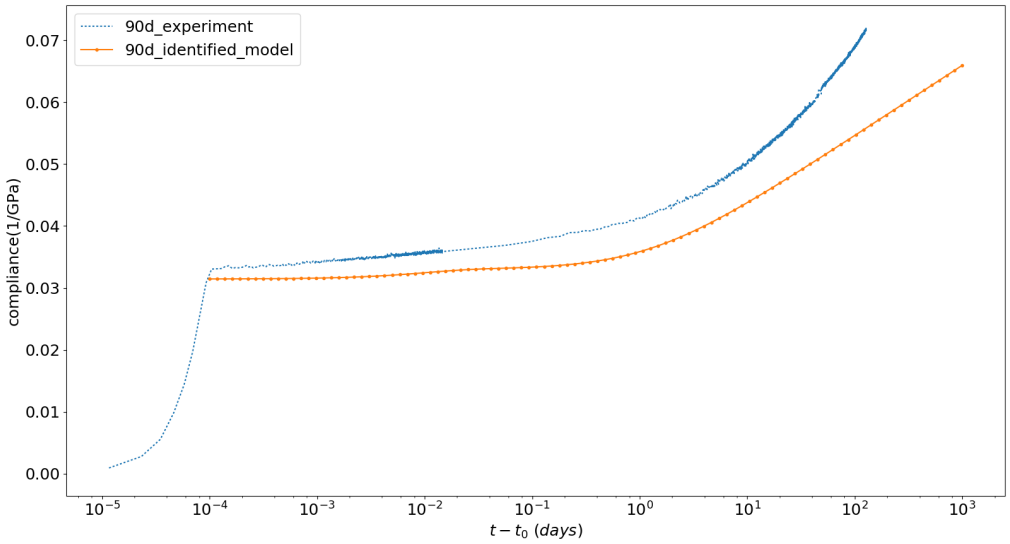

FIGURE 11.32 : Example : evolution of the basic creep compliance and comparison of the modeling results with the experimental results, mortar scale, $t_0 = 90$ days.

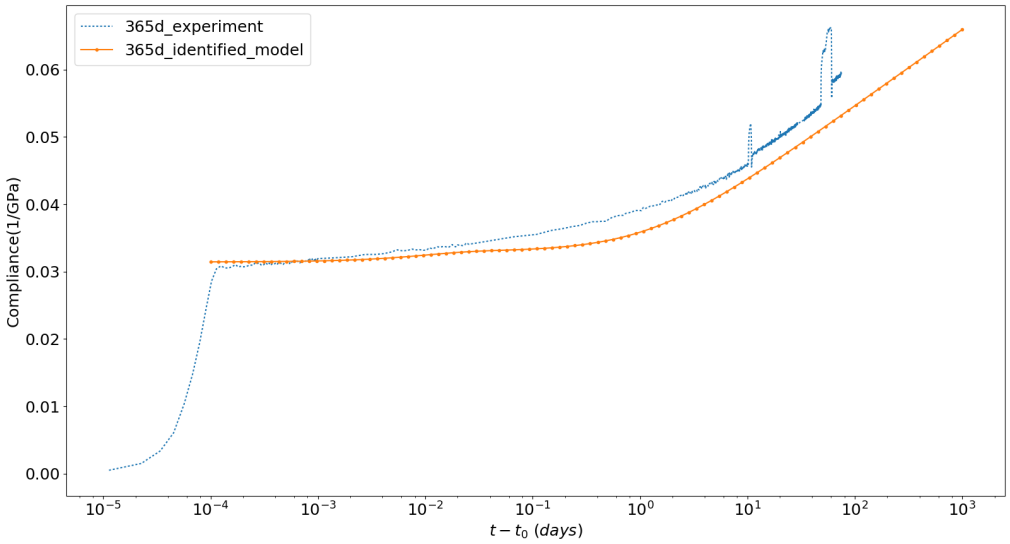

FIGURE 11.33 : Example : evolution of the basic creep compliance and comparison of the modeling results with the experimental results, mortar scale, $t_0 = 365$ days.

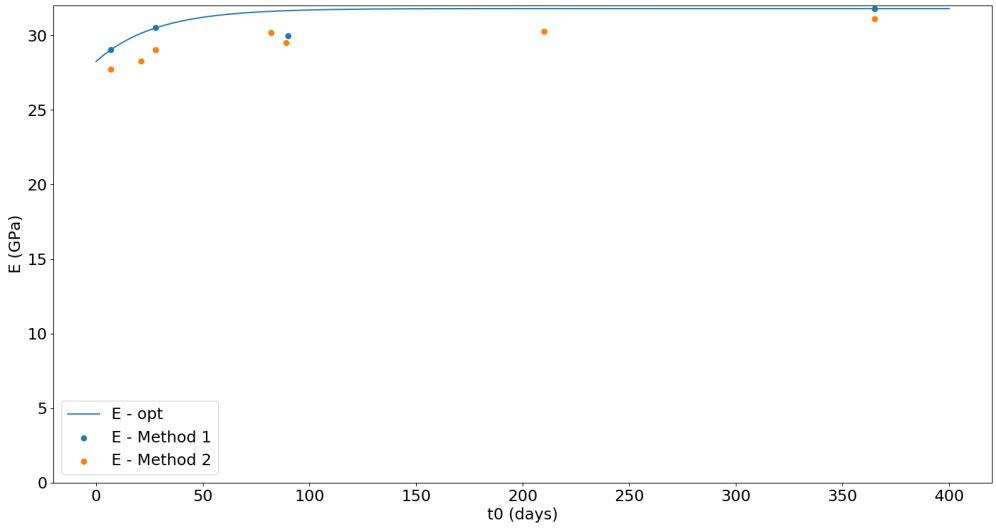

FIGURE 11.34 : Example : evolution of $E(t_0)$ of the Creep test as functions of t_0 with comparison of two methods to identify the experimental value $E(t_0)$, scale of mortar.

11.4.6 Physical submodel for identified parameters at scale of VeRCoRs concrete

The same form of the physical submodel could be defined to describe the parameters as a function of age of loading t_0 at the scale of the VeRCoRs concrete, as in Eq.11.26.
The method of nonlinear optimization is applied with the Eq.11.26 to calculate the proper parameters t_{ini}, A_{ini}, A_∞ and τ_f for $E(t_0)$, $C(t_0)$ and $\tau(t_0)$. Here, the parameters t_{ini}, A_{ini}, A_∞ and τ_f are optimized to each function for $E(t_0)$, $C(t_0)$ and $\tau(t_0)$ with the obtained experimental data from the two creep test benches for $t_0 = 2, \quad 7, \quad 28, \quad 90$ days. Then with the deducted function $E(t_0)$, $C(t_0)$ and $\tau(t_0)$ for $t_0 = 2, \quad 7, \quad 28, \quad 90$ days, the values of $E(t_0)$, $C(t_0)$ and $\tau(t_0)$ with other age of loading t_0 could be calculated. Fig.11.35, Fig.11.36 and Fig.11.37 show the evolution of $E(t_0)$, $C(t_0)$ and $\tau(t_0)$ of the two creep test benches as functions of t_0.

An evident difference could be identified from the comparison of the same parameter of $C(t_0)$ and $\tau(t_0)$ between the two different benches. Nevertheless, the values of $E(t_0)$ are quite similar between the two benches. At the scale of the VeRCoRs concrete, it is more difficult to maintain the regularity of the evolution as a function of t_0 for the parameters identified from the Bench 2 than from the Bench 1. The cause may be that there were in total two times of oscillation of the experimental temperature (with the age of loading $t_0 = 28$ days : the experimental temperature rised frome 20°C to 26°C after 46 days of loading time during one day ; with the age of loading $t_0 = 90$ days : the experimental temperature rised frome 20°C to 28°C after 6 days of loading time during one day, Fig.11.39). These accidents influenced the experimental results of the Bench

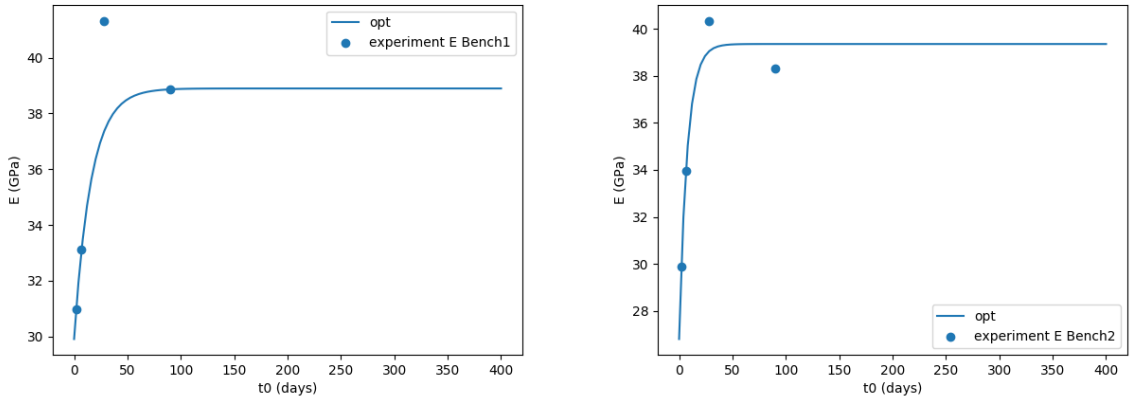

FIGURE 11.35 : Example : evolution of $E(t_0)$ of the two creep test benches as functions of t_0, the VeRCoRs concrete scale.

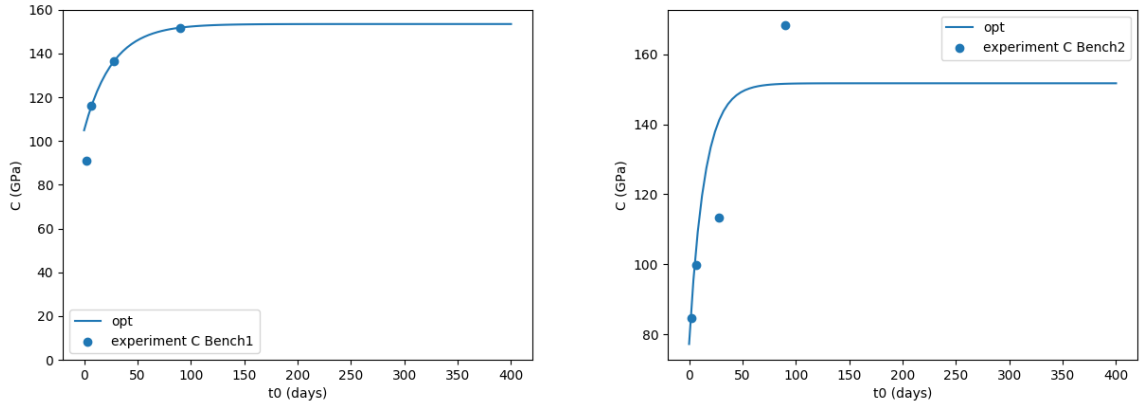

FIGURE 11.36 : Example : evolution of $C(t_0)$ of the two creep test benches as functions of t_0, the VeRCoRs concrete scale.

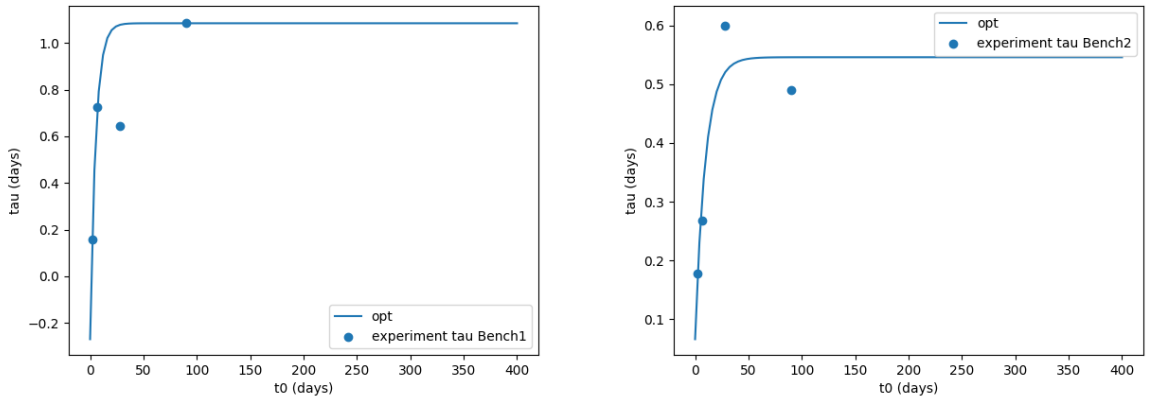

FIGURE 11.37 : Example : evolution of $\tau(t_0)$ of the two creep test benches as functions of t_0, the VeRCoRs concrete scale.

2 for the creep experiments with the ages of loading $t_0 = 28,\ 90$ days.

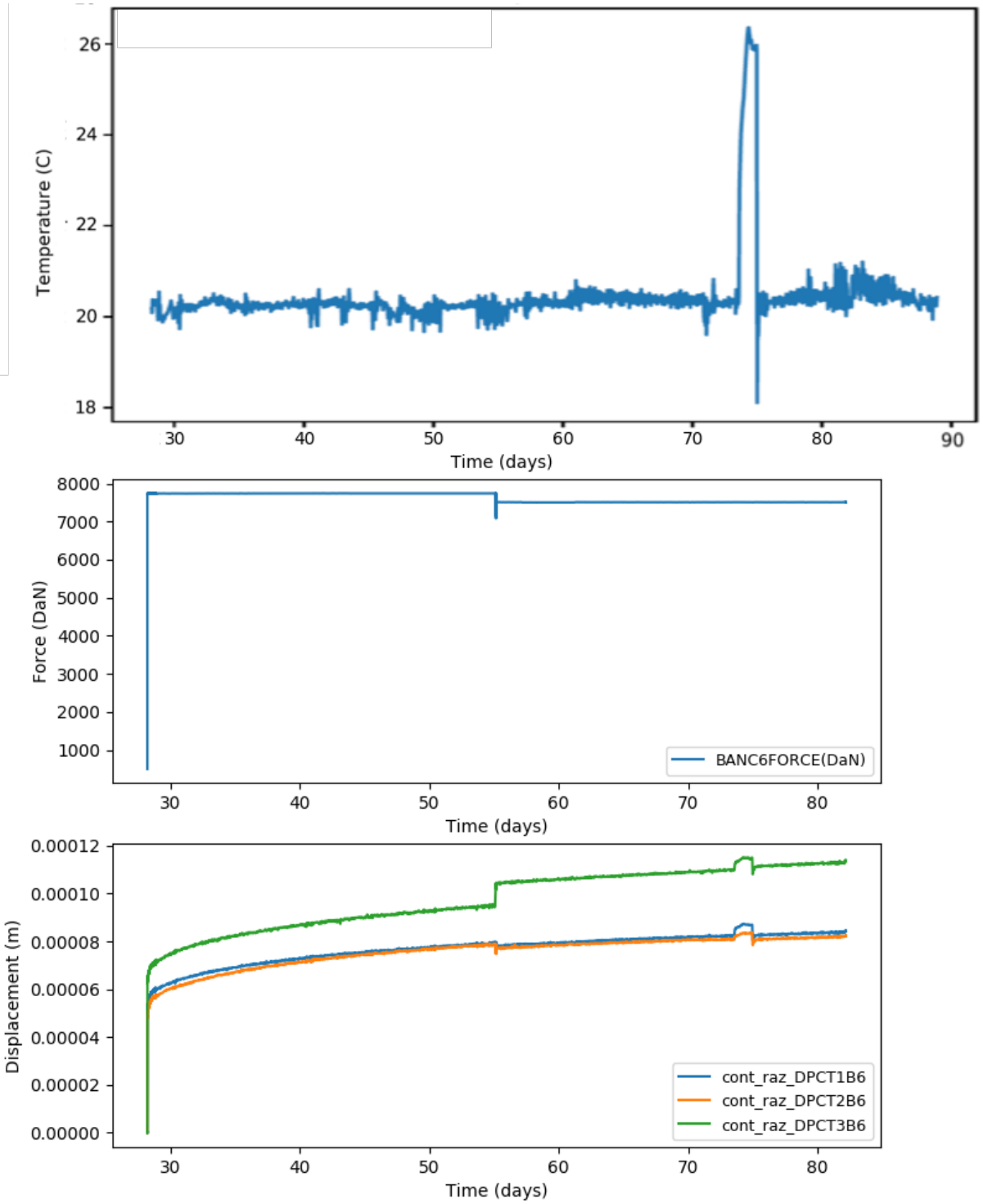

FIGURE 11.38 : Evolution of loaded force, of temperature and of displacement measured by the 3 LVDT displacement sensors installed on the Bench 2 for the creep experiment at the scale of the VeRCoRs concrete with the age of loading $t_0 = 28$ days.

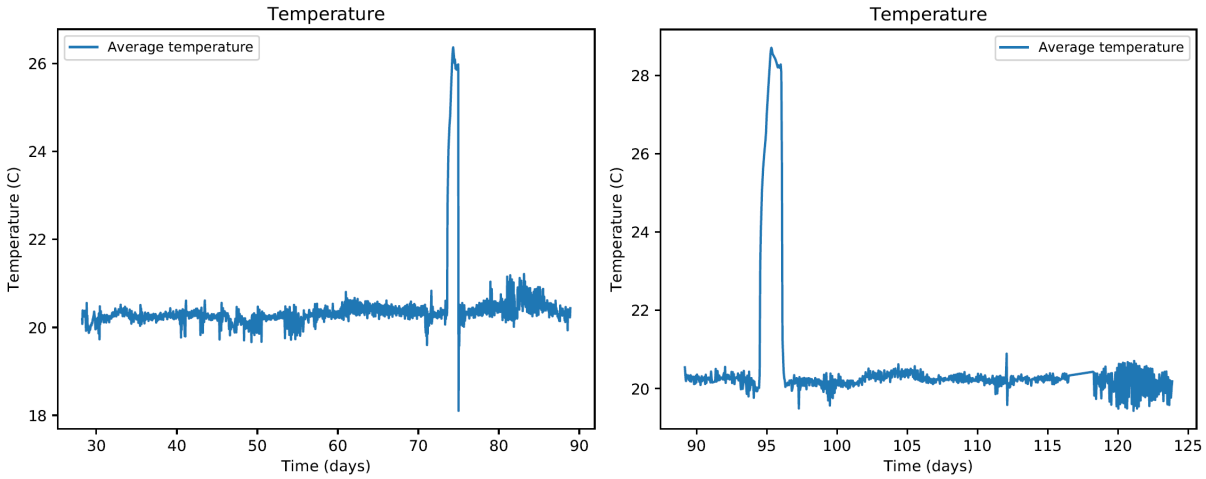

FIGURE 11.39 : Example : evolution of $\tau(t_0)$ of the two creep test benches as functions of t_0, the VeRCoRs concrete scale.

As shown in Fig.11.38 and in Fig.11.39, the oscillation added noise to the experimental results, which makes the data of the Bench 2 at the scale of the VeRCoRs concrete with the age of loading $t_0 = 28,\ 90$ days less reliable than that of the Bench 1.

11.4.7 Identified Young's modulus at scale of VeRCoRs concrete

In addition, another comparison is carried out on Young's modulus $E(t_0)$ identified by different methods.
On one hand, the method of nonlinear optimization is then applied with the Eq.11.26 to calculate the proper parameters t_{ini}, A_{ini}, A_∞ and τ_f for $E(t_0)$ with t_0 as any age of loading from the identified parameters $E(t_0)$ with $t_0 = 2,\quad 7,\quad 28,\quad 90$ days (Method 1).
On the other hand, the parameters $E(t_0)$ with $t_0 = 2,\quad 6,\quad 7,\quad 21,\quad 28,\quad 82,\quad 90$ days could also be calculated with the experimental results of the loaded force variation ΔF and the average displacement variation $\overline{\Delta\xi}$ during the loading and unloading period with ages of loading $t_0 = 2,\quad 7,\quad 28,\quad 90$ days and ages of unloading $t_0' = 6,\quad 21,\quad 82$ days (Method 2).
Moreover, at the scale of the VeRCoRs concrete, we have also carried out the simple compression test to determine Young's modulus directly in EDF, in CEA and in CEBTP.
Fig.11.40 shows the comparison of these two methods.

Fig.11.40 shows that the experimental results of $E(t_0)$ identified by the Method 2 are less than those identified by the Method 1.
The reason indicates the same principe. the evolution of strain/stress ϵ/σ is ploted in a semi-log graph (as in Fig.11.16), which forms the plot with the pure elastic behaviour period and the long-term viscoelastic behaviour period. The well defined elastic behaviour period in the semi-log graph helps to avoid the influence of the viscoelastic behaviour of the material and calculate

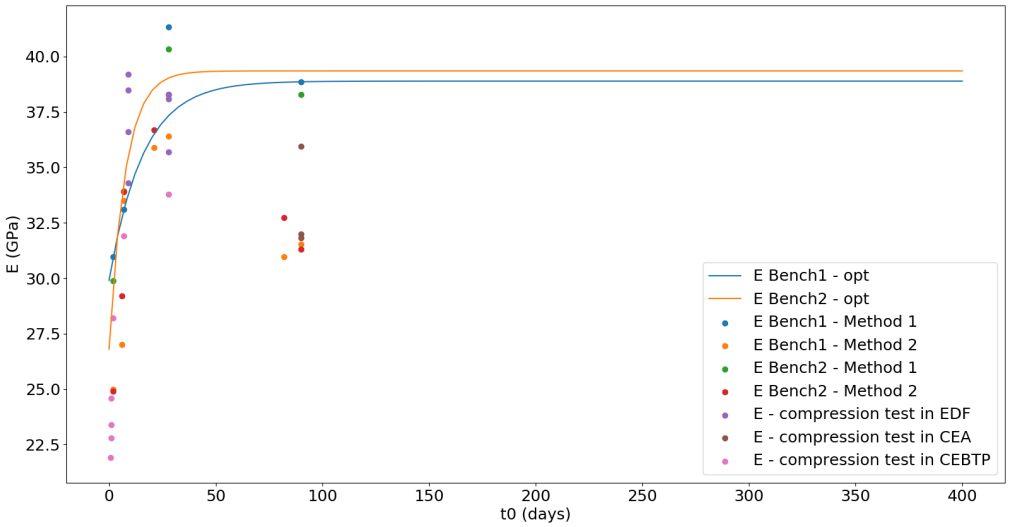

FIGURE 11.40 : Example : evolution of $E(t_0)$ of the Creep test as functions of t_0 with comparison of simple compression test results and of two methods to identify the experimental value $E(t_0)$, scale of the VeRCoRs concrete.

the elastic $E(t_0)$ precisely. However, during the application of the Method 2, the loaded force variation ΔF and the average displacement variation $\overline{\Delta\xi}$ are calculated as Eq.11.27 and Eq.11.28. Here, the values of F_{end} is measured as the last value of the loaded force during the loading step or the first value of the loaded force during the unloading step (which is certainly the maximum force in the loading ou unloading step). But during the last moment of the loading step or the first moment of the unloading step, material loaded enters already in the viscoelastic period. So the Method 1 measures the initial tangent modulus and the Method 2 measurs the secant modulus (Fig.11.28). This is the reason why the Method 2 underestimate $E(t_0)$.
In addition, a part of the data of the Young's modulus measured by the simple compression test to determine Young's modulus directly in EDF, in CEA and in CEBTP are similar to the results given by the function $E(t_0)$. Precisely, the results in CEBTP indicate well the evolution of the Young's modulus at the early ages and the results detemined by our compression tests in EDF indicate well the evolution in the long term.

11.4.8 Rate of uniaxial creep compliance

The rate $dJ(t_0)/dt$ of the uniaxial creep compliance is displayed in Fig.11.41, Fig.11.42 and Fig.11.43.

In Fig.11.41, Fig.11.42 and Fig.11.43, wavelet transforms are applied for denoising. Wavelet trans-

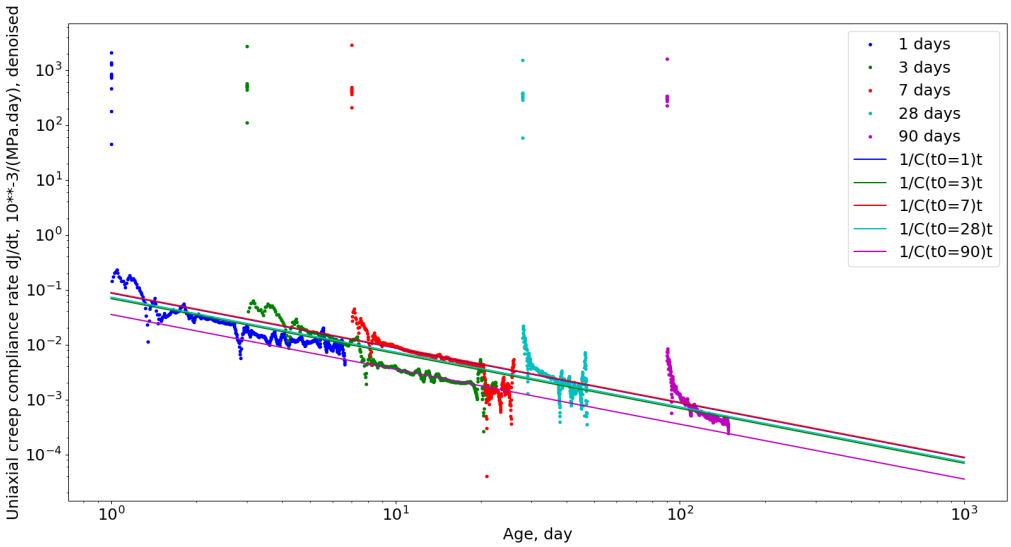

FIGURE 11.41 : Uniaxial creep compliance rate for cement paste samples loaded at different ages. Dots are experimental data. Lines are obtained from hybrid models of creep for $C(t_0)$.

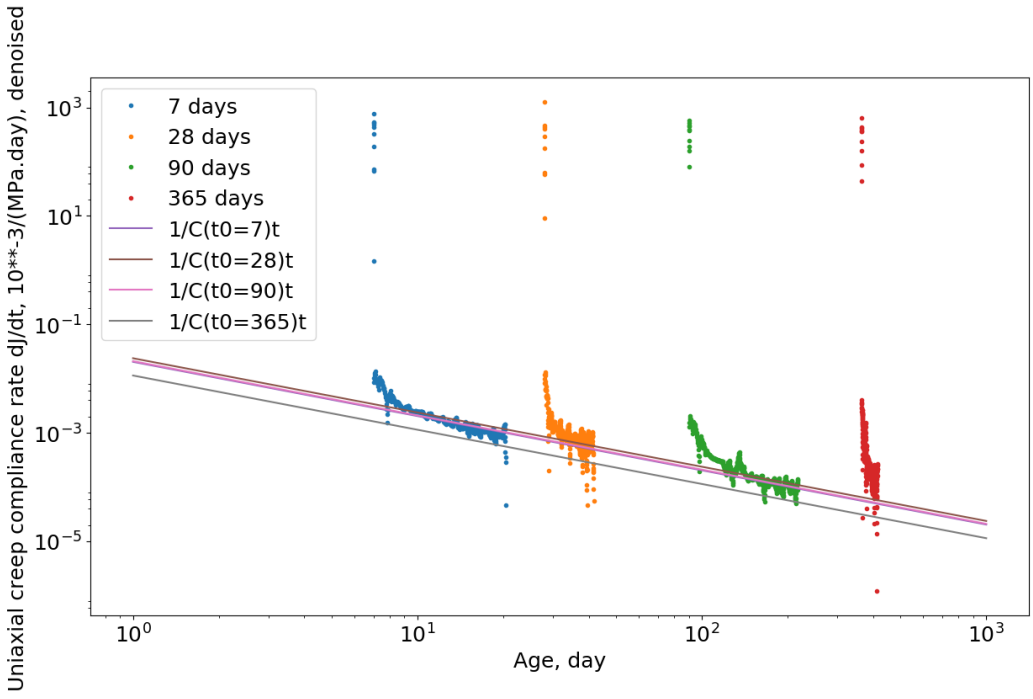

FIGURE 11.42 : Uniaxial creep compliance rate for mortar samples loaded at different ages. Dots are experimental data. Lines are obtained from hybrid models of creep for $C(t_0)$.

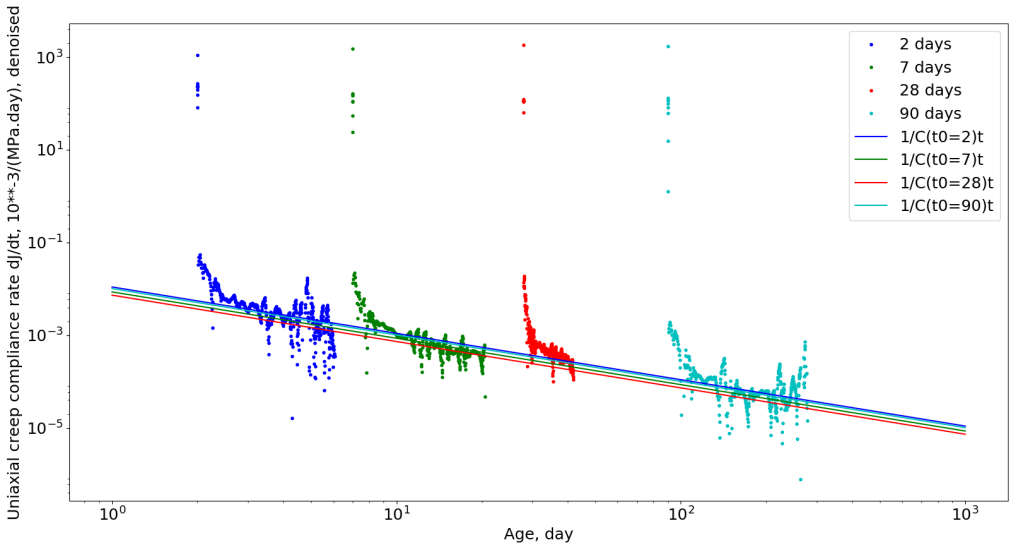

FIGURE 11.43 : Uniaxial creep compliance rate for the VeRCoRs concrete samples loaded at different ages. Dots are experimental data. Lines are obtained from hybrid models of creep for $C(t_0)$.

forms can decompose a serie of experimental results into several scales that represent different frequency bands, and at each scale, the position of this serie's instantaneous structures can be determined. Such a property has been used for denoising.[182]
It could be clearly observed that, after one day of loading, the rate of the uniaxial creep compliance decreased as the inverse of time : indeed, for large times, $dJ(t_0)/dt \approx 1/C(t_0)t$, where $C(t_0)$ are indentified by the experimental results with the hybrid model. The only exception occurs at $t_0 = 1$ year at the scale of mortar, but the main cause is that the experimental data for $t_0 = 1$ year is not enough to arrive at the level of the asymptotic trend of $1/C(t_0 = 1\ year)t$. The further cumulation of the experimental data for $t_0 = 1$ year could solve this incoherence.
Such an observation translates into a uniaxial creep compliance which, on the long-term, evolves logarithmically with respect to time.

11.4.9 Upscaling using homogenization

At first, the Table 11.2, the Table 11.3 and the Table 11.4 are used to present the identified parameters t_{ini}, A_{ini}, A_∞ and τ_f for each mechanical parameter $E(t_0)$, $C(t_0)$ and $\tau(t_0)$ at each scale of material.

With the same principle introduced in the previous section, the Mori–Tanaka homogenization scheme and the self-consistent homogenization scheme are then applied to upscale the ageing

TABLE 11.2 : Identified parameters at the scale of cement paste.

	t_{ini} (days)	τ_f (days)	A_∞	A_{ini}
$E(t_0)$	0.0144	12.4223	7.8103 GPa	11.5463 GPa
$C(t_0)$	0.00281	10.1038	18.4177 GPa	9.7595 GPa
$\tau(t_0)$	4.3104	13.8665	1.7831 days	0.5343 day

TABLE 11.3 : Identified parameters at the scale of mortar.

	t_{ini} (days)	τ_f (days)	A_∞	A_{ini}
$E(t_0)$	0.0156	27.7992	3.5418 GPa	28.2506 GPa
$C(t_0)$	1.5604	13.9382	17.7561 GPa	61.4131 GPa
$\tau(t_0)$	6.6002	1.0611	2.2451 days	0.0000 day

TABLE 11.4 : Identified parameters at the scale of the VeRCoRs concrete.

	t_{ini} (days)	τ_f (days)	A_∞	A_{ini}
$E(t_0)$	0.6121	15.9412	8.6483 GPa	30.2469 GPa
$C(t_0)$	1.5042	14.4063	67.0811 GPa	84.6233 GPa
$\tau(t_0)$	1.1779	5.2722	1.0839 days	0.0014 day

viscoelastic behaviour from the scale of cement paste to the scale of mortar (with cement paste as the ageing viscoelastic matrix and sand as the inclusion), and from the scale of mortar to the scale of concrete (with mortar as the ageing viscoelastic matrix and coarse aggregate as the inclusion).

The ageing viscoelastic behaviours for the matrix phase (the phase of cement paste for the scale of mortar, and the phase of mortar for the scale of the VeRCoRs concrete) are defined by the hybrid model in this section, with the parameters of model identified on the experiments.

The Mori–Tanaka and the self-consistent homogenization schemes are then applied to calculate the effective ageing uniaxial compliance function at the scale of mortar and of the VeRCoRs concrete.

The effective ageing uniaxial compliance function is plotted in Fig.11.44 ane Fig.11.45 as continuous lines with the method mentioned in [166].

According to the comparison between the upscaling results in Fig.11.44, the evolution of the creep compliance result based on the parameters as functions of t_0 is close to that based on Interpolation/extrapolation of identified experimental data. So it can be concluded that the deducted function $E(t_0)$, $C(t_0)$, $\tau(t_0)$ and $E_{Kelvin}(t_0)$ could be applied to calculate the values of $E(t_0)$, $C(t_0)$, $\tau(t_0)$ and $E_{Kelvin}(t_0)$ with other age of loading t_0.

The comparison results are acceptable, which demonstrate that the ageing compliance model is well adapted to the experimental results. And this model can be applied to predict the ageing creep compliance of the VeRCoRs concrete right from the scale of the microstructure of cement

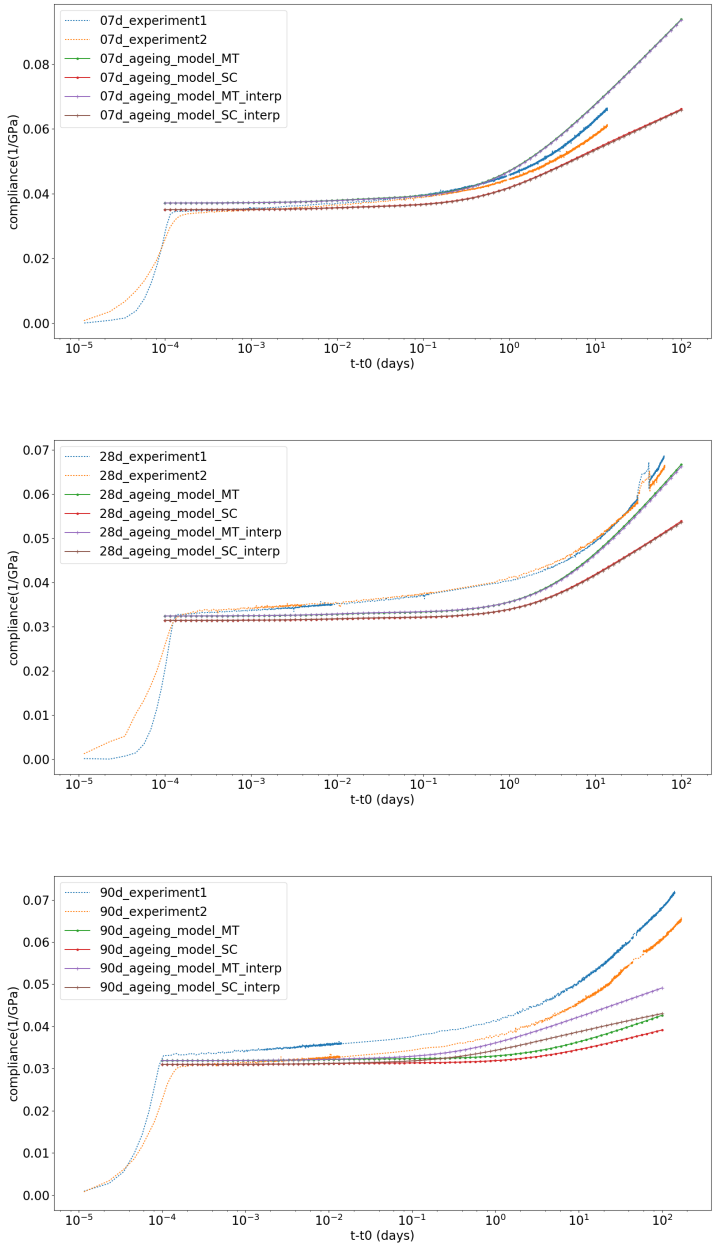

FIGURE 11.44 : Effective uniaxial compliance [157] functions of mortar ($w/c = 0.525$), plotted for various ages of loading t_0 =7 days, 28 days and 90 days. Comparison between the experimental results on mortar (2 dotted lines) and the upscaling using the Mori–Tanaka homogenization scheme (green continuous line based on the parameters as functions of t_0 and purple continuous line based on Interpolation/extrapolation of identified experimental data) and the self-consistent homogenization scheme (red continuous line based on the parameters as functions of t_0 and brown continuous line based on Interpolation/extrapolation of identified experimental data) from the scale of cement paste to the scale of mortar.

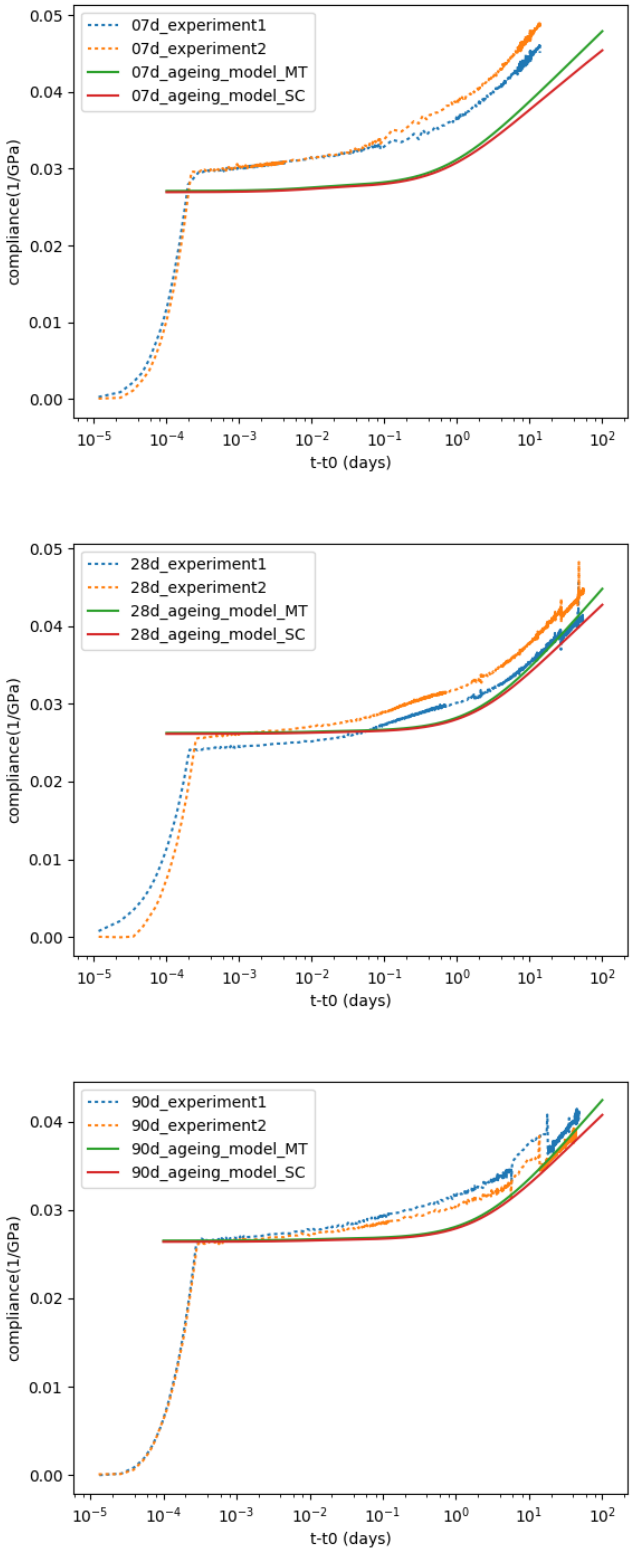

FIGURE 11.45 : Effective uniaxial compliance [157] functions of the VeRCoRs concrete (w/c=0.525), plotted for various ages of loading t_0 =7 days, 28 days and 90 days. Comparison between the experimental results on the VeRCoRs concrete (2 dotted lines) and the upscaling using the Mori–Tanaka homogenization scheme (green continuous line) and the self-consistent homogenization scheme (red continuous line) from the scale of mortar to the scale of the VeRCoRs concrete.

paste.

Comparing between the upscaling using the Mori–Tanaka homogenization scheme and the self-consistent homogenization scheme, it could be concluded that the Mori-Tanaka homogenization scheme gives the modeling results closer to the experimental results. The reason might be that the procedure of the upscaling using the Mori–Tanaka homogenization scheme has been applied in the context of materials exhibiting a matrix-inclusion morphology, which is more adapted to the morphology of mortar (with cement paste as the matrix and sand as the inclusions) and that of the VeRCoRs concrete (with mortar as the matrix and coarse aggregates as the inclusions) than the self-consistent homogenization scheme applied in the context of materials exhibiting polycrystalline microstructures.

However, the model shows the tendency to underestimate the experimental results. It thus opens to us new ways for improving the quality of the model by :

1. Taking into account the cement paste/aggregate interface ;
2. Developing the microcracking of the REV during hydration.

Chapitre 12

Comparisons between cement paste model and basic creep experimental results

On one hand, an application to the self-consistent scheme for cement paste has been carry out in the first Part of this thesis. On the other hand, the basic creep experimental results of cement paste have been obtained in the experiments described in the sencond Part of this thesis. This chapter compares the ageing modeling results and the experimental results at the scale of cement paste.
A simplified point of view is adopted in the first Part of this thesis : both anhydrous and hydrates are not detailed but considered as single phases. In other words, only three phases coexist : anhydrous, hydrates, and capillary porosity. As the drained behaviour is sought, capillary water is disregarded.
To extend the precision of the ageing model, adaptation of the a multiscale micromechanics-hydration model [25] to ageing viscoelasticity is carried out. For the purpose of homogenization, the volume fractions of the more detailed reacting phases are required, which are determined by means of an advanced kinetics model of the four main hydration reactions of ordinary portland cement paste.

Sommaire

12.1 Four main hydration reactions of ordinary portland cement paste

The determination of the volume fractions from cement chemistry requires two steps : (1) determination of the hydration degree of each reaction from reaction kinetic laws and (2) consideration of the volume change associated with each reaction.

12.1.1 Hydration kinetics model

It is common practice in physical chemistry (see, e.g., Atkins [139]) to describe the kinetics of hydration of each clinker phase X ($X = C_3S,\ C_2S,\ C_3A,\ and\ C_4AF$) by nucleation and growth kinetic laws that link the reaction rate $d\xi_X/dt$ to the driving force for the chemical reaction, called the affinity $A(\xi_X)$, in addition to any kinetics constant that determines the time scale of the chemical reaction.
The detail of this hydration kinetics model and the determination of the volume fractions of each phase is described in [25].

12.2 Application to ageing creep of cement paste due to hydration

It is necessary to mention the multiscale microstructure of cement-based materials used in [25] to describe the multiscale concept in the article.
The adaptation of this model is then carried out to realize the homogenization of evolving microstructure with viscoelastic phases.

12.2.1 Mechanism at Level I scale according to evolution of C-S-H gel

As mentioned in [25], from a morphological point of view, the $C-S-H$ matrix can be considered as a two-phase material, composed of a stiffer inclusion phase ($C-S-H_b$ phase) embeded into a softer matrix phase ($C-S-H_a$ phase). At early ages, the volume fractions of these two phases depend on the progress of the C_3S and C_2S clinker hydration. This level is the starting point for the ageing homogenization approach developed in this chapter.
The mechanical parameters of both styles of $C-S-H$ (the bulk and shear stiffness (k and μ) and viscosities (η and γ)) are obtained by [25] (Table 12.1).

The Mori-Tanaka scheme is appropriate for materials that exhibit a strong matrix-inclusion

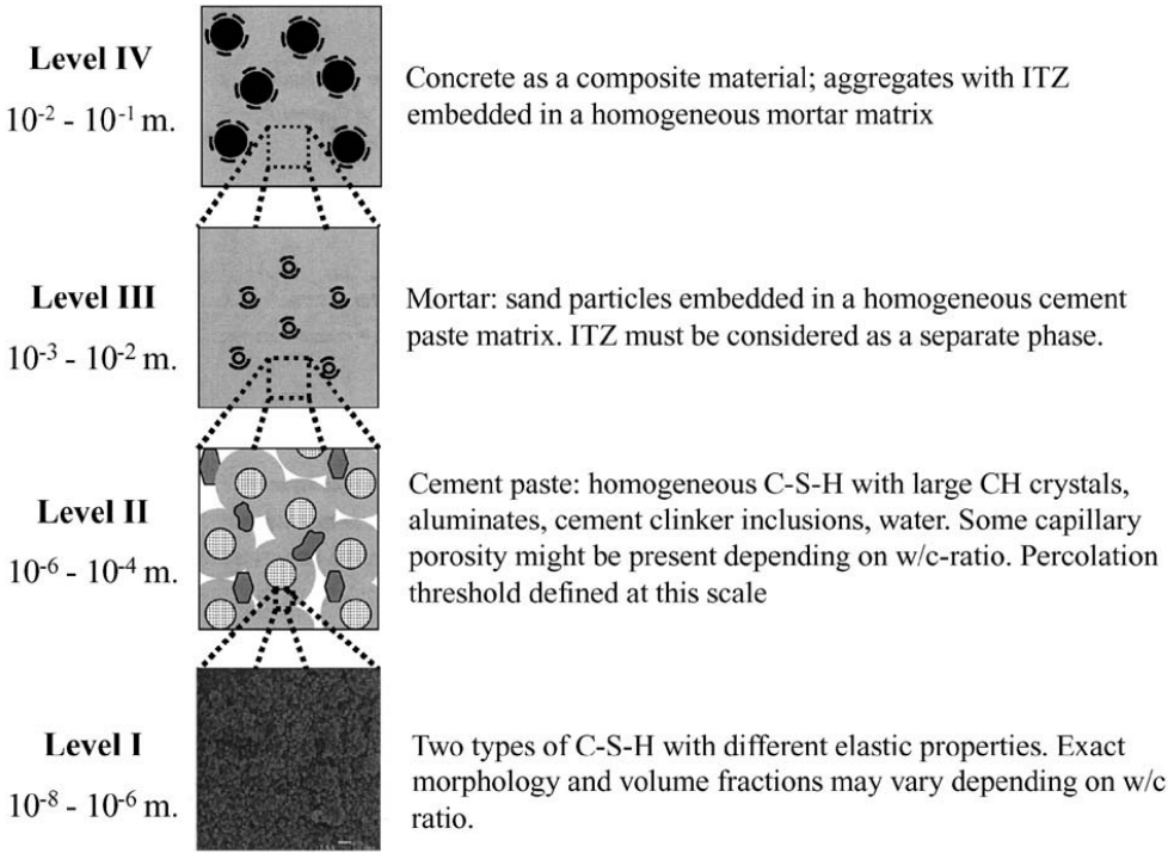

FIGURE 12.1 : Multiscale microstructure of cement-based materials, adapted from [46].

TABLE 12.1 : Mechanical parameters (stiffness and viscosities) of $C-S-H$ gel.

Type	E (GPa)	ν	η	γ
$C-S-H_a$	21.7	0.24	0.2	0.133
$C-S-H_b$	29.4	0.24	0.2	0.133

morphology and mechanical interactions in between particles. This scheme is chosen for the two-phase spherical inclusion composites at Level I (two styles of $C-S-H$ gel).
Specifically, the process for establishing the Level I-related evolution mechanism of $C-S-H$ gel is as follows :

1. Calculate the volume fractions of $C-S-H_a$ and $C-S-H_b$ as function of hydration degree using the kinetic model of hydration. ;
2. For each discretization step, calculate the relaxation matrix of the homogenized $C-S-H$ gel by the Mori-Tanaka scheme ;
3. Apply the homogenized relaxation matrix of the $C-S-H$ gel to the modeling of the fictitious phases of the "pore -> $C-S-H$" and "anhydrous -> $C-S-H$" transformations.

It should be noted that the volume fractions of $C-S-H_a$ and $C-S-H_b$ at each time step at the level I scale ($f^i_{C-S-H_{a1}}$ and $f^i_{C-S-H_{b1}}$) are calculated by their relative volume fractions in the whole $C-S-H$ matrix at the level II scale ($f^i_{C-S-H_{a2}}$ and $f^i_{C-S-H_{b2}}$) :

$$f^i_{C-S-H_{a1}} = \frac{f^i_{C-S-H_{a2}}}{f^i_{C-S-H_{a2}} + f^i_{C-S-H_{b2}}} \tag{12.1}$$

$$f^i_{C-S-H_{b1}} = \frac{f^i_{C-S-H_{b2}}}{f^i_{C-S-H_{a2}} + f^i_{C-S-H_{b2}}} = 1 - f^i_{C-S-H_{a1}} \tag{12.2}$$

12.2.2 Homogenization scheme applied at level II scale

The first Part of the thesis shows that the application of a self-consistent scheme to estimate creep compliance by homogenization is feasible. This scheme describes well materials characterized by perfect disorder (polycrystal). Being related to percolation theory, it allows one to account for a percolation threshold. This homogenization scheme, therefore, is chosen for the Level II homogenization to account for a solid percolation threshold[46][25]. That is, modeling the ageing creep compliance at the scale of cement paste.
According to the microstructure evolution that we defined in the first Part, the $C-S-H$ gel phase is simulated by the Maxwell rheological model and the other phases are simulated by the elastic model.
There are two phase transformation processes at the Level II scale :

1. The dissolution of the four phases of the clinker ;
2. The precipitation of the $C-S-H$ gel, CH and aluminates.

With the same principe described in the first Part, the idea of the proposed extension of Bažant solidification theory is to affect an equivalent ageing linear viscoelastic behaviour to each point in the REV.
The subdomain $\Omega_{a\to h}$ is precised to $\Omega_{a\to C-S-H}$ and $\Omega_{p\to h}$ is precised to $\Omega_{p\to C-S-H}$, $\Omega_{p\to CH}$ and $\Omega_{p\to aluminates}$.

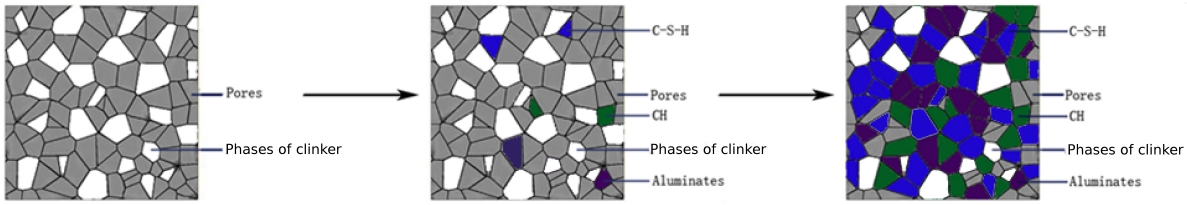

FIGURE 12.2 : Phase transformation processes at the Level II scale.

Three kinds of input data are required : the current values of the volume fractions f_i, the bulk and shear stiffness (k and μ) and viscosities (η and γ) and the sum of fictitious aging viscoelastic phases. Volume fractions are provided by the micromechanical-multi-scale hydration model [25]. The properties of the elementary phases come from [25][161] and are gathered in Table 12.2.

TABLE 12.2 : Mechanical parameters (stiffness and viscosities) for each phase.

Phase	Mechanical parameters
$C-S-H$ gel	$E_{CSH} = 71.6GPa$, $\nu = 0.27$, $\tau = 3.9h$ [158]
CH	$E_{CH} = 38GPa$, $\nu_{CH} = 0.305$
Aluminates	$E_A = 20GPa$, $\nu_A = 0.24$
Anhydrous	$E_X = 135GPa$, $\nu_X = 0.3$
Pore	$k_p = 0$, $\mu_p = 0$

12.3 Comparisons between modeling results and basic creep experimental results

The Fig.12.3 shows the comparisons between ageing creep compliance modeling results and basic creep experimental results.

The red curves are the experimental results and the blue ones are the modeling results.

At the age of loading $t_0 = 1,\ 3,\ 7$ days, the model underestimate directly the instantaneous elastic stiffness of cement paste.

At the age of loading $t_0 = 28$ days, the instantaneous elastic stiffness is well calculated by the model, but the modeling creep compliance value is larger than the experimental result, meaning that the ageing effect is much too taken into account by the model.

At the age of loading $t_0 = 90$ days, the model overestimate directly the instantaneous elastic stiffness of cement paste.

The cause of the differences between the modeling results and the experimental results may be that the input value of the caracteristic time of the dashpot in the model is too small, which means that the mechanical parameters obtained in [25][46][161] are not perfectly correspond to the real mechanical properties of cement paste that we have used for the menufacture of the

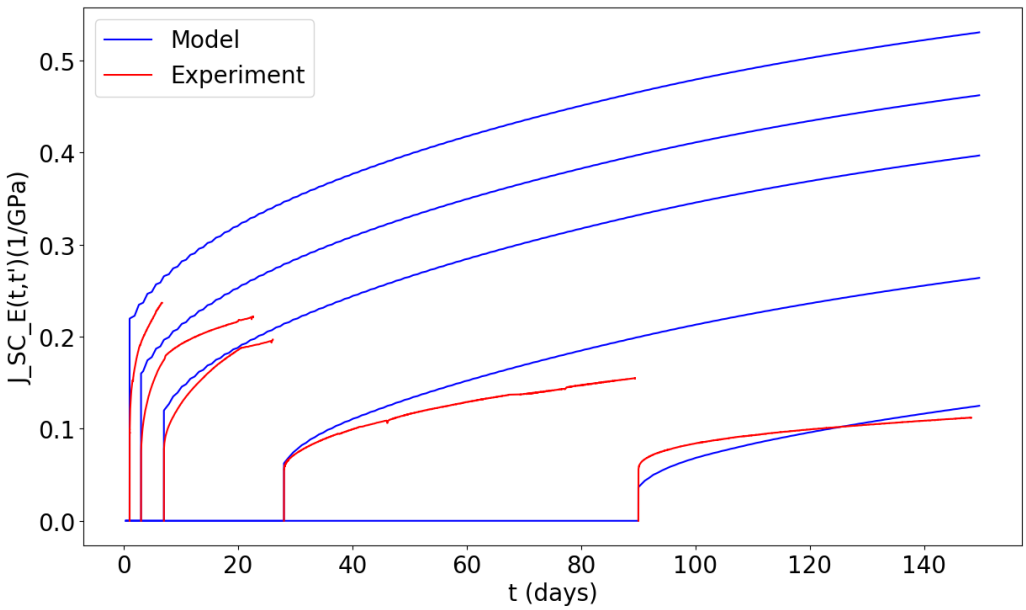

FIGURE 12.3 : Comparisons between ageing creep compliance modeling results and basic creep experimental results.

VeRCoRs concrete. Moreover, compared to the real process of hydration, the hydration model used here is a little simplified.
Nevertheless, the ageing creep model described in the first Part supplies all the tools to calculate the ageing behaviour. Once the more coherent elementary material parameters related to the VeRCoRs concrete are obtained and a more realistic hydration model is developed, more satisfactory results could be obtained.

12.4 Comparisons between "AIO" modeling results and basic creep experimental results

12.4.1 "AIO" morphological model [167]

The "AIO" model corresponds to a more refined, multi-scale, description of hydration which considered two types of hydrates : high density or inner products, and low density or outer products. It combines a topo-chemical mechanism at the surface of anhydrous grains, and precipitation in pore space. At the cement paste scale, anhydrous grains are progressively transformed into inner products, from their boundary inwards. These composite particles (anhydrous and inner products), of constant radius, are surrounded by outer products. The density of the latter increases, due to precipitation of more and more hydrate particles at the lower scale. Both inner products and the solid phase of outer products are assumed to be made up of the same material,

hydrates, which, at the lower scale, are a packing of the C-S-H elementary bricks and gel pores (Fig.12.4). This model of microstructure evolution during hydration is investigated at the cement paste scale (Fig.12.5).

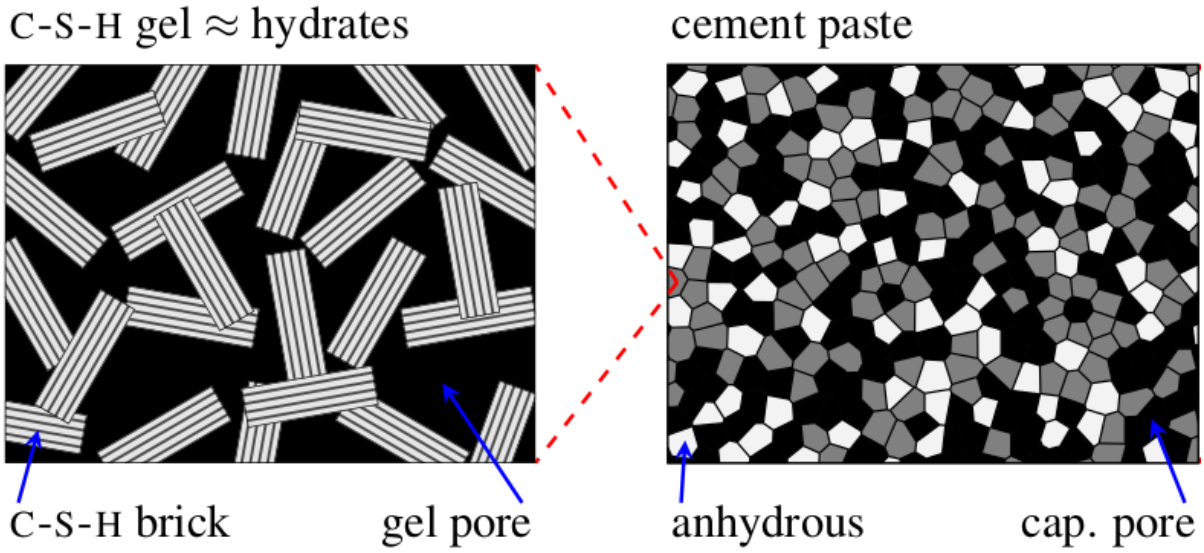

FIGURE 12.4 : Multiscale morphological model of cement paste (schematic 2D representation of 3D model).

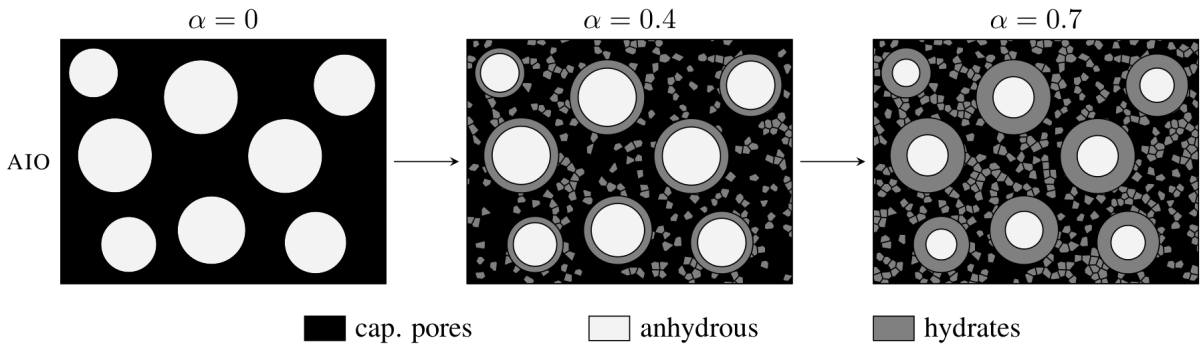

FIGURE 12.5 : Snapshots at hydration degrees $\alpha = 0,\ 0.4,\ 0.7$ of time-dependent morphological models of hydrating cement paste (schematic 2D representation of 3D model). Progressive transformation of anhydrous to inner products and densification of outer products due to precipitation of hydrates (AIO, anhydrous-inner-outer) is considered.

12.4.2 Input parameters

As far as cement hydration is concerned, the Powers model [145] is used to estimate the amount of anhydrous, hydrates and capillary pores as functions of the hydration degree α. Hydration kinetics are modelled using the EDF software tool $Vi(CA)_2T$ [169][170], see Fig.12.6.

Morphological and mechanical parameters are gathered in Table 12.3. Note that even if the vis-

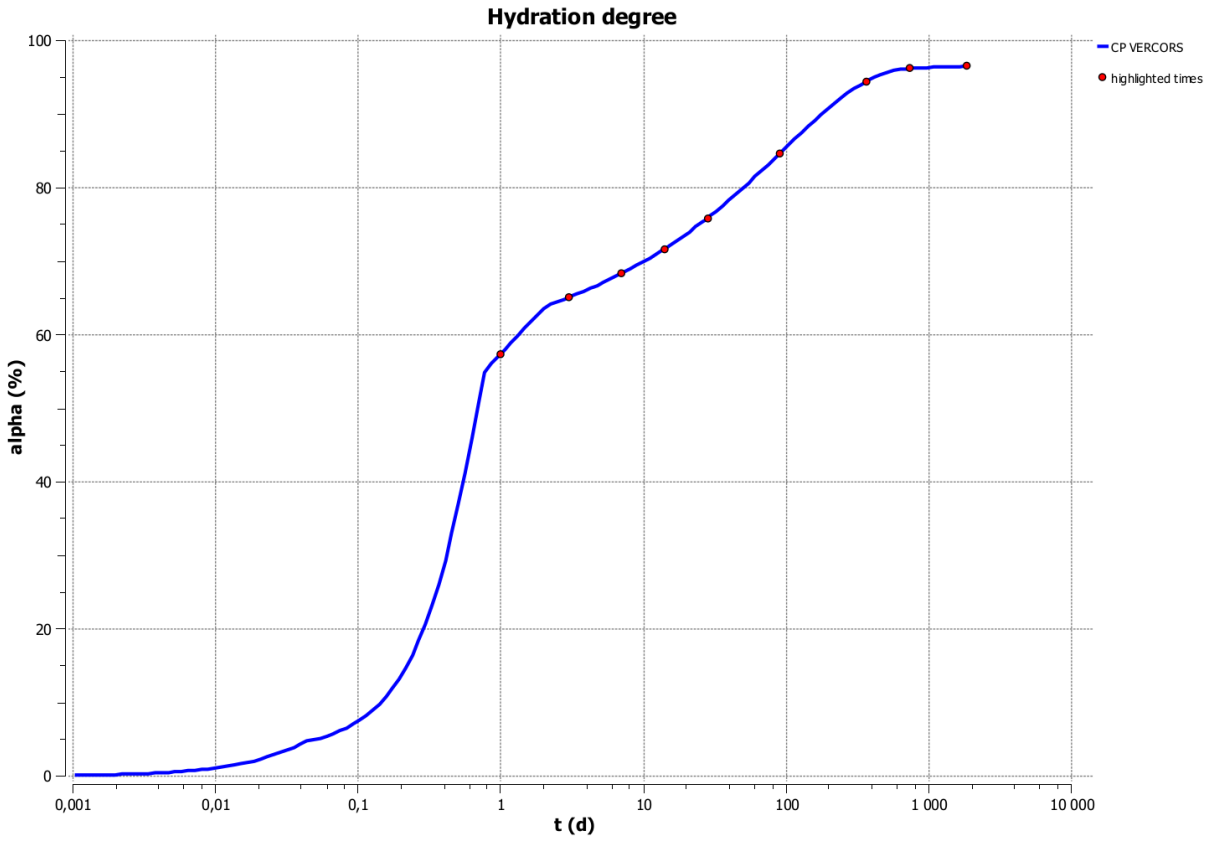

FIGURE 12.6 : Hydration degree of cement paste of the VeRCoRs concrete, estimated using $Vi(CA)_2T$ v2.1.2 [169][170].

coelastic behaviour at the scale of C-S-H gel is of the Maxwell type, at the gel scale the uniaxial effective creep function appears as shown in Fig.12.7 over a wide range of times, from about 1 day to 1 year.

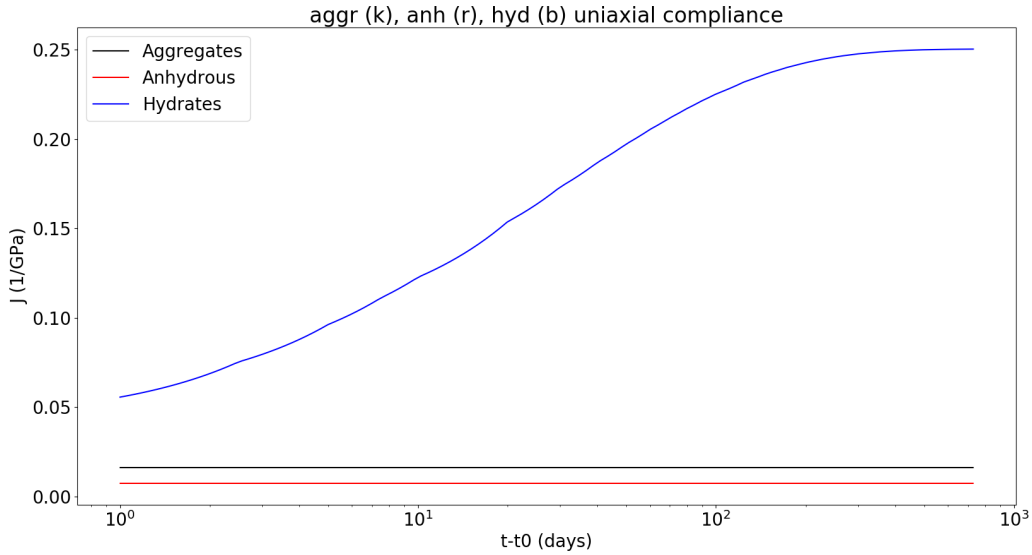

FIGURE 12.7 : Uniaxial creep compliance of C-S-H gel (non ageing linear viscoelastic), anhydrous and aggregates (both elastic).

TABLE 12.3 : Morphological and mechanical input data (χ : aspect-ratio, ϕ : porosity, E : Young's modulus, ν : Poisson's ratio, τ : Maxwell characteristic time of sliding sheets).

	Morphology	Mechanics
C-S-H elementary brick	$\chi = 0.12$[70][165]	$E = 71.6GPa$ [165], $\nu = 0.27$ [165], $\tau = 3.9h$ [158]
Hydrate (C-S-H gel)	$\phi = 0.3$[165]	
Anhydrous		$E = 135GPa$ [194], $\nu = 0.3$ [194]

12.4.3 Model results and comparison to experimental data

Uniaxial creep responses for various loading ages $= 1\ day,\ 3\ days,\ 7\ days,\ 28\ days,\ 90\ days$ are compared to experimental data on Fig.12.8.

The "AIO" model is not sensitive enough to loading age when loaded later. The absolute creep strains are overestimated by a factor of about 2, meaning that the ageing effect is much too taken into account by the model. But it is also important to note that the "AIO"-type model is shown as relevant to predict elasticity at the age larger than 1 day. However, At the age of loading $t_0 = 1$ day, the model underestimate directly the instantaneous elastic stiffness of cement paste.

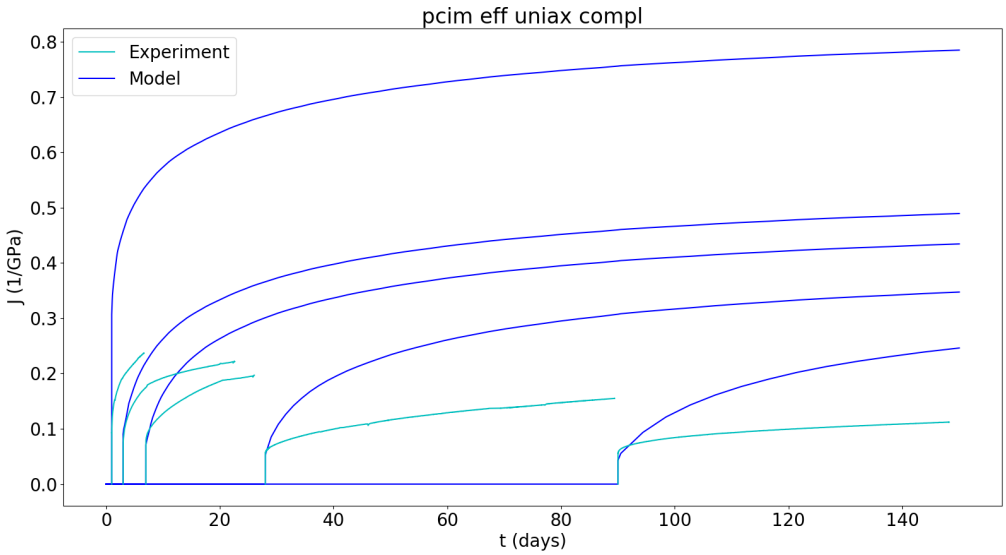

FIGURE 12.8 : Uniaxial basic creep compliance of cement paste of the VeRCoRs concrete for loadings at $t_0 = 1,\ 3,\ 7,\ 28,\ 90$ days, as a function of time. Blue line : modelled using the anhydrous-inner-outer (AIO) morphology at the paste scale. Cyan line : experimental data from EDF described in the Part II.

The morphological model and the chosen homogenization schemes can be improved at the cement paste scale because considering C-S-H as the only hydrates is a limitation. Partitioning hydrates into C-S-H and other elastic ones would reduce the creep strains and this has been shown in the previous section. Furthermore, using a spherical shape to describe the outer hydrates solid particles has proven to yield erroneous setting times [165]. Two ways of improvements are presented in the Part I of this thesis and in [10] on this aspect. On the other hand, considering that hydrates have a constant and uniform (across cement paste) gel porosity may not be realistic : improvements are also shown in the Part I of this thesis. Moreover, the Maxwell model without the fitting procedure based on the experimental results is the simplest and a raw one usable to describe the sliding behaviour of sheets in C-S-H bricks. Its characteristic time has been fit to be consistent with the experimental results and the upscaling results with the fit parameters shown in the previous chapter verify the necessity of corrected model parameters. Last but not least, the cement hydration model, based on Powers model and simple kinetics, could also be improved as phase transformation kinetics have an important influence on the effective ageing viscoelastic behaviour [161], for which a modeling trial will be show in the next chapter.

Chapitre 13

Hydration model with moving boundary conditions

To improve the hydration model described in the first part of this thesis, a more realistic evolution of the dissolution of the anhydrous and the precipitation of the hydrates with more realistic morphology is necessary. A efficient strategy for modeling tricalcium silicate hydration based on through-solution-phase kinetics is demonstrated. This study extends a continuum-based single particle model by including ionic transport and precipitation of the C-S-H gel. Model parameters were fixed based on known values. [79] This chapter aims to generate one of the possible evolutif morphological models for cement hydration that is in good agreement with available experimental results and predictions of homogenization modeling methods shown in the previous parts.
In detail, the processes of the disolution of the clinker grain and the precipitation of the C-S-H gel are modeled, including the nature and influence on kinetics of an early surface hydrate, the moving solid-liquid interface, the manner in which microscopic growth processes lead to the characteristic morphologies of hydration products at larger length scales, and the role played by diffusion in the hydration period.

Sommaire

13.1 Introduction of the moving interface problem

The study of the hydration of cement paste could begin with the modeling of the chemical reaction of Alite (monoclinic tricalcium silicate [C3S(m)]). Alite reacts with water to produce the cementitous gel-phase product calcium silicate hydrate (C-S-H).[204] The present chapter proposes and demonstrates a method that incorporates ion transport and alite reaction. Concerning this type of study, [79] has given a brief review of recent modeling efforts and related experimental data before.

Early C_3S dissolution and subsequent hydration could be described by introducing a transition from etch pit to step retreat dissolution and a coupling work conjoining dissolution with boundary nucleation and growth.[105] This approach causes a sudden transition from very fast to very slow dissolution.[102].

Bullard [37] coupled reaction mechanisms, transport processes and geometry for describing C_3S hydration in a platform called HydratiCA and such concepts as the metastable layer and the calcium hydroxide nucleation [38] were proposed with the aide of HydratiCA.

μic [27] describes the hydration based on a space-filling hypothesis.[104] On the other hand, Masoero et al. [125] proposed another model based on a limited reaction zone hypothesis.

"Advanced single particle model,"[26] proposed a continuum mechanical approach combining transport processes in applying [34]. Biernacki and Xie [26] coupled physics and chemistry, developing a continuum-based single particle model. In the improvement of the model, multi-ionic transport and portlandite precipitation is taken into account. Benchmark work is carried out for the comparison with the experimental datasets and HydratiCA estimates.

In this section on the hydration model with the moving boundary condition, we study the dissolution-diffusion process with a moving interface, and give analytical and numerical solutions to this problem. The section summarizes the main ideas on dissolution of solids governed by diffusion of solute in the adjacent solvent phase, thus making the results accessible to hydration process of cement paste.

For example, during the hydration, the anhydrous core reacts with water. Taking C_3S as an example (the C_2S, C_3A, C_4AF and other anhydrous compositions could also be considered), it dissolves and releases the ions Ca^{2+}, OH^- and $H_2SiO_4^{2-}$, [see Reaction 13.1 below] which eventually precipitate as calcium silicate hydrate [Reaction 13.2] by reacting with additional water. The balance of these ions moves away from the C_3S core surface, through the C-S-H layer, and into the bulk solution where they react to precipitate as a solid by-product, calcium hydroxide [Reaction 13.3].

$$(CaO)_3SiO_2 + 3H_2O \longleftrightarrow 3Ca^{2+}_{(aq)} + H_2SiO^{2-}_{4(aq)} + 4OH^-_{(aq)} \tag{13.1}$$

$$(CaO)_{1.7}SiO_2(H_2O)_{4.9} \longleftrightarrow 1.7Ca^{2+}_{(aq)} + H_2SiO^{2-}_{4(aq)} + 3.2H_2O + 1.4OH^-_{(aq)} \tag{13.2}$$

$$Ca(OH)_2 \longleftrightarrow Ca^{2+}_{(aq)} + 2OH^-_{(aq)} \tag{13.3}$$

Dissolution of solid in liquid is encountered in hydration process of everyday life. In the period from 1870 to 1890, Stefan conducted several experiments on diffusion in gases and liquids under various initial and boundary conditions and published a series of papers. In his last paper on diffusion [147], Stefan gave a detailed description of the dissolution process governed by diffusion of the solute in the adjacent solvent phase.

13.2 First application of Stefan analysis of dissolution-diffusion processes in one-dimensinal Cartesian coordinate system

Fick's first law relates the diffusive flux to the concentration under the assumption of steady state. It postulates that the flux goes from regions of high concentration to regions of low concentration, with a magnitude that is proportional to the concentration gradient (spatial derivative), or in simplistic terms the concept that a solute will move from a region of high concentration to a region of low concentration across a concentration gradient.
In the analytical model, $\phi(x,t)$ is the concentration of liquid phase, $t \in [0,\infty[$ is the time variable, x is the space variable and $S(t)$ is the position of the moving boundary (liquid - solid interface). At first, to facilite the modeling, we suppose that the dissolution and diffusion processes happen in an infinite medium in one-dimensinal Cartesian coordinate system. $J(x,t) \in [0,\infty[$ is the flux. In one (spatial) dimension, the law is :

$$J = -D\frac{\partial \phi}{\partial x} \tag{13.4}$$

where

- J is the "diffusion flux," of which the dimension is amount of substance per unit area per unit time, so it is expressed in such unit as $mol\ m^{-2}s^{-1}$. J measures the amount of substance that will flow through a unit area during a unit time interval. J is function of the space x and of the time t.
- D is the diffusion coefficient or diffusivity. Its dimension is area per unit time, so typical units for expressing it would be m^2/s.
- ϕ (for ideal mixtures) is the concentration, of which the dimension is amount of substance per unit volume. It might be expressed in the unit of mol/m^3.
- x is position, the dimension of which is length. It might thus be expressed in the unit m.

D is proportional to the squared velocity of the diffusing particles, which depends on the temperature, viscosity of the fluid and the size of the particles according to the Stokes-Einstein relation. In dilute aqueous solutions the diffusion coefficients of most ions are similar and have values that at room temperature are in the range of 0.6×10^{-9} to $2 \times 10^{-9} m^2/s$. As the movement of the components must satisfy the principle of the conservation of the solution particle numbers, the

equation must be supplemented by the equation of conservation :

$$\frac{\partial \phi}{\partial t} + \frac{\partial J}{\partial x} = 0 \tag{13.5}$$

where t denotes the time.
In this section, we are working on the assumption that isotropic material is studied (i.e. D is scalar and constant for all species). But it is important to emphasize that the study on the material with D as function of the distance from the anhydrous core and of the time is shown in the later section of this chapter.
The time-derivative, combined with Eq.(13.4), results in the so-called second Fick's law,

$$\frac{\partial \phi}{\partial t} - D\frac{\partial^2 \phi}{\partial x^2} = 0 \tag{13.6}$$

Based on the laws of conservation of matter, the model is supplemented by the condition of Stefan, describing that the quantity of the particles diffused by the flux from the interface equals to the quantity of the particles dissolved from the solid phase :

$$J(x = S(t), t) = -(\phi_s - \phi_l)\dot{S}(t) \tag{13.7}$$

where

- $S(t)$ is the position of the interface, so it is expressed in such unit as m. $S(t)$ is function of the time t.
- ϕ_s is the volumetric quantity of the solid phase, so typical unit for expressing it would be mol/m^3.
- ϕ_l is the local equilibrium concentration of the ion right at the interface, of which the dimension is amount of substance per unit volume. It might be expressed in the unit of mol/m^3, and might be a function of time in the advanced model. At first, we are working on the assumption that only one ion constituting the solid phase. The study applied on the hydration of cement paste with multiple types of ion constituting the solid phase are shown in the next sections.

The configuration studied is based in infinite medium. Two phases are considered here : the solid phase for $x < S(t)$ and the liqud phase for $x > S(t)$.
The boundary conditions to be satisfied by Eq.(13.6) are

$$\begin{cases} x = S(t) : \phi(x = S(t), t) = \phi_l \\ x \to \infty : J(x \to \infty, t) \to 0 \end{cases} \tag{13.8}$$

The boundary conditions limit that :

- For $x = S(t)$, the concentration at the interface equals to the local equilibrium concentration of the ion.

- For $x \to \infty$, there is no flux of the diffusion of the ion.

The initial conditions to be satisfied are

$$\begin{cases} x < S(t) : \phi(x, t = 0) = \phi_s \\ x > S(t) : \phi(x, t = 0) = 0 \\ S(t = 0) = S_0 \end{cases} \tag{13.9}$$

The differential equation (13.6), taken together with the boundary conditions equations (13.8) present the first complete closed mathematical analysis of dissolution of solids in liquids.

13.3 Numerical solutions for Partial differential equation with Stefan Conditions in one-dimensional spherical coordinate system

The previous section indicates that the application of Stefan analysis of dissolution-diffusion processes in one-dimensinal Cartesian coordinate system is possible. In addition, to develope a more realistic model, we could turn to solve the one-dimensional spherical one-phase Stefan problem by doing it semi-automatically in using the theoretical structure of the application of Stefan analysis of dissolution-diffusion processes in one-dimensinal spherical coordinate system. The numerical solution is found out for the partial differential equation with the application of a volume-based finite difference approach. We begin by immobilizing the moving boundary by using a normalized variable. In one-dimensional spherical coordinate system, so the radius variable r is then used to replace x.

Let us introduce the following normalized variable

$$\xi = \frac{r - S(t)}{R_e - S(t)},\ \xi \in [0, 1] \tag{13.10}$$

and make a simple finite difference method over ξ.

Here, R_e is the outer radius of the spherical radius.

The differential equation in new variables is (the concentration ϕ is only function of ξ and t) :

$$\frac{\partial \phi}{\partial t} = D(\frac{1}{(R_e - S(t))^2}\frac{\partial^2 \phi}{\partial \xi^2} + \frac{2}{r}\frac{1}{R_e - S(t)}\frac{\partial \phi}{\partial \xi}) - \frac{r - R_e}{(R_e - S(t))^2}\dot{S}(t)\frac{\partial \phi}{\partial \xi} \tag{13.11}$$

With this transformation, Eqs.13.8 become

$$\begin{cases} \xi = 0 : \phi(\xi = 0, t) = \phi_l \\ \xi = 1 : J(\xi = 1, t) \to 0 \end{cases} \tag{13.12}$$

For $t \geq 0$,we will have $\xi = 0$ for the position of the solid-liquid interface,and therefore a fixed-boundary problem. If we divide the interval [0,1] by n subintervals, we come to the following finite difference scheme. A list is created, of which the first element saves S(t) and the other

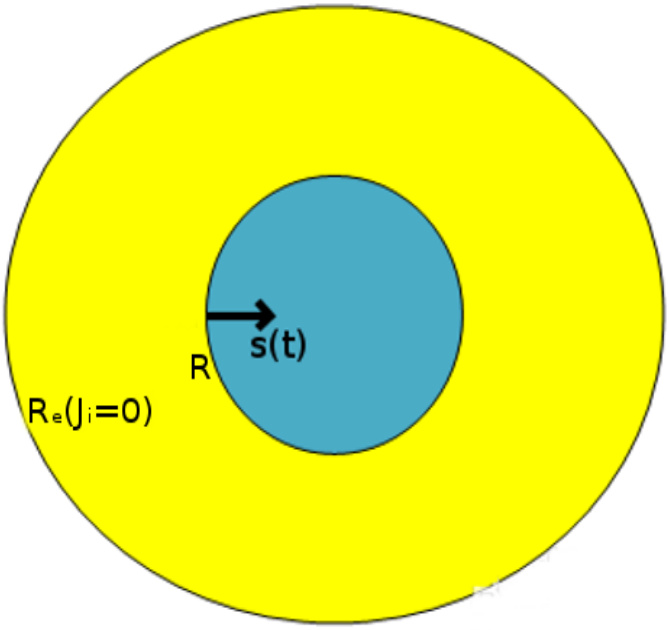

FIGURE 13.1 : Illustration of the REV in one-dimensional spherical coordinate system.

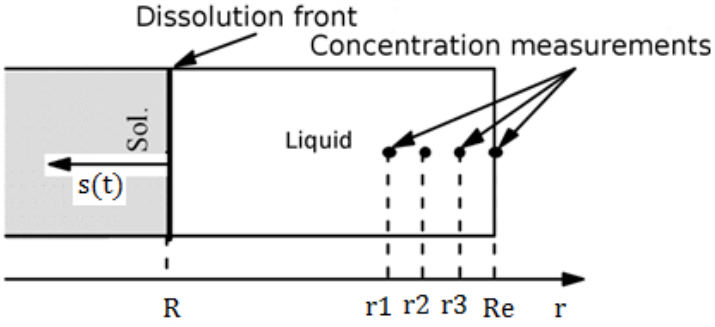

FIGURE 13.2 : Illustration of the moving interface S(t), function of time.

elements save the molar concentrations in each space of the liquid phase at the given instant ($\phi(\xi_i, t)$). The initial conditions are also given by this list and the solver of integration is applied. It remains to decompose the interpolation function and return to the initial variable r.
Using a first-order and a second-order central difference for the derivative at position ξ_i we get the recurrence equation :

$$\begin{cases} \frac{\partial \phi}{\partial \xi}(\xi_i, t) \approx \frac{\phi(\xi_{i+1},t)-\phi(\xi_{i-1},t)}{\xi_{i+1}-\xi_{i-1}} \\ \frac{\partial^2 \phi}{\partial \xi^2}(\xi_i, t) \approx \frac{\frac{\phi(\xi_{i+1},t)-\phi(\xi_i,t)}{\xi_{i+1}-\xi_i} - \frac{\phi(\xi_i,t)-\phi(\xi_{i-1},t)}{\xi_i-\xi_{i-1}}}{\frac{\xi_{i+1}-\xi_{i-1}}{2}} \end{cases} \tag{13.13}$$

Then another list is created, of which the first element saves $\frac{dS(t)}{dt}$ and the other elements save the $\frac{\partial \phi}{\partial \xi}$.

13.4 Analytical solutions for partial differential equation with Stefan Conditions

In this section, the analytical solutions for partial differential equation with Stefan conditions are listed seperately in one-dimensional Cartesian coordinate system and in one-dimensional spherical radial coordinate system, to precise if self-similar solution exists in different coordinate systems, thus aiding different types of modeling.

13.4.1 In one-dimensional Cartesian coordinate system for an infinite medium

Using the dimensionless variables, i.e. time and position could be defined as

$$\xi = \frac{x}{\sqrt{Dt}} \tag{13.14}$$

So we could find a self-similar solution for the function $\phi = \phi(x, t)$ and for $S = S(t)$ which state a square-root behaviour as a function of time with an initial value.
The dimensionless model results is :

$$-\frac{1}{2}\frac{\frac{d\phi(\xi)}{d\xi}\xi}{t} = D\frac{\frac{d^2\phi(\xi)}{d\xi^2}}{Dt^2} \tag{13.15}$$

We solve the differential equation (13.15) for the function $\phi(\xi)$, with independent variable ξ.

$$\phi(\xi) = C1 + erf(\frac{\xi}{2})C2 \tag{13.16}$$

The Stefan and initial conditions deliver the equations for the determination of the constants C1 and C2 :

$$x \to \infty, \xi \to \infty : \phi(\xi) = 0 \tag{13.17}$$

It is supposed that the concentration of the liquid phase at the interface equals to ϕ_l :

$$x = S(t), \xi = 1 : \ \phi(\xi) = \phi_l \tag{13.18}$$

So the constants C1 and C2 are :

$$\begin{cases} C1 = \frac{\phi_l}{erf(\frac{S(t)}{2\sqrt{Dt}})} \\ C2 = \frac{\phi_l}{erf(\frac{S(t)}{2\sqrt{Dt}})} \end{cases} \tag{13.19}$$

Solving for C1 and C2 gives the Neumann-solution of the concentration in function of x and t as follows

$$\phi(x,t) = -\frac{\phi_l}{erf(\frac{S(t)}{2\sqrt{Dt}}) - 1} + \frac{erf(\frac{x}{2\sqrt{Dt}})\phi_l}{erf(\frac{S(t)}{2\sqrt{Dt}}) - 1} \tag{13.20}$$

Trial of $S(t) = S_0 + k\sqrt{t}$, substitution of it into above solution and use of the initial condition $S_0 = 0$ gives

$$\frac{\sqrt{D}e^{-\frac{k^2}{4D}}\phi_l}{\sqrt{\pi}(erf(\frac{k}{2\sqrt{D}} - 1))} = \frac{k(\phi_s - \phi_l)}{2} \tag{13.21}$$

k is then estimated by the above equation.

13.4.2 In one-dimensional spherical radial coordinate system for a finite medium

When the model is developed in the spherical coordinate system, $\xi = \frac{r - S(t)}{R_e - S(t)}$ is set to give the differential equation for $\phi = \phi(\xi)$. The initial value of the position of the moving interface between the solid phase and the liquid phase $S_0 > 0$ to offer the material to dissolve at the beginning, which results in the condition of Stefan written as :

$$\sqrt{D}\times \left(\frac{\sqrt{\pi}erf(\frac{S_0+k\sqrt{t}}{2\sqrt{Dt}})\phi_l Dt}{erf(\frac{S_0+k\sqrt{t}}{2\sqrt{Dt}})\sqrt{D}(S_0+k\sqrt{t})\sqrt{t\pi}+2Dte^{-\frac{(S_0+k\sqrt{t})^2}{4Dt}}-(S_0+k\sqrt{t})\sqrt{\pi Dt}}\right.$$

$$\left. - \frac{\frac{(S_0+k\sqrt{t})\sqrt{\pi}erf(\frac{S_0+k\sqrt{t}}{2\sqrt{Dt}})}{\sqrt{Dt}}+2e^{-\frac{(S_0+k\sqrt{t})^2}{4Dt}})\phi_l D^{\frac{2}{3}}t^{\frac{2}{3}}}{((S_0+k\sqrt{t})(erf(\frac{S_0+k\sqrt{t}}{2\sqrt{Dt}})(S_0+k\sqrt{t})\sqrt{\pi Dt}+2Dte^{-\frac{(S_0+k\sqrt{t})^2}{4Dt}}-(S_0+k\sqrt{t})\sqrt{\pi Dt}}\right)$$

$$=$$

$$\frac{k}{2}\times \left(\phi_s + \frac{\phi_l(S_0+k\sqrt{t})\sqrt{\pi Dt}}{erf(\frac{S_0+k\sqrt{t}}{2\sqrt{Dt}})\sqrt{D}(S_0+k\sqrt{t})\sqrt{t\pi}+2Dte^{-\frac{(S_0+k\sqrt{t})^2}{4Dt}}-(S_0+k\sqrt{t})\sqrt{\pi Dt}}\right.$$

$$\left. - \frac{\frac{(S_0+k\sqrt{t})\sqrt{\pi}erf(\frac{S_0+k\sqrt{t}}{2\sqrt{Dt}})}{\sqrt{Dt}}+2e^{-\frac{(S_0+k\sqrt{t})^2}{4Dt}}\phi_l Dt}{erf(\frac{S_0+k\sqrt{t}}{2\sqrt{Dt}})(S_0+k\sqrt{t})\sqrt{\pi Dt}+2Dte^{-\frac{(S_0+k\sqrt{t})^2}{4Dt}}-(S_0+k\sqrt{t})\sqrt{\pi Dt})}\right)$$

We couldn't find a self-similar solution for the function $\phi = \phi(r,t)$ and for $S = S(t)$ which states a square-root behaviour as a function of time with a non-null initial value. So the condition of Stefan should be released. That is to say, the interfacial concentration of species ϕ_i should not be a constant, but a function of time mathematically.

We suppose always :

$$\xi = \frac{r}{\sqrt{Dt}} \tag{13.22}$$

As a result, the equation of the concentration in function of ξ could be presented as :

$$\begin{cases} \phi(\xi) = C1sph + \frac{(\sqrt{\pi}erf(\frac{\xi}{2})\xi + 2e^{-\frac{\xi^2}{4}})C2sph}{\xi} \\ C1sph = -\sqrt{\pi}C2sph \\ \phi(\xi) = C2sph\phi_0(\xi) \end{cases} \tag{13.23}$$

Here, $C1sph$ and $C2sph$ are integration constants.
The expression could be obtained :

$$\phi_0(\xi) = -\sqrt{\pi} + \sqrt{\pi}erf(\frac{\xi}{2} + \frac{2e^{-\frac{\xi^2}{4}}}{\xi}) \tag{13.24}$$

At the interface :

$$\xi_i = \frac{S(t)}{\sqrt{Dt}} \tag{13.25}$$

With (13.25) :

$$\dot{S}\sqrt{Dt} = \dot{\xi}_i Dt + \frac{\xi_i D}{2} \tag{13.26}$$

And with (13.24) and (13.25) :

$$\phi_0(\xi_i) = \frac{\phi_l}{C2sph} = \widetilde{\phi_l} \tag{13.27}$$

Moreover, the flux at the interface and the normalized concentration in the particle are denoted as follows :

$$J(\xi) = -\frac{D}{\sqrt{Dt}}C2sph\phi_0(\xi_i) = -(\phi_s - \phi_l)\dot{S} \tag{13.28}$$

$$\widetilde{\phi_s} = \frac{\phi_s}{C2sph} \tag{13.29}$$

With (13.26), (13.28) and (13.29) :

$$\int_0^{\xi_i} \frac{1}{\frac{\phi_0'(y)}{\widetilde{\phi_s} - \phi_0(y)} - \frac{y}{2}} dy = \int_0^t \frac{1}{z} dz \tag{13.30}$$

Setting $\alpha = \frac{1}{\xi(r=S(t))}$ gives the following equations :

$$t = \frac{\alpha^2}{(4\alpha^3 e^{-\frac{1}{4\alpha^2}} - 2\alpha e^{-\frac{1}{4\alpha^2}} - \sqrt{\pi}erf(\frac{1}{2\alpha}) + \phi_s + \sqrt{\pi})^{\frac{2}{3}}} \tag{13.31}$$

With

$$S(\alpha) = \frac{\sqrt{(Dt)}}{\alpha} \tag{13.32}$$

The position $S(\alpha)$, function of α, could be obtained. With (13.24) and $\alpha = \frac{1}{\xi(r=S(t))}$, the normalized concentration of the ion at the interface could be obtained (the normalized variables are : the diffusion coefficient : $D = 1$, the concentration of the the particles $\phi_s = 1$).
In the Figure 13.4, the normalized concentration of the ion at the interface $\phi(t)$, function of time,

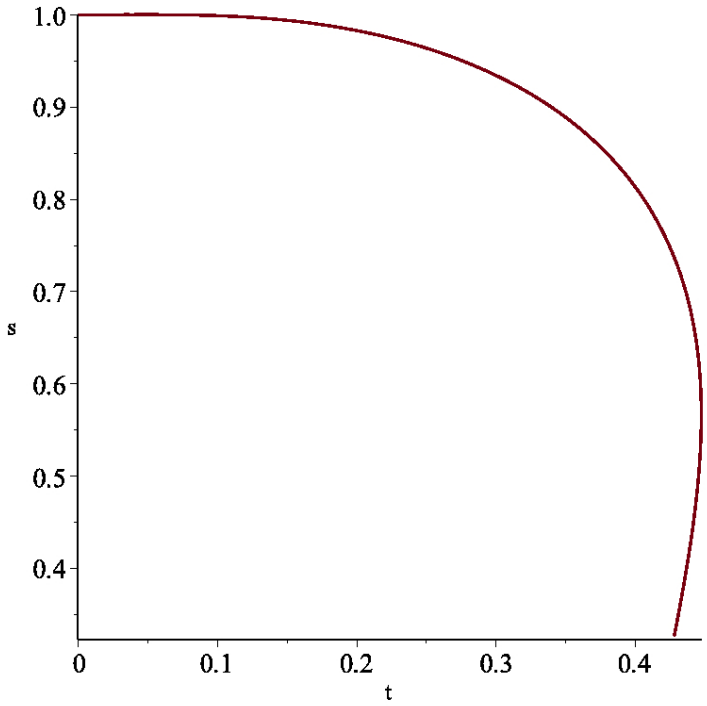

FIGURE 13.3 : Normalized position of the interface S(t), function of time.

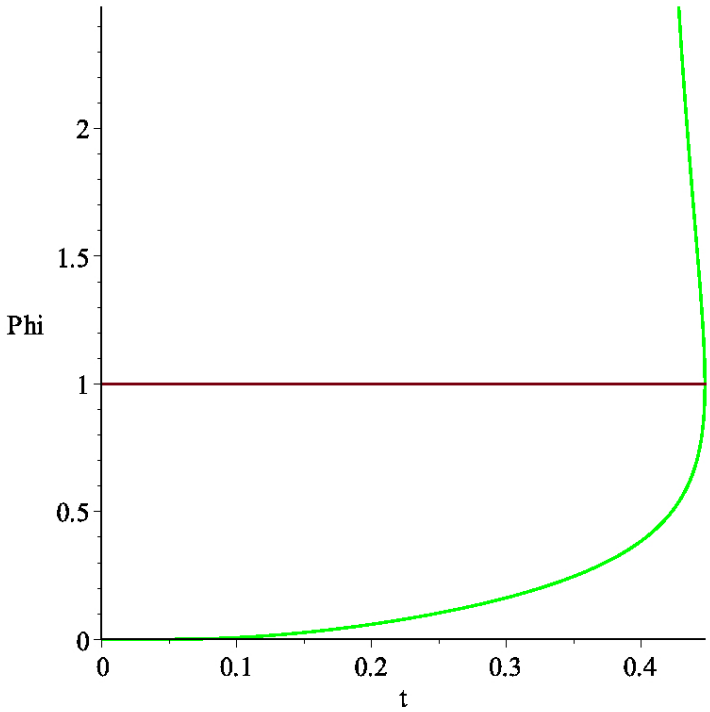

FIGURE 13.4 : Normalized concentration of the ion at the interface $\phi_{interface}(t)$, function of time.

is presented and there is a part of concentration higher than the normalized concentration of the elements in the particle $\phi_s = 1$ (the part over the red line in Figure 13.4). But in reality, the concentration of the ion at the interface is never higher than the concentration in the particle. So only the part under the red line is correct. With this result, we can calculate the correct time interval, thus the correct interface position interval with (13.32). Here, the evolution of the interface position is a function of $t^{0.5}$.
Moreover, if the normalized concentration of the elements in the particle ϕ_s is too faible (e.g. $\phi_s = 1$), because of the relatively fast dissolution velocity, the normalized concentration of the ion at the interface $\phi(\alpha) = 0$ at first. Then $\phi(\alpha)$ increases when more and more ions are accumulated at the interface but could not be diffused instantly. And then the precipitation of hydrates starts.

13.5 Simplified hydration model in dissolution-precipitation application

The dissolution of C_3S increases the ion concentrations. At first the product of the concentrations is smaller than the solubility product K_{sp} for C_3S, so the C_3S continues to dissolve. After the over-saturation, the solution is no longer at equilibrium because the product of the concentrations of the ions is too large. In formal terms, the ion product Q_{sp} for the solution arrives at the value of the solubility product K_{sp} for C_3S, so the C_3S stops dissolving.

$$Q_{sp}^{C_3S} \geq [Ca_{(aq)}^{2+}]^3[H_2Si0_{4(aq)}^{2-}][OH^-]^4 \tag{13.33}$$

The precipitation of $C-S-H$ gel follows similar principles. When the ion product arrives at the value of the solubility product K_{sp} for $C-S-H$ gel, the precipitation begins.

$$Q_{sp}^{C-S-H} \geq [Ca_{(aq)}^{2+}]^{1.7}[H_2Si0_{4(aq)}^{2-}][OH^-]^{1.4} \tag{13.34}$$

With this principle, the Stefan analysis of dissolution-diffusion-precipitation processes is rewritten specie by specie. The reaction of precipitation comes back to equilibrium after the excess ions precipitate from solution as solid $C-S-H$ gel. The evolution of the interface and the concentration of each ion can be calculated, which are presented as follows.
In Fig.13.6, the x-axis marks the moments during the hydration and the y-axis marks the position of the interface. With the high w/c ratio, there are more space for the diffusion of the ions dissolved, so the displacement of the solid-liquid interface is more evident than the case with a lower w/c ratio.
In Fig.13.7, the x-axis marks the coordinate of the space in the REV and the y-axis marks the concentration of ion. te is the saturation moment in the liquid phase. The figure shows that the interface moves in the direction to the center of the anhydrous core. And the concentration of ion increases as the time evolves until the saturation of the liquid phase.
In Fig.13.8, the x-axis marks the coordinate of the space in the REV and the y-axis marks the

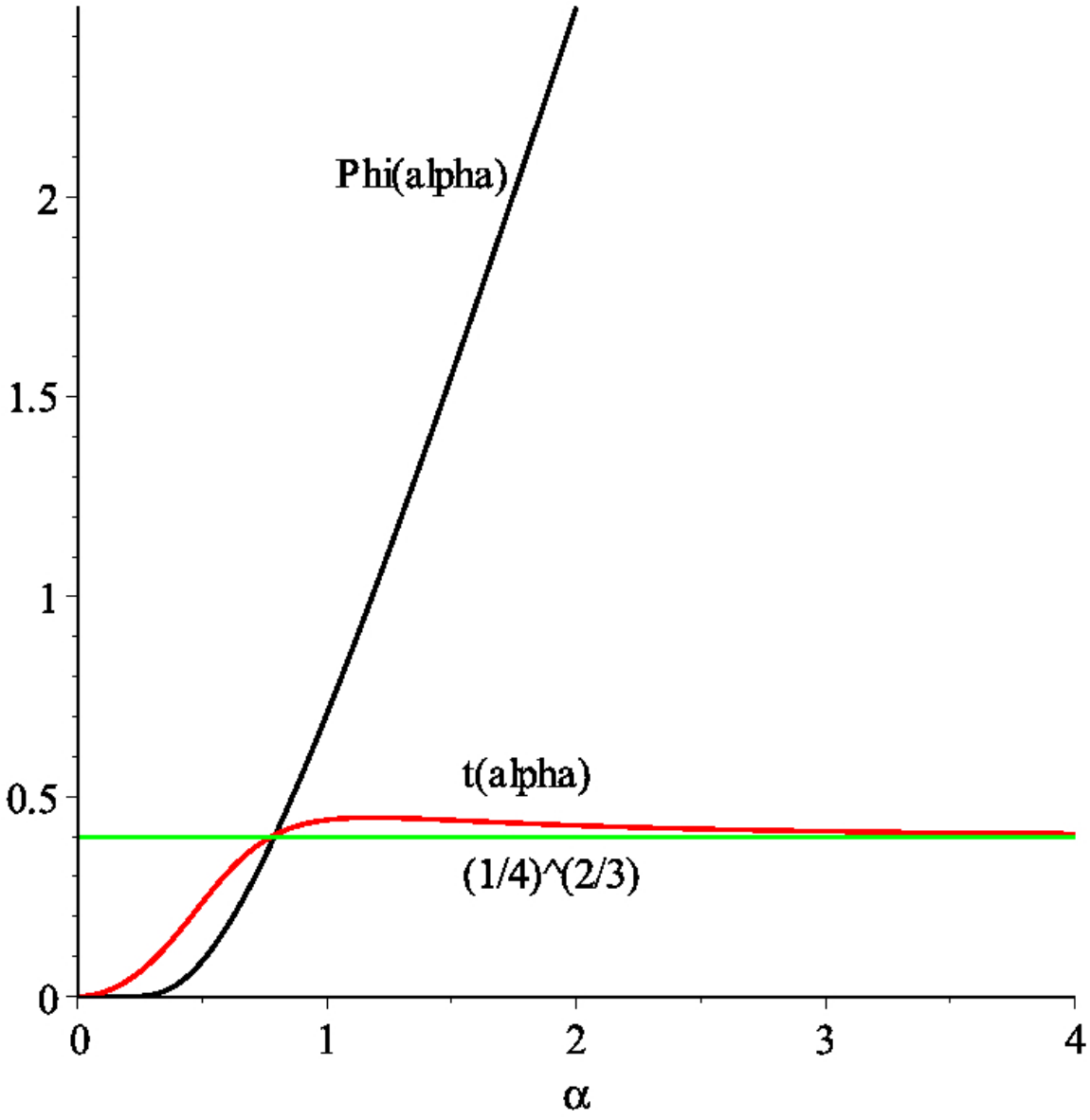

FIGURE 13.5 : Comparison of the time and the normalized concentration of the ion at the interface ϕ as functions of α.

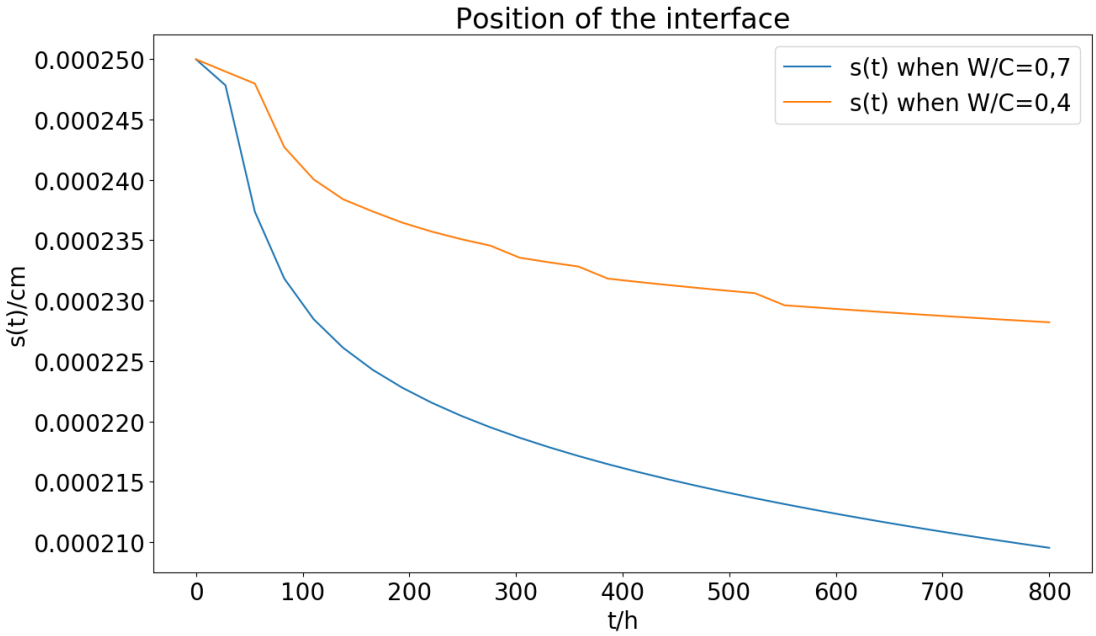

FIGURE 13.6 : Evolution of the solid-liquid interface with different w/c ratio.

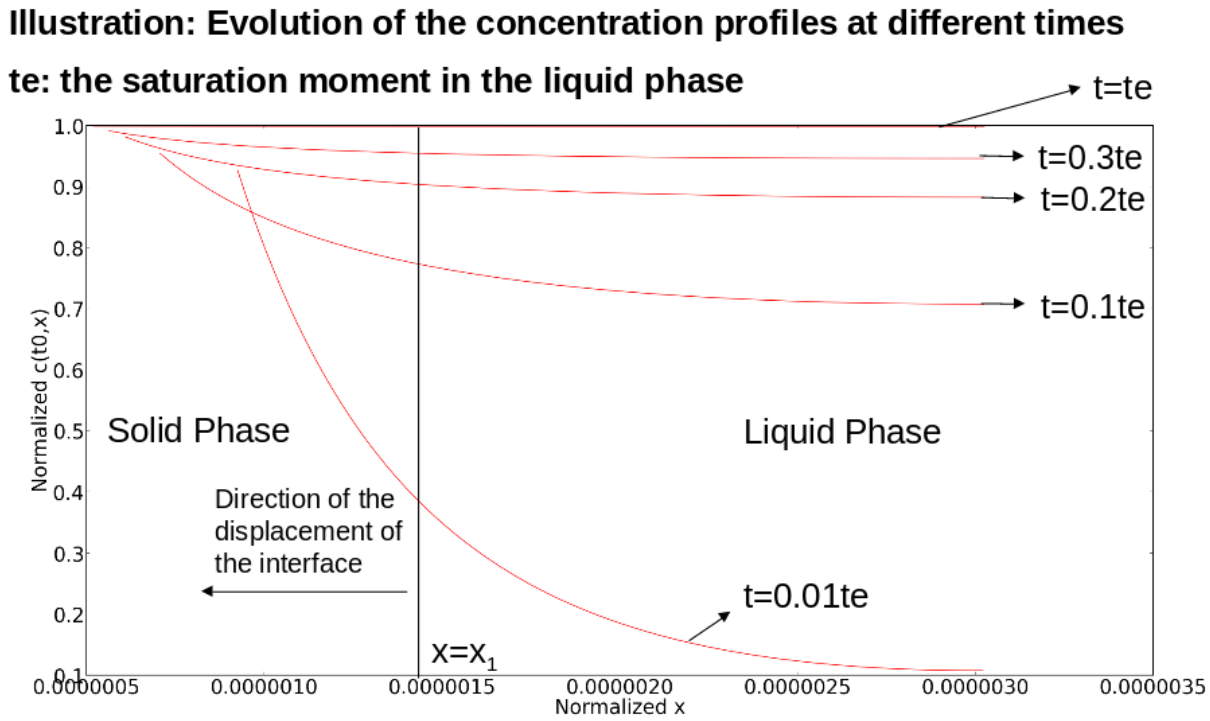

FIGURE 13.7 : Evolution of the concentration profiles at different times, te : the saturation moment in the liquid phase.

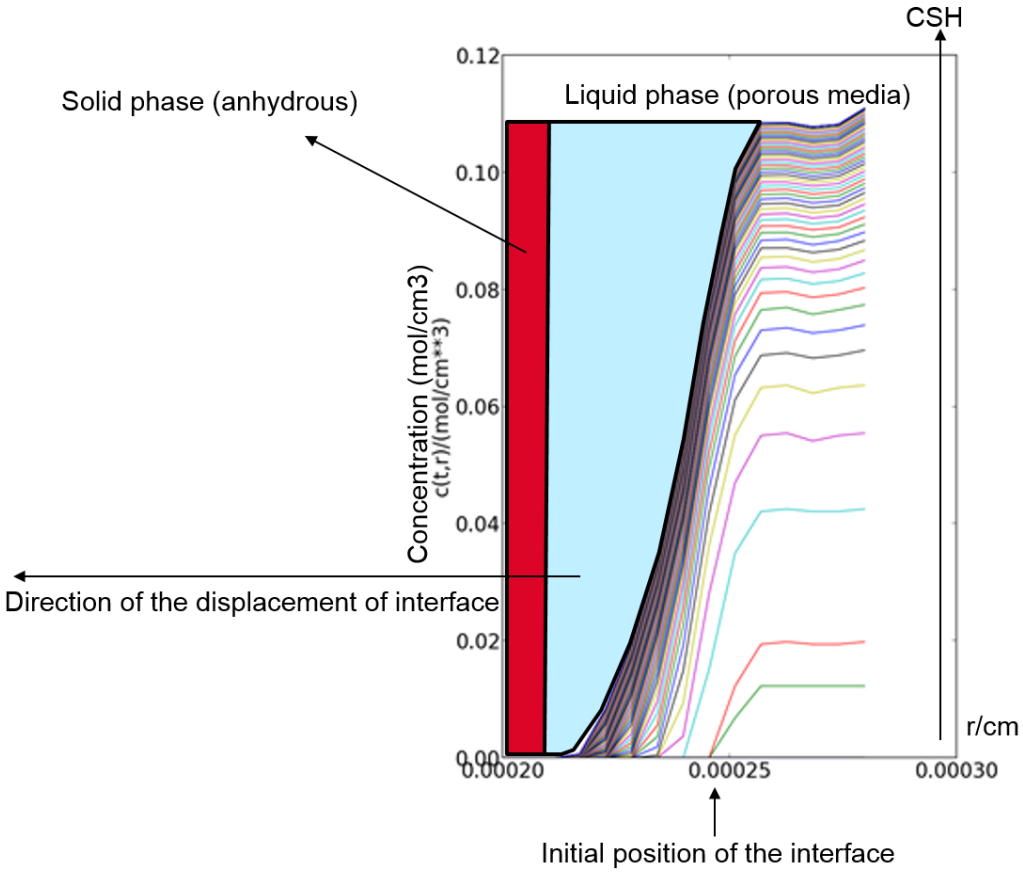

FIGURE 13.8 : Cumulative development of the $C-S-H$ concentration profiles.

concentraion of the precipitated $C-S-H$ gel. The figure also shows that the interface moves in the direction to the center of the anhydrous core. And the concentration of the precipitated $C-S-H$ gel increases as the time evolves.
But the problem of this modeling result is that there exists always porous space (the blue colour zone) between the anhydrous phase (the red colour zone) and the zone of the precipitated $C-S-H$ gel. The cause might be that the diffusion coefficient of each ion stays constant, which should varies with the local porosity in reality. So it is necessary to take into account the diminution of the diffusion coefficient as a function of the local volume fraction of the precipitated phases or of the local porosity.

13.6 Diffusion coefficient as a function of porosity

13.6.1 Archie's first law in engineering

In petroleum engineering, Archie's first law [6] is used as a tool to obtain the cementation exponent of rock units. This exponent can then be used to calculate the volume of hydrocarbons in the rocks, and hence reserves can be calculated. [76] Archie's law is given by the equation :

$$\rho(\Phi) = \rho_f \Phi^{-m} \tag{13.35}$$

where $\rho(\Phi)$ is the resistivity of the fully water-saturated rock sample, ρ_f is the resistivity of the water saturating the pores, Φ is the porosity of the rock, m is the cementation exponent [75], and the ratio $\rho(\Phi)/\rho_f$ is called the formation factor. Archie's law in this form was initially empirical, although it was recognised that certain values of the cementation exponent were associated with special cases that could be theoretically proven.

13.6.2 Extension of Archie's first law to diffusion coefficient and improved spherical model.

The extension is always based on the one-dimensional spherical coordinate system shown in the Fig.13.1 and in the Fig.13.2.
The diminution of the diffusion coefficient as a function of the local porosity could be described with the form of Archie's first law :

$$D_i(\Phi) = D_i^f \Phi^{-m} \tag{13.36}$$

where $D_i(\Phi)$ is the diffusion coefficient of the ion i as a function of the local porosity ; D_i^f is the diffusion coefficient of the ion i when the local porosity equals to 1, indicating the condition where there is not yet the precipitated hydrates ; Φ is the loacal porosity as a function of the radius variable r in one-dimensional spherical coordinate system ($\Phi(r)$), m is always the cementation exponent.

Here, the application of Archie's first law is a first trial. In the perspective of the future work, we can use a law with homogenization.
In the porous space of the hydration model, the solid phases are the precipitated hydrates, so the local porosity at each space quantified by the radius variable r and the time t could be written as :

$$\Phi(r,t) = 1 - f_s(r,t) \tag{13.37}$$

where $f_s(r,t)$ is the volume fraction of the solid phase as a function of t and r.
So the diffusion coefficient D is exactly a function of t and r. Since D is no longer a constant, the second Fick's law should be rewritten as (for the ion i) :

$$\frac{\partial \phi_i}{\partial t} = \frac{\partial}{\partial r}[D_i(r,t)\frac{\partial \phi_i}{\partial r}] = \frac{\partial D_i(r,t)}{\partial r}\frac{\partial \phi_i}{\partial r} + D_i(r,t)\partial r\frac{\partial^2 \phi_i}{\partial r^2} \tag{13.38}$$

The condition of Stefan describing that the quantity of the particles of the ion i diffused by the flux from the interface equals to the quantity of the particles of the ion i dissolved from the solid phase is rewritten as :

$$J_i(r = S(t), t) = -(\phi_i^s - \phi_i^l)\dot{S}(t) \tag{13.39}$$

where

- ϕ_i^s is the volumetric quantity of the ion i in the solid phase, so typical units for expressing it would be mol/m^3.
- ϕ_i^l is the local equilibrium concentration of the ion i right at the interface, of which the dimension is amount of substance per unit volume. It might be expressed in the unit of mol/m^3, and might be a function of time in the advanced model.

The configuration studied is based in finite medium. Two phases are considered here : the solid phase for $r < S(t)$ and the liqud phase for $S(t) < r < R_e$.
The boundary conditions to be satisfied for each ion i by Eq.(13.39) are

$$\begin{cases} r = S(t) : \phi(r = S(t), t) = \phi_i^l \\ r = R_e : J_i(r = R_e, t) \to 0 \end{cases} \tag{13.40}$$

The boundary conditions limit that :

- For $r = S(t)$, the concentration of the ion i at the interface equals to the local equilibrium concentration of the ion i.
- For $r = R_e$, there is no flux of the diffusion of the ion i.

The initial conditions to be satisfied are

$$\begin{cases} r < S(t) : \phi(r, t = 0) = \phi_i^s \\ r > S(t) : \phi(r, t = 0) = 0 \\ S(t = 0) = S_0 \end{cases} \tag{13.41}$$

Then the normalized variable in the Eq.(13.10) is applied to develope the model.
The ion product Q_{sp}^{C-S-H} at each position r of the REV is calculated and the precipitated $C-S-H$ gel appears at the position r once the Eq.(13.34) is satisfied.

13.7 First attempt of application of the output of hydration model with moving boundary conditions

Here, the application of the hydration model with moving boundary conditions is simplified. C_3S represents all the anhydrous and the $C-S-H$ gel represents all the hydrates in the REV. This work is to illustrate the possibility of bridging the simplified hydration model and the micromechanical creep model.
Material properties for all simulation runs are listed in Table 13.1. [79]

TABLE 13.1 : Material Properties of Multi-Ionic Single Particle Model.

Parameter	Value	Units	Description
ρ_{C_3S}	3.2	g/cm^3	Density of C_3S
ρ_{CSH}	2.2	g/cm^3	Density of $C-S-H$
ρ_w	1	g/cm^3	Density of water
w_{C_3S}	228.3	$g/g-mol$	Molecular weight of C_3S
w_{CSH}	243.6	$g/g-mol$	Molecular weight of $C-S-H$
R	0.00025	cm	Initial radius of C_3S particle
w/c	0.525		Water to cement ratio

The density and molecular mass of C_3S, $C-S-H$ and water are all fixed because they are either known or generally agreed upon, that is, the molecular weight of $C-S-H$ is taken as 243.6 g/mol assuming a constant stoichiometry for $C-S-H$ of $C_{1.7}SH_{4.9}$. Other input values adopted that have been used in the model are listed in Table 13.2.[38]

TABLE 13.2 : Equilibrium Constants and Material Properties That Were Fixed in the Multi-Ionic hydration Model.

Parameter	Value	Units	Description
$K_{eq}^{C_3S}$	$10^{-17.8}$		Equilibrium constant of C_3S dissolution
K_{eq}^{CSH}	$10^{-12.96}$		Equilibrium constant of $C-S-H$ dissolution
$D_{Ca^{+2}}$	2.592×10^{-4}	cm^2/h	Diffusion coefficient of Ca^{2+} ions in layer containing $C-S-H$
$D_{H_2SiO_4^{-2}}$	2.52×10^{-4}	cm^2/h	Diffusion coefficient of $H_2SiO_4^{2-}$ ions in layer containing $C-S-H$
$D_{OH^{-1}}$	1.9×10^{-3}	cm^2/h	Diffusion coefficient of OH^- ions in layer containing $C-S-H$

The cumulative development of the $C-S-H$ concentration profiles from each time step of

the modeling is, on one hand, used to calculate the the remaining concentration of the ions in the layer where $C-S-H$ exists, thus configurate the input diffusion coefficient value for the calculation of the next time step by Archie's first law ; on the other hand, used to calculate the local volume fraction of the precipitated $C-S-H$ solid phase, thus applying the homogenized relaxation matrix of the $C-S-H$ gel to the modeling of the fictitious phases of the "pore -> $C-S-H$" and the "anhydrous -> $C-S-H$" transformations.
In this application, the hydration time is discretized by 155 time steps. As the REV is presented in one-dimensional spherical coordinate system, the radius of the REV is divided evenly into 155 segments. So the REV could be regarded as a multi-layer sphere with 155 layers. The evolution of the volume fraction of the precipitated $C-S-H$ gel is shown in Fig.13.9. In Fig.13.9, at each

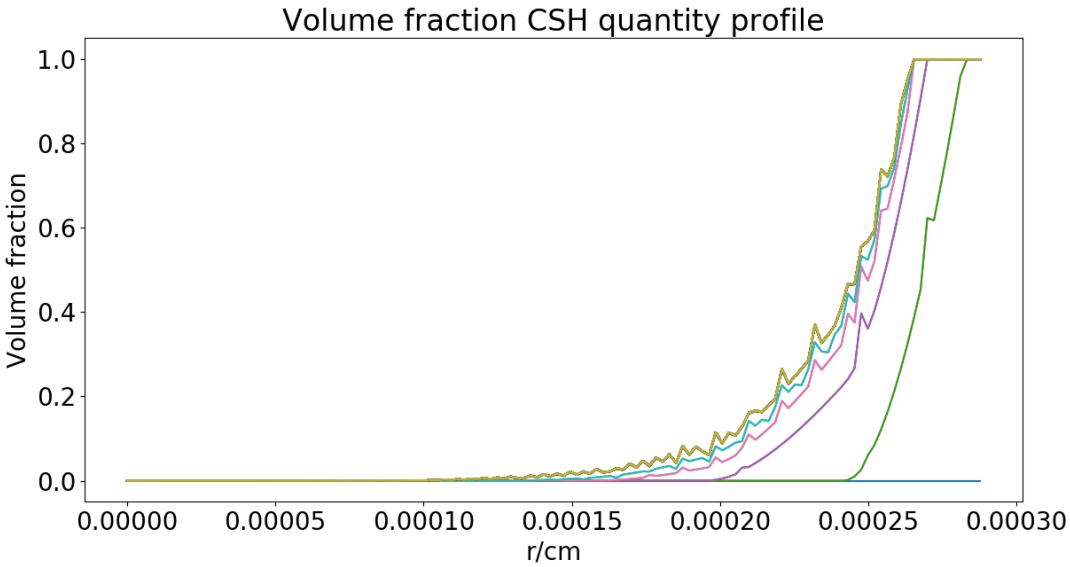

FIGURE 13.9 : Evolution of the volume fraction of the precipitated $C-S-H$ gel.

time step, one curve indicating the volume fraction of the precipitated $C-S-H$ gel located by the radius of the REV r (x-axis) is added in the figure.
However, one attention should be paid that, the hydration model with the diffusion coefficients of the ions collected from [38] shows that the volume fraction of the precipitated $C-S-H$ gel arrives at the value of 1 in the outside part of the REV, which may cause the anormal modeling ressults. As a result, in the layers filled with the precipitated $C-S-H$ gel, the hypothese that the ions could be stocked in the gel phase might be proposed.
On the other hand, the "waves" (the non smooth part) in the curves are the results of the diminution of the diffution capability in some space influced by the formation of the $C-S-H$ layer.
In the morphological part, the local volume fraction of the precipitated $C-S-H$ solid phase is calculated by the multi-ionic hydration model as shown in Fig.13.10. In Fig.13.10, R represents the initial radius of C_3S particle. So the layers inside the initial radius of C_3S particle experience the "anhydrous -> $C-S-H$" transformations and f_i indicates the local volume fraction of the precipitated $C-S-H$ phase in the Layer i. So the equivalent ageing linear viscoelastic

behaviour of theses layers follows the evolution in Fig.4.1(b). And the layers outside the initial radius of C_3S particle experience the "pore -> $C-S-H$" transformations and f_j indicates the local volume fraction of the precipitated $C-S-H$ phase in the Layer j. As a result, the ageing behaviour could be described as in Fig.4.1(a).

The density of each layer increases, due to precipitation of more and more hydrate particles at

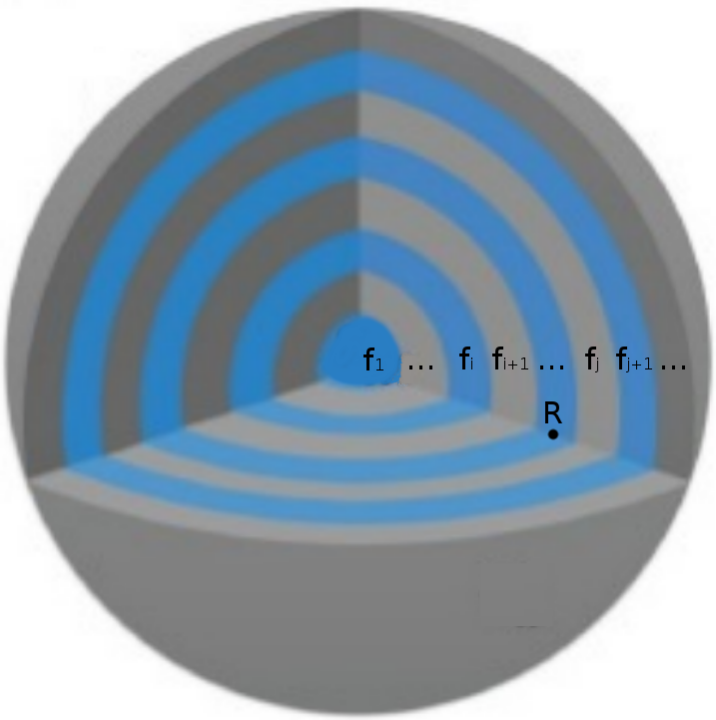

FIGURE 13.10 : Morphological indication of the local volume fraction of the precipitated $C-S-H$ solid phase in each layer of the REV.

the lower scale. This principe is similar to the "AIO" model in [167], but with the more detailed information for the layered sphere. The snapshots at hydration degrees $\alpha = 0,\ 0.4,\ 0.7$ of time-dependent morphological models of hydrating cement paste (schematic 2D representation of 3D model) is shown in Fig.13.11, where progressive transformation of anhydrous in each layer and densification of each layer due to precipitation of hydrates is considered.

In Fig.13.11, the scale of cement paste is in the row of "Large scale". Each layer at this scale has its own degree of densification due to precipitation of hydrates at the "small scale". At the large scale, as different layers have different time of beginning of densification, different phases have different volume fraction of the phase of hydrates. The local volume fraction of the phase of hydrates for each layer in the Fig.13.11 is represented by different spectral colors : the red – bright green color segment for high volume fraction and the cyan - blue color segment for low volume fraction. During hydration, there are more and more layers that start to densify. Simultaneously, zooming on each layer, more and more hydrates is precipitated at the small scale, so the spectral color rises from the cyan - blue color segment to the red – bright green color segment during the hydration. The self-consistent homogenization scheme is applied in the small scale

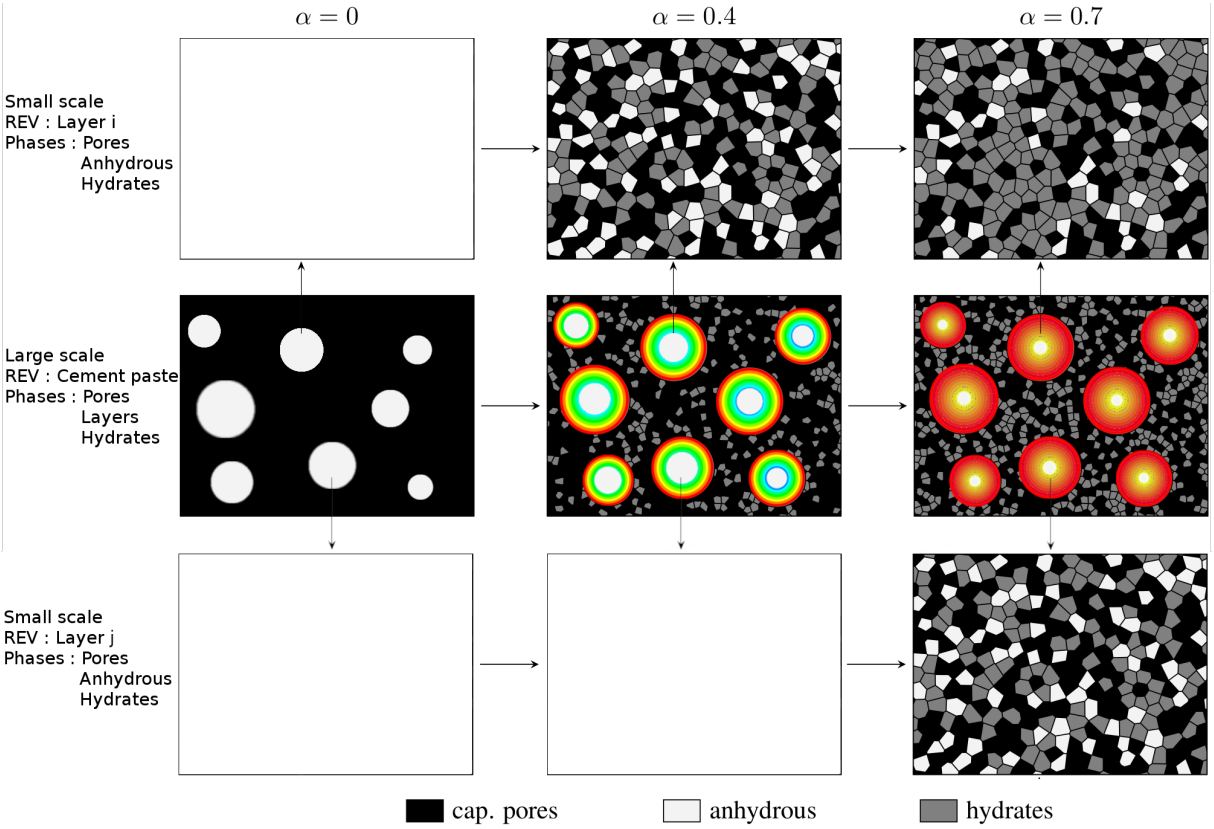

FIGURE 13.11 : Snapshots at hydration degrees $\alpha = 0,\ 0.4,\ 0.7$ of time-dependent morphological models of hydrating cement paste (schematic 2D representation of 3D model), progressive transformation of anhydrous to each layer and densification of each layer due to precipitation of hydrates is considered.

to calculate the homogenised mechanical properties for each layer. And the volume fraction of the precipitated hydrates of the outmost layer is used for the calculation of the homogenised mechanical properties for the matrix at the scale of cement paste. Then the mechanical property of the REV with multi-layer spheres embeded in the matrix is calculated.

As a result, the application of the output of this hydration model with moving boundary conditions to our "AIO" multi-layer ageing creep compliance micromecal model is carried out. On the other hand, the "AHP" model [167] using the output of this hydration model with moving boundary conditions is also applied to compare the difference of this two type of models. In the "AHP" model, the principe of a double-scale model described in the Part I is adopted : the self-consistent homogenization scheme is applied in the small scale to calculate the homogenised mechanical properties for each "C-S-H gel - pore" clusters (small mixture on the large scale). Then the mechanical property of the REV compose of the phases of "C-S-H gel - pore" clusters is calculated by the self-consistent scheme.[167] So the volume fraction of each phase of "C-S-H gel - pore" cluster in the the "AHP" model corresponds to that of each layer in the "AIO" model in this modeling process.

The Fig.13.12 shows the comparisons between this multi-layer "AIO" ageing creep compliance modeling results and the "AHP" modeling results.

The red curves are the "AHP" modeling results and the blue ones are the "AIO" modeling

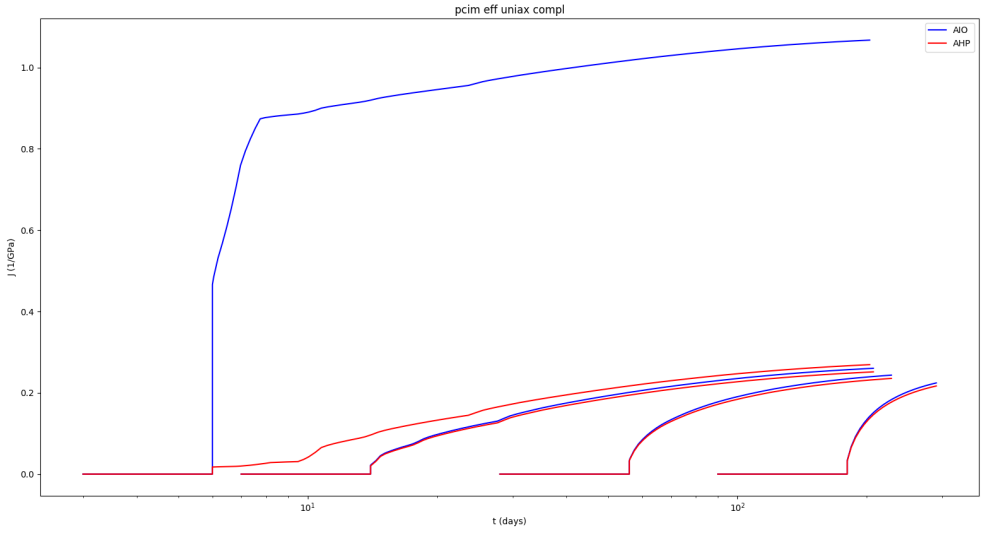

FIGURE 13.12 : Comparisons between the multi-layer "AIO" ageing creep compliance modeling results and the "AHP" modeling results, using hydration model with moving boundary conditions (age of loading $t_0 = 3,\ 7,\ 28,\ 90$ days).

results.

At the age of loading $t_0 = 3$ days, there is a big difference between the results of this two models. However, the modeling results at $t_0 = 7,\ 28,\ 90$ days are quite similar for these two models. The reason may be that with the simplified hydration model, when $t_0 \leq 7$ days, enough hydrates has

been produced in all the layers for the the "AIO" model and in most of the phases the "AHP" model, so the composition of the REV becomes similar, which results in the ageing similar creep compliance curves for these two models. On one hand, for the "AHP" model, the creep compliance results at $t_0 = 3$ days and $t_0 = 7$ days are similar, which indicates that the ageing effect is not evident in the "AHP" model when the hydration model with moving boundary conditions is applied. On the other hand, the "AIO" model and the "AHP" model begin to give more realistic results when $t_0 \leq 7$ days. In general, the "AIO" multi-layer model estimates better the ageing effect at ealier age of loading.

It is quite probable that there are differences between the two modeling results and the experimental results. The cause of the differences may be that the input value of the caracteristic time of the dashpot in the model is too small, which means that the mechanical parameters obtained in [70][165][158] are not perfectly correspond to the real mechanical properties of the $C-S-H$ gel that we have used for the model. Moreover, the hydration model with moving boundary conditions used here has not yet taken into account the precipitation of aluminates and other by-products.

On the other hand, while Bullard and Flatt [38] use a value of $10^{-17.8}$ for the equilibrium constants for the reaction of the $C-S-H$ formation, a much lower value is suggested by Juilland et al. [102] of 10^{-22}. As small changes in this value are already able to dramatically alter the C/S ratio in solution, the changes of the order of magnitude of this value might influence the reaction of dissolution and precipitation. In addition, Fig.13.9 shows that the volume fraction of the precipitated $C-S-H$ gel arrives at the value of 1 in the outside part of the REV, which indicates that the ions can be diffused to the outmost surface of the REV quickly, reminding us to investigate the veriaty of the diffusion coefficients of the ions [38], too.

It could be concluded that the lack of some details in the simplified hydration model (more types of anhydrous and hydrates) and the accumulation of the precipitated hydrates in the outmost layers might create the divergence between the creep modeling results coupling the hydration model with moving boundary conditions and the creep experimental results. However, it is always important to connect the hydration model to the micromechanical model on the pursuit of a better morphological model for cementitious materials. The studies presented in this section proposes a first coupling work between the evolutif hydration model and the micromechanical homogenization mechanical model, and leaves the prospect of further refining the hydration model for more realistic results.

Conclusion and Prospects

With the aim of contributing to the resolution of certain safety and durability problems of prestressed concrete structures owned or built by EDF, this thesis work has led to the development of multi-scale analytical and numerical methods for the ageing viscoelastic behaviour of the highly heterogeneous viscoelastic materials for the construction of containment building. This part gives the main conclusions and perspectives for each of the topics covered in this thesis : mean-field homogenization of time-evolving microstructures with viscoelastic phases, multi-scale homogenization of linear viscoelastic composite materials, creep experiment procedures, post-processing and analyse of the experimental results and improvement of hydration model.

Part I :

An approach to upscale the mechanical behavior of composite materials undergoing geometrical evolutions of their microstructure is proposed. Mean field homogenization is considered. Viscoelastic behaviors are considered for the phases. While the evolving nature of microstructure does not prevent the use of mean-field homogenization in the case of elastic phases, special care has to be taken for viscoelastic phases. Indeed, time appears both in the elementary behaviors and in the evolution of microstructure. Even if the phases are non-ageing, the effective behavior is ageing viscoelastic.

Extending Bažant's solidification theory, an equivalent composite is built, whose microstructure is constant but made up of ageing linear viscoelastic fictitious phases. Taking advantage of recent advances in ageing linear viscoelastic homogenization, the effective behavior of this equivalent composite can then be estimated. Note that this approach is not restricted to nonageing phases in the evolving microstructure : ageing phases are as straightforward to consider. Qualitatively, compliance functions from evolving microstructure are closer to the experimental ones reported in [186].

Aging viscoelastic estimations are consistent with the effective elastic moduli. Further validation has been carried out by comparison to FEM numerical simulations.

In addition, a multi-scale morphological model has been designed to model outer hydrates, avoiding the late setting issue. It is used in the ageing viscoelastic homogenization technique considering microstructure evolution. Even if this first application focuses on simplified inputs, the technique is flexible enough to be able to use any kinetics curve and any isotropic linear viscoelastic behavior.

The proposed application is deliberately crude to focus on the description of the homogenization approach rather than on unnecessary technical details. However, the model could be improved in several aspects :

- More realistic behaviors of C-S-H should be used ;
- A study of the influence of the stress state over dissolution and precipitation processes should be performed ;
- Ageing mechanisms other than hydration should be taken into account.

Part II :

This part details the general procedure for carrying out the creep experiment procedure on cement paste, mortar and concrete with the mix design of the VeRCoRs concrete.

The purpose of the experiments described in this part is the characterization of autogenous shrinkage, and basic creep under uniaxial compression at 20 °C. These characterizations were carried out on two geometries : small cylindrical specimens with the dimension of $3.6cm \times 18cm$, and big cylindrical specimens with the dimension of $8cm \times 29cm$.

In addition to the creep under load of cementitious materials for the VeRCoRs concrete, the protocol described in this part allows the characterization of the recovery of creep of cementitious materials.

The protocol describes the organisation of the shrinkage and the creep experiments with the phases as follows :

- Manufacturing of specimens, including the calculation of the mix design parameters, the mixing procedures, the tests on fresh batch and the casting and vibration ;
- Preparation and instrumentation of the specimens, including the details of the choice of the specimens, cutting and grinding of the specimens, and sealing and installation of the instrumentation supports ;
- Analyse of raw experimental results.

According to the analyse of raw experimental results, the procedure could be improved in several aspects. Firstly, deployment methodologies could be carried out to reinforce the robustness and performance of the central software platform for each test bench and the air conditioning to avoid the oscillation on the registered experimental data. Moreover, creep experiments could be continued at the age of loading $t_0 > 400$ days to extend the comparison between the modeling results and the experimental results and to reach the asymptotic to log function. In addition, the lateral deformation could be measured (this is the access to the Poisson's ratio of creep, which is always regarded as a constant.

Part III :

In the first subpart, identification of the parameters for the ageing viscoelastic model based on the experimental results is carried out and validation of model fitting results show the coherence between the modeling results and the experimental results.

With the parameters identified from the experiments, a micromechanical model of constitutive law (an expression of the ageing relaxation and ageing compliance) can be developed to perform the multi-scale homogenization of the VeRCoRs concrete. Different models, namely a logarithmic function of time, a generalized Maxwell model, a generalized Kelvin model and a hybrid model based on a logarithmic function coupled with a Kelvin unit are applied for the identification of parameters to estimate the material compliance.

In addition, physical submodels have beens defined to describe the evolution of parameters as a function of age of loading t_0. And the evolutions of Young's modulus estimated by the physical

submodel are succesfully compared with the experimental measurements of Young's modulus carried out in EDF, in CEA and in CEBTP at different ages of loading.
Then this part proposes the application of a semianalytical approach to estimate the effective ageing viscoelastic behaviour characterized by the compliance tensors as functions of two time variables. Different homogenization schemes are then applied to upscale the ageing viscoelastic behaviour from the scale of cement paste to the scale of mortar (with cement paste as the ageing viscoelastic phase and sand as the elastic phase), and from the scale of mortar to the scale of concrete (with mortar as the ageing viscoelastic phase and coarse aggregate as the elastic phase). The comparison results are acceptable, which demonstrates that the ageing compliance model is well adapted to the experimental results. And this model can be applied to predict the ageing creep compliance of the VeRCoRs concrete right from the scale of the microstructure of cement paste.
However, some results show the tendency to underestimate the experimental results. It thus opens to us new ways for improving the quality of the model by :

- Taking into account the cement paste/aggregate interface ;
- Developing the microcracking of the VER during hydration.

Then one chapter compares the ageing modeling results described in the Part I and in [167] with the experimental results at the scale of cement paste. To extend the precision of the ageing model, adaptation of the a multiscale micromechanics-hydration model [25] to ageing viscoelasticity is carried out. It is observed that, compared to the real process of hydration, the hydration model used here is a little simplified.
So the last chapter of this thesis tries to improve the hydration model described in the Part I of this thesis and in [25], because a more realistic evolution of the dissolution of the anhydrous and the precipitation of the hydrates with correct morphologie is necessary. A strategy for modeling tricalcium silicate hydration based on through-solution-phase kinetics is then developed in the last chapter. This study extends a continuum-based single particle model by including multi-ionic transport, nonlinear reaction kinetics and precipitation of the $C-S-H$ gel. Model parameters were fixed based on known values. This chapter proposes an simplifeid morphological model for cement hydration that could be applied with homogenization modeling methods shown in the other parts of this thesis.
In detail, the processes of disolution of clinker grain and precipitation of $C-S-H$ gel are modeled, including the nature and influence on kinetics of an early surface hydrate, the moving solid-liquid interface, the manner in which microscopic growth processes lead to the characteristic morphologies of hydration products at larger length scales, and the role played by diffusion in the hydration period. The diffusion coefficient in the model $D(r)$ is a function of the porosity $\Phi(r)$ varying with the distance from the interfaces r.
According to the modeling results of this hydration model, the procedure could be improved in several aspects. Firstly, accouting for different anhydrous and hydrates could be a practical method to develope a more realistic model. Furthermore, the densification of $C-S-H$ gel could also be considered.

The lack of some details in the simplified hydration model (more types of anhydrous and hydrates) and the accumulation of the precipitated hydrates in the outmost layers might create the difference between the actuel creep modeling results coupling the hydration model with moving boundary conditions and the creep experimental results. But it is always helpful to connect the hydration model to the micromechanical model on the pursuit of a better morphological model for cementitious materials. This first proof of concept establishes the program structure between the evolutif hydration model and the homogenization mechanical model, leaving the prospect of refining the hydration model for future works.

Bibliographie

[1] Chapitre 1er : Dispositions générales relatives à la sécurité nucléaire, article l591-1.code de l'environnement, livre v : Prévention des pollutions, des risques et des nuisances, titre ix : La sécurité nucléaire et les installations nucléaires de base; article l591-1 crée par l'ordonnance n 2012-6 du 5 janvier 2012. 2012. http://www.legifrance.gouv.fr/affichCode.do?idArticle=LEGIARTI000025108609&idSectionTA=LEGISCTA000025108607&cidTexte=LEGITEXT000006074220&dateTexte=20150504. [p. 3]

[2] Z. A. Moschovidis and T. Mura. Two-ellipsoidal inhomogeneities by the equivalent inclusion method. *Journal of Applied Mechanics*, 42, 12 1975. [p. 9]

[3] J. Abate and W. Whitt. A unified framework for numerically inverting laplace transforms. *INFORMS Journal on Computing*, 18(4):408–421, 2006. [p. 45]

[4] G. Abiar. Cinétique de dessiccation et déformations différées du béton (analyse et modélisation). 1986. [p. 11]

[5] A. Aili, M. Vandamme, J.-M. Torrenti and B. Masson. Is long-term autogenous shrinkage a creep phenomenon induced by capillary effects due to self-desiccation? *Cement and Concrete Research*, 108:186 – 200, 2018. [p. 12, 15]

[6] G. E. Archie. The electrical resistivity log as an aid in determining some reservoir characteristics. *Transactions of the American Institute of Mining and Metallurgical Engineers*, 146:54–62, 1942. [p. 214]

[7] I. Avramov. The role of stress development and relaxation on crystal growth in glass. *Journal of Non-Crystalline Solids*, 353(30):2889–2892, 2007. [p. 55]

[8] M. Azenha, F. Magalhães, R. Faria and A. Cunha. Measurement of concrete e-modulus evolution since casting: A novel method based on ambient vibration. *Cement and Concrete Research*, 40(7):1096–1105, 2010. [p. 40]

[9] C. Badulescu, N. Lahellec and P. Suquet. Field statistics in linear viscoelastic composites and polycrystals. *European Journal of Mechanics - A Solids*, 49:329–344, 2015;2014;. [p. 9, 10]

[10] J.-F. Barthélémy, A. Giraud, F. Lavergne and J. Sanahuja. The eshelby inclusion problem in ageing linear viscoelasticity. *International Journal of Solids and Structures*, 97-98:530–542, 2016. [p. 10, 73, 86, 198]

[11] B. Bary, C. Bourcier and T. Helfer. Analytical and 3d numerical analysis of the thermoviscoelastic behavior of concrete-like materials including interfaces. *Advances in Engineering Software*, 112:16–30, 2017. [p. 64]

[12] B. Bary, M. B. Haha, E. Adam and P. Montarnal. Numerical and analytical effective elastic properties of degraded cement pastes. *Cement and Concrete Research*, 39(10):902–912, 2009. [p. 64]

[13] Bazant, Carreira and A. Walser. Creep and shrinkage in reactor containment shells. *Journal of Structural Engineering*, 101(10):2117–2131, 1 1975. [p. 13, 14]

[14] Z. Bažant. Viscoelasticity of solidifying porous material - concrete. 1977. `https://books.google.fr/books?id=QiLdmQEACAAJ`. [p. 10]

[15] Z. Bazant. Viscoelasticity of solidifying porous material - concrete. *CBI Forsk*, (5), 1 1977. [p. 80]

[16] Z. Bazant. Thermodynamics of solidifying or melting viscoelastic material. *Journal of Engineering Mechanics - ASCE*, 105(6):933–952, 12 1979. [p. 23, 53]

[17] Z. Bazant. Material models for structural creep analysis. 1988. [p. 86]

[18] Z. P. Bazant. Viscoelasticity of solidifying porous material - concrete. *ASCE J Eng Mech Div*, 103(6):1049–1067, 1977. `https://www.scopus.com/inward/record.uri?eid=2-s2.0-0017636164&partnerID=40&md5=3279bbf6f50e66427f8ef1f6c4f3a060`, cited By 58. [p. 23, 53, 71]

[19] Z. P. Bazant and J. C. Chern. Concrete creep at variable humidity: constitutive law and mechanism. *Materials and Structures*, 18(1):1–20, 1985. [p. 11]

[20] Z. P. Bažant. Numerical determination of long-range stress history from strain history in concrete. *Matériaux et Constructions*, 5(3):135–141, 1972. [p. 58]

[21] Z. P. Bažant. Prediction of concrete creep and shrinkage: past, present and future. *Nuclear Engineering and Design*, 203(1):27–38, 2001. [p. 51]

[22] Z. P. Bažant, A. A. Asghari and J. Schmidt. Experimental study of creep of hardened portland cement paste at variable water content. *Matériaux et Constructions*, 9(4):279–290, 1976. [p. 11]

[23] Z. R. Bažant and G. . Li. Comprehensive database on concrete creep and shrinkage. *ACI Materials Journal*, 105(6):635–637, 2008. `www.scopus.com`, Cited By :33. [p. 11, 13]

[24] F. Benboudjema. Modélisation des déformations différées du béton sous sollicitations biaxiales. Application aux enceintes de confinement de bâtiments réacteurs des centrales nucléaires. 2002. [p. 7, 11]

[25] O. Bernard, F.-J. Ulm and E. Lemarchand. A multiscale micromechanics-hydration model for the early-age elastic properties of cement-based materials. *Cement and Concrete Research*, 33(9):1293–1309, 2003. [p. 9, 22, 27, 41, 189, 190, 192, 193, 227]

[26] J. J. Biernacki and T. Xie. An advanced single particle model for c3s and alite hydration: Single particle model for c3s hydration. *Journal of the American Ceramic Society*, 94(7):2037–2047, 2011. [p. 201]

[27] S. Bishnoi and K. L. Scrivener. Studying nucleation and growth kinetics of alite hydration using ic. *Cement and Concrete Research*, 39(10):849–860, 2009. [p. 201]

[28] V. Blanc, L. Barbie, R. Largeiiton and R. Masson. Homogenization of linear viscoelastic three phase media: Internal variable formulation versus full-field computation. *Procedia Engineering*, 10:1893–1898, 2011. [p. 10]

[29] L. Boltzmann. Zur theorie der elastischen nachwirkung. *Annalen der Physik*, 241(11):430–432. `https://onlinelibrary.wiley.com/doi/abs/10.1002/andp.18782411107`. [p. 5]

[30] A. Boumiz. Mechanical properties of cement pastes and mortars at early ages evolution with time and degree of hydration. *Advanced Cement Based Materials*, 3(3-4):94–106, 1996. [p. 40]

[31] M. Briffaut, F. Benboudjema, J.-M. Torrenti and G. Nahas. Concrete early age basic creep: Experiments and test of rheological modelling approaches. *Construction and Building Materials*, 36(36):373–380, 2012. [p. 23, 60]

[32] J. Brooks. 3 - dimensional stability and cracking processes in concrete. p. 45 –85, 2007. [p. 13]

[33] J. J. Brooks. 30-year creep and shrinkage of concrete. *Magazine of Concrete Research*, 57(9):545–556, 2005. `https://doi.org/10.1680/macr.2005.57.9.545`. [p. 12, 13]

[34] P. W. Brown, J. Pommersheim and G. Frohnsdorff. A kinetic model for the hydration of tricalcium silicate. *Cement and Concrete Research*, 15(1):35–41, 1985. [p. 201]

[35] R. D. Browne and R. Blundell. The influence of loading age and temperature on the long term creep behaviour of concrete in a sealed, moisture stable, state. *Matériaux et Constructions*, 2(2):133–143, 1969. [p. 12]

[36] B. Budiansky. On the elastic moduli of some heterogeneous materials. *Journal of the Mechanics and Physics of Solids*, 13(4):223–227, 1965. [p. 36]

[37] J. W. Bullard. A determination of hydration mechanisms for tricalcium silicate using a kinetic cellular automaton model. *Journal of the American Ceramic Society*, 91(7):2088–2097, 2008. [p. 201]

[38] J. W. Bullard and R. J. Flatt. New insights into the effect of calcium hydroxide precipitation on the kinetics of tricalcium silicate hydration. *Journal of the American Ceramic Society*, 93(7):1894, 2010. [p. 201, 216, 217, 221]

[39] J. W. Bullard, H. M. Jennings, R. A. Livingston, A. Nonat, G. W. Scherer, J. S. Schweitzer, K. L. Scrivener and J. J. Thomas. Mechanisms of cement hydration. *Cement and Concrete Research*, 41(12):1208–1223, 2011. [p. 21]

[40] J. Byfors. Plain concrete at early ages. *Swedish Cement and Concrete Research Institute, Stockholm, Sweden*, 1980. [p. 40]

[41] I. Carol and Z. k. P. Ba ant. Viscoelasticity with aging caused by solidification of nonaging constituent. *Journal of Engineering Mechanics*, 119(11):2252–2269, 1993. [p. 23, 53]

[42] P. P. Castañeda. New variational principles in plasticity and their application to composite materials. *Journal of the Mechanics and Physics of Solids*, 40(8):1757–1788, 1992. [p. 9]

[43] W. Y. C.C. Yang, R. Huang and I. Sue. Aggregate effect on elastic moduli of cement-based composite materials. *Journal of Marine Science and Technologyc*, 3(1):5–10, 1995. [p. 7, 8]

[44] L. Charpin, Y. Le Pape, E. Coustabeau, E. Toppani, G. Heinfling, C. Le Bellego, B. Masson, J. Montalvo, A. Courtois, J. Sanahuja and N. Reviron. A 12year edf study of concrete creep under uniaxial and biaxial loading. *Cement and Concrete Research*, 103:140–159, 2018. [p. 109]

[45] L. Charpin, Y. L. Pape, E. Coustabeau, B. Masson and J. Montalvo. Edf study of 10-year concrete creep under unidirectional and biaxial loading: Evolution of the poisson coefficient under sealed and unsealed conditions. `https://ascelibrary.org/doi/abs/10.1061/9780784479346.163`. [p. 3]

[46] G. Constantinides and F.-J. Ulm. The effect of two types of c-s-h on the elasticity of cement-based materials: Results from nanoindentation and micromechanical modeling. *Cement and Concrete Research*, 34(1):67–80, 2004. [p. 9, 22, 41, 42, 191, 192, 193, 257]

[47] C. W. Correns. Growth and dissolution of crystals under linear pressure. *Discuss. Faraday Soc.*, 5:267–271, 1949. `http://dx.doi.org/10.1039/DF9490500267`. [p. 55]

[48] U. J. Counto. The effect of the elastic modulus of the aggregate on the elastic modulus, creep and creep recovery of concrete. *Magazine of Concrete Research*, 16(48):129–138, 1964. `https://doi.org/10.1680/macr.1964.16.48.129`. [p. 7]

[49] A. Courtois, J.-M. Henault, A. Simon, Y.-L. Beck and J. Salin. La surveillance en exploitation des enceintes de confinement et des aéroréfrigérants à tirage naturel du parc nucléaire d'edf. *Revue Générale Nucléaire*, (2):49–59, 2011. [p. 3]

[50] O. Coussy. Mechanics of porous continua. 1995. [p. 14]

[51] S. . S. T. M. for Creep and Shrinkage. Measurement of time-dependent strains of concrete. *Materials and Structures*, 31(8):507–512, 1998. [p. 5]

[52] S. . S. T. M. for Creep and Shrinkage. Measurement of time-dependent strains of concrete. *Materials and Structures*, 31(8):507–512, 1998. [p. 11]

[53] T. Crochon, T. Schönherr, C. Li and M. Lévesque. On finite-element implementation strategies of schapery-type constitutive theories. *Mechanics of Time-Dependent Materials*, 14(4):359–387, 2010. [p. 10]

[54] B. Delsaute. New approach for monitoring and modeling of the creep and shrinkage behaviour of cement pastes, mortars and concretes since setting time. 2016. [p. 133]

[55] S. Diamond. The microstructure of cement paste and concrete—a visual primer. *Cement and Concrete Composites*, 26(8):919–933, 2004. [p. 25]

[56] W. P. S. Dias, G. A. Khoury and P. J. E. Sullivan. Mechanism of creep in concrete. *Roorkee University Research Journal*, 12:37–47, 1970. [p. 7]

[57] C. F. Dunant, B. Bary, A. B. Giorla, C. Péniguel, J. Sanahuja, C. Toulemonde, A.-B. Tran, F. Willot and J. Yvonnet. A critical comparison of several numerical methods for computing effective properties of highly heterogeneous materials. *Advances in Engineering Software*, 58:1–12, 2013. [p. 8]

[58] F. Dupray. Comportement du béton sous fort confinement : Étude en compression et en extension triaxiales à l'échelle mésoscopique. [p. 8]

[59] V. F. P. Dutra, S. Maghous, A. C. Filho and A. R. Pacheco. A micromechanical approach to elastic and viscoelastic properties of fiber reinforced concrete. *Cement and Concrete Research*, 40(3):460–472, 2010. [p. 9]

[60] Y. El Assami. Homogenization of non-ageing linearly viscoelastic materials by the equivalent inclusion method : application to cementitious materials. 05 2015. [p. 9, 46]

[61] J. Escoda. Modélisation morphologique et micromécanique 3d de matériaux cimentaires. 2012. [p. 8, 17]

[62] J. D. Eshelby. The determination of the elastic field of an ellipsoidal inclusion, and related problems. *Proceedings of the Royal Society of London, Series A, Mathematical and Physical Sciences*, 241(1226):376–396, 1957. [p. 34]

[63] J. D. Eshelby. The determination of the elastic field of an ellipsoidal inclusion, and related problems. *Proceedings of the Royal Society of London. Series A, Mathematical and Physical Sciences*, 241(1226):376–396, 1957. [p. 36]

[64] R. J. Flatt, G. W. Scherer and J. W. Bullard. Why alite stops hydrating below 80 relative humidity. *Cement and Concrete Research*, 41(9):987 – 992, 2011. [p. 12]

[65] A. Foucault, S. Michel-Ponnelle and E. Galenne. A new creep model for npp containment behaviour prediction. 2012. [p. 3]

[66] E. Gal and R. Kryvoruk. Meso-scale analysis of frc using a two-step homogenization approach. *Computers and Structures*, 89(11):921 – 929, 2011. `http://www.sciencedirect.com/science/article/pii/S0045794911000393`, Computational Fluid and Solid Mechanics 2011. [p. 8]

[67] E. Galenne and B. Masson. A new mock-up for evaluation of the mechanical and leaktightness behaviour of npp containment building. *Proc., CCSC 2012*, 2012. [p. 4]

[68] E. Galenne, S. Michel-Ponnelle, J. Salin, G. Moreau, J. Sanahuja and C. Toulemonde. The aim of computational methods for managing concrete structures in nuclear power plants. 1:51–60, 2014. `www.scopus.com`, Cited By :1. [p. 4]

[69] E. J. Garboczi and J. G. Berryman. Elastic moduli of a material containing composite inclusions: effective medium theory and finite element computations. *Mechanics of Materials*, 33(8):455–470, 2001. [p. 8]

[70] S. Garrault, E. Finot, E. Lesniewska and A. Nonat. Study of c-s-h growth on c3s surface during its early hydration. *Materials and Structures*, 38(4):435–442, May 2005. `https://doi.org/10.1007/BF02482139`. [p. 197, 221]

[71] J. Garrigues. M¡ ecani ue es milieu# continus. 2001. [p. 33]

[72] J. Gaver, D. P.. Observing stochastic processes, and approximate transform inversion. *Operations Research*, 14(3):444–459, 1966. [p. 45]

[73] J. R. G.E. Troxell and R. Davis. Long-time creep and shrinkage tests of plain and reinforced concrete. p. 1101–1120, 1958. [p. 13]

[74] M. P. G.J. Kommendant and D. Pirtz. Study of concrete properties for prestressed concrete reactor vessels. 1976. Technical Report UCSESM 76-3. [p. 12]

[75] P. Glover. What is the cementation exponent? a new interpretation. *The Leading Edge*, 28(1):82–85, 2009. `https://doi.org/10.1190/1.3064150`. [p. 214]

[76] P. W. J. Glover. Archie's law - a reappraisal. *Solid Earth Discussions*, pp. 1–18, 2016. [p. 214]

[77] J. Glucklich and O. Ishai. Creep mechanism in cement mortar. *Journal Proceedings*, 59:923–948, 1962. [p. 11]

[78] K. S. Gopalakrishnan, A. M. Neville and A. Ghali. Elastic and time-dependent effects of aggregate-matrix interaction. *Matériaux et Construction*, 3(4):225–236, Jul 1970. https://doi.org/10.1007/BF02474011. [p. 7]

[79] M. Gottapu and J. J. Biernacki. A multi-ionic continuum-based model for c3 s hydration. *Journal of the American Ceramic Society*, 98(10):3029–3041, 2015. [p. 199, 201, 216]

[80] L. Granger. Comportement différé du béton dans les enceintes de centrales nucléaires : analyse et modélisation. [p. 5, 8, 11, 13, 14, 23]

[81] Z. C. Grasley and D. A. Lange. Constitutive modeling of the aging viscoelastic properties of portland cement paste. *Mechanics of Time-Dependent Materials*, 11(3):175–198, 2007. [p. 5]

[82] S. T. Gu, B. Bary, Q. C. He and M. Q. Thai. Multiscale poro creep model for cement based materials. *International Journal for Numerical and Analytical Methods in Geomechanics*, 36(18):1932–1953, 2012. [p. 22, 41, 43]

[83] K. K. H. Rusch and H. Hilsdorf. Der einfluss des mineralogischen charakters der zuschlage auf das kriechen von beton. 1962. [p. 13]

[84] T. Hansen. Theories of multi-phase materials applied to concrete, cement mortar and cement paste. p. 16–23, 1966. [p. 7]

[85] Z. Hashin. Viscoelastic behavior of heterogeneous media. *Journal of Applied Mechanics*, 32(3):630–636, 1965. [p. 9]

[86] Z. Hashin and S. Shtrikman. A variational approach to the theory of the elastic behaviour of multiphase materials. *Journal of the Mechanics and Physics of Solids*, 11(2):127–140, 1963. [p. 7]

[87] M. Irfan-ul Hassan, B. Pichler, R. Reihsner and C. Hellmich. Elastic and creep properties of young cement paste, as determined from hourly repeated minute-long quasi-static tests. *Cement and Concrete Research*, 82:36–49, 2016. [p. 52, 60]

[88] N. Herrmann, H. S. Müller, S. Michel-Ponnelle, B. Masson and M. Herve. The pace-1450 experiment – investigations regarding crack and leakage behaviour of a pre-stressed concrete containment. pp. 1487–1495, 2018. [p. 4]

[89] E. Herve and A. Zaoui. n- layered inclusion-based micromechanical modelling. *International Journal of Engineering Science*, 31(1):1–10, 1993. [p. 8]

[90] A. Hilaire. Étude des déformations différées des bétons en compression et en traction, du jeune au long terme : application aux enceintes de confinement. 11 2014. [p. 7]

[91] A. Hilaire, F. Benboudjema, A. Darquennes, Y. Berthaud and G. Nahas. Modeling basic creep in concrete at early-age under compressive and tensile loading. *Nuclear Engineering and Design*, 269:222 – 230, 2014. `http://www.sciencedirect.com/science/article/pii/S002954931300383X`, Special Issue - The International Conference on Structural Mechanics in Reactor Technology (SMiRT21), New Delhi India, Nov 06-11, 2011. [p. 7]

[92] R. Hill. A self-consistent mechanics of composite materials. *Journal of the Mechanics and Physics of Solids*, 13(4):213–222, 1965. [p. 36]

[93] T. J. Hirsch. Modulus of elasticity of concrete affected by elastic moduli of cement paste matrix and aggregate. 59, 1962. [p. 7]

[94] T. Honorio, B. Bary and F. Benboudjema. Multiscale estimation of ageing viscoelastic properties of cement-based materials: A combined analytical and numerical approach to estimate the behaviour at early age. *Cement and Concrete Research*, 85:137–155, 2016. [p. 23]

[95] T. Honorio, B. Bary, J. Sanahuja and F. Benboudjema. Effective properties of n-coated composite spheres assemblage in an ageing linear viscoelastic framework. *International Journal of Solids and Structures*, 124:1–13, 2017. [p. 63]

[96] S. Huang, J. Sanahuja, L. Dormieux, B. Bary, E. Lemarchand and M. Hervé. Double scale model of the aging creep of low density hydrates of cement paste. `https://ascelibrary.org/doi/abs/10.1061/9780784480779.127`. [p. 22]

[97] K. Ioannidou, K. J. Krakowiak, M. Bauchy, C. G. Hoover, E. Masoero, S. Yip, F.-J. Ulm, P. Levitz, R. J. . Pellenq and E. D. Gado. Mesoscale texture of cement hydrates. *Proceedings of the National Academy of Sciences*, 113(8):2029–2034, 2016. [p. 73]

[98] U. G. J. C. Michel and P. Suquet. Constitutive relations involving internal variables based on a micromechanical analysisc. p. 301–312, 2002. [p. 10]

[99] L. Jason and B. Masson. Comparison between continuous and localized methods to evaluate the flow rate through containment concrete structures. *Nuclear Engineering and Design*, 277:146–153, 2014. [p. 4]

[100] A. R. Jayapalan, M. L. Jue, K. E. Kurtis and D. Viehland. Nanoparticles and apparent activation energy of portland cement. *Journal of the American Ceramic Society*, 97(5):1534–1542, 2014. [p. 11]

[101] M. Juenger, H. Lamour, P. Monteiro, E. Gartner and G. Denbeaux. Direct observation of cement hydration by soft x-ray transmission microscopy. *Journal of Materials Science Letters*, 22(19):1335–1338, 2003. cited By 21. [p. 25]

[102] P. Juilland, E. Gallucci, R. Flatt and K. Scrivener. Dissolution theory applied to the induction period in alite hydration. *Cement and Concrete Research*, 40(6):831–844, 2010. [p. 201, 221]

[103] H. Kada-Benameur, E. Wirquin and B. Duthoit. Determination of apparent activation energy of concrete by isothermal calorimetry. *Cement and Concrete Research*, 30(2):301–305, 2000. [p. 11]

[104] D. M. Kirby and J. J. Biernacki. The effect of water-to-cement ratio on the hydration kinetics of tricalcium silicate cements: Testing the two-step hydration hypothesis. *Cement and Concrete Research*, 42(8):1147–1156, 2012. [p. 201]

[105] A. Kumar, S. Bishnoi and K. L. Scrivener. Modelling early age hydration kinetics of alite. *Cement and Concrete Research*, 42(7):903–918, 2012. [p. 201]

[106] N. Lahellec and P. Suquet. Effective response and field statistics in elasto-plastic and elasto-viscoplastic composites under radial and non-radial loadings. *International Journal of Plasticity*, 42:1 – 30, 2013. `http://www.sciencedirect.com/science/article/pii/S0749641912001350`. [p. 9]

[107] R. Largenton, J.-C. Michel and P. Suquet. Extension of the nonuniform transformation field analysis to linear viscoelastic composites in the presence of aging and swelling. *Mechanics of Materials*, 73:76–100, 2014. [p. 10]

[108] F. d. Larrard. Structures granulaires et formulation des bétons. 2000. [p. 8]

[109] F. Lavergne. Contribution to the study of the time-dependent strains of viscoelastic composite materials. (2015PESC1171), Dec. 2015. `https://pastel.archives-ouvertes.fr/tel-01300510`. [p. 5]

[110] F. Lavergne, K. Sab, J. Sanahuja, M. Bornert and C. Toulemonde. Investigation of the effect of aggregates' morphology on concrete creep properties by numerical simulations. *Cement and Concrete Research*, 71:14–28, 2015. [p. 3]

[111] F. Lavergne, K. Sab, J. Sanahuja, M. Bornert and C. Toulemonde. Homogenization schemes for aging linear viscoelastic matrix-inclusion composite materials with elongated inclusions. *International Journal of Solids and Structures*, 80:545–560, 2016. [p. 23, 86]

[112] Q. V. Le, F. Meftah, Q. . He and Y. Le Pape. Creep and relaxation functions of a heterogeneous viscoelastic porous medium using the mori-tanaka homogenization scheme and a discrete microscopic retardation spectrum. *Mechanics of Time-Dependent Materials*, 11(3):309–331, 2007. [p. 43]

[113] R. Le Roy, F. Le Maou and J. M. Torrenti. Long term basic creep behavior of high performance concrete: data and modelling. *Materials and Structures*, 50(1):1–11, 2017. [p. 12, 13, 145, 251]

[114] R. L'Hermite and M. Mamillan. Nouveaux résultats et récentes études sur le fluage du béton. *Matériaux et Construction*, 2(1):35–41, Jan 1969. https://doi.org/10.1007/BF02473653. [p. 12]

[115] X. Li, Z. C. Grasley, J. W. Bullard and E. J. Garboczi. Computing the time evolution of the apparent viscoelastic/viscoplastic poisson's ratio of hydrating cement paste. *Cement and Concrete Composites*, 56:121–133, 2015. [p. 23]

[116] X. Li, Z. C. Grasley, E. J. Garboczi and J. W. Bullard. Modeling the apparent and intrinsic viscoelastic relaxation of hydrating cement paste. *Cement and Concrete Composites*, 55:322–330, 2015. [p. 23, 55, 59]

[117] B. Lothenbach, K. Scrivener and R. D. Hooton. Supplementary cementitious materials. *Cement and Concrete Research*, 41(3):217–229, 2011. [p. 25]

[118] B. Lothenbach and F. Winnefeld. Thermodynamic modelling of the hydration of portland cement. *Cement and Concrete Research*, 36(2):209–226, 2006. [p. 25]

[119] . F.-J. U. Luc Dormieux, . Djimédo Kondo. Microporomechanics. 2006. [p. 29]

[120] S. Maghous and G. J. Creus. Periodic homogenization in thermoviscoelasticity: case of multilayered media with ageing. *International Journal of Solids and Structures*, 40(4):851–870, 2003. [p. 10]

[121] L. Maia, M. Azenha, R. Faria and J. Figueiras. Identification of the percolation threshold in cementitious pastes by monitoring the e-modulus evolution. *Cement and Concrete Composites*, 34(6):739–745, 2012. [p. 40]

[122] L. Maia, M. Azenha, M. Geiker and J. Figueiras. E-modulus evolution and its relation to solids formation of pastes from commercial cements. *Cement and Concrete Research*, 42(7):928, 2012. [p. 40]

[123] J. Mandel. Sur les corps viscoelastiques lineaires dont les proprietes dependent de lage. *Comptes rendus hebdomadaires des séances de l'académie des sciences*, 247(2):175–178, 1958. [p. 9]

[124] J. Mandel. Cours de mécanique des milieux continus. 1966. [p. 23, 44]

[125] E. Masoero, J. J. Thomas and H. M. Jennings. A reaction zone hypothesis for the effects of particle size and water-to-cement ratio on the early hydration kinetics of c3s. *American Ceramic Society. Journal of the American Ceramic Society*, 97(3):967, 2014. [p. 201]

[126] B. Masson. La durée de fonctionnement des enceintes de confinement. *Revue Générale Nucléaire*, (3):64–68, 2015. [p. 3]

[127] R. Masson, R. Brenner and O. Castelnau. Incremental homogenization approach for ageing viscoelastic polycrystals. *Comptes Rendus Mécanique*, 340:378–386, 2012. [p. 9, 57]

[128] J. Mazars, F. Hamon and S. Grange. A new 3d damage model for concrete under monotonic, cyclic and dynamic loadings. *Materials and Structures*, 48(11):3779–3793, 2015. [p. 3]

[129] J. C. Michel and P. Suquet. Nonuniform transformation field analysis. *International Journal of Solids and Structures*, 40(25):6937–6955, 2003. [p. 10]

[130] V. Monchiet and G. Bonnet. A polarization based fft iterative scheme for computing the effective properties of elastic composites with arbitrary contrast. *International Journal for Numerical Methods in Engineering*, 89(11):1419–1436, 2012. [p. 10]

[131] P. J. M. Monteiro. A note on the hirsch model. *Cement and Concrete Research*, 21(5):947–950, 1991. [p. 7, 8]

[132] T. Mori and K. Tanaka. Average stress in matrix and average elastic energy of materials with misfitting inclusions. *Acta Metallurgica*, 21(5):571–574, 1973. [p. ix, 8, 29, 35]

[133] H. Moulinec and F. Silva. Comparison of three accelerated fft based schemes for computing the mechanical response of composite materials. *International Journal for Numerical Methods in Engineering*, 97(13):960–985, 2014. [p. 10]

[134] H. Moulinec and P. Suquet. A numerical method for computing the overall response of nonlinear composites with complex microstructure. *Computer Methods in Applied Mechanics and Engineering*, 157(1):69–94, 1998. [p. 8, 10]

[135] J. C. Nadeau. A multiscale model for effective moduli of concrete incorporating itz water–cement ratio gradients, aggregate size distributions, and entrapped voids. *Cement and Concrete Research*, 33(1):103–113, 2003. [p. 8]

[136] A. Neville. Properties of concrete. 2011. [p. 13]

[137] A. M. Neville, W. H. W. H. Dilger and J. J. Brooks. Creep of plain and structural concrete. 1983. Includes bibliographical references and indexes. [p. 13]

[138] T. T. H. Nguyen, B. Bary and T. de Larrard. Coupled carbonation-rust formation-damage modeling and simulation of steel corrosion in 3d mesoscale reinforced concrete. *Cement and Concrete Research*, 74:95–107, 2015. [p. 64]

[139] . J. d. P. Peter Atkins. Atkins' physical chemistry. 2002. [p. 190]

[140] B. Pichler and C. Hellmich. Upscaling quasi-brittle strength of cement paste and mortar: A multi-scale engineering mechanics model. *Cement and Concrete Research*, 41(5):467–476, 2011. [p. 41]

[141] B. Pichler, C. Hellmich and J. Eberhardsteiner. Spherical and acicular representation of hydrates in a micromechanical model for cement paste: prediction of early-age elasticity and strength. *Acta Mechanica*, 203(3):137–162, 2009. [p. 22, 40, 41]

[142] B. Pichler, C. Hellmich, J. Eberhardsteiner, J. Wasserbauer, P. Termkhajornkit, R. Barbarulo and G. Chanvillard. Effect of gel–space ratio and microstructure on strength of hydrating cementitious materials: An engineering micromechanics approach. *Cement and Concrete Research*, 45:55–68, 2013. [p. 40, 41]

[143] B. Pichler, M. Shahidi and C. Hellmich. Interfacial micromechanics assessment of classical rheological models. i: Single interface size and viscosity. *Journal of Engineering Mechanics*, 142(3):4015092, 2016. [p. 51]

[144] S. E. Pihlajavaara. A review of some of the main results of a research on the ageing phenomena of concrete: Effect of moisture conditions on strength, shrinkage and creep of mature concrete. *Cement and Concrete Research*, 4(5):761–771, 1974. [p. 11]

[145] T. Powers and T. Brownyard. Studies of the physical properties of hardened portland cement paste. 1948. `https://books.google.fr/books?id=Pc1YAAAAYAAJ`. [p. 25, 79, 195]

[146] S. Prasannan and Z. k. P. Ba ant. Solidification theory for concrete creep. i: Formulation. *Journal of Engineering Mechanics*, 115(8):1691–1703, 1989. [p. 23, 53]

[147] S. Problem and C. Vuik. Some historical notes about the stefan problem. 05 1994. [p. 202]

[148] O. C. Q. H. Vu, R. Brenner and H. Moulinec. Une methode incrementale pour l'homogeneisation viscelastique lineaire de polycristaux. 2011. [p. 10]

[149] J.-M. Ricaud and R. Masson. Effective properties of linear viscoelastic heterogeneous media: Internal variables formulation and extension to ageing behaviours. *International Journal of Solids and Structures*, 46(7):1599–1606, 2009. [p. 10, 57]

[150] I. G. Richardson. The nature of the hydration products in hardened cement pastes. *Cement and Concrete Composites*, 22(2):97–113, 2000. [p. 25]

[151] F. Riesz and B. Sz.-Nagy. Functional analysis. 1990. [p. 159]

[152] c. RILEM Technical Committee TC-242-MDC (Zdeněk P. Bažant. Rilem draft recommendation: Tc-242-mdc multi-decade creep and shrinkage of concrete: material model and structural analysis: Model b4 for creep, drying shrinkage and autogenous shrinkage of normal and high-strength concretes with multi-decade applicability. *Materials and Structures*, 48(4):753–770, 2015. [p. 11]

[153] P. Rossi, N. Godart, J. L. Robert, J. P. Gervais and D. Bruhat. Investigation of the basic creep of concrete by acoustic emission. *Materials and Structures*, 27(9):510, Nov 1994. `https://doi.org/10.1007/BF02473211`. [p. 7]

[154] P. Rossi, J.-L. Tailhan, F. L. Maou, L. Gaillet and E. Martin. Basic creep behavior of concretes investigation of the physical mechanisms by using acoustic emission. *Cement and Concrete Research*, 42(1):61 – 73, 2012. http://www.sciencedirect.com/science/article/pii/S0008884611002110. [p. 7, 51]

[155] Y. Rougier, C. Stolz et A. Zaoui. Représentation spectrale en viscoélasticité linéaire des matériaux hétérogènes. *Comptes Rendus de l'Academie des Sciences Serie II*, 316 :1517–1522, 1993. [p. 9]

[156] R. L. Roy. Déformations instantanées et différées des bétons à hautes performances. 1996. [p. 8, 22, 52, 59]

[157] J. Salençon. Viscoélasticité pour le calcul des structures. p. 151, 2009. https://hal.archives-ouvertes.fr/hal-00870155. [p. 5, 136, 153, 156, 158, 186, 187, 255, 257]

[158] D. L.-L. P. Y. Sanahuja, J. and C. Toulemonde. Modélisation micro-macro du fluage propre du béton. 2009. [p. 22, 43, 52, 193, 197, 221]

[159] J. Sanahuja. Efficient homogenization of ageing creep of random media: Application to solidifying cementitious materials. https://ascelibrary.org/doi/abs/10.1061/9780784413111.023. [p. v, vii, 11]

[160] J. Sanahuja. Effective behaviour of ageing linear viscoelastic composites: Homogenization approach. *International Journal of Solids and Structures*, 50(19):2846–2856, 2013. [p. v, vii, 10, 11, 23, 57, 58, 59, 71, 75, 86]

[161] J. Sanahuja. Homogenization of solidifying random porous media: Application to ageing creep of cementitious materials. 2015. [p. 23, 59, 80, 152, 158, 193, 198, 249]

[162] J. Sanahuja and M. Di Ciaccio. From micromechanisms to mechanical behaviour: An application to the ageing creep of a cement paste. *CONCREEP 2015: Mechanics and Physics of Creep, Shrinkage, and Durability of Concrete and Concrete Structures - Proceedings of the 10th International Conference on Mechanics and Physics of Creep, Shrinkage, and Durability of Concrete and Concrete Structures*, pp. 1024–1027, 2015. cited By 0. [p. 23]

[163] J. Sanahuja and L. Dormieux. Creep of a c-s-h gel: a micromechanical approach. *Anais da Academia Brasileira de Ciências*, 82(1):25–41, 2010. [p. 51]

[164] J. Sanahuja, L. Dormieux and G. Chanvillard. Modelling elasticity of a hydrating cement paste. *Cement and Concrete Research*, 37(10):1427–1439, 2007. [p. 22, 41, 42, 72, 252]

[165] J. Sanahuja, L. Dormieux and G. Chanvillard. A reply to the discussion "does c–s–h particle shape matter?" f.-j. ulm and h. jennings of the paper "modelling

elasticity of a hydrating cement paste", ccr 37 (2007). *Cement and Concrete Research*, 38(8):1130 – 1134, 2008. http://www.sciencedirect.com/science/article/pii/S0008884608000859. [p. 41, 197, 198, 221]

[166] J. Sanahuja and S. Huang. Mean-field homogenization of time-evolving microstructures with viscoelastic phases: Application to a simplified micromechanical model of hydrating cement paste. *Journal of Nanomechanics and Micromechanics*, 7(1):04016011, 2017. [p. 22, 71, 135, 152, 160, 185]

[167] J. Sanahuja, S. Huang, L. Dormieux, B. Bary and E. Lemarchand. Relating microstructure development to ageing creep: application to vercors concrete. [p. xiii, 189, 194, 218, 220, 227]

[168] J. Sanahuja, S. Huang, L. Dormieux, B. Bary, E. Lemarchand and M. Hervé. Porous materials undergoing time-dependent phase transformations: Effective ageing viscoelasticity. https://ascelibrary.org/doi/abs/10.1061/9780784480779.128. [p. 85]

[169] J. Sanahuja, N.-C. Tran, L. Charpin and L. Petit. Material properties prediction for long term operation of nuclear power plants civil engineering structures: challenges at edf. p. 12, 2016. [p. 195, 196, 257]

[170] C. L. Sanahuja J., Tran N.-C. and P. L.. Vi(ca)2t v2 : can a concrete material properties simulation code be both physics-based and engineer-friendly. 2016. [p. 8, 195, 196, 257]

[171] R. Schapery. Approximate methods of transform inversion for viscoelastic stress analysis. 2, 01 1962. [p. 9]

[172] S. Scheiner and C. Hellmich. Continuum microviscoelasticity model for aging basic creep of early-age concrete. *Journal of Engineering Mechanics*, 135(4):307–323, 2009. [p. 23, 58]

[173] G. W. Scherer. Crystallization in pores. *Cement and Concrete Research*, 29(8):1347–1358, 1999. [p. 55]

[174] G. W. Scherer. Stress from crystallization of salt. *Cement and Concrete Research*, 34(9):1613–1624, 2004. [p. 55]

[175] A. Sellier, L. Lacarrière, S. Multon, T. Vidal and X. Bourbon. Nonlinear basic creep and drying creep modeling. 05 2012. [p. 7]

[176] M. Shahidi, B. Pichler and C. Hellmich. Viscous interfaces as source for material creep: A continuum micromechanics approach. *European Journal of Mechanics - A/Solids*, 45:41–58, 2014. [p. 51]

[177] L. Stefan, F. Benboudjema, J.-M. Torrenti and B. Bissonnette. Prediction of elastic properties of cement pastes at early ages. *Computational Materials Science*, 47(3):775–784, 2010. [p. 27]

[178] H. Stehfest. Algorithm 368: Numerical inversion of laplace transforms [d5]. *Commun. ACM*, 13(1):47–49, Jan. 1970. http://doi.acm.org/10.1145/361953.361969. [p. 9]

[179] H. Stehfest. Algorithm 368: Numerical inversion of laplace transforms [d5]. *Communications of the ACM*, 13(1):47–49, 1970. [p. 45]

[180] A. F. Stock, D. J. Hannantt and R. I. T. Williams. The effect of aggregate concentration upon the strength and modulus of elasticity of concrete. *Magazine of Concrete Research*, 31(109):225–234, 1979. https://doi.org/10.1680/macr.1979.31.109.225. [p. 8]

[181] E. Stora, Q. . He and B. Bary. Influence of inclusion shapes on the effective linear elastic properties of hardened cement pastes. *Cement and Concrete Research*, 36(7):1330–1344, 2006. [p. 41]

[182] A. Subhashini, P. C. o. a. Assistant Professor and C. A. P. C. T. N. . Science, Avinashi Road. A new approach on denoising for 1d, 2d and 3d images based on discrete wavelet transformation and thresholding. *International Journal of Advanced Research in Computer Science*, 9(1):708–710, 2018. [p. 184]

[183] Z. Sun, G. Ye and S. Shah. Microstructure and early-age properties of portland cement paste - effects of connectivity of solid phases. *ACI Materials Journal*, 102(2):122–129, 3 2005. [p. 40]

[184] P. Sémété, B. Février, Y. L. Pape, J. Delorme, J. Sanahuja and A. Legrix. Concrete desorption isotherms and permeability determination: effects of the sample geometry. *European Journal of Environmental and Civil Engineering*, 21(1):42–62, 2017. https://doi.org/10.1080/19648189.2015.1090930. [p. 3]

[185] B. T. Tamtsia and J. J. Beaudoin. Basic creep of hardened cement paste a re-examination of the role of water. *Cement and Concrete Research*, 30(9):1465–1475, 2000. [p. 51, 52]

[186] B. T. Tamtsia, J. J. Beaudoin and J. Marchand. The early age short-term creep of hardening cement paste: load-induced hydration effects. *Cement and Concrete Composites*, 26(5):481–489, 2004. [p. 40, 52, 60, 85, 225, 251]

[187] J. Taplin. A method for following the hydration reaction in portland cement paste. *Aust. J. Appl. Sci.*, 10(3):329–345, 1959. [p. 40]

[188] P. Termkhajornkit, Q. H. Vu, R. Barbarulo, S. Daronnat and G. Chanvillard. Dependence of compressive strength on phase assemblage in cement pastes: Beyond gel–space ratio — experimental evidence and micromechanical modeling. *Cement and Concrete Research*, 56:1–11, 2014. [p. 41]

[189] J. M. Torrenti and F. Benboudjema. Mechanical threshold of cementitious materials at early age. *Materials and Structures*, 38(3):299–304, 2005. [p. 40, 41, 42]

[190] N. W. Tschoegl, C. A. Tschoegl and S. O. service). Phenomenological theory of linear viscoelastic behavior : An introduction. 1989. [p. 153]

[191] F.-J. Ulm, F. Le Maou and C. Boulay. Creep and shrinkage coupling: New review of some evidence. *REVUE FRANCAISE DE GENIE CIVIL*, 3:21–38, 1999. [p. 7, 12]

[192] A. Ulrik Nilsen and P. J. M. Monteiro. Concrete: A three phase material. *Cement and Concrete Research*, 23(1):147–151, 1993. [p. 8]

[193] M. Vandamme and F. . Ulm. Nanoindentation investigation of creep properties of calcium silicate hydrates. *Cement and Concrete Research*, 52:38–52, 2013. [p. 8]

[194] K. Velez, S. Maximilien, D. Damidot, G. Fantozzi and F. Sorrentino. Determination by nanoindentation of elastic modulus and hardness of pure constituents of portland cement clinker. *Cement and Concrete Research*, 31(4):555–561, 2001. [p. 39, 197]

[195] K. Velez and F. Sorrentino. Characterization of cementitious materials by nanoindentation. *Kurdowski Symp. on Science of Cement and Concrete, Akapit-Wydaw, Naukowe*, p. 67–77, 2001. [p. 39]

[196] V. Volterra. Sopra le funzioni che dipendono da altre funzioni. 1887. `https://books.google.fr/books?id=lTCenQAACAAJ`. [p. 57]

[197] V. Volterra. Theory of functionals and of integral and integro-differential equations. 2005. `https://books.google.fr/books?id=HhAoddpkcWgC`. [p. 57]

[198] Q. H. Vu, R. Brenner, O. Castelnau, H. Moulinec and P. Suquet. A self-consistent estimate for linear viscoelastic polycrystals with internal variables inferred from the collocation method. *Modelling and Simulation in Materials Science and Engineering*, 20(2):024003, 2012. [p. 9]

[199] V. Waller. Relations entre composition des bétons, exothermie en cours de prise et résistance en compression. 2000. [p. 11]

[200] E. Wiechert. Ueber elastische nachwirkung, inaugural-dissertation ... am 19. februar 1889 ... vertheidigt von emil wiechert ... `https://books.google.fr/books?id=xzhhQwAACAAJ`. [p. 153]

[201] E. Wiechert. Gesetze der elastischen nachwirkung für constante temperatur. *Annalen der Physik*, 286(10):335–348, 1893. [p. 153]

[202] F. H. Wittman. Creep and shrinkage in concrete structures. 1982. [p. 7]

[203] F. H. Wittmann. Creep and shrinkage mechanisms. p. 129–161, 1982. [p. 51]

[204] T. Xie and J. J. Biernacki. The origins and evolution of cement hydration models. *Computers and Concrete*, 8(6):647–675, 2011. [p. 201]

[205] M. P. Yssorche-Cubaynes and J.-P. Ollivier. La microfissuration d'autodessiccation et la durabilité des bhp et bthp. *Materials and Structures*, 32(1):14–21, Jan 1999. [p. 12]

[206] A. Zaoui. Continuum micromechanics: Survey. *Journal of Engineering Mechanics*, 128(8):808–816, 2002. [p. 29]

[207] P. Zdenllk. Theory of creep and shrinkage in 'concrete structures: A ·precis of recent developments. [p. 86]

[208] Q. Zhang, R. L. Roy, M. Vandamme and B. Zuber. Long-term creep properties of cementitious materials: Comparing microindentation testing with macroscopic uniaxial compressive testing. *Cement and Concrete Research*, 58:89 – 98, 2014. `http://www.sciencedirect.com/science/article/pii/S0008884614000052`. [p. 8]

[209] X. Zhang, Y. Yang and C. K. Ong. A novel way of estimation of the apparent activation energy of cement hydration using microwave technique. *Journal of Materials Science*, 34(13):3143–3147, 1999. [p. 11]

[210] V. Šmilauer and Z. P. Bažant. Identification of viscoelastic c-s-h behavior in mature cement paste by fft-based homogenization method. *Cement and Concrete Research*, 40(2):197–207, 2010. [p. 10, 22, 43]

Main notations

$\underline{A}$	order 1 tensor
$\underline{\underline{A}}$	order 2 tensor
$\mathbb{A}$	order 4 tensor
$T_1 \cdot T_2$	contracted product of two tensors
$T_1 : T_2$	double contracted product of two tensors
$T_1 \otimes T_2$	tensor product
$\mathbf{1}$	identity order 2 tensor
$tr\boldsymbol{A}$	trace of A, $tr\boldsymbol{A} = \boldsymbol{A} : 1$
$\boldsymbol{A}^{dev}$	deviator of $\boldsymbol{A}$, $\boldsymbol{A}^{dev} = \boldsymbol{A} - 1/3(tr\boldsymbol{A})1$
${}^t\boldsymbol{A}$	transpose of an order 2 tensor
T^{-1}	inverse of an order 2 or 4 tensor
$\mathbb{I}$	identity order 4 tensor for symmetric tensors, $\mathbb{I} : \boldsymbol{S} = \boldsymbol{S}$ where S is a symmetric tensor
$\mathbb{J}$	tensor extracting the spherical part of a symmetric order 2 tensor, $\mathbb{J} = 1/31 \otimes 1$
	$\mathbb{J} : \boldsymbol{S} = 1/3(tr\boldsymbol{S})1$ where $\boldsymbol{S}$ is a symmetric order 2 tensor
$\mathbb{K}$	tensor extracting the deviatoric part of a symmetric order 2 tensor, $\mathbb{K} = \mathbb{I} - \mathbb{J}$
	$\mathbb{K} : \boldsymbol{S} = \boldsymbol{S}^{dev}$ where $\boldsymbol{S}$ is a symmetric order 2 tensor
$\boldsymbol{grad}(\underline{A})$	gradient of an order 1 tensor
$\underline{div}(\boldsymbol{A})$	divergence of an order 2 tensor
$f \circ x$	Volterra integral operator,
	denoted $y = f \circ x$ or $y(t) = f(t,.) \circ x(.)$ or $y(t) = \int_{\infty}^{t} f(t,t')dx(t')$
H(x)	Heaviside function
$[v]$	vector
$[\![m]\!]$	square matrix
$[\![m]\!] \cdot [v]$	matrix–vector product
$[\![m_1]\!] \cdot [\![m_2]\!]$	t product of two matrices
$[\![I]\!]$	identity square matrix
$[\![m]\!]^{-1}$	inverse of square matrix $[\![m]\!]$
Ω	REV (representative elementary volume) domain
Ω_j	j phase j domain in REV
f_j	volume fraction of phase j in REV
ϕ	porosity of REV
$\langle a \rangle_j$	spatial average of field a over phase j

$\langle a \rangle$	spatial average of field a over the whole REV
ξ	microscopic displacement vector
$\boldsymbol{\epsilon}$	microscopic linearized strain tensor
$\boldsymbol{\sigma}$	microscopic stress tensor
$\boldsymbol{E}$	macroscopic linearized strain tensor
Σ	macroscopic stress tensor
$\mathbb{C}(t,t')$ or $\mathbb{C}$	relaxation tensor
$\mathbb{S}(t,t')$ or $\mathbb{S}$	compliance tensor, $\mathbb{S} = \mathbb{C}^{-1}$
	if behaviour is isotropic, $\mathbb{C} = 3k\mathbb{J} + 2g\mathbb{K}$ and $\mathbb{S} = J^k/3\mathbb{J} + J^g/2\mathbb{K}$, with :
J^k	bulk compliance
J^g	shear compliance
J^E	uniaxial compliance,
	defined as $\epsilon_{11} = J^E \circ \sigma_{11}$ when applied stress history is $\boldsymbol{\sigma} = \sigma_{11}\underline{e}_1 \otimes \underline{e}_1$
$k = J^{k-1}$	bulk relaxation
$g = J^{g-1}$	shear relaxation
$E = J^{E-1}$	uniaxial relaxation

Elementary parts of rheologic models :

k	stiffness of spring, when representing bulk behaviour
g	stiffness of spring, when representing shear behaviour
η	viscosity of dashpot, when representing bulk behaviour
γ	viscosity of dashpot, when representing shear behaviour
$\mathbb{A}(t,t')$ or $\mathbb{A}$	strain localization tensor operator
$\mathbb{A}_p^q(t,t')$ or $\mathbb{A}_p^q$	strain localization tensor operator over a sphere p embedded into an infinite medium q
${}^jA_p^q$	spherical component of $\mathbb{A}_p^q$, if it is isotropic
${}^kA_p^q$	deviatoric component of $\mathbb{A}_p^q$, if it is isotropic, thus $\mathbb{A}_p^q = {}^jA_p^q\mathbb{J} + {}^kA_p^q\mathbb{K}$

Liste des tableaux

Table des figures